N73-22396
NASA CR-2229

NASA CONTRACTOR REPORT

NASA CR-2229

60 GHz RADIOMETRIC LOCAL VERTICAL SENSOR EXPERIMENT

by C. Herbert Grauling, Jr.

Prepared by
WESTINGHOUSE DEFENSE AND ELECTRONIC SYSTEMS CENTER
Baltimore, Md. 21203
for Langley Research Center

NATIONAL AERONAUTICS AND SPACE ADMINISTRATION • WASHINGTON, D. C. • APRIL 1973

1. Report No.	2. Government Accession No.	3. Recipient's Catalog No.
NASA CR-2229		

4. Title and Subtitle	5. Report Date
60 GHz RADIOMETRIC LOCAL VERTICAL SENSOR EXPERIMENT	April 1973
	6. Performing Organization Code
7. Author(s) C. Herbert Grauling, Jr.	8. Performing Organization Report No.
9. Performing Organization Name and Address Westinghouse Defense and Electronic Systems Center Systems Development Division Baltimore, Maryland 21203	10. Work Unit No.
	11. Contract or Grant No. NAS1-10131
12. Sponsoring Agency Name and Address National Aeronautics and Space Administration Washington, D.C. 20546	13. Type of Report and Period Covered Contractor Report
	14. Sponsoring Agency Code

15. Supplementary Notes

16. Abstract

This final report summarizes the major contract results. The experiment concept involves the use of millimeter wave radiation from the atmospheric oxygen to provide vertical sensing information to a satellite-borne radiometer. The radiance profile studies require the calculation of ray brightness temperature as a function of tangential altitude and atmosphere model, and the computer program developed for this purpose is discussed. Detailed calculations have been made for a total of 12 atmosphere models, including some showing severe warming conditions. The experiment system analysis investigates the effect of various design choices on system behavior. Calculated temperature profiles are presented for a wide variety of frequencies, bandwidths, and atmosphere models. System performance is determined by the convolution of the brightness temperature and an assumed antenna pattern. A compensation scheme to account for different "plateau" temperatures is developed and demonstrated. Curves of predicted system behavior, both at low altitudes and synchronous, are presented for many different atmosphere combinations, antenna pattern shapes, and antenna beamwidths. The millimeter wave components developed for the local vertical sensor are discussed, with emphasis on the antenna, low noise mixer, and solid-state local oscillator. Planning for two follow-on engineering model experiments is presented. It is concluded that a viable sensing technique exists, useful over a wide range of altitude with an accuracy generally on the order of 0.01 degree or better.

17. Key Words

Radiance Profile
Oxygen
Millimeter Wave
Radiometer
Vertical Sensor
Attitude Control
Atmosphere
Horizon Sensor
Brightness
Temperature
Components

18. Distribution Statement

19. Security Classif. (of this report)	20. Security Classif. (of this page)	21. No. of Pages	22. Price
Unclassified	Unclassified	206	$3.00

Page Intentionally Left Blank

TABLE OF CONTENTS

	Page
1. INTRODUCTION	1
2. EXPERIMENT CONCEPT	3
3. RADIANCE PROFILE STUDIES	9
3.1 Assumptions and Approach	9
3.2 Refractive Index and Attenuation	12
3.3 Brightness Temperature	15
3.4 Computer Program	19
3.5 Atmosphere Models	25
3.6 Brightness Temperature Profiles	35
3.7 Convergence	37
4. EXPERIMENT SYSTEM ANALYSIS	41
4.1 Frequency Effects	41
4.2 Bandwidth Effects	42
4.3 Local Oscillator Stability	60
4.4 Convolution	65
4.5 Compensation for Plateau Height	66
4.6 Predicted Performance	69
4.7 Beamwidth Effects	85
4.8 12 Atmosphere Performance	99
4.9 Experiment System Analysis	107
4.10 Independent Verification of Spacecraft Attitude	112

	Page
5. MILLIMETER WAVE COMPONENTS	115
5.1 Antenna	116
5.1.1 Requirements	116
5.1.2 Design Considerations	116
5.1.3 Slot Fabrication	118
5.1.4 Test Array Measurements	119
5.1.5 Breadboard Model	125
5.1.6 Conclusions	130
5.2 Millimeter Wave Mixer	133
5.2.1 Schottky Barrier Diodes	133
5.2.2 Contacting Techniques	133
5.2.3 Radiation Tests	135
5.2.4 Single Ended Mixer Performance	136
5.2.5 Diode Mount	142
5.2.6 Balanced Mixer Considerations	145
5.3 Solid-State Local Oscillator	146
5.3.1 Silicon Avalanche Diode Oscillators (ADO)	147
5.3.2 Diode Design	149
5.3.3 Oscillator Design to Meet Environmental Requirements	157
5.3.4 Local Oscillator Noise	161
5.4 Radiometer Switch	165
6. ENGINEERING MODEL DEVELOPMENT PLANNING	173
6.1 Atmospheric Data	173
6.2 Vertical Brightness Temperature Profile	174
6.3 Nadir Brightness Temperature Experiment	187
6.4 Local Vertical Sensor Experiment	188
Appendix A. Radiometer Sensitivity	191
References	195

LIST OF ILLUSTRATIONS

Figure		Page
1	Antenna Coordinate System	5
2	A Portion of the Oxygen Spectrum	7
3	Temperature vs Altitude for Model Atmospheres	28
4	Temperature Difference from 1962 Standard Atmosphere vs Altitude for Model Atmospheres	29
5	Pressure Ratio Referred to 1962 Standard Atmosphere vs Altitude for Model Atmospheres	30
6	Attenuation Constant vs Frequency, Atmosphere No. 1	31
7	Attenuation Constant vs Frequency, Atmosphere No. 8	32
8	Attenuation Constant vs Frequency, Atmosphere No. 9	33
9	Attenuation Constant vs Frequency, Atmosphere No. 11	34
10	Brightness Temperature Profile, Spot Frequency, Atmosphere No. 1, Horizon Region	36
11	Brightness Temperature Profile, Spot Frequency, Atmosphere No. 9, Horizon Region	38
12	Brightness Temperature Profile, Spot Frequency, Atmosphere No. 1, Nadir Region	43
13	Brightness Temperature Profile, Spot Frequency, Atmosphere No. 9, Nadir Region	44
14	Brightness Temperature Profile, Bandwidth Average, Atmosphere No. 1, Horizon Region, Frequency Band Above 60.79 GHz.	45
15	Brightness Temperature Profile, Bandwidth Average, Atmosphere No. 9, Horizon Region, Frequency Band Above 60.79 GHz.	46
16	Brightness Temperature Profile, Bandwidth Average, Atmosphere No. 1, Nadir Region, Frequency Band Above 60.79 GHz.	48
17	Brightness Temperature Profile, Bandwidth Average, Atmosphere No. 9, Nadir Region, Frequency Band Above 60.79 GHz	49

Figure		Page
18	Comparison of Brightness Temperature Profiles, Atmosphere No. 1, Horizon Region, for Spot Frequencies and Bandwidth Averages	50
19	Comparison of Brightness Temperature Profiles, Atmosphere No. 9, Horizon Region, for Spot Frequencies and Bandwidth Averages	51
20	Brightness Temperature Versus Frequency, Atmosphere No. 11	52
21	Brightness Temperature Versus Frequency, Atmosphere No. 1	53
22	Brightness Temperature Versus Frequency, Atmosphere No. 8	54
23	Brightness Temperature Versus Frequency, Atmosphere No. 9	55
24	Brightness Temperature Profile, 200-MHz Bandwidth Average, Center Frequency of 60.89 GHz, Comparison of Atmospheres, Horizon Region	58
25	Brightness Temperature Profile, 200-MHz Bandwidth Average, Center Frequency of 60.89 GHz, Comparison of Atmospheres, Nadir Region	59
26	Brightness Temperature Profile, Representative Atmospheres 1, 8, 9, 11, 60.79 - 60.99 GHz	61
27	Brightness Temperature Profile, Atmospheres 4, 5, 6, 10 Compared to Extremes 9, 11, 60.79 - 60.99 GHz	62
28	Brightness Temperature Profile, Atmospheres 16, 17, 18, 19 Compared to Extremes 9, 11, 60.79 - 60.99 GHz	63
29	Brightness Temperature Differences for 200-MHz Bandwidth Average (60.79 - 60.99 GHz), 11 Atmospheres Referred to 1962 Standard Atmosphere	64
30	Comparison of Brightness Temperature Profile (Standard Atmosphere) and Convolved Patterns (Uniform Illumination and Gaussian Beam), 200-nmi Altitude	67
31	Comparison of Brightness Temperature Profile and Convolved Patterns (Cosine and Uniform Illumination, Gaussian Beam), 200-nmi Altitude	68
32	LVS Output Characteristic, 200-nmi Altitude, Uncompensated	71

Figure		Page
33	LVS Output Characteristic, 200-nmi Altitude, Compensation Angles 1.0, 1.5, 2.0 Degrees	72
34	Effect of Antenna Pattern on Compensated LVS Output Characteristics, Atmosphere 1-1	73
35	Detailed LVS Error Characteristic, 200-nmi Altitude, Uncompensated, 1-Degree Beamwidth	75
36	Detailed LVS Error Characteristic, 200-nmi Altitude, Compensated, 1-Degree Beamwidth	76
37	Detailed LVS Error Characteristic, 600-nmi Altitude, Uncompensated, 1-Degree Beamwidth	77
38	Detailed LVS Error Characteristic, 600-nmi Altitude, Compensated, 1-Degree Beamwidth	78
39	Detailed LVS Error Characteristic, Synchronous Altitude, Uncompensated, 1-Degree Beamwidth	79
40	Detailed LVS Error Characteristic, Synchronous Altitude, Compensated, 1-Degree Beamwidth	80
41	Predicted LVS Output Characteristic Showing Effect of Compensation Angle, 200-nmi Altitude	82
42	Predicted LVS Output Characteristic Showing Effect of Compensation Angle, 600-nmi Altitude	83
43	Predicted LVS Output Characteristic Showing Effect of Compensation Angle, Synchronous Altitude	84
44	LVS Output Characteristic Comparing Different Beam Shapes, Uncompensated	86
45	LVS Output Characteristic Comparing Different Beam Shapes, Compensated	87
46	Effect of Beamwidth on LVS Output Characteristic, Atmosphere 1-1	88
47	Effect of Beamwidth on LVS Output Characteristic, Atmosphere 11-9, Uncompensated	89
48	Effect of Beamwidth on LVS Output Characteristic, Atmosphere 11-9, Compensated	91
49	Effect of Beamwidth on LVS Output Characteristic, Coarse Angle Scale	92
50	Beamwidth Effect at Synchronous Altitude, Uncompensated	93

Figure		Page
51	Beamwidth Effect at Synchronous Altitude, Compensated	94
52	Temperature Slope, Atmosphere 11-9, Uncompensated, for Three Satellite Altitudes	96
53	Temperature Slope, Atmosphere 11-9, Compensated, for Three Satellite Altitudes	97
54	Temperature Slope, Atmosphere 1-1, Compensated, for Three Satellite Altitudes	98
55	Brightness Temperature Profile (Standard Atmosphere) and Convolved Patterns (Cosine Illumination), 60-km Altitude	100
56	Predicted LVS Output, 12 Atmospheres, 200-nmi Altitude, Uncompensated	101
57	Predicted LVS Output, 12 Atmospheres, 200-nmi Altitude, Compensated	102
58	Predicted LVS Output, 12 Atmospheres, 600-nmi Altitude, Uncompensated	103
59	Predicted LVS Output, 12 Atmospheres, 600-nmi Altitude, Compensated	104
60	Predicted LVS Output, 12 Atmospheres, Synchronous Altitude, Uncompensated	105
61	Predicted LVS Output, 12 Atmospheres, Synchronous Altitude, Compensated	106
62	80-Element Resonant Array	117
63	Test Sample Measurement Setup	120
64	Spread in Slot Resistance as Measured from a Group of 15 Slots	122
65	Spread in (X/R) as Measured from a Group of 15 Slots	123
66	Effect of Phase and Amplitude Error on Sidelobe Level	124
67	Lines of Constant X/R	125
68	E-Plane (Azimuth) at 61.05 GHz	127
69	H-Plane (Elevation) at 61.05 GHz	128
70	Theoretical vs Measured Azimuth Pattern	129
71	Overall View of 80-Slot Breadboard Antenna	131

Figure		Page
72	Breadboard Antenna Showing H-Plane Flare	132
73	Section of Diode Showing Details of the Overlay Pad	135
74	GaAs Schottky Barrier Diode Chip (0.38 x 0.38 mm) Having Individual 5-μm Diodes with a 20-μm Overlay Pad for Wire Bonding	136
75	Conversion Loss vs LO Drive and Bias	138
76	Computed Mixer Conversion Loss for the Broadband Case (Image Termination Equals Signal Termination)	140
77	Computed Mixer Conversion Loss for Short Circuited Image	140
78	Minimum Mixer Conversion Loss for Both the Image Shorted and Image Terminated Cases as a Function of f/f_{co}	141
79	Double-Diode Wafer	143
80	Closeup of Double-Diode Wafer	144
81	Photograph of RG-98/U Waveguide Wafer Diode Mount	145
82	30-GHz ADO Mount	148
83	Westinghouse Developed Silicon ADO: Silicon Disc Dimension: 40 μm Diameter by 20 μm High (Scanning Electron Microscope Photograph)	150
84	Westinghouse Developed Diode Closeup View	150
85	Calculated Breakdown Voltage and Impurity Concentration vs Frequency for Abrupt Junctions in Si and GaAs	152
86	Calculated Maximum Current Desnity and Depletion Layer Width vs Frequency for Abrupt Junctions in Si and GaAs	153
87	ADO Local Oscillator Power Source	158
88	Millimeter Wave Oscillator Cavity Dimension	159
89	Oscillator Performance Data	160
90	Differential LO Power Reflection from an Assymetric Radiometer Switch and Corresponding Phasor Diagram	167
91	3-Puck Switching Wye Circulator	171
92	Weighting Function DEL WF1 vs Altitude, Atmosphere No. 1, Frequency Above 60.37-GHz LO	176

Figure		Page
93	Weighting Function DEL WF1 vs Altitude, Atmosphere No. 1, Frequency Below 60.37-GHz LO	177
94	Integrated Weighting Function WF vs Altitude, Atmosphere No. 1, Above LO	179
95	Weighting Function DEL WF1 vs Altitude, Atmosphere No. 9, Frequency Above 60.37-GHz LO	180
96	Weighting Function DEL WF1 vs Altitude, Atmosphere No. 19, Frequency Above 60.37-GHz LO	181
97	Altitude for Weighting Function DEL WF1 Peak vs Intermediate Frequency Above LO Showing Possible Channel Selection	182
98	Altitude for Weighting Function DEL WF1 Peak vs Intermediate Frequency Above LO (Expanded Frequency Scale)	183
99	Pressure for Weighting Function DEL WF1 Peak vs Intermediate Frequency Above LO	184
100	Pressure for Weighting Function DEL WF1 Peak vs Intermediate Frequency Above LO	185
101	Millimeter Wave Brightness Temperature Experiment on Spacecraft	187
102	Nadir Brightness Temperature Radiometer	189

60 GHz RADIOMETRIC LOCAL VERTICAL SENSOR EXPERIMENT

By C. Herbert Grauling Jr.
Westinghouse Defense and Electronic Systems Center
Systems Development Division

1. INTRODUCTION

This final report summarizes the major results on Contract No. NAS1-10131 for the development of the Radiometric Local Vertical Sensor Experiment. This is a new sensor operating in the millimeter wave portion of the electromagnetic spectrum. It is a limb looking device, much the same in concept as the infrared limb sensor. The primary limb component detected is the oxygen in the atmosphere; this is of high concentration (almost 21 percent), uniformly distributed around the earth, and a very strong absorber at frequencies near 60 GHz.

The differences in absorber characteristics between the two spectral regions result in comparable, but quite different, profile shapes and characteristics. A large portion of this report is devoted to obtaining the characteristics of the oxygen profile, and many different model atmospheres are considered. This result depends on the basic physical phenomenon of absorption and emission by the atmosphere, and is not under the control of the system designer.

The next major section of the report considers the manner in which various system design choices affect the performance obtained. Items considered include frequency, bandwidth, atmosphere model, antenna pattern, and beamwidth. It is concluded that a viable experiment exists, capable in general of an accuracy of 0.01 degree or better even under maximum expected atmosphere differences.

The two concluding sections of the report discuss the millimeter component development results and plans, and preliminary planning for future engineering model experiments.

Page Intentionally Left Blank

2. EXPERIMENT CONCEPT

The Radiometric Local Vertical Sensor investigated under Contract NAS1-10131 represents a new class of sensor operating in the millimeter wave portion of the electromagnetic spectrum. This sensor is intended to provide a local vertical reference for a spacecraft, based on radiometric measurements of the 60-GHz radiation from the molecular oxygen in the earth's atmosphere. The goal of this contract was to establish feasibility of such a microwave sensor experiment through appropriate analytical studies and the development of critical millimeter wave components. The theoretical analysis and hardware development discussed in this report demonstrate that feasibility has been established.

The sensor concept is readily explained. The earth, when viewed from the spacecraft at an appropriate frequency, say 60.8 GHz, will appear essentially as a uniformly bright circular disc with well-defined edges, and with very low background outside the disc. Details of the actual profile will be discussed later in this report. The near step-function behavior of the observed brightness temperature is caused by the changing attenuation characteristic of the atmosphere in the 30- to 40-kilometer altitude region. An antenna pointed at the edge of this noise disc will exhibit an apparent temperature which is the product of the disc temperature and the fraction of the antenna beam filled by the disc. Assuming circular symmetry in the oxygen mantle, the local vertical has been found when the input noise signal (i.e., the apparent temperature as measured by the radiometer) is the same in all radial directions. Since the physical parameters of temperature and pressure in the 30- to 40-kilometer altitude region can be expected to remain reasonably constant and independent of local influences on the earth below, the oxygen in this region can serve as a precise reference for determination of local

vertical. It is this hypothesis which has been investigated in the current theoretical studies and which would be tested in a future flight experiment.

System geometry may be represented by figure 1. Assuming spherical symmetry, the local vertical passes through the spacecraft and the center of the earth. A direction in space, measured from the spacecraft, is defined by two angles. The angle θ, or nadir angle, is measured from the local vertical, and the angle ϕ is measured in a circumferential direction in a plane normal to the local vertical. Using the local vertical as a polar axis, ϕ is equivalent to longitude, and if the pointing direction from the spacecraft intersects the earth's horizon, then the value of θ is equivalent to the latitude at which the horizon exists. For the case of the oxygen mantle, the apparent horizon is not quite as abrupt as this geometry would imply. The calculated brightness temperature versus altitude curve is, however, quite sharp, and the approximate half-temperature point will be considered as the oxygen horizon. This point occurs at an altitude of about 34 kilometers, with only minor variations depending on the atmosphere model and frequency selected, as will be demonstrated later in this report.

The basic sensor system uses four antenna beams and two radiometers to provide position information along two quadrature axes, with the two beams on a given axis pointed at opposite horizons of the earth. These two beams are symmetrically depressed with respect to the spacecraft horizontal axis so that a change in spacecraft attitude will cause the signal from one beam to increase and the signal from the other to decrease. The resulting temperature difference is sensed by a Dicke-type radiometer, and used either to indicate displacement from local vertical or to control spacecraft attitude by means of a null-seeking servo loop. Assuming spherical symmetry of the earth and its atmosphere, the accuracy of such a vertical sensor is limited only by the sharpness of the antenna beams and the temperature resolution of the radiometer. For an antenna beamwidth of 1 degree, the rate of change of temperature with pointing angle, as seen by the radiometer, is about 400 kelvins per degree. Since the radiometer can readily be

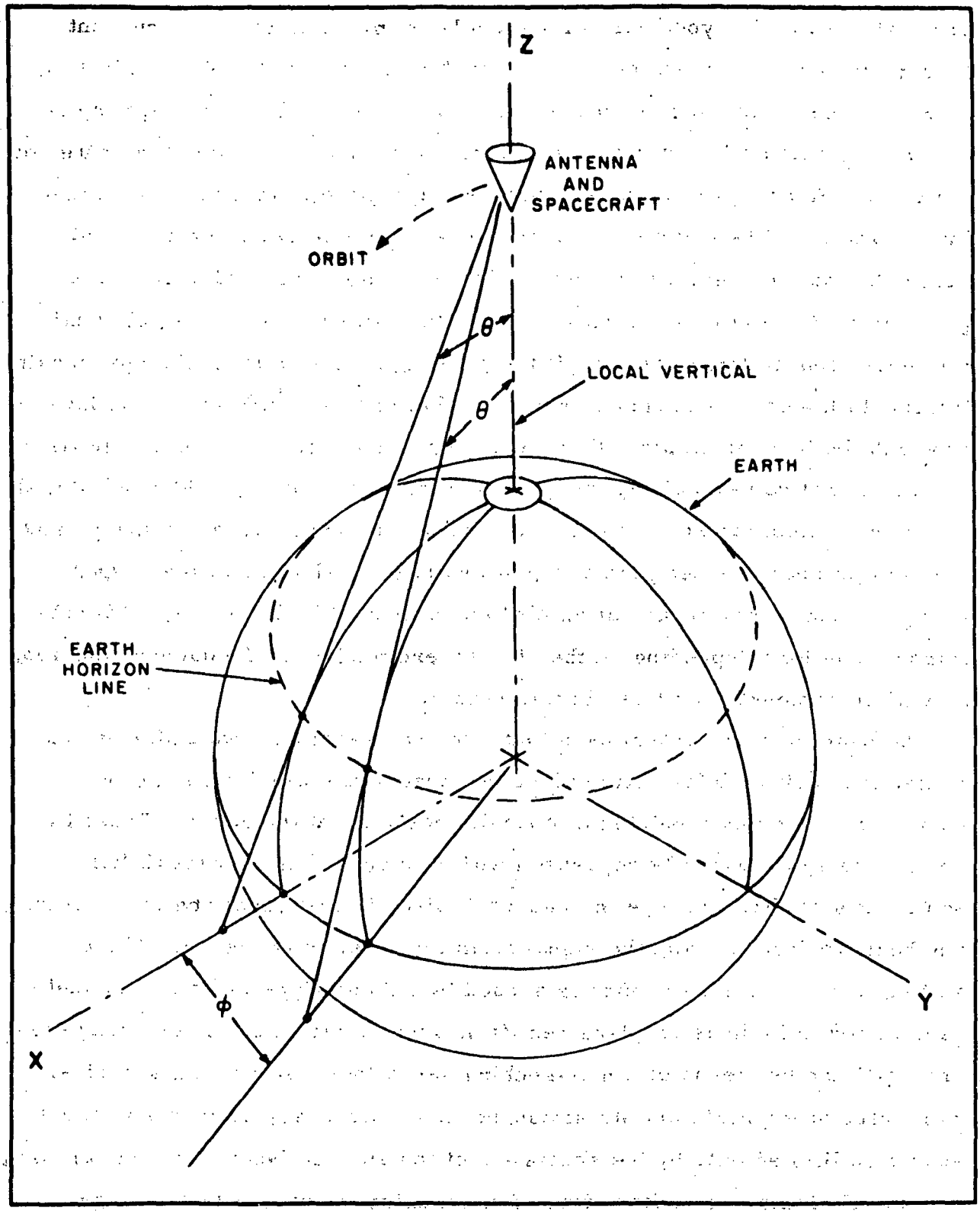

Figure 1. Antenna Coordinate System

made to resolve 1 kelvin, a sensitivity better than 0.003 degree is indicated. The accuracy actually achieved will be determined largely by how well the spherical symmetry assumption is satisfied. The question of atmospheric effects thus becomes of prime importance in predicting performance of the local vertical sensor, and much of the analytical studies has been concentrated in this area.

The two antenna beams on a given axis, viewing opposite horizons, can conceivably be looking at somewhat different atmosphere structures. For an east-west axis along the equator, there should be little problem; but for a north-south axis centered on the equator, one hemisphere tends toward summer conditions as the other tends toward winter. At very low satellite altitudes, the atmospheres must be essentially the same, although a gradient situation can exist. As satellite altitude increases, the separation of the observed atmospheres also increases, and hence a different brightness temperature profile becomes more probable. In the real case of the aspherical earth, the bisector of the angle between the horizons may not pass through the center of the earth, as assumed above, but it is still a valid measure of pointing attitude control applications.

The absorption of electromagnetic energy by the oxygen in the atmosphere results from an interaction between the magnetic dipole moment of the oxygen molecule and the electromagnetic field. The spectrum observed represents fine-structure transitions between the different spin states associated with a given rotational state. For each rotational state, N, two transitions are possible, designated N+ and N-. Microwave absorption by oxygen was first discussed by Van Vleck,[1] and the transition frequencies used in this report are those given by Meeks and Lilley.[2] Figure 2 shows some of the strong lines near the center of the oxygen absorption complex, giving resonant frequency in GHz, spacing between lines in MHz, and rotational quantum number, N, for each line. In calculating attenuation and index of refraction in the atmosphere, it is necessary to sum over all rotational states with appreciable population at the temperatures encountered in the atmosphere.

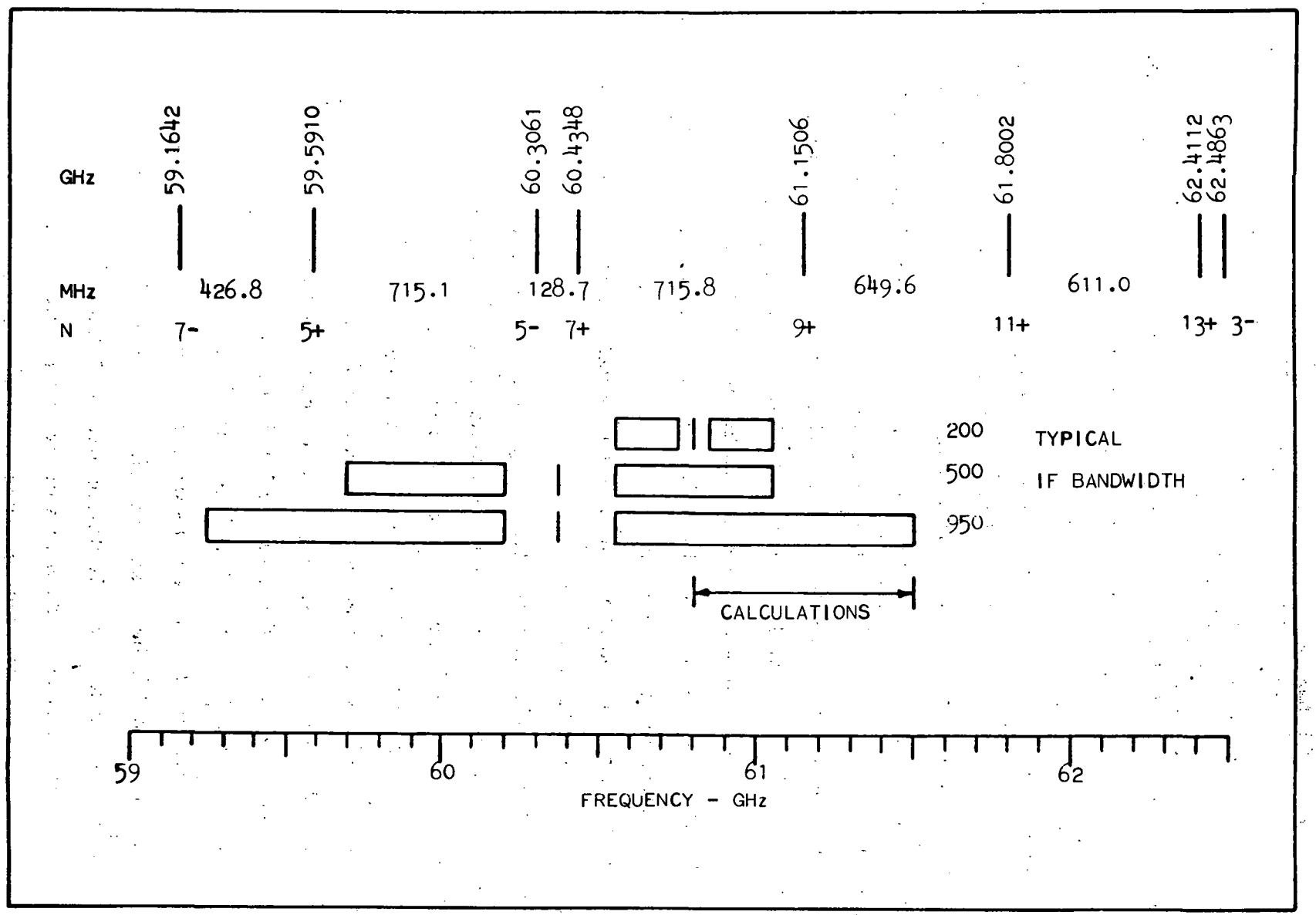

Figure 2. A Portion of the Oxygen Spectrum

Our calculations use values of N from 1 to 45 (only odd values are permitted because of the exclusion principle) so that the effects of 45 lines in the complex from about 50 to 70 GHz plus the single line at 118.75 GHz are considered.

Viewed as an emitter, the oxygen radiates not only at the resonant frequencies but over the entire band of frequencies at which significant attenuation occurs. For the vertical sensing application, the region between resonance lines is actually more useful because it provides a greater delineation of brightness temperature with altitude as well as sufficient bandwidth for the radiometer. Also illustrated in figure 2 are several possible operating frequency regions that can be considered for the vertical sensor. A double sideband radiometer is assumed, with the line representing the local oscillator and the box the IF passband on either side. For example, the entire band may be contained between the 7+ and 9+ lines, with the LO at about 60.8 GHz; or the LO may be located between the 5- and 7+ lines at about 60.37 GHz, and the IF passband may include or avoid a resonance line, as shown. Detailed brightness temperature profiles have been calculated over the frequency interval noted in the figure, and this will be discussed later in the report.

3. RADIANCE PROFILE STUDIES

A given ray leaving the spacecraft antenna and entering the earth's atmosphere will undergo a small bending effect due to the index of refraction of the atmosphere and will be attenuated by an amount determined by its frequency. In general, both index of refraction and attenuation constant increase with pressure and hence become larger at lower altitudes. The ray will either strike the earth, or it will pass completely through the atmosphere and out the other side. When viewed from the spacecraft, this ray will exhibit a brightness temperature which, in accordance with the well known equations of radiative transfer,[3,4] is determined by the physical temperature of the attenuating regions through which it passed, plus a contribution based on its termination. For a frequency near 60 GHz, the atmosphere attenuation can become quite large due to absorption by oxygen, as discussed earlier, and the observed brightness temperature becomes a rapidly varying function of the nadir angle, θ, in the vicinity of the oxygen horizon. The objective of the radiance profile studies is to determine the detailed variation of brightness temperature as a function of ray pointing direction for any given combination of frequency and assumed atmosphere model. This brightness temperature profile information, in turn, serves as an input to the experiment system analysis so that the behavior of the sensor system may be predicted and the influence of various design choices investigated.

3.1 ASSUMPTIONS AND APPROACH

For the purpose of determining the brightness temperature profile, a spherically symmetric earth and atmosphere is assumed in order to present a tractable problem. Two separate but related calculations are required. One is the actual brightness temperature calculation, which depends on the temperature and attenuation constant of the absorbing medium and the path

length in this medium. The other is a ray trace calculation to determine the path of the ray, in order that the appropriate values of temperature, attenuation, and path length may be determined for the brightness temperature calculation. Both of these calculations may be expressed in integral form. However, their nature is such that a closed form result does not exist; therefore, a numerical integration process using a digital computer is employed.

A particular model atmosphere is expressed in the form of a series of spherical shells, with the atmospheric parameters of pressure, temperature, and water vapor content defined at the altitudes corresponding to the shell boundaries. The computer program requires that index of refraction and attenuation constant be known at interior points in each shell; hence, some interpolation technique is required. One possible approach is to interpolate pressure and temperature and calculate the other parameters at each desired point. Another approach, and the one adopted in our program, is to compute the index and attenuation on the shell boundaries and then to interpolate these quantities for intermediate points. The rationale behind this choice is readily explained. Both the microwave absorption coefficient and the refractive index (expressed as $\epsilon = n-1$) are essentially proportional to a power of atmospheric pressure, which in turn varies very nearly as a negative exponential function of altitude over the entire altitude range. This pressure variation, which spans roughly six orders of magnitude, is the major variable factor in the electrical parameters; and, hence, the values of index and attenuation at an intermediate height within any given shell may be obtained by interpolation using exponential functions fitted to the parameter values calculated on the shell boundaries. The use of this particular interpolation technique represents an assumption in our program, but a major advantage is gained. The results should be almost identical to those obtained by interpolating an exponential function of pressure to obtain the intermediate point. However, the intermediate parameters may be obtained by a simple square root, or at worst, a simple exponential; whereas if pressure and temperature are interpolated, a new quantum mechanical sum over all resonance lines is

again required. Thus, computer processing time is greatly reduced at no loss in accuracy.

Two facets of the approach chosen should be noted. From the above discussion, it is clear that although the model atmosphere is defined in terms of discrete shells (i. e., at discrete heights) both the absorption and the index are permitted to vary across the shell and are interpolated as described. Thus, the ray tracing technique approximates a continuously bending ray in a continuously changing atmosphere and hence represents an excellent simulation of the real case.

In addition, the basic philosophy employed in the brightness temperature computer program is that if all expressions used are differentially correct, then the results may be tested by decreasing the step size and noting the convergence. Assuming the desired convergence, this result will be the most accurate obtainable, within the limits of the basic assumptions and the data available. To implement this philosophy, both the opacity (integrated attenuation constant) and brightness temperature contributions of each of a number of roughly equal increments (segments) along the ray path are calculated and summed. A maximum step size is used as a parameter in the program, and this can be reduced as necessary to test convergence. The program is adaptive in that each shell is subdivided as necessary so that the path length in any segment is less than the maximum allowed. If the total path in any shell is less than this maximum, no subdividing is employed, and the shell is treated as containing only one segment. In those shells which are subdivided, all segment lengths are roughly equal, and the number of segments is adjusted as necessary to provide the minimum number consistent with the assigned maximum path length.

Under the assumption of spherical symmetry, as discussed above, the refractive index is a function of height above a smooth earth, and the structure is horizontally homogeneous. The appropriate expression for the bending of a ray in this atmosphere is Snell's law for polar coordinates:[5, 6]

$$n(r) \cdot r \cdot \sin \alpha = \text{constant}, \qquad (1)$$

where α is the angle between the radius vector of length r and the direction of the ray (i. e., the tangent at that point), and n(r) is the index of refraction, explicitly written as a function of r.

In the vicinity of a satellite at radius R_s, assumed well outside the earth's atmosphere, the index n becomes unity, the path is a straight line, and α becomes the nadir angle θ. Thus

$$R_s \sin \theta = \text{constant} = \rho, \tag{2}$$

where ρ is defined as the normal distance from the center of the earth to the unrefracted ray from the satellite, a simple geometrical interpretation. This radius, ρ, will be used to characterize the ray whose brightness temperature is to be calculated, and it will be referred to as tangential radius. It will usually be used in the form of a tangential altitude by subtracting the earth's radius, thus

$$H = \rho - R_E \tag{3}$$

The temperature profiles to be discussed later show brightness temperature versus tangential altitude, because this is a somewhat more general characterization than the angle variable implied earlier in this chapter. The use of tangential altitude permits one profile to be used for many satellite altitudes by a simple geometrical transformation, and yet it provides a precise delineation of the critical portion of the profile near the horizon. For values of H greater than the maximum atmosphere layer considered, the ray misses the atmosphere and assumes the temperature of space. H can also be less than zero, in which case the ray strikes the earth and $H = -R_E$ represents a ray along the nadir.

3.2 REFRACTIVE INDEX AND ATTENUATION

An important section of the radiance profile studies involves the calculation of the electrical parameters of index of refraction and attenuation constant from the physical parameters of temperature, pressure, and water vapor content of the atmosphere. Physically, this is handled as a subroutine of the main computer program. Theoretically, what is involved is a complete

quantum mechanical representation of the index and attenuation in the vicinity of the oxygen absorption complex, along with the appropriate parameters for dry air and water vapor, including the water line at 22.235 GHz.

In the vicinity of an absorption line, anomalous dispersion will occur; i.e., the index of refraction varies as a function of frequency across the line. Since the oxygen lines are relatively intense, the effect on the index was also calculated because a very small change in bending can cause the ray to follow a different path and hence see a significantly different attenuation and brightness temperature. The form of the index and absorption functions are similar, since they arise from the real and imaginary parts, respectively, of the complex dielectric constant of the atmosphere.

The absorption coefficient, γ, is expressed in terms of loss per unit length, and on the curves presented later in this chapter it is given in dB per kilometer as a convenient unit. The index of refraction, n, is a number slightly greater then unity, and it is frequently expressed in terms of the refractivity, ϵ, where $\epsilon = n-1$. In fact, the basic calculation from the physical atmosphere parameters yields the refractivity, ϵ, and, the index, n, is then derived by adding ϵ to unity.

The oxygen absorption coefficient calculations used in our program follow the procedure outlined by Meeks and Lilley.[2] Their empirical relation for the width of the pressure broadened line is followed as is the approximate procedure of adding the doppler broadening term to the pressure term to obtain a total linewidth. Zeeman effect has not been included in the program, but its overall effect is small; it is primarily significant above about 50 kilometers where the brightness temperature is already low and approaching that of space. A recent paper by Reber, et. al., gives a slightly different empirical relation for the pressure broadening term.[7] This expression has not been evaluated as yet but should be to determine the comparative effect. No large changes are anticipated, because their zenith attenuation values are comparable to ours. The calculation of absorption by water vapor follows the work of Barrett and Chung.[8]

There is, however, one significant difference between our work and that of Meeks and Lilley. They neglect refraction effects and assume a horizontally stratified plane atmosphere. We are primarily interested in the grazing ray in the vicinity of the oxygen horizon, and, hence, we must consider both the spherical geometry and the refraction effects. As noted earlier, the refractive index variation in the vicinity of the oxygen resonance complex was calculated, and this derivation is based on principles given by Van Vleck.[1]

It should be noted here that the least accurate part of the entire brightness temperature calculation for a given model atmosphere is the conversion of the physical atmosphere parameters to electrical ones. This conversion requires an empirical relationship, and it is here that it should be interesting to compare the effect of the Meeks and Lilley line broadening expression with that of Reber, et. al.. A slight shift in the absolute values of the brightness temperature profile for a given atmosphere would be expected, but the relative effects of various atmosphere models, which in the final analysis is what determines the accuracy of the sensor system, should remain almost totally unchanged.

It is interesting to consider some of the parameter changes that occur in the atmosphere. Over the altitude range from 0 to 100 kilometers, the pressure varies by roughly six orders of magnitude. At 60.8 GHz, assuming dry air, the refractivity, ϵ, varies by a similar amount, but the absorption coefficient, γ, varies by almost 10 orders of magnitude. Over a large portion of the range, attenuation varies essentially as the square of the pressure, since attenuation is proportional to pressure times a linewidth parameter and linewidth is also proportional to pressure at this frequency. At a resonance line, this rapid change in attenuation is greatly reduced, and γ is almost constant with altitude and pressure over a rather wide region. This again points out the desirability of operating the local vertical sensor in the region between resonance lines, where a rapid change of attenuation and, hence, brightness temperature, occurs. At 60.8 GHz, the dispersive

refractivity term due to the oxygen resonance is three orders of magnitude less than the total refractivity; but at 61.13 GHz, which is still 20 MHz (and many linewidths for altitudes above 40 kilometers) away from resonance, it is already contributing several percent of the total ϵ, an amount sufficient to justify its inclusion in the calculation.

3.3 BRIGHTNESS TEMPERATURE

A greatly simplified expression for the brightness temperature, T_B, of a given ray, as viewed by the satellite, may be written as:

$$T_B = \int T e^{-\tau} \gamma \, ds \tag{4}$$

where T is the temperature, and γ the absorption coefficient associated with an elemental length of path, ds, along the ray. The quantity, τ, represents the total opacity measured from the satellite to the element in question, and the integral is taken over the complete path from the satellite through the atmosphere. The expression $e^{-\tau}$ represents the fraction of the noise power transmitted through the lossy medium from the elemental source to the point of observation. Expressed in terms more familiar to those working in the microwave area, τ represents twice the path attenuation in nepers, or equivalently, the loss in dB divided by 4.343, a constant equal to $10 \log_{10} e$. Clearly, the opacity is also given by an integral, namely:

$$\tau = \int \gamma' \, ds' , \tag{5}$$

where the integral is taken from the satellite to the segment ds of equation 4, and the prime notation refers to an elemental segment in this integral.

If the ray is not completely absorbed in the atmosphere it either passes into space and is absorbed, or it strikes the earth and will be assumed to be absorbed. (This latter assumption is not critical in the frequency band being considered, because the attenuation is so large. For other applications in a different frequency region, one might want to consider reflection rather than absorption at this interface.) In either case, an extra term is added to equation 4, of the form $T_o e^{-\tau_o}$, where T_o is the temperature of the absorbing termination and τ_o is the total path opacity.

In order to proceed with the calculation of T_B, it is necessary to establish a value for ds in equation 4. This value is obtained by a ray tracing calculation. Combination of equations 1 and 2 yields

$$nr \sin \alpha = \rho \tag{6}$$

as the general expression for the ray in the assumed spherical atmosphere. As an example, assume an atmosphere model extending to 100-kilometer altitude and assume ρ is selected so that the tangential altitude, H (see equation 3), is 30 kilometers. As the ray enters the atmosphere, it moves from an altitude of 100 kilometers toward an altitude of 30 kilometers. In addition, it also starts to bend downward, and since n increases as altitude decreases, the amount of bending increases until the ray reaches its point of closest approach to the earth. At this point $\sin \alpha = 1$ and

$$n(r_c) \cdot r_c = \rho \tag{7}$$

where r_c is the radius of closest approach. Clearly, since $n > 1$, $r_c < \rho$, and the altitude of closest approach r_c is somewhat less than H. From this point on bending continues in the same direction but at a decreasing rate until the ray finally passes out the other side of the atmosphere. It is also clear that the length of this curved path through the atmosphere is greater than if the ray had merely followed a straight path tangent to H. The fact that the minimum altitude dips below H means that a somewhat higher absorption coefficient is encountered. Thus, the values of τ, γ, and ds applicable to equation 4 are all greater on the curved path than they would be on a straight path, but the values are not yet known. The only well defined quantities, suitable for integration limits encountered in this ray trace example, are the altitude limit of the atmosphere and the radius r_c. Thus, an expression for s in terms of r would appear to be the next logical step.

A combination of Snell's law, from equation 6 with the polar coordinate differential element, yields

$$ds = \frac{nr\,dr}{\sqrt{n^2 r^2 - \rho^2}} \tag{8}$$

In integral form

$$S = \int ds = \int \frac{nr\,dr}{\sqrt{n^2 r^2 - \rho^2}} \tag{9}$$

where S is now the total path length. Only one half the path, from the altitude limit (expressed in r) to r_c need be calculated, as the other half is identical under the spherical symmetry assumption. Since n is a function of r, this integral, like the former ones, does not have a known closed-form answer.

This integral can be evaluated numerically by forming a series of partial sums and adding them to produce the desired total summation. This involves working with finite segments Δr rather than the mathematical differential dr. There is an approximation involved here, of course, but by using more steps of a smaller size we should be able to approach arbitrarily close to the true integral. This is the basis of the earlier comments about keeping the expressions differentially correct, so that the results may be tested by decreasing the step size and noting the convergence.

For numerical integration the appropriate form of equation 8 becomes

$$\Delta s = \frac{nr\,\Delta r}{\sqrt{n^2 r^2 - \rho^2}} \tag{10}$$

Since Δr is now a finite step size, the question arises as to where n and r should be measured. The total path is subdivided into a number of prescribed increments of r, and the midpoint in r (or equivalently, in h) is chosen as representative of the given segment. Thus, finally

$$\Delta s = \frac{\bar{n}\,\bar{r}\,(r_2 - r_1)}{\sqrt{\bar{n}^2 \bar{r}^2 - \rho^2}} \tag{11}$$

where r_2 and r_1 are the boundaries of the segment, and $\bar{n}$ is the value of n at $\bar{r} = \frac{r_1 + r_2}{2}$. It is this expression which is summed to produce the equivalent of equation 9. After subdividing the entire altitude range as finely as desired, it is possible to tabulate the length of each segment from equation 11 and keep

a running subtotal to give the total length from the point of entering the atmosphere to the segment in question.

Similarly, both equations 4 and 5 may be treated as a summation of discrete partial sums. It is important to note that the identical altitude subdivisions, used in equation 11, can be applied to these equations. Hence, all three equations can be integrated simultaneously to yield the individual shell (or segment if desired) contribution plus the running subtotal of all shells to that point.

For completeness, we express the new forms for equations 5 and 4 as

$$\Delta\tau_j = \bar{\gamma}_j \quad \Delta s_j \tag{12}$$

and

$$\Delta T_{B_j} = \bar{T}_j e^{-\left(\frac{\Delta\tau_j}{2} + \sum_{1}^{j-1} \Delta\tau_i \right)} \Delta\tau_j \tag{13}$$

These expressions continue the concept of evaluating the parameters at the midpoint of the segment, and equation 13 utilizes total opacity calculated to the midpoint of the segment whose contribution is being evaluated. This is readily shown to be the proper treatment for a low-loss segment ($\Delta\tau \ll 1$) having constant T and γ, but the derivation will not be included here.

All material, necessary for calculation of the ray brightness temperature, is now available, and the detailed steps in the computer program will be discussed in the following section. It is preferred to treat each shell as a separate entity in the calculation. Thus, the operation of subdividing is applied to each shell individually, and a good estimate of total path length expected in the shell can be employed to determine the required number of segments. In addition, a readout of the results after the calculation for each shell is available, if desired. This readout permits a check on general program behavior and also clearly shows the atmosphere regions which are the major contributors to the observed brightness temperature. In addition, some basic program modifications will be considered in order to provide better computational accuracy.

3.4 COMPUTER PROGRAM

The basic theoretical concepts in the brightness temperature calculation were given in paragraph 3.3. In developing the program, discussed in this section, three additional computational concepts were considered. First, the results had to be accurate in order to perform reliable convergence tests. This implies that the machine must carry an adequate number of significant digits. Secondly, since many computations are obviously involved, the program must be efficient to prevent excessive machine time. This is really an economic tradeoff in that a more efficient program can calculate a larger number of cases for comparison of results. Thirdly, an attempt was made to write all expressions in a manner especially suited to digital computation, and several examples of this will be noted. It was felt that, with reasonable care, the necessary accuracy could be obtained with the computer in single precision, and the degree to which this was achieved will be demonstrated later.

The program initially sets the radius of the earth, $R_E = 6,356.912$ kilometers, corresponding to the polar radius and the temperature of space to 4 K. The temperature of the earth will be set to the lowest atmosphere shell boundary, at 0 altitude. The following steps are then performed by the program:

a. Read in the desired atmosphere model. This defines the shell boundaries in terms of altitude, pressure, and temperature. At present water vapor content is also read in, but this can be changed to calculate water vapor from atmospheric density and a water vapor mixing ratio.

b. Select the desired frequency.

c. Calculate ϵ and γ on the shell boundaries. This is accomplished with the subroutine discussed in an earlier section. The values, of course, are dependent on frequency and are stored in a table for later use. In any given shell, these parameters are assumed to vary as an exponential function of altitude, for example,

$$\epsilon(h) = ce^{-\alpha h} \tag{14}$$

where the constants are obtained by a two-point fit at the shell boundaries. This expression leads to an interpolation formula for the value at an interior point in the kth shell, with boundaries k and k-1, as follows

$$\epsilon(h) = \epsilon_{k-1} \left(\frac{\epsilon_k}{\epsilon_{k-1}} \right)^{\frac{h-h_{k-1}}{h_k - h_{k-1}}} \tag{15}$$

A similar expression applies to $\gamma(h)$. In many cases an even simpler formula will be used. Referring to equation 15, if h is taken at the midpoint of the shell (i.e., at $\bar{h} = \frac{h_k + h_{k-1}}{2}$), then the desired parameter becomes a simple geometric mean thus

$$\epsilon(\bar{h}) = \sqrt{\epsilon_{k-1} \cdot \epsilon_k} \tag{16}$$

Square root is a faster machine operation then raising to a power, and its use can save significant running time since a similar calculation must ultimately be applied to each segment of the path.

d. Select the desired value of Δs_{max}, the maximum path length step that will be permitted. This is a fundamental parameter in the program, and the one that is varied to demonstrate convergence.

e. Select H, the tangential altitude of the desired ray.

f. Calculate $\rho_E = n(R_E) \cdot R_E$. From equation 7, this represents the tangential radius that permits the point of closest approach to just equal the earth's radius. The calculation is actually performed in the form

$$h_E = R_E \cdot \epsilon(R_E) \tag{17}$$

where $\epsilon(R_E)$ is the refractivity at $h = 0$; that is, at the surface of the earth, which is the lowest shell boundary. The use of altitude in equation 17 permits more significant digits to be carried than in the corresponding equation for radius.

g. Start the ray tracing process by testing whether the ray hits or misses the earth. If $H \leq h_E$, the ray strikes the earth, and the integration calculations start at the upper atmosphere shell and terminate at h = 0

(or $r = R_E$). If $H > h_E$, the ray passes the earth at a point of closest approach, h_c, and proceeds through the other side of the atmosphere.

h. If $H > h_E$ from the above step, an iterative application of Newton's method to equation 7 results in a determination of the value of h_c, the lower altitude limit of the integration process.

i. Set up the arc length calculation. Basically, this comes from equation 11,

$$\Delta s = \frac{\bar{n}\,\bar{r}\,(r_2 - r_1)}{\sqrt{n^2 r^2 - \rho^2}}$$

The demoninator of this equation is better expressed as $\sqrt{(\bar{n}\,\bar{r} - \rho)(\bar{n}\,\bar{r} + \rho)}$ for computational purposes, since, from equation 7, $nr = \rho$ at $h = h_c$ and hence the first term is close to 0. This concept can be carried still further for better machine accuracy without the use of double precision by use of the expression $\sqrt{(\bar{r} - \rho + \bar{\epsilon}\,\bar{r})(\bar{r} + \rho + \bar{\epsilon}\,\bar{r})}$ or finally, by use of $\sqrt{(\bar{h} - H + \bar{\epsilon}\,\bar{r})(\bar{h} + H + 2R_E + \bar{\epsilon}\,\bar{r})}$. It should be noted that even the order in which the terms are written can be significant in maintaining computational accuracy.

j. Calculate the estimated total path length for the upper shell, from step i above.

k. Subdivide the shell to meet the Δs_{max} requirement. In general, equal altitude steps are used, and the number of segments is found by dividing the estimated length by Δs_{max} and using the next higher power of 2. This permits the use of a square root interpolation for ϵ and γ similar to that suggested in step c and also provides an allowance for the fact that equal altitude steps do not produce equal path length steps. Calculate Δs for each segment from step i above.

l. Set up the brightness temperature calculation. This involves the use of equation 12 for the opacity of each segment, and equation 13 to determine the contribution of each segment to the brightness temperature.

m. Sum the individual segment contributions to obtain the total Δs, $\Delta \tau$, and ΔT_B for the shell.

n. Repeat steps j through m for the remaining shells in order, maintaining overall totals for S, τ, and T_B. If the ray hits the earth, integration stops at h = o. If the ray misses the earth, integration proceeds downward until $h = h_c$, at which point h is again increased toward the upper atmosphere limit. In this case, certain data, stored as h decreases, is reused as h increases to avoid the need for recomputing this information. Segment temperature and opacity repeat in reverse order, but total opacity continues to increase.

o. Calculate the contribution from the ray termination, either earth or space, as discussed in connection with equation 4, and add to determine final T_B value.

p. For the grazing ray case, equal altitude divisions do not provide sufficiently equal path length increments in the vicinity of h_c, and a different subdividing technique is employed. The two bottom shells (i.e., the one containing h_c and the next one above it) are divided into essentially equal length segments by using altitude divisions which are proportional to the squares of the integers representing the segments. This criterion is used on the two lowest shells whenever the tangential altitude, H, of the ray is greater than -100 kilometers. For this purpose, a ray which strikes the earth is defined as having h_c = o.

q. Stops are provided in the program to help reduce computer running time. Two stops are employed, either of which causes the calculation to stop at the completion of a shell. One is based on total opacity, currently set to stop at a total value of 65 dB. The other stop occurs if the contribution from any given shell (except the lowest one) is both less than 10^{-4} K and less than the previous shell when suitably adjusted for differing shell thicknesses.

The above 17 steps (a through q) represent the basic structure of the computer program for brightness temperature, which at the same time

determines path length and opacity. This basic program has been further improved by developing more precise formulas for the incremental values of Δs, $\Delta \tau$, and ΔT_B than those given in equations 11, 12, and 13. In addition to increased computational accuracy, these new formulas are designed to account for the nonvanishing step size. Hence their use should result in more rapid convergence of the results as step size is reduced, and computer time can be reduced by using a larger step size.

A major change has been made in the path length calculation. A consideration of equation 7 shows that the denominator in equation 9 becomes zero at the point of closest approach of the ray. Thus, the integrand becomes infinite at this point, but the integral for length must remain finite. This unfortunate situation causes a significant error in the incremental expression for Δs given in equation 11. Since n and r are evaluated at the midjoint of the segment, this expression never becomes infinite. However, the length of the first segment adjacent to r_c (i.e., when $r_1 = r_c$ in equation 11) will always be too small by a factor of $\sqrt{2}$, no matter how small a segment is selected. Successive segments show rapidly decreasing errors, but many segments are required to make the total length error in a given shell tolerable. The revised length increment may be written basically as

$$\Delta s = \frac{2 \bar{n} \bar{r} (r_2 - r_1)}{\sqrt{\bar{n}^2 r_2^2 - \rho^2} + \sqrt{\bar{n}^2 r_1^2 - \rho^2}} \quad . \tag{18}$$

For computational accuracy, the square roots in the denominator should be handled as in step i of the computer program. If $\bar{n}$ in the second square root were replaced by n_1, the value at the lower altitude end of the segment, this root would be zero at $r_1 = r_c$. The total denominator, however, is not zero, and Δs is the correct incremental length for this segment. Since $\bar{n} < n_1$, the second square root of equation 18 actually becomes negative at the bottom segment and should be set equal to zero. For all other segments, the expression is well behaved, and this new formula for Δs gives the most

accurate value known over the entire altitude range. For $\bar{r}$ far from r_c and Δr small, equation 18 reduces to the same value as equation 11.

The modification to the opacity expression is in the form of a series correction term that accounts for the height differential over the segment. The attenuation constant, γ, was earlier assumed to vary exponentially over a shell, in the form

$$\gamma(h) = ce^{-ah} \quad . \tag{19}$$

(This equation is similar to equation 14, but new values of c and a are now required since the expression is for γ and not for ϵ.) When this variation is taken into account, the total opacity of a segment is slightly greater than that obtained by using the product of the midpoint value and the segment length, as in equation 12. The appropriate expression is

$$\Delta\tau_j = \bar{\gamma}_j \Delta s_j \left[1 + \frac{\left(a\frac{\Delta h}{2}\right)^2}{3!} + \frac{\left(a\frac{\Delta h}{2}\right)^4}{5!} + \frac{\left(a\frac{\Delta h}{2}\right)^6}{7!} \right] \tag{20}$$

where Δh is the altitude change over the jth segment, and a, as obtained by fitting equation 19 at the shell boundaries, is given by

$$a = \frac{1}{h_k - h_{k-1}} \ln\left(\frac{\gamma_{k-1}}{\gamma_k}\right) \tag{21}$$

For a grazing ray near h_c, this correction will not have much effect, as the height change per segment is small. Its greatest overall effect will be for rays directed along the nadir. To demonstrate the effectiveness of this correction, total opacity was calculated using the standard dry atmosphere in a model consisting of 20 shells, each 5 kilometers thick. For values of Δh varying from the full 5 kilometers down to less than 0.1 kilometer, the same total opacity, to eight significant digits, was obtained for a ray along the nadir.

Modifications to the brightness temperature equation provide a more accurate expression for the temperature contribution of a given segment. The details of this change are beyond the scope of this report. It is sufficient to note that an attempt is made to account for the physical temperature

differential across the segment and that the expression uses the temperatures at both ends of the segment, rather than at its midpoint as was used in equation 13. In addition, the exponential term uses total opacity only to the edge of segment, and not to its midpoint.

Some results of the convergence tests will be given at the end of this section.

3.5 ATMOSPHERE MODELS

To date, 19 possible atmosphere models have been considered. The first is taken from the 1962 Standard Atmosphere,[9] and the next 14 from the 1966 Supplement.[10] The remaining 4 will be discussed in more detail below. These atmosphere models have been numbered consecutively for convenience, based on the order in which they appear in table 1. Throughout the remainder of this report, these atmospheres will be referred to by these arbitrarily assigned numbers for convenience and identification.

TABLE 1

ATMOSPHERE MODELS

Atmosphere No.	Description		Notes
1	Standard	*	
2	15° N Annual		
3	30° N January		
4	30° N July	*	
5	45° N January	*	
6	45° N July	*	
7	Mid Latitude Spring/Fall		
8	60° N January	*	
9	60° N January (Cold)	*	80 km max
10	60° N January (Warm)	*	80 km max
11	60° N July	*	
12	75° N January		30 km max
13	75° N January (Cold)		30 km max
14	75° N January (Warm)		30 km max
15	75° N July		30 km max
16	#250 of CR-66184	*	90 km max
17	#257 of CR-66184	*	90 km max
18	#2 Peak Warming - West Geirinish	*	90 km max
19	#3 Advanced Stage - West Geirinish	*	90 km max

* Used for brightness temperature calculation

The models, considered for use in brightness temperature calculations, have been chosen to provide a data point at each kilometer of altitude, if available from the table, up to a maximum altitude of 100 kilometers. These 1-kilometer points thus correspond to the shell boundaries discussed earlier, and this spacing was assumed to be sufficiently close to provide accurate brightness temperature results. At 100 kilometers, only frequencies extremely close to a precise resonance line see any effect from the atmosphere, and hence above this altitude the atmosphere is considered as a lossless vacuum, i.e., $\gamma = 0$, $\epsilon = 0$. Only one model, number 1, provides a complete set of data points. Model numbers 12, 13, 14, and 15 provide a point at each kilometer, but stop abruptly at 30 kilometers. Since a ray with a tangential altitude of 30 kilometers already exhibits roughly 90 percent of the total available brightness temperature, these models are useless for calculation purposes. Atmosphere numbers 9 and 10 provide data every kilometer, but stop at 80 kilometers. This is sufficiently high to be quite useful, and hence each is treated as a complete atmosphere, but with nothing above 80 rather than 100 kilometers. These limits are noted in table 1. The other models from the 1966 Supplement extend above 100 kilometers in the table, but data from 90 to 100 kilometers is available only every 2 kilometers.

In addition to the conventional tabulated atmosphere models, it was desired to investigate the performance of the local vertical sensor using some more "extreme" models, such as those associated with stratospheric or "explosive" warmings. The final 4 atmosphere models were provided through the courtesy of Mr. Richard E. Davis of Langley Research Center. He selected several models from NASA CR-66184[11] as showing evidence of stratospheric warming, and from these we have selected model numbers 16 and 17. These models extend to 90 kilometers, as noted, but have a rather irregular spacing ranging from 0.4 to 2.4 kilometers between data points. Temperature data on the severe mid-winter stratospheric warming of 1967-68 has been published by Karen Labitzke[12] and others.[13] Mr. Davis processed the Labitzke data[12] for West Geirinish, Scotland, (latitude 57°N) and provided atmosphere

models with data every kilometer to 90 kilometers. Two of these models, assumed to be most severe, are used as numbers 18 and 19.

Figure 3 shows the temperature variation of 15 model atmospheres with altitude. Over the region between 30 and 60 kilometers, where most of the brightness temperature contribution occurs for grazing rays, the average temperature is rising with altitude. Figure 4 shows the temperature difference and figure 5 the pressure ratio, both referred to the standard atmosphere at the corresponding altitude.

These curves clearly show that, over the altitude range of 30 to 60 kilometers, atmospheres 9 and 11 represent extreme cases both in pressure and temperature. This is not too surprising when the descriptions are noted, namely 60° N January (Cold) for No. 9 and 60° N July for No. 11. Atmosphere numbers 1 and 8 are roughly equally spaced between these two extremes, particularly in pressure, and hence these four atmosphere models will be considered representative of most cases likely to be encountered. Various calculations comparing these four cases will be presented.

The absorption coefficient varies directly with pressure and inversely with the third power of temperature, neglecting for the present somewhat similar effects in the pressure broadening terms. Thus, atmosphere number 11 can be expected to have the most loss, and number 9 the least, in the interesting region from say 30 to 60 kilometers. Similarly, No. 11, with its higher loss and higher temperature, would be expected to exhibit a higher brightness temperature than No. 9. These effects will be demonstrated in the curves to be presented.

Figures 6, 7, 8, and 9 illustrate attenuation constant as a function of frequency for the four model atmospheres selected as representative samples. The frequency range encompasses the center five resonance lines shown in the spectrum of figure 2. These curves show the general attenuation behavior discussed above, especially at 40 kilometers and above, the parameters on the curves. These curves also illustrate two other important points.

Figure

Page

18 Comparison of Brightness Temperature Profiles, Atmosphere No. 1, Horizon Region, for Spot Frequencies and Bandwidth Averages 50

19 Comparison of Brightness Temperature Profiles, Atmosphere No. 9, Horizon Region, for Spot Frequencies and Bandwidth Averages 51

20 Brightness Temperature Versus Frequency, Atmosphere No. 11 52

21 Brightness Temperature Versus Frequency, Atmosphere No. 53

22 Brightness Temperature Versus Frequency, ... 54

23 Brightness Temperature Versus Frequency, ... 55

Profile, 200-MHz Bandwidth 58

Frequency of 89 GHz, Comparison 59

200 MHz Bandwidth 60

Comparison 61

Atmo- 10 62

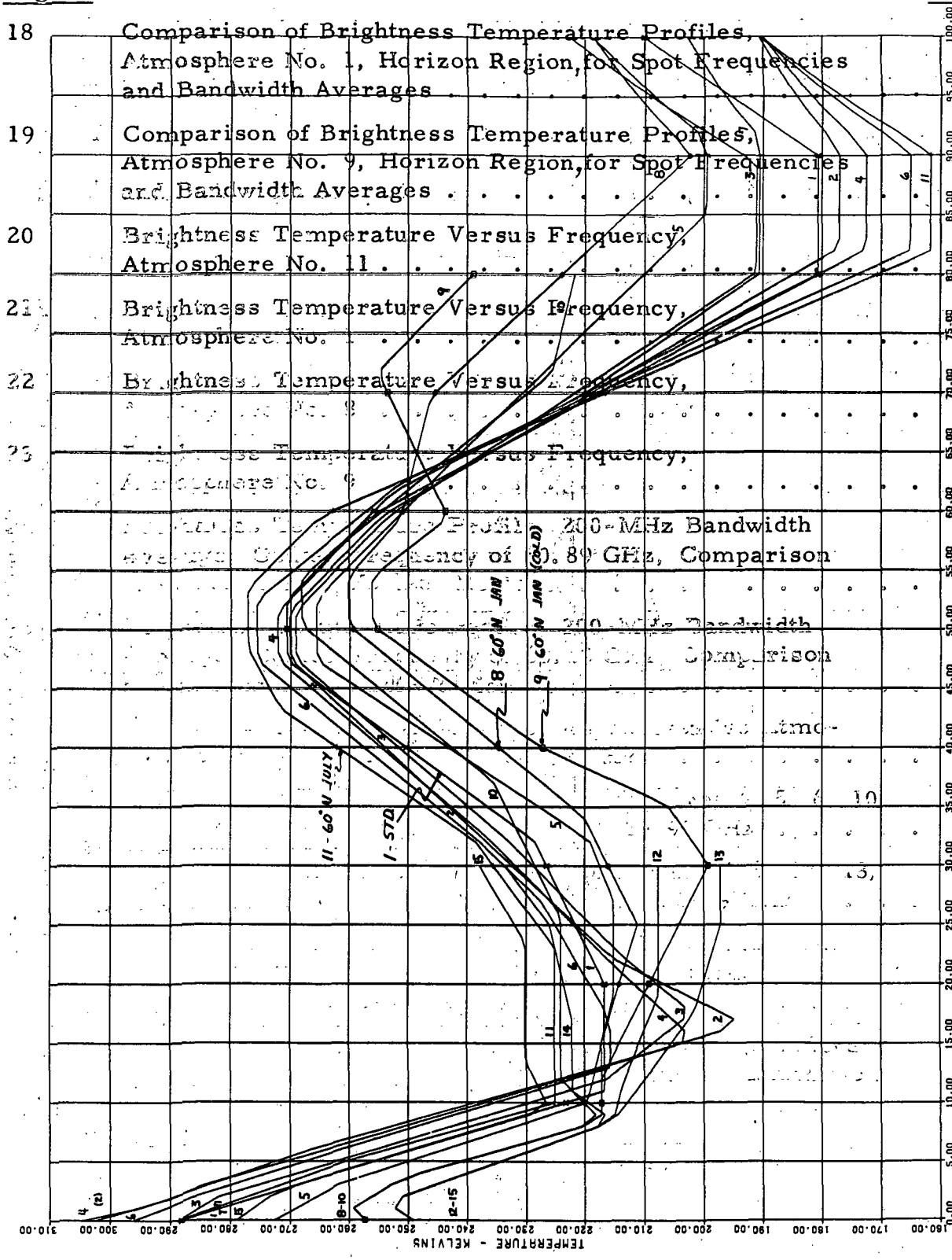

Figure 3. Temperature vs Altitude for Model Atmospheres

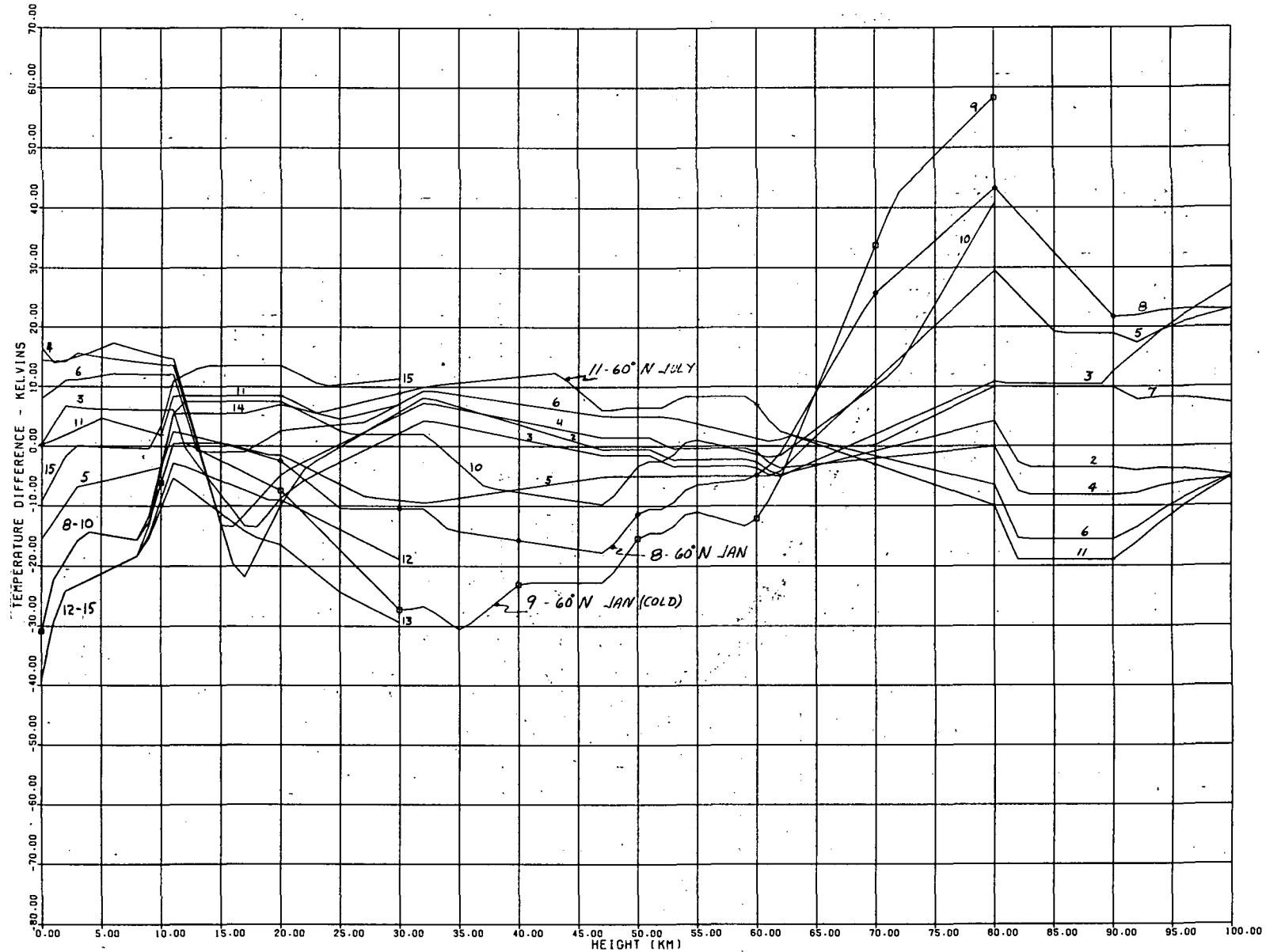

Figure 4. Temperature Difference from 1962 Standard Atmosphere vs Altitude for Model Atmospheres

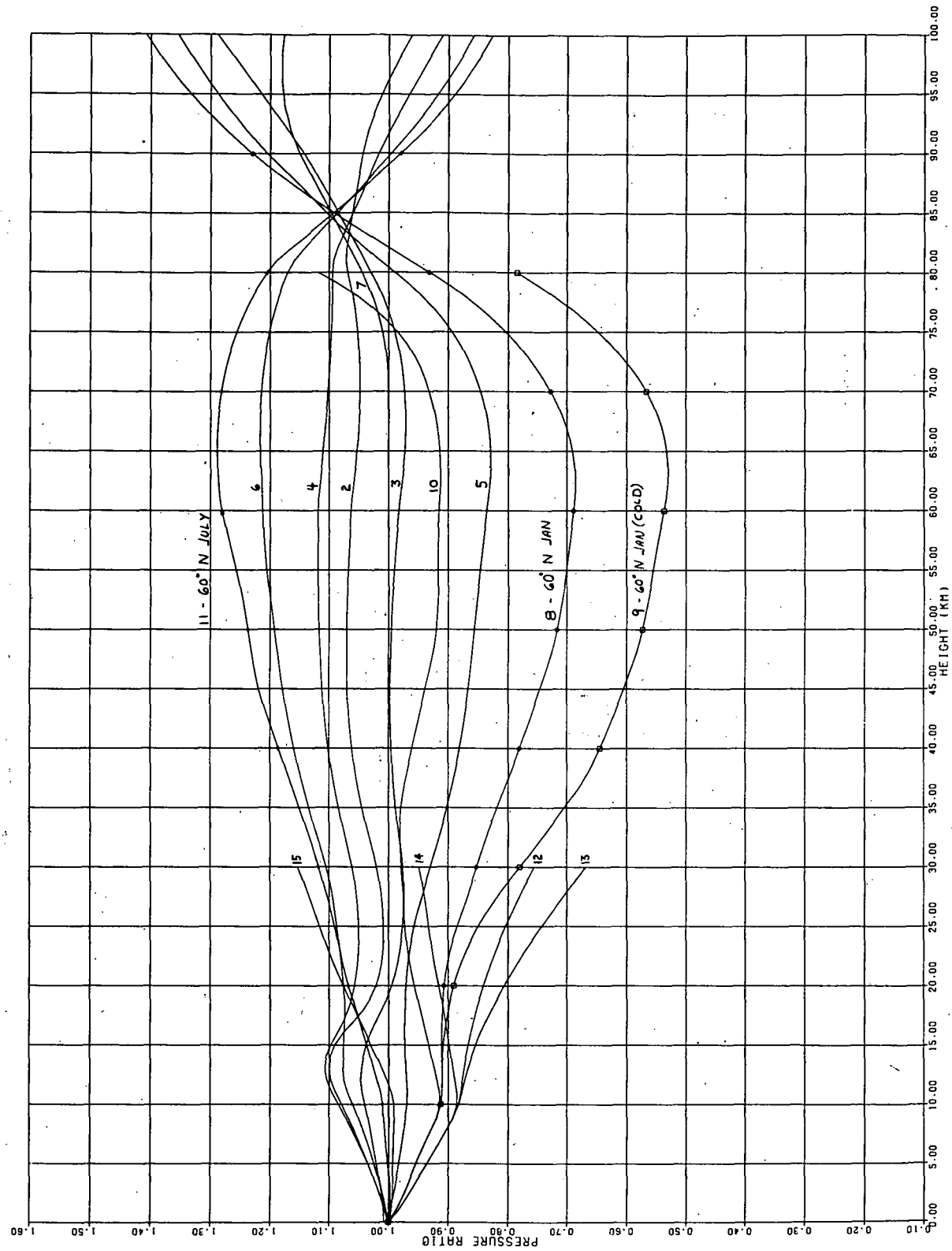

Figure 5. Pressure Ratio Referred to 1962 Standard Atmosphere vs Altitude for Model Atmospheres

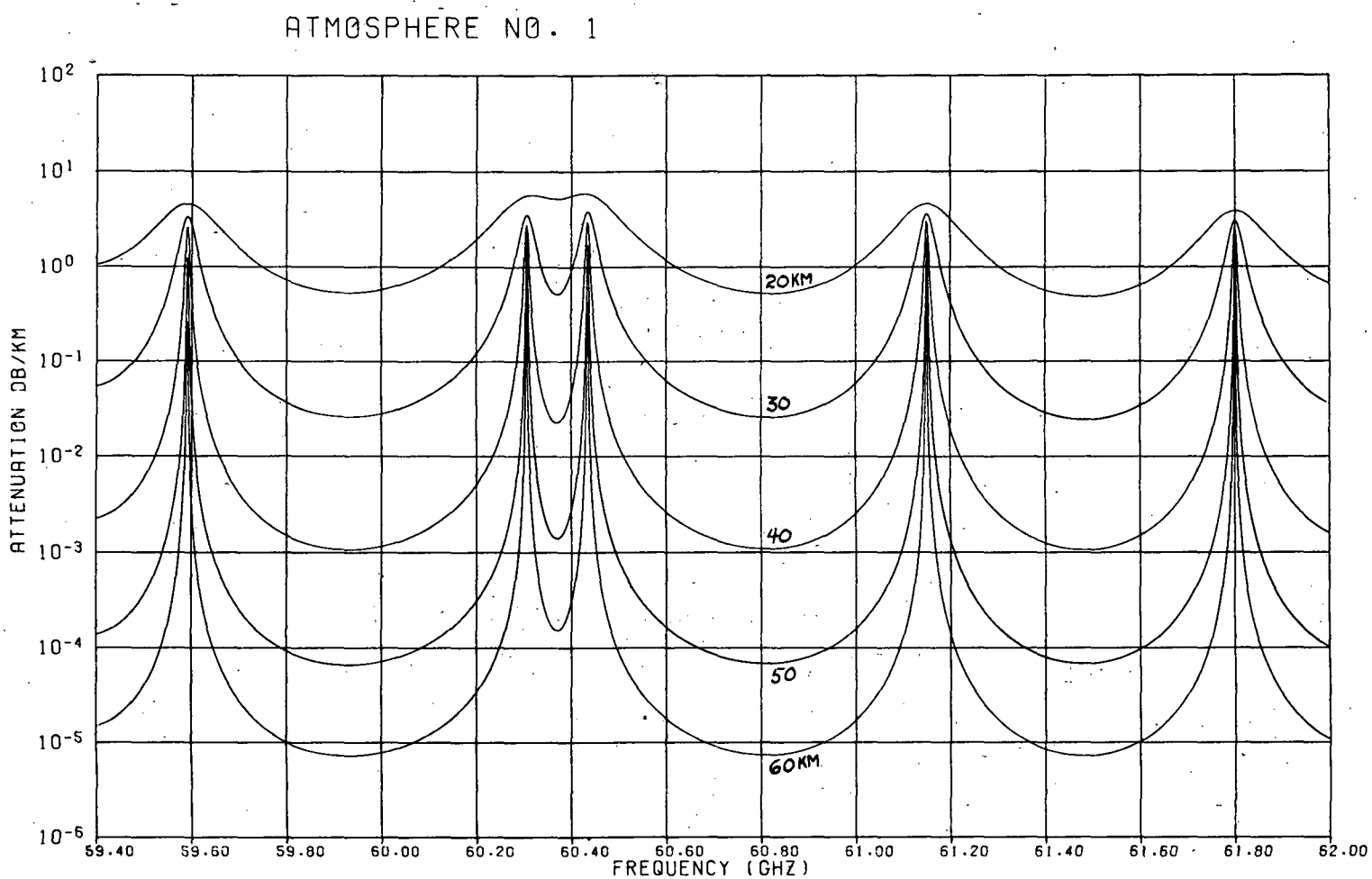

Figure 6. Attenuation Constant vs Frequency, Atmosphere No. 1

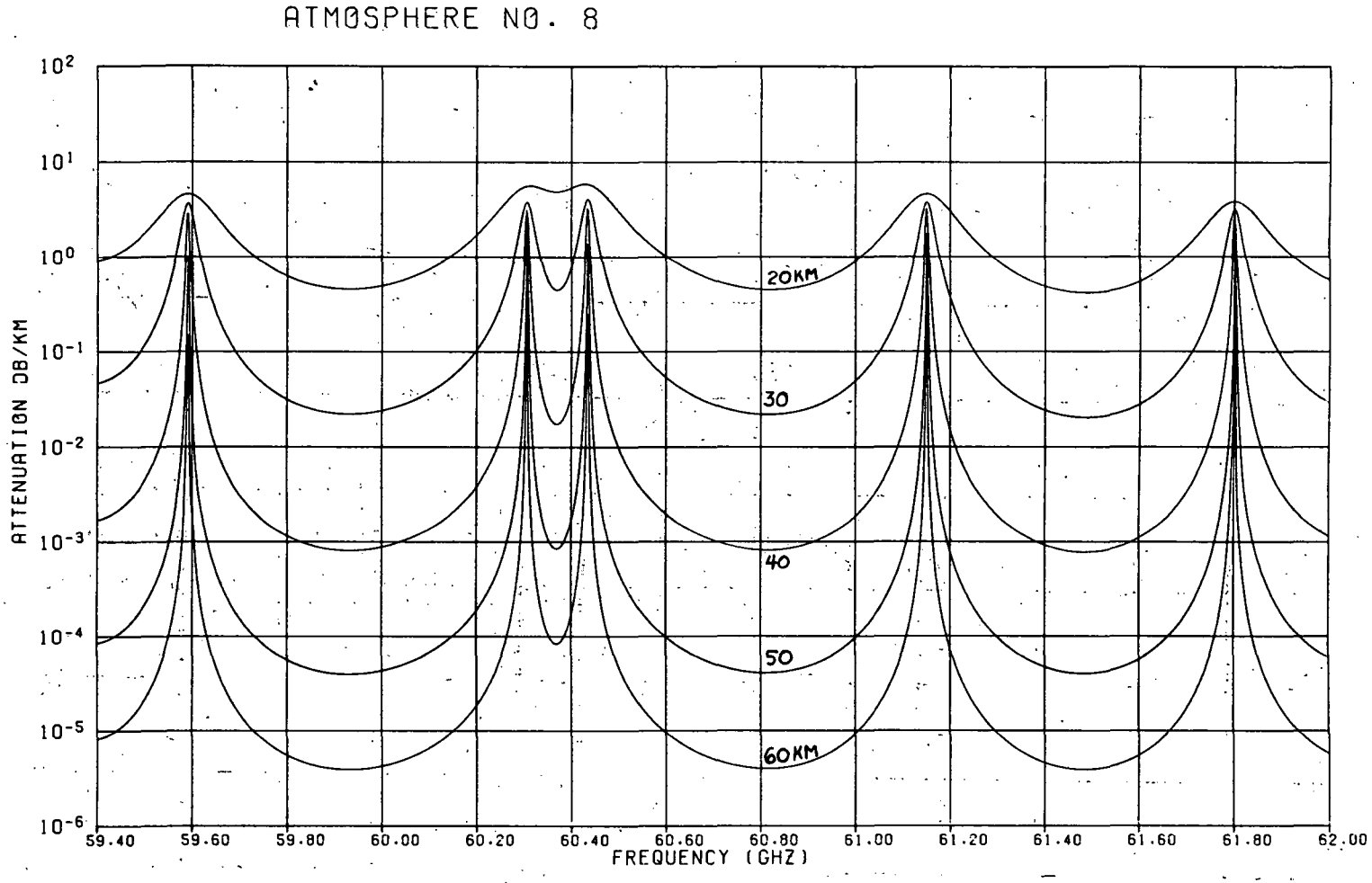

Figure 7. Attenuation Constant vs Frequency, Atmosphere No. 8

60 GHz RADIOMETRIC LOCAL VERTICAL SENSOR EXPERIMENT

By C. Herbert Grauling Jr.
Westinghouse Defense and Electronic Systems Center
Systems Development Division

1. INTRODUCTION

This final report summarizes the major results on Contract No. NAS1-10131 for the development of the Radiometric Local Vertical Sensor Experiment. This is a new sensor operating in the millimeter wave portion of the electromagnetic spectrum. It is a limb looking device similar in concept as the infrared horizon sensor. The primary [illegible] detected is the oxygen in the atmosphere which is of high concentration (almost 21 percent), uniformly distributed around the earth and a strong absorber at frequencies [illegible].

The differences in absorber [illegible] regions result in comparable [illegible] characteristics. A [illegible] characteristics [illegible] are considered [illegible] absorption and [illegible] the system [illegible]

[illegible] vertical [illegible] and beam [illegible]

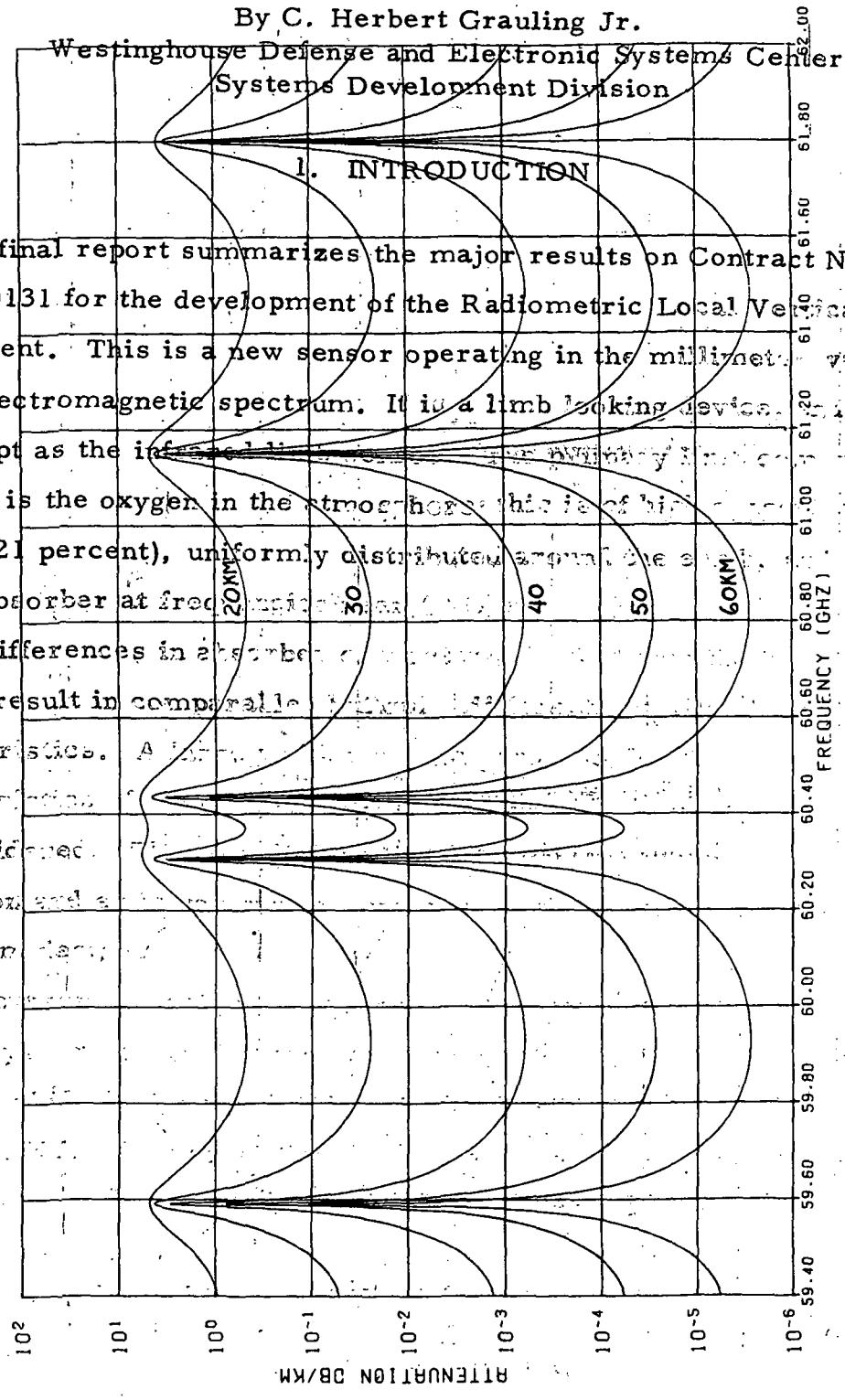

Figure 8. Attenuation Constant vs Frequency, Atmosphere No. 9

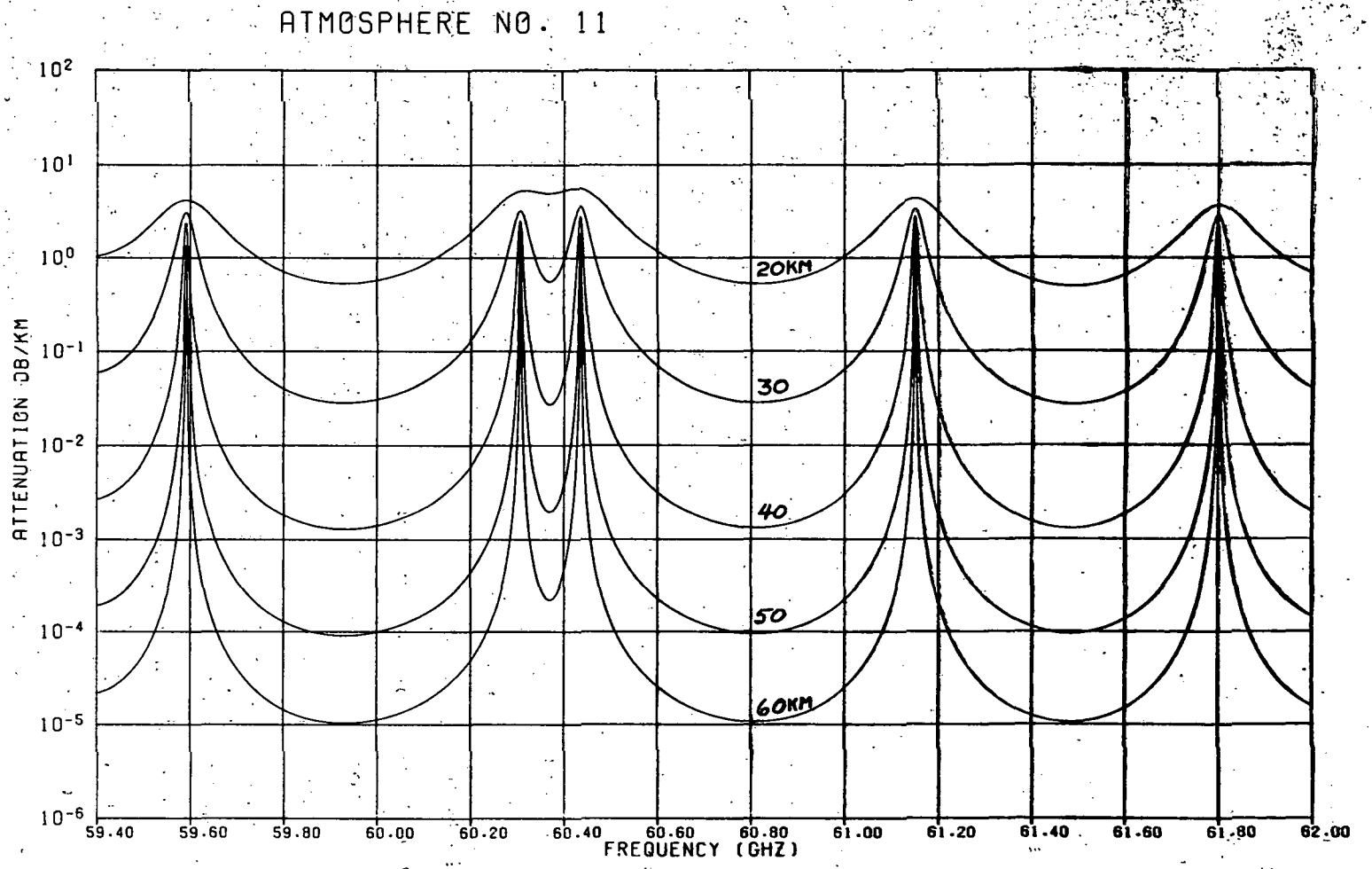

Figure 9. Attenuation Constant vs Frequency, Atmosphere No. 11

First, there is a violent change in attenuation with frequency, and, in the more interesting altitude range, this change is roughly two orders of magnitude or more from the valley to near a resonance line. There is no really "flat" region between the lines - the curve merely dips to a minimum and rises again. The expected attenuation change with altitude is roughly 10 orders of magnitude, and about 5 are shown in the altitude region noted on the curves. It is, of course, this rapid attenuation change with altitude that causes the oxygen horizon to appear so sharp. Secondly, the inherent symmetry of the curves should be noted. Brightness temperature is primarily a function of attenuation, coupled with the physical temperature of the atmosphere. Detailed calculations of brightness temperature have so far been made only over the region noted in figure 2, i.e., from about 60.8 to 61.5 GHz. The curves in these last four figures show that this region is representative of the other regions considered. Although additional detailed calculations in these other frequency ranges may indicate minor variations, clearly all contingencies have been anticipated.

3.6 BRIGHTNESS TEMPERATURE PROFILES

Figure 10 shows a typical brightness temperature profile generated by use of the computer program discussed in earlier sections. This curve plots brightness temperature versus tangential altitude in the horizon region and is for atmosphere No. 1 (standard). The curve is plotted for various spot frequencies from 60.79 to 61.51 GHz, and these values are shown as parameters on the curves. Most of the frequencies are in pairs, approximately equally spaced from the resonance line at 61.1506 GHz. Those frequencies below resonance use plain curves, and those at or above resonance are identified by a diamond. Again, as in the attenuation curves, the pronounced symmetry should be noted. The position of the curves is easily explained. Between 60.79 and 60.89 GHz only a small shift takes place, due to a small increase in attenuation. By 60.99 GHz, the attenuation increase is more than 2:1, and the shift is quite noticeable. As the frequency increases closer to resonance, the curve shifts markedly to higher tangential altitude,

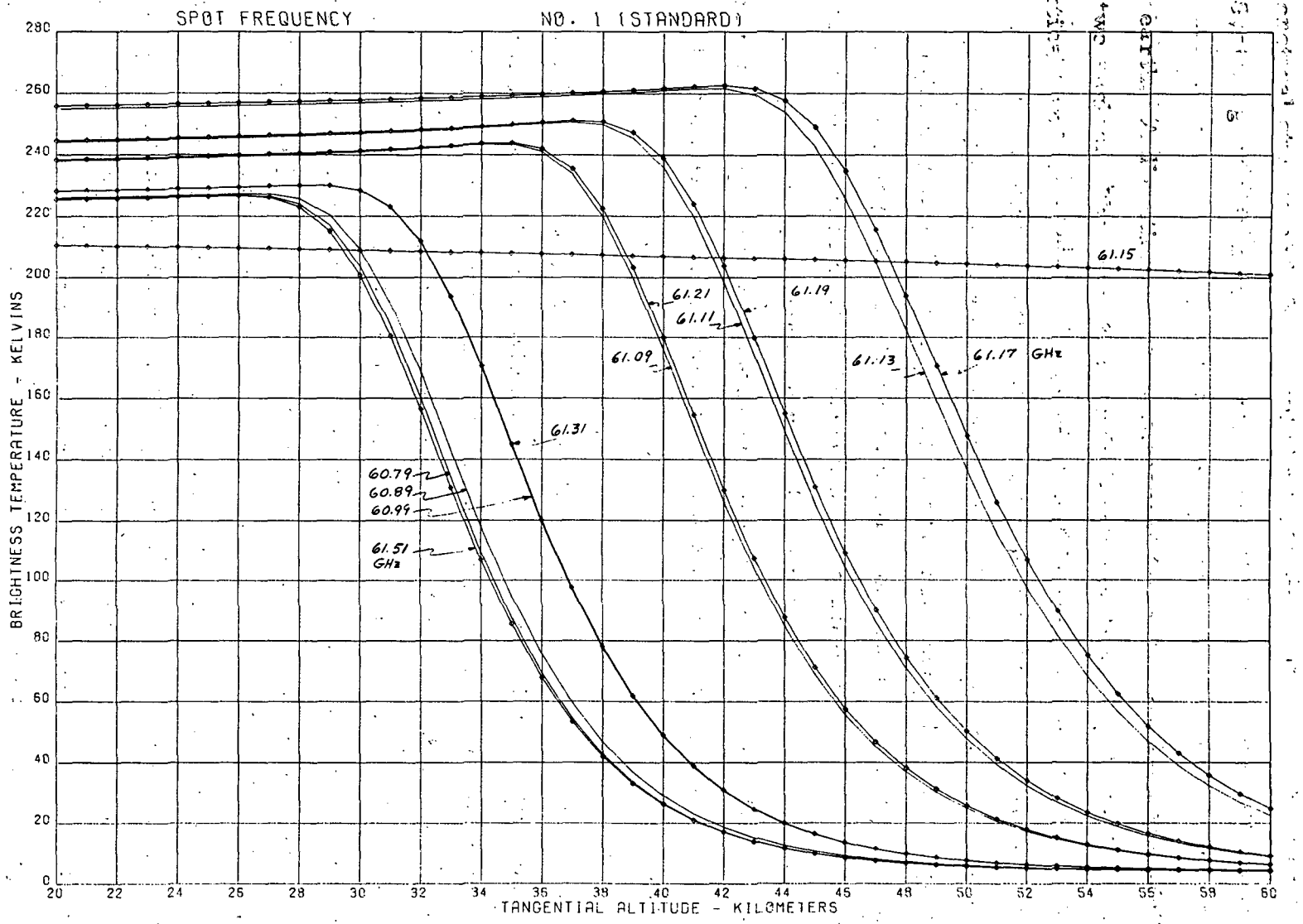

Figure 10. Brightness Temperature Profile, Spot Frequency, Atmosphere No. 1, Horizon Region

because the ray is absorbed higher in the atmosphere. As noted earlier, the temperature in this region is increasing, and hence the plateau of the brightness temperature also increases. The ray at the frequency near resonance is absorbed much higher in the atmosphere. The T_B change for this frequency is slight in the altitude region shown, but the value is lower since the temperature higher in the atmosphere has decreased.

Figure 11 shows the corresponding curve for atmosphere No. 9 (60° N January (Cold)). The behavior and shape is essentially the same, with the major differences being caused by atmosphere differences already discussed. Due to the decreased attenuation in this atmopshere, a lower tangential altitude is needed for the horizon, and a lower plateau temperature results from the colder air temperature. One interesting feature is the 61.15-GHz curve, which displays a considerably higher temperature, rather than a lower one as with No. 1. This frequency is apparently absorbed well above 60 kilometers, where this model exhibits a higher temperature than other model atmospheres.

3.7 CONVERGENCE

The basic philosophy expressed in the computer program was to keep all expressions differentially correct so that step size could be reduced and convergence observed. In order to permit a large range of values of Δs_{max} to be accommodated, the standard atmosphere, divided into 20 steps of 5 kilometers each was used. The results of a temperature calculation are presented in table 2 for two values of tangential altitude, 40 and 30 kilometers. From the brightness temperature profile of figure 10, these altitudes correspond roughly to the 10 and 90 percent points of the sharp edge. The parameter Δs_{max} was varied from 0.1 to 100 kilometers in this test, a range of 1,000:1.

The basic results in table 2 were obtained from a CDC 6400 time sharing computer, and they are compared with the earlier results from the Univac 1108 on which our production runs were made. Both machines are operating in single precision, but the 6400 carries 14 digits while the 1108 carries only 8. The results from the 6400 show a definite monotonic trend with rapidly

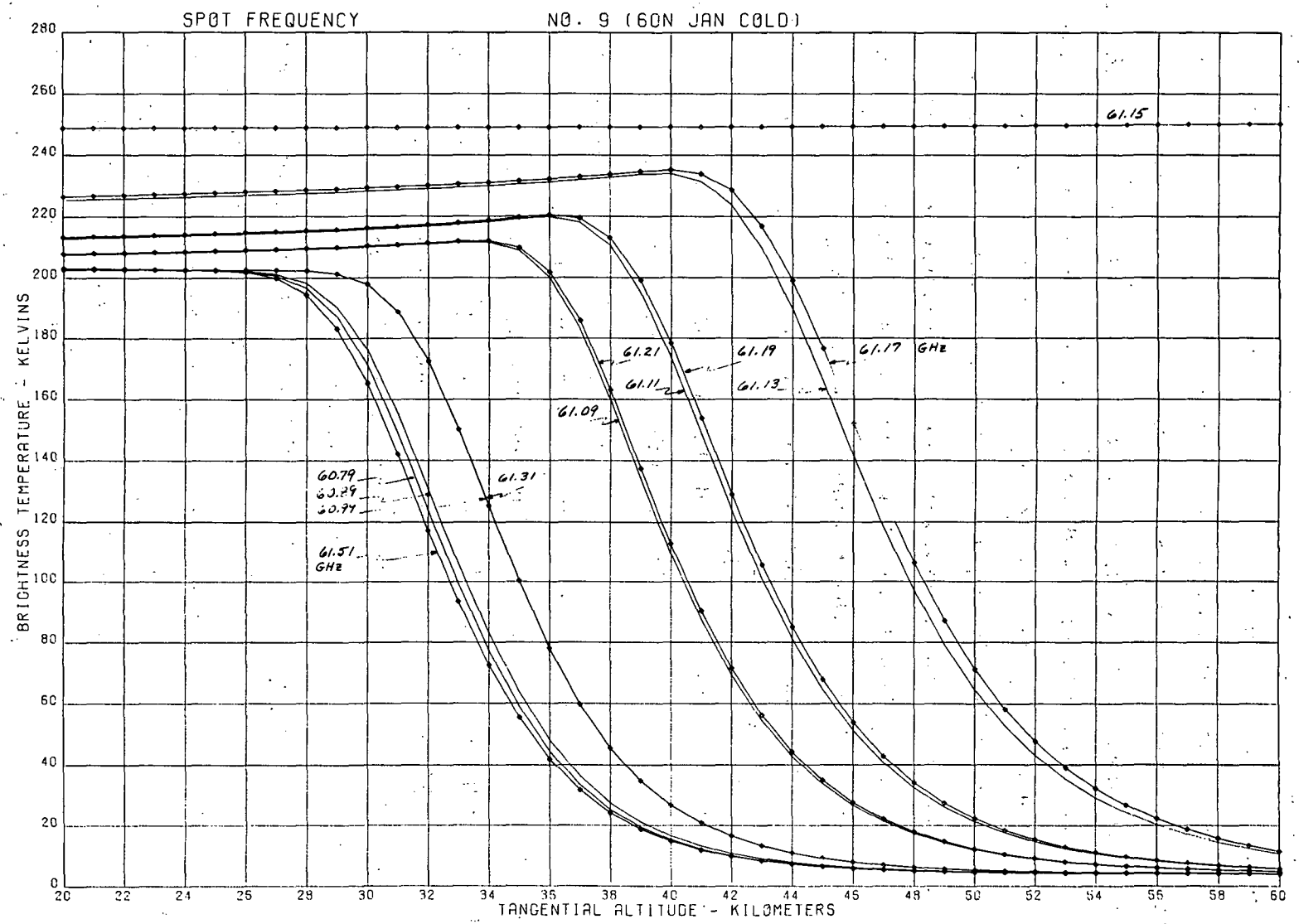

Figure 11. Brightness Temperature Profile, Spot Frequency, Atmosphere No. 9, Horizon Region

decreasing differences, so that convergence has definitely been demonstrated. Based only on this data, one could assume that the last value shown, that for 0.1 kilometer, is probably good to 5 decimal places in temperature. Of course, this is so far beyond the accuracy of any realistic model atmosphere as to have little meaning, but it does demonstrate the capability of the program. The large number of segments required should also be noted, and the fact that the average length for this example is about 70 percent of the maximum permitted. The use of a step size as small as 0.1 kilometer would result in an intolerably long running time for production runs and would never be considered. It does, however, serve as a check on the program and, in addition, permits one to evaluate the accuracy obtained with a more realistic step size. The fact that the total observed change is less than 1 degree, is, at least in part, attributable to the precise nature of the basic expressions for Δs, $\Delta \tau$, and ΔT_B.

Results from the 1108 are comparable to those of the 6400 for the larger step sizes. However, as a very large number of segments is required, the 1108 with its 8 digits is unable to cope with the problem of handling many small numbers with significant digits beyond the machine capacity, and it begins to drop digits in the answer. This effect may be suspected at 0.5 kilometer and is quite pronounced at the smaller step sizes. Even for a small number of segments, the 1108 answer is slightly below that of the 6400, presumably for the same reason. Both machines perform the same calculation, and both work with the same number of segments.

Also shown in table 2 is another tabulation of similar data, this time for atmosphere No. 1 treated as a 100-step model. Details of the convergence are almost identical as is the estimated accuracy. However, the final answer is roughly 0.3 degree lower out of 200 than for the 20-step case. This is due to the difficulty of getting a precise interpolation across a shell, with no intermediate data. The most logical temperature interpolation, and that used in the program, is a linear variation across the shell. The 1-kilometer data, however, has a break in temperature at the 32-kilometer altitude.

A straight line fit between 30 and 35 kilometers will give a temperature too high in comparison to the finer structured data, and hence a somewhat higher brightness temperature.

TABLE 2

CONVERGENCE TEST

RHO	AV LEN	DELSM	NSEG	T	T (1108)
		20-Step Atmosphere No. 1			
40.00	54.9088	100.00	32	26.062147	26.06213
40.00	35.1375	50.00	50	26.383229	26.38321
40.00	14.1680	20.00	124	26.469718	26.46970
40.00	7.1416	10.00	246	26.487784	26.48777
40.00	3.6000	5.00	488	26.492785	26,49276
40.00	1.5250	2.00	1152	26.494243	26.49422
40.00	0.7632	1.00	2302	26.494457	26.49443
40.00	0.3819	0.50	4600	26.494512	26.49447
40.00	0.1495	0.20	11750	26.494527	26.49444
40.00	0.0748	0.10	23498	26.494529	26.49437
30.00	52.7478	100.00	36	202.667206	202.66714
30.00	35.1578	50.00	54	203.335930	203.33587
30.00	14.3822	20.00	132	203.524893	203.52483
30.00	7.2460	10.00	262	203.577585	203.57752
30.00	3.6509	5.00	520	203.590613	203.59053
30.00	1.4832	2.00	1280	203.594400	203.59430
30.00	0.7422	1.00	2558	203.594946	203,59482
30.00	0.3712	0.50	5114	203.595086	203.59490
30.00	0.1485	0.20	12780	203.595125	203.59474
30.00	0.0743	0.10	25558	203.595131	203.59391
		100-Step Atmosphere No. 1			
40.00	14.1688	100.00	124	26.219225	
40.00	13.9434	50.00	126	26.276138	
40.00	11.7122	20.00	150	26.348809	
40.00	7.2596	10.00	242	26.363257	
40.00	3.6601	5.00	480	26.367324	
40.00	1.4122	2.00	1244	26.368538	
40.00	0.7067	1.00	2486	26.368716	26.36835
40.00	0.3536	0.50	4968	26.368762	
40.00	0.1446	0.20	12146	26.368774	
40.00	0.0723	0.10	24288	26.368776	
30.00	13.1847	100.00	144	202.934956	
30.00	13.0034	50.00	146	203.052036	
30.00	11.1673	20.00	170	203.222208	
30.00	7.2460	10.00	262	203.265384	
30.00	3.6509	5.00	520	203.276017	
30.00	1.4404	2.00	1318	203.279176	
30.00	0.7213	1.00	2632	203.279628	203.27916
30.00	0.3608	0.50	5262	203.279746	
30.00	0.1413	0.20	13438	203,279779	
30.00	0.0706	0.10	26874	203.279784	

DELSM = Maximum Segment Length, km (parameter)
T = Brightness Temperature from CDC 6400, K
T(1108) = Brightness Temperature from Univac 1108, K
RHO = Tangential Altitude, km
AV LEN = Average Segment Length, km
N SEG = Number of Segments

4. EXPERIMENT SYSTEM ANALYSIS

The experiment system analysis is concerned with the question of how the various possible design choices affect the behavior of the sensor system. Generation of the brightness temperature profile was considered in the last section. Given a specific atmosphere model and frequency of operation, there is a resulting brightness temperature profile versus tangential altitude that can be calculated by the computer program, and some examples were shown. This profile is a function of atmospheric characteristics and is not under the control of the system designer. The designer can, however, control the choice of operating frequency or frequencies and the passband which is accepted by the radiometer. He also has control over the antenna pattern and antenna pointing direction, as well as some minor electrical parameters, such as integration time, which influence system sensitivity. In this section, many additional brightness temperature profiles will be examined, along with possible frequency and bandwidth choices. The question of the convolution of the antenna pattern with the profile, to determine antenna temperature as a function of pointing angle, will be considered, as will the development of the sensor output characteristic as a function of boresight pointing. A novel compensation scheme to reduce the error caused by differing atmospheres on opposite sides of the earth will be considered, and the system error characteristic for various antenna patterns and beamwidths will be investigated. Finally, some proposed design choices will be presented.

4.1 FREQUENCY EFFECTS

The variation of T_B with frequency has already been seen in figures 10 and 11. Although a rather sharp curve, with a slope of approximately 25 K/kilometer, exists for a frequency of 60.79 GHz in figure 10, the use of a frequency

340 MHz away, and about 20 MHz from a resonance, causes the apparent edge to shift almost 20 kilometers. These edges, of course, are what would be seen by an infinitesimally sharp antenna beam, and this case will never be realized. In many cases, particularly at high satellite altitude, this edge is essentially a step function, but its actual position still influences the accuracy achieved. Figure 11 shows a similar result, but the edge shift due to the same frequency change is closer to 15 than 20 kilometers.

Figures 12 and 13 are the companion curves to figures 10 and 11, but they illustrate the region from the nadir to the edge of the earth. A scale change occurs at H= -50 kilometers, accounting for the apparent break in the curves. Also, the plotter connects data points with straight lines, and this causes the curves to look somewhat abrupt. The vertical scale is 10 K per division rather than 20 as on the previous curves. Only frequencies below and near resonance, the latter again with a diamond marker, are shown in order to avoid cluttering the curves. Consideration of these four spot frequency curves could lead to the belief that the edge is not very stable and that a severe frequency control problem exists.

4.2 BANDWIDTH EFFECTS

Examination of the next group of curves, however, shows that the situation is not really that bad. Figures 14 and 15 again show the brightness temperature in the horizon region for two atmospheres, but now the temperature has been averaged over a given bandwidth in MHz, as noted by the parameter on the curve. Both the profile curves, figures 10 and 11, and the attenuation curves, figures 6, 7, 8, and 9, indicated the need for some such average, and the manner in which it is calculated will be discussed later. These bandwidth average curves are very well behaved up to 300-MHz bandwidth and are not really spread too far for higher bandwidths, in contrast to the spot frequency curves. The 520- and 720-MHz curves are identified by the diamonds, and the inherent symmetry is again noted since the 720-MHz curve falls almost

again required. Thus, computer processing time is greatly reduced at no loss in accuracy.

Two facets of the approach chosen should be noted. From the above discussion, it is clear that although the model atmosphere is defined in terms of discrete shells (i.e., at discrete heights) both the absorption and the index are permitted to vary across the shell and are interpolated as described. Thus, the ray tracing technique approximates a continuously bending ray in a continuously changing atmosphere and hence represents an excellent simulation of the real case.

In addition, the basic philosophy employed in the brightness temperature computer program is that if all expressions used are differentially correct, then the results may be tested by decreasing the step size and noting the convergence. Assuming the desired convergence, this result will be the most accurate obtainable, within the limits of the basic assumptions and the data available. To implement this philosophy, both the opacity (integrated attenuation constant) and brightness temperature contributions of each of a number of roughly equal increments (segments) along the ray path are calculated and summed. A maximum step size is used as a parameter in the program, and this can be reduced as necessary to test convergence. The program is adaptive in that each shell is subdivided as necessary so that the path length in any segment is less than the maximum allowed. If the total path in any shell is less than this maximum, no subdividing is employed, and the shell is treated as containing only one segment. In those shells which are subdivided, all segment lengths are roughly equal, and the number of segments is adjusted as necessary to provide the minimum number consistent with the assigned maximum path length.

Under the assumption of spherical symmetry, as discussed above, the refractive index is a function of height above a smooth earth, and the atmosphere is locally homogeneous. The appropriate expression for the refraction in this atmosphere is Snell's law for polar coordinates:[5,6]

$$r \cdot \sin \alpha = \text{constant},$$

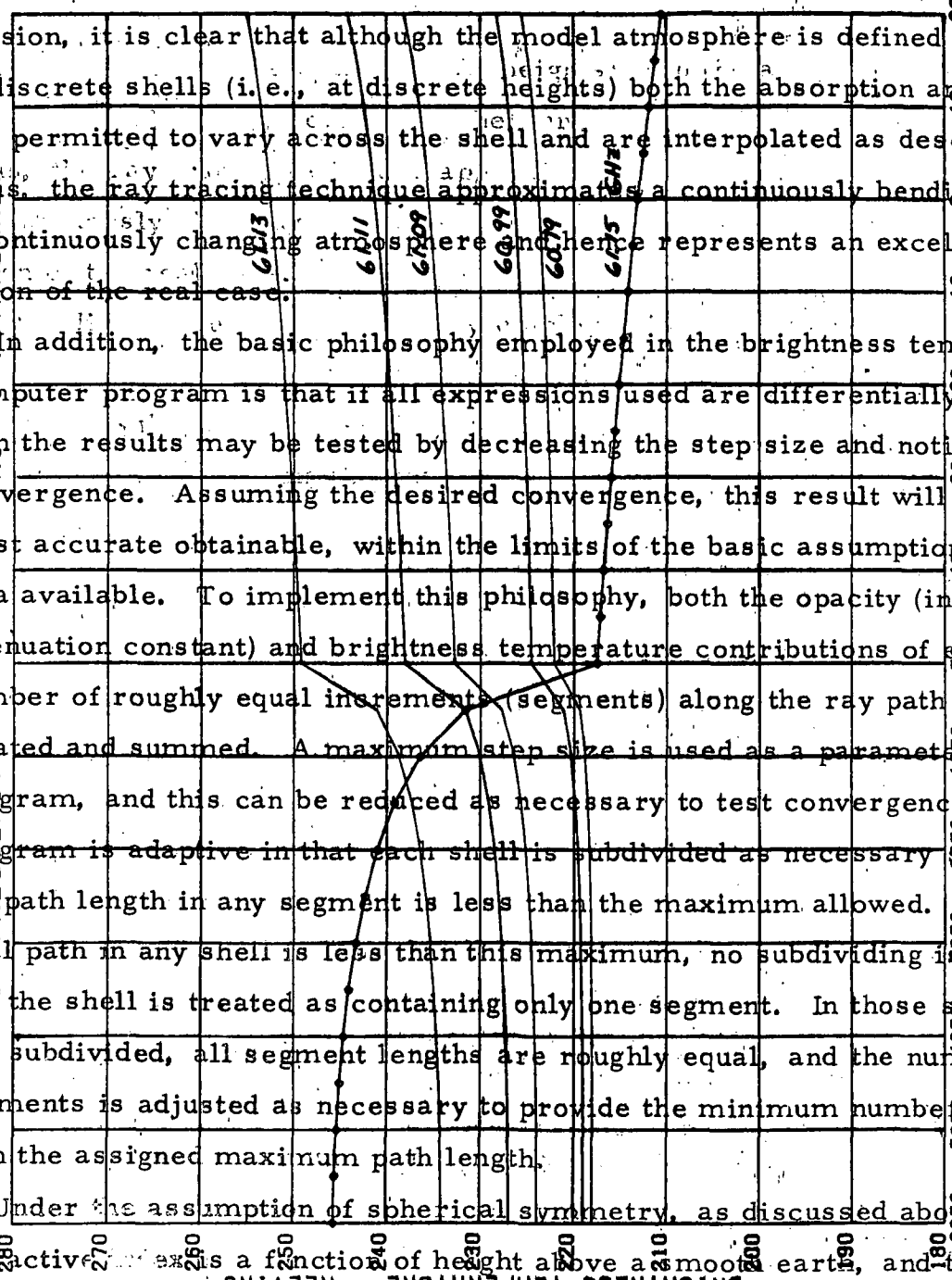

Figure 12. Brightness Temperature Profile, Spot Frequency, Atmosphere No. 1, Nadir Region

where α is the angle between the radius vector of length r and the direction of the ray (i. e., the tangent at that point), and n(r) is the index of refraction explicitly written as a function of r.

In the vicinity of a satellite at radius R_s, assumed well outside the earth's atmosphere, the index n becomes unity, the path is a straight line, and α becomes the nadir angle, θ. Thus

$$R_s \sin\theta = \text{constant} = \rho \qquad (2)$$

where ρ is defined as the normal distance from the center of the earth to the unrefracted ray from the satellite, a simple geometrical interpretation. This radius, ρ, will be used to characterize the ray whose brightness temperature is to be calculated, and it will be referred to as tangential radius. It will usually be used in the form of a tangential altitude by subtracting the earth's radius, thus

$$H = \rho - R_E \qquad (3)$$

The temperature profiles to be discussed later show brightness temperature versus tangential altitude, because this is a somewhat more general characterization than the angle variable implied earlier in this chapter. The use of tangential altitude permits one profile to be used for many satellite altitudes by a simple geometrical transformation, and yet it provides a precise delineation of the critical portion of the profile near the horizon. For values of H greater than the maximum atmosphere layer considered, the ray misses the atmosphere and assumes the temperature of space. H can also be less than zero, in which case the ray strikes the earth and $H = -R_E$ represents a ray along the nadir.

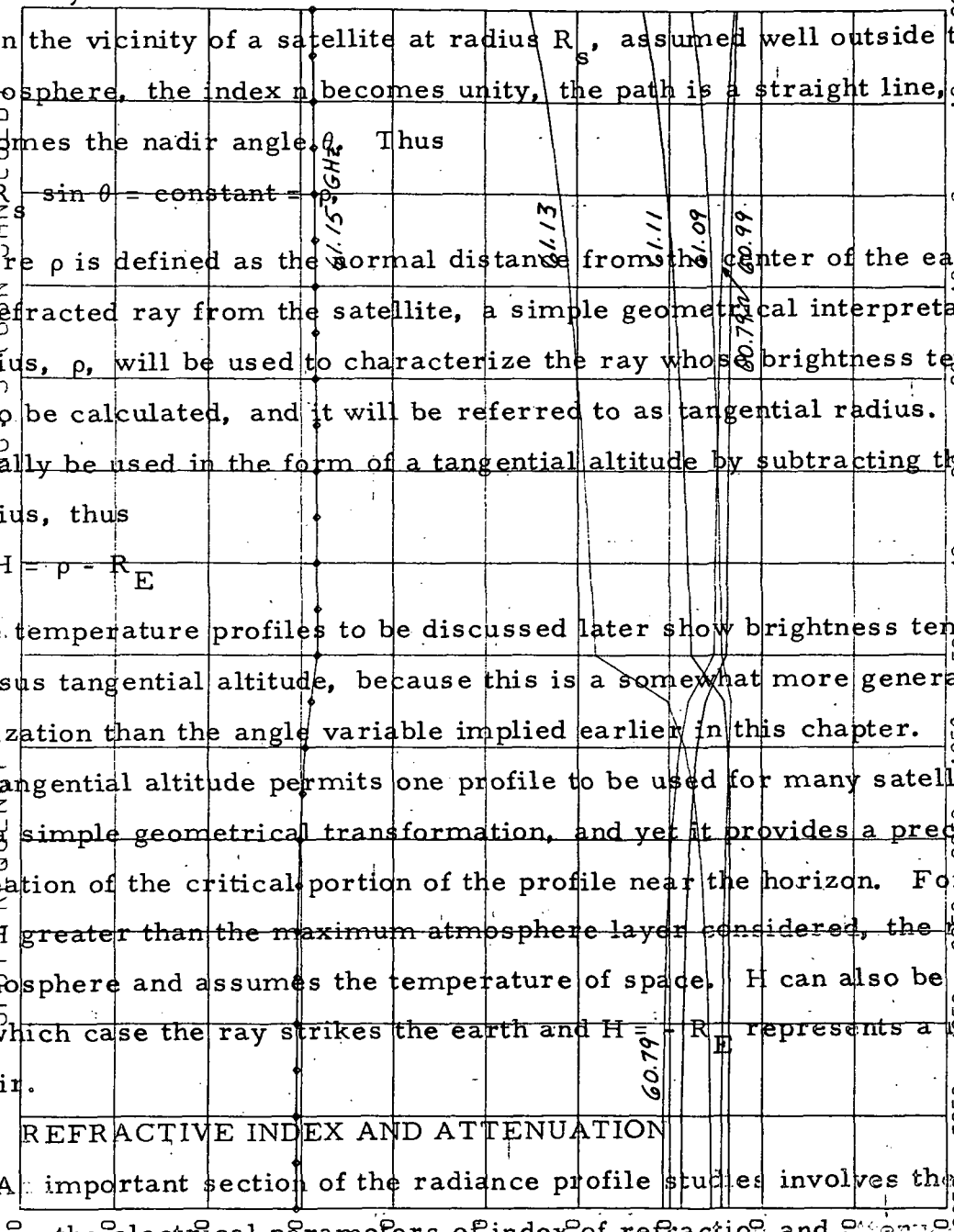

Figure 13. Brightness Temperature Profile, Spot Frequency, Atmosphere No. 9, Nadir Region

3.2 REFRACTIVE INDEX AND ATTENUATION

An important section of the radiance profile studies involves the calculation of the electrical parameters of index of refraction and attenuation coefficient from the physical parameters of temperature, pressure, water vapor content of the atmosphere. Physically, this is handled as a subroutine to the main computer program. Theoretically, what is involved is

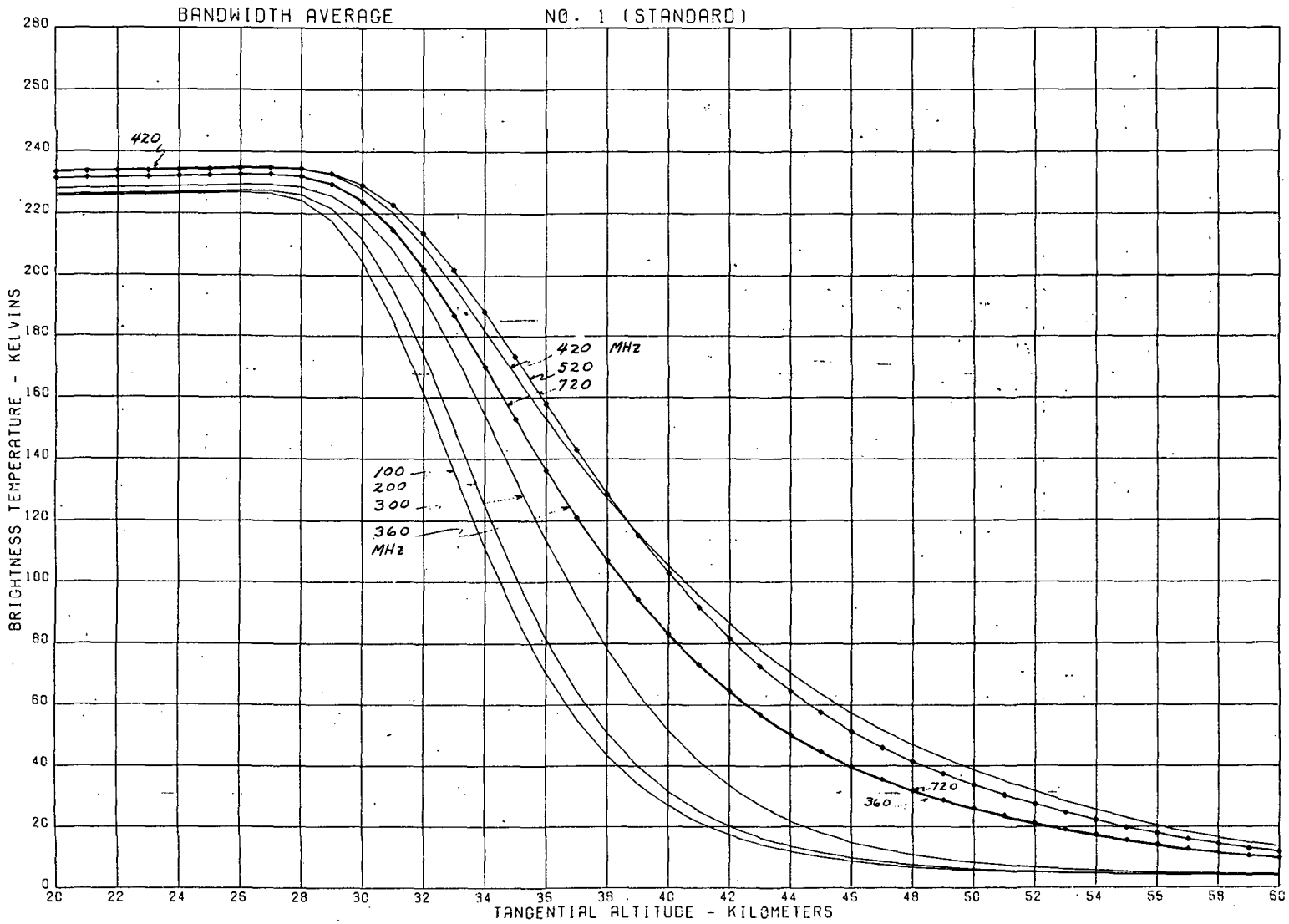

Figure 14. Brightness Temperature Profile, Bandwidth Average, Atmosphere No. 1, Horizon Region, Frequency Band Above 60.79 GHz

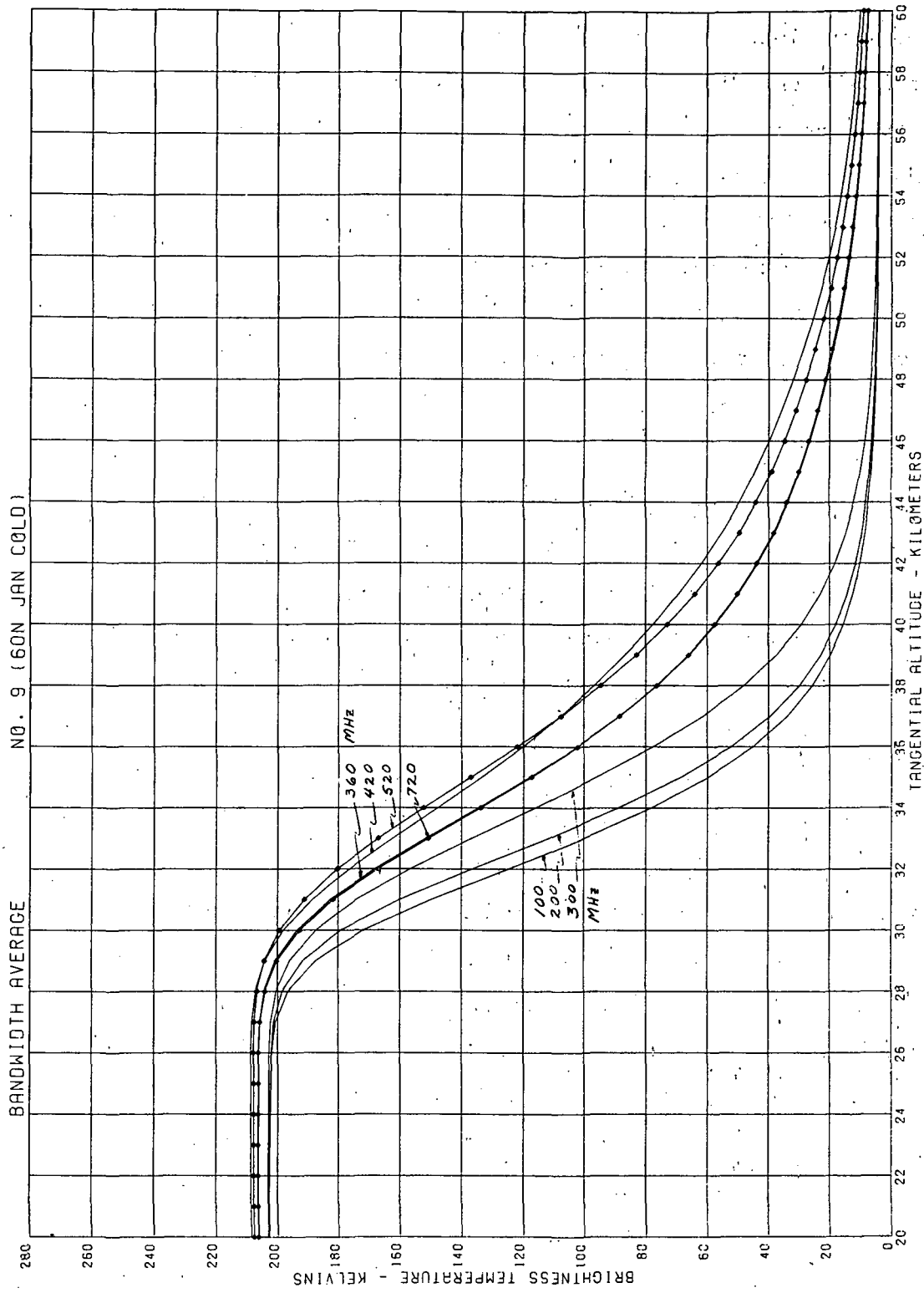

Figure 15. Brightness Temperature Profile, Bandwidth Average, Atmosphere No. 9, Horizon Region, Frequency Band Above 60.79 GHz

exactly on the 360-MHz curve. The major effect for these higher bandwidths is a decrease in slope of the edge, showing that the sensitivity is decreased somewhat by allowing the resonance region in the passband. The bandwidths selected for these curves are the frequency region between 60.79 GHz and many of the frequencies noted on the spot frequency curves, in order to permit a sensible comparison. It will also be noted that the bandwidth average curves maintain similar edge shift and plateau height differences characteristic of the spot frequency curves.

Figures 16 and 17 are the companion curves to figures 14 and 15 illustrating the nadir region. On these curves, the 300-and 420-MHz bandwidth data is identified by the diamonds.

Figure 18 for atmosphere No. 1 and figure 19 for atmosphere No. 9 illustrate a comparison of the spot frequency and bandwidth average curves. Four spot frequencies and two bandwidth averages are shown. The 200-MHz average curve is shifted less than one third of the distance between the 60.79 and 60.99-GHz curves, and a similar relation holds for the 260-MHz and 61.05-GHz curves. Thus, there is a definite weighting effect from frequencies in the center of the valley between two resonance peaks. This tends to make the bandwidth average curves quite well behaved, and of essentially the same slope, provided too large a bandwidth is not used. These curves illustrate that an IF passband selection, similar to the top two sets of boxes in figure 2, is a quite reasonable choice for the local vertical sensor experiment and that a final selection between these two would probably be made on other grounds.

The next four sets of curves, figures 20, 21, 22, and 23, show brightness temperature versus frequency for several tangential altitudes. These curves are, in effect, a form of vertical cross section of the preceding profile curves and will be used to illustrate the manner in which the bandwidth average is obtained. In figure 20, the plain curves represent the calculated ray brightness temperature and diamonds identify the bandwidth average. This average is calculated as follows. All curves start at 60.79 GHz. The area under the

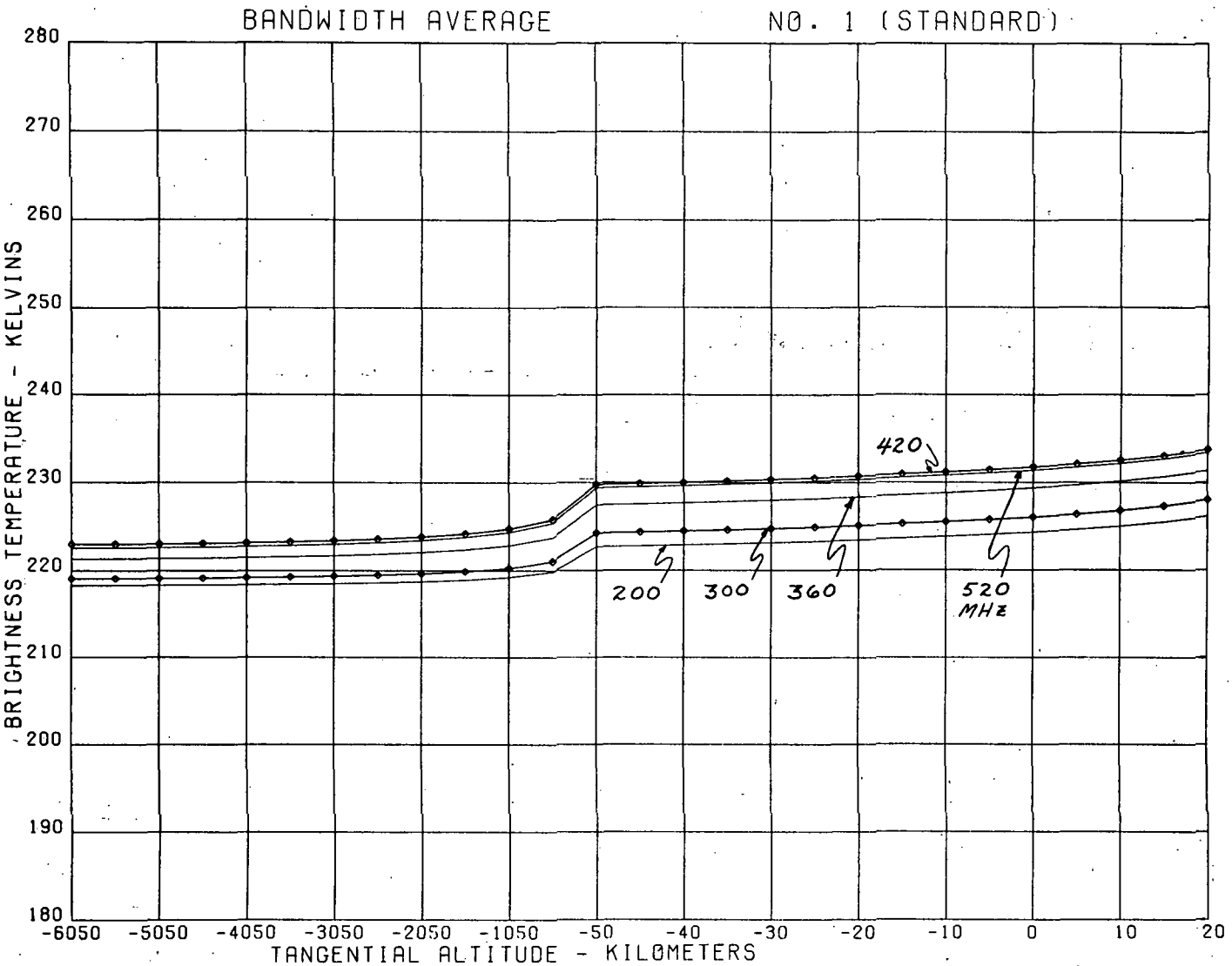

Figure 16. Brightness Temperature Profile, Bandwidth Average, Atmosphere No. 1, Nadir Region, Frequency Band Above 60.79 GHz

In integral form

$$S = \int ds = \int \frac{nr\,dr}{\sqrt{n^2 r^2 - \rho^2}} \qquad (9)$$

where S is now the total path length. Only one half the path, from the altitude limit (expressed in r) to r_c need be calculated, as the other half is identical under the spherical symmetry assumption. Since n is a function of r, this integral, like the former ones, does not have a known closed-form answer.

This integral can be evaluated numerically by forming a series of partial sums and adding them to produce the desired total summation. This involves working with finite segments Δr rather than the mathematical differential dr. There is an approximation involved here, of course, but by using more steps of a smaller size we should be able to approach arbitrarily close to the true integral. This is the basis of the earlier comments about keeping the expressions differentially correct, so that the results may be tested by decreasing the step size and noting the convergence.

For numerical integration the appropriate form of equation 8 becomes

$$\Delta s = \frac{nr\,\Delta r}{\sqrt{n^2 r^2 - \rho^2}} \qquad (10)$$

Since Δr is now a finite step size, the question arises as to where n and r should be measured. The total path is subdivided into a number of prescribed increments of r, and the midpoint in r (or equivalently, in h) is chosen as representative of the given segment. Thus, finally

$$\Delta s = \frac{\bar{n}\,\bar{r}\,(r_2 - r_1)}{\sqrt{\bar{n}^2 \bar{r}^2 - \rho^2}} \qquad (11)$$

where r_2 and r_1 are the boundaries of the segment, and $\bar{n}$ is the value of n at

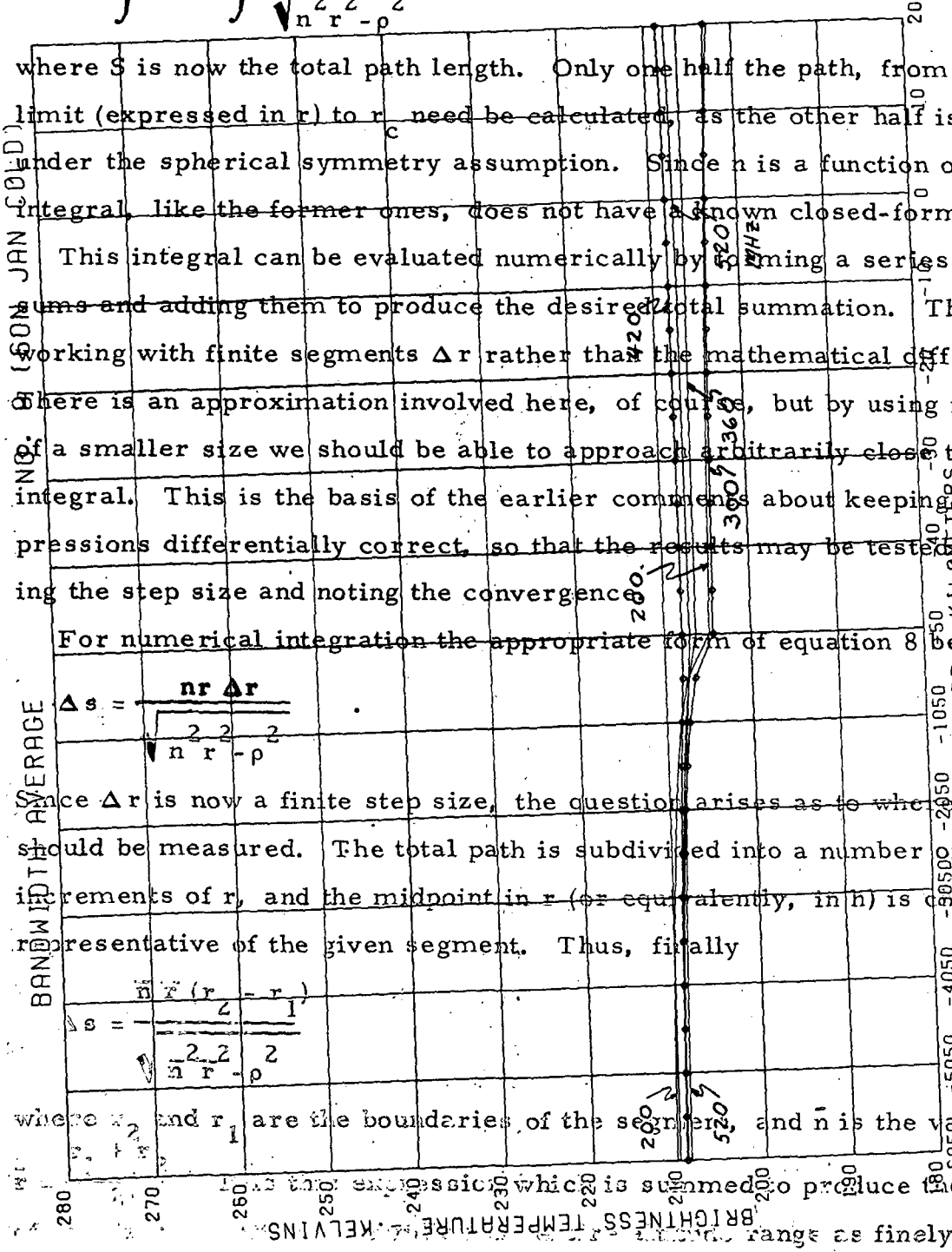

Figure 17. Brightness Temperature Profile, Bandwidth Average Atmosphere No. 9, Nadir Region, Frequency Band Above 60.79 GHz

the expression which is summed to produce the equivalent

range as finely as desired,

and keep

a running subtotal to give the total length from the point of entering the atmosphere to the segment in question.

Similarly, both equations 4 and 5 may be treated as a summation of discrete partial sums. It is important to note, as the [illegible] used in equations [illegible] tions can be integrated [illegible] if desired, [illegible]

For completeness, we express the new forms for equations [illegible] and

$$\Delta\tau_j = \bar{\gamma}_j \, \Delta s_j$$

$$\Delta T_{B_j} = \bar{T}_j e^{-\left(\frac{\Delta\tau_j}{2} + \sum_1^{j-1} \Delta\tau_i\right)} \Delta\tau_j \qquad (1$$

These expressions continue the concept of evaluating the parameters at the [illegible]

All material necessary for calculation of the raw brightness temperature is now available, and the detailed steps in the computer program will be discussed in the following section. It is preferred to treat each shell as a separate entity in the calculation. Thus, the operation of subdividing is applied to each shell individually, and a good estimate of total path length expected in the shell can be employed to determine the required number of segments. In addition, a readout of the results after the calculation for each shell is available, if desired. This readout permits a check on general program behavior and also clearly shows the atmosphere regions which are the major contributors to the observed brightness temperature. In addition, [illegible] to give [illegible]

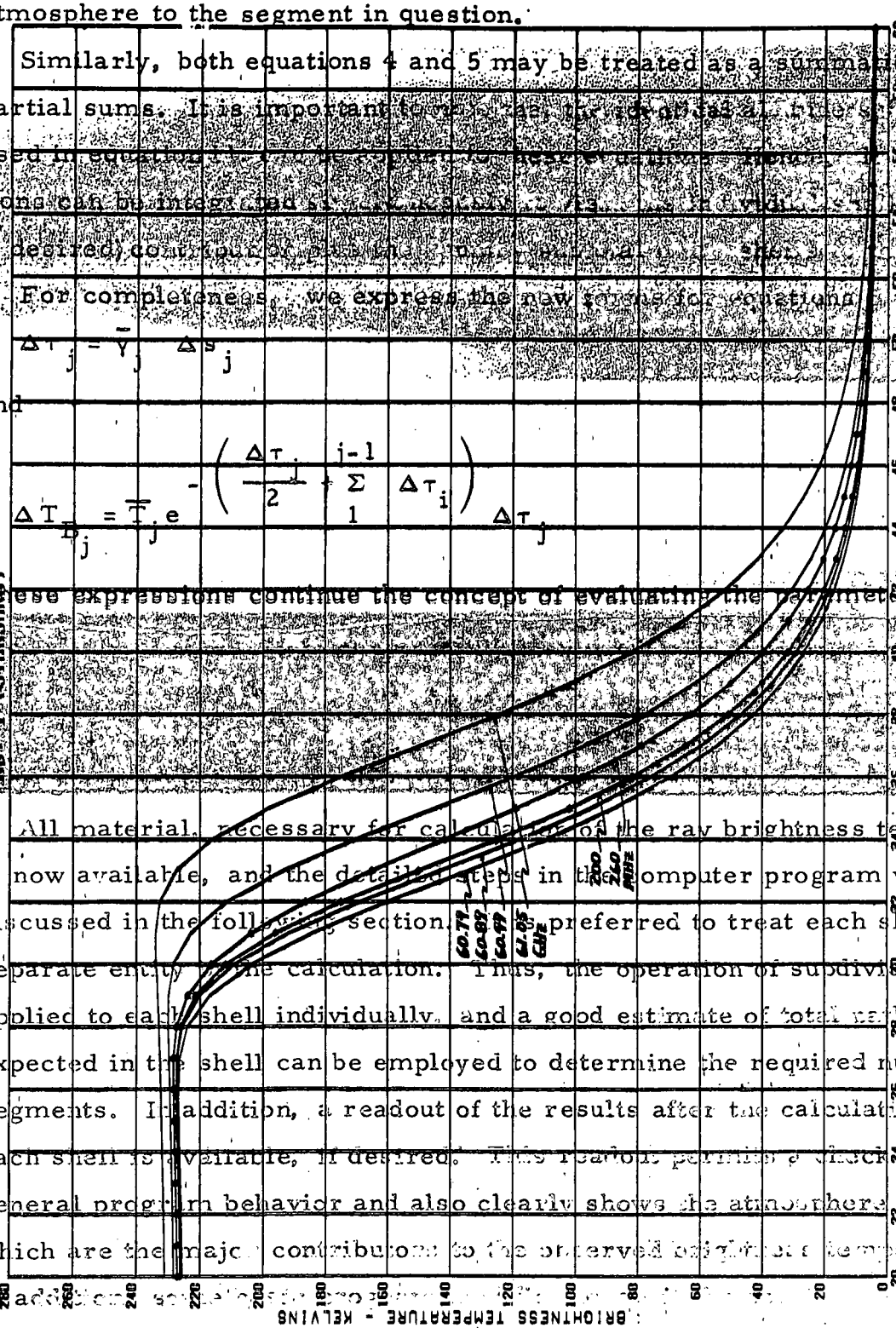

Figure 18. Comparison of Brightness Temperature Profiles, Atmosphere No. 1, Horizon Region, for Spot Frequencies and Bandwidth Averages

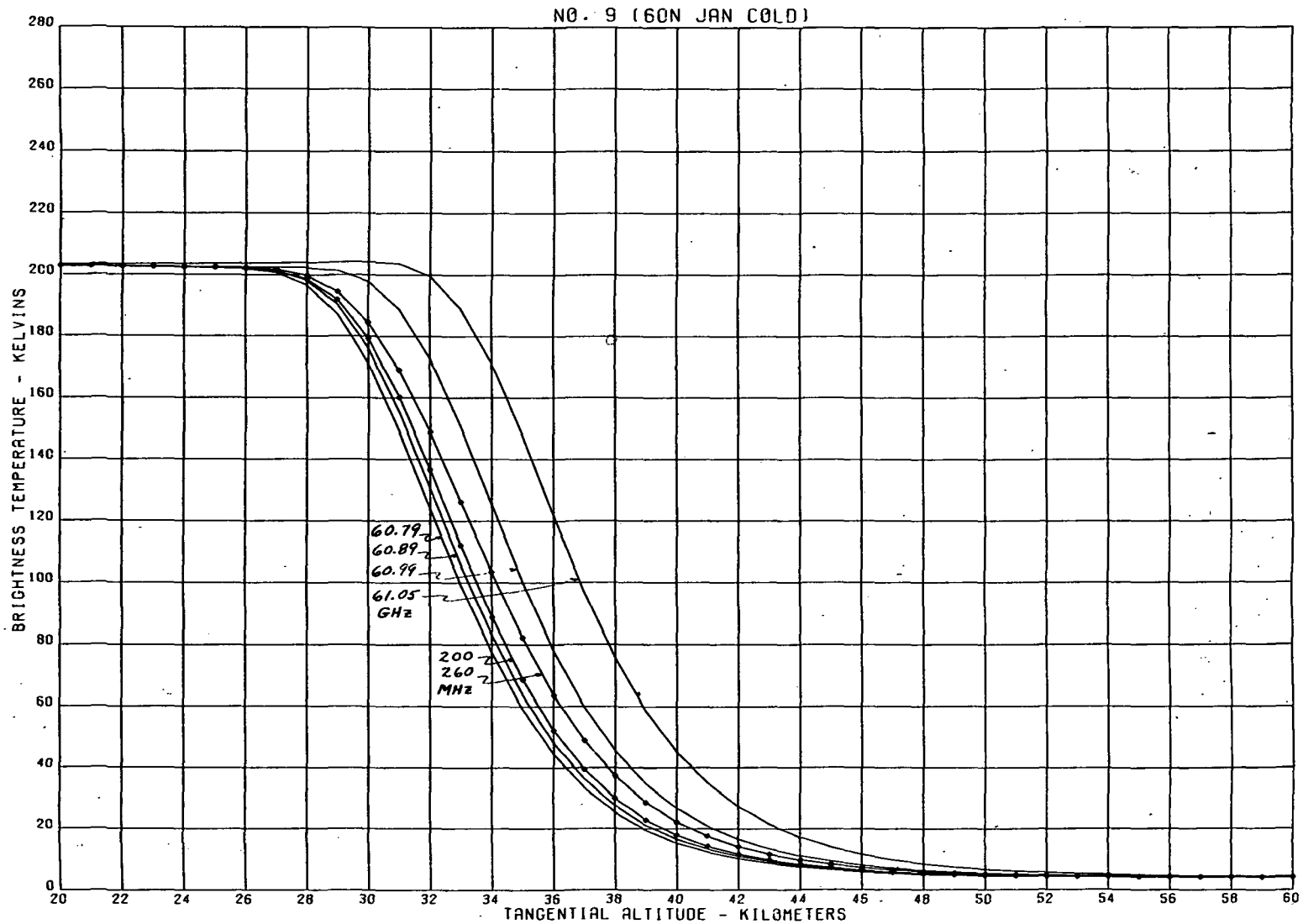

Figure 19. Comparison of Brightness Temperature Profiles, Atmosphere No. 9, Horizon Region, for Spot Freqencies and Bandwidth Averages

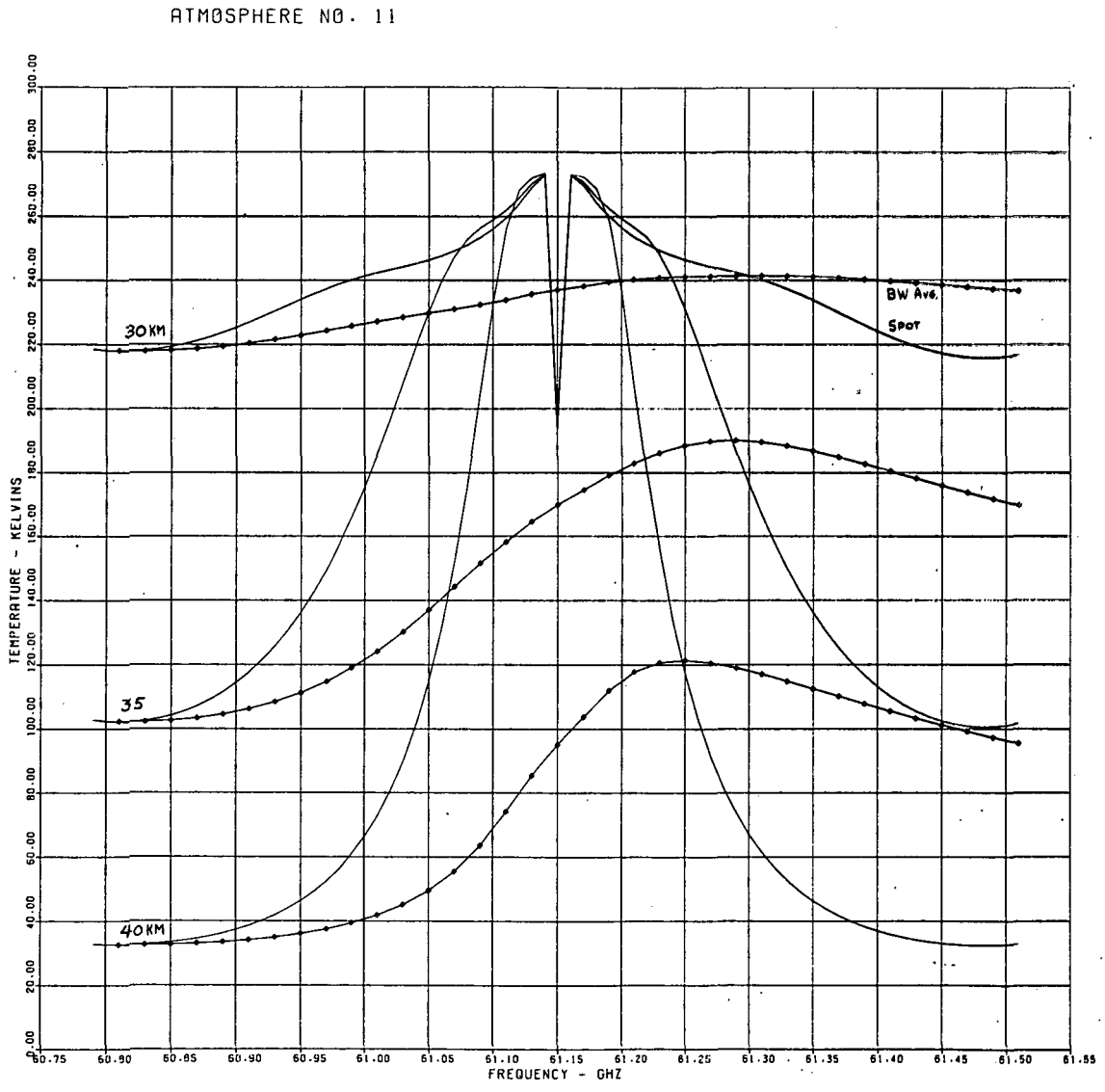

Figure 20. Brightness Temperature Versus Frequency, Atmosphere No. 11

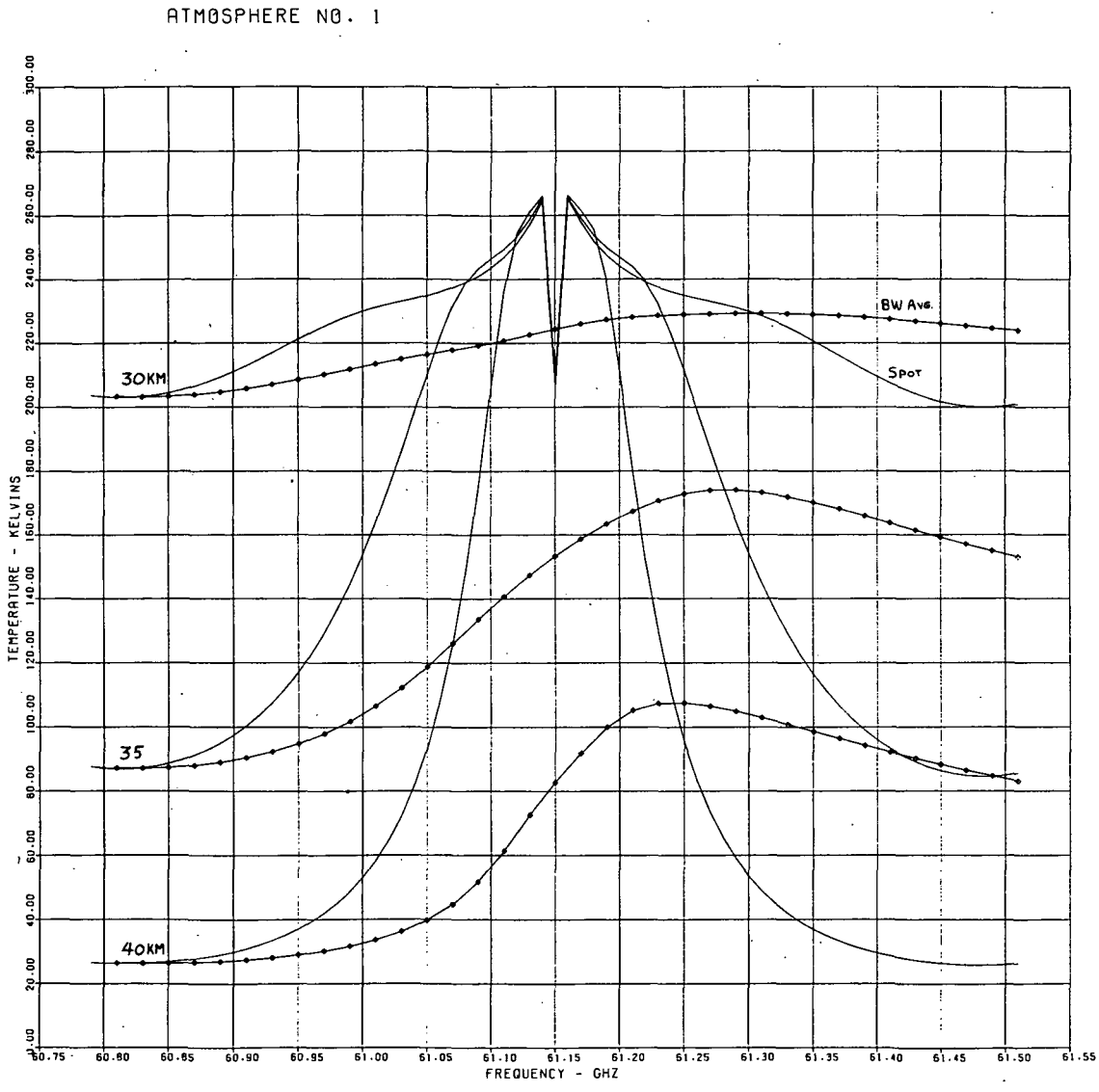

Figure 21. Brightness Temperature Versus Frequency, Atmosphere No. 1

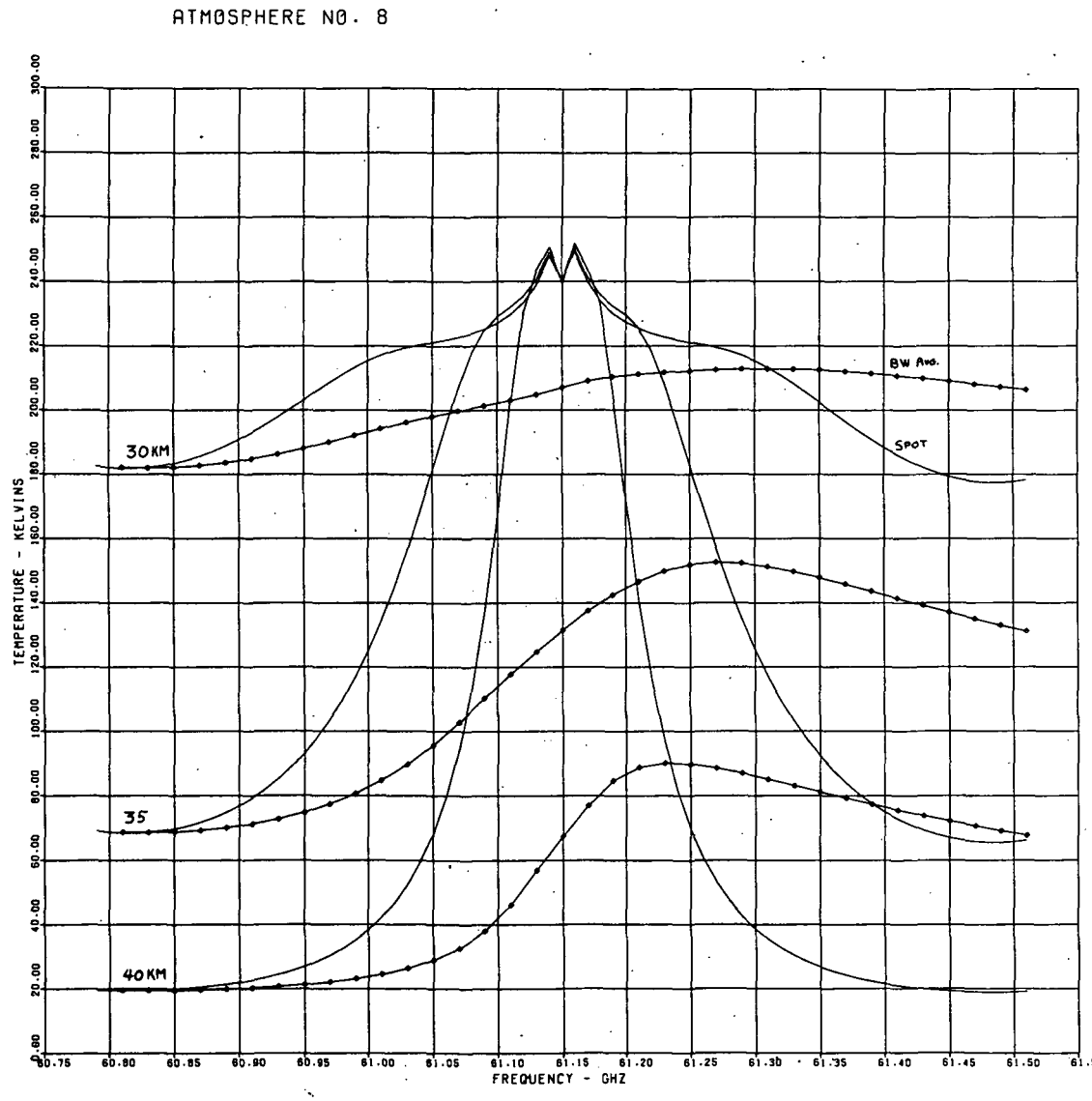

Figure 22. Brightness Temperature Versus Frequency, Atmosphere No. 8

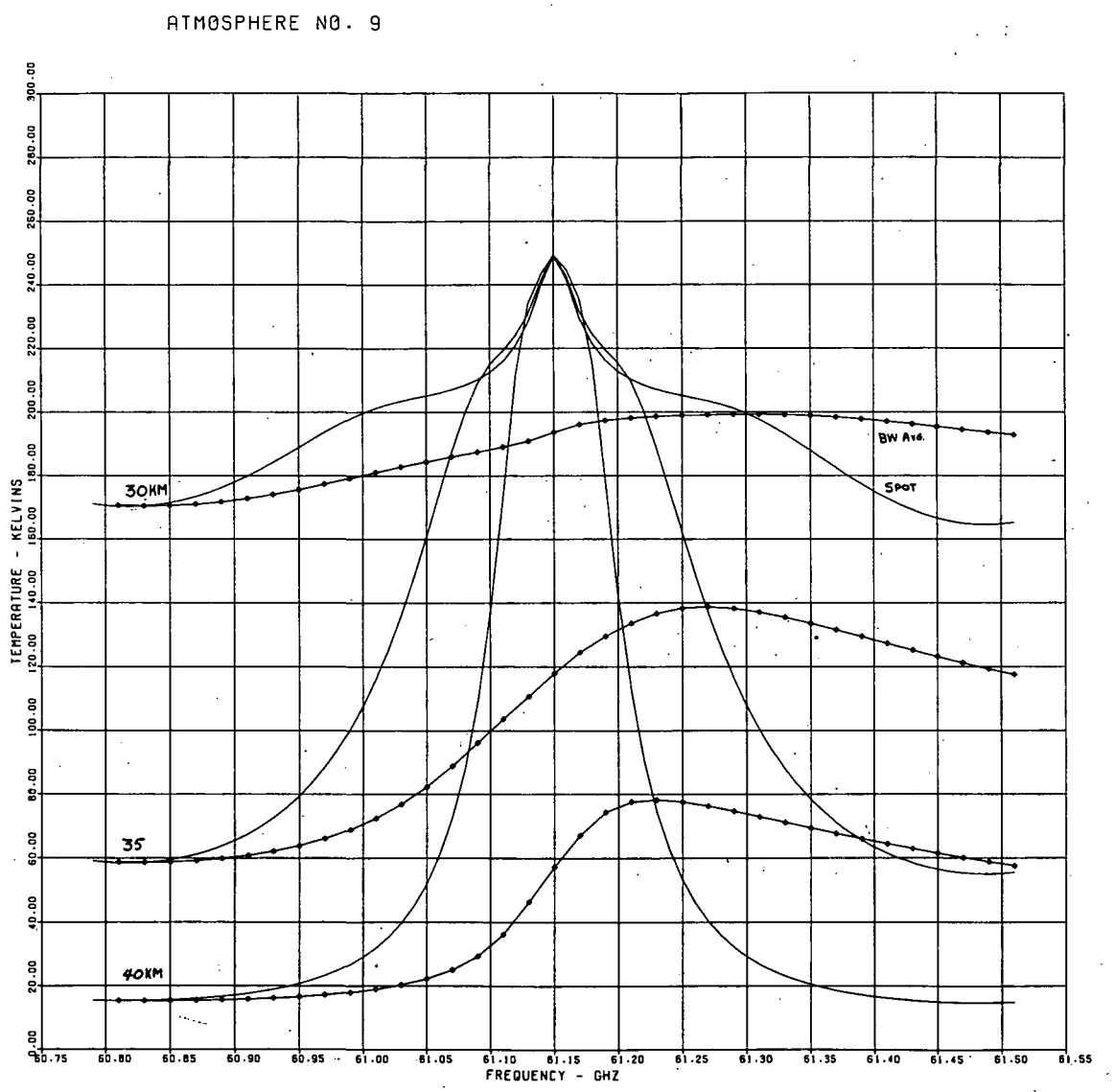

Figure 23. Brightness Temperature Versus Frequency, Atmosphere No. 9

plain curve, from 60.79 to the frequency identified by a diamond, is calculated by Simpson's rule and is then divided by the frequency span to give the average temperature over this range, which is the ordinate of that particular diamond. Thus, the diamonds represent a running average of a bandwidth calculation. This average is well behaved as long as the frequency span is not too great, but it varies rapidly in the vicinity of the resonance line. It is fairly well behaved in the middle of the next valley, but not much is gained from this and the requirement on total RF bandwidth is considerably increased.

These figures also illustrate the "notch" at the resonance, as discussed by Meeks and Lilley.[2] Only one point close to resonance has been calculated so this notch appears as a vee rather than a smooth curve, but the major properties are still evident. In figure 20, atmosphere No. 11 is hot and high pressure, and the 60.8-GHz rays are absorbed at the highest altitude of any case yet calculated. At the resonance, absorption is still higher in the atmosphere, but here the temperature has dropped sharply, creating the notch. In figure 21, atmosphere No. 1, both pressure and temperature have changed and the notch is not quite as deep. In figure 22, atmosphere No. 8, the notch is quite small. Finally, in figure 23, atmosphere No. 9, the notch has disappeared and has been replaced by a peak. This is the lowest pressure atmosphere considered, and hence the horizon occurs at the lowest tangential altitude. This atmosphere exhibits a rising temperature trend toward higher altitudes and thus produces a peak. As in the case of Meeks and Lilley, Zeeman effects have not as yet been included, and this could significantly alter the effect near this resonance line. In all four cases, however, the bandwidth average curves are well behaved over a resonable bandwidth range.

A brief mention of the magnitude of the computing effort is in order. Detailed calculations of brightness temperature have been made for 12 of the 19 model atmospheres listed in table 1. Four were dismissed as being incomplete, number 7 is the same as standard below 70 kilometers, and numbers 2 and 3 were considered rather similar to standard. In order to calculate the bandwidth averages already displayed on the various profile curves,

a total of 73 frequencies, 10 MHz apart, from 60.79 to 61.51 GHz were employed. Calculations were made for a total of 90 tangential altitudes in order to provide sufficient data for interpolation in the convolution process yet to be discussed. Thus, for each of the four representative atmospheres 1, 8, 9, 11 the brightness temperature of a total of 90 x 73 or 6,570 rays was calculated and cataloged. Atmospheres 4, 5, 10 employed 70 altitudes and 73 frequencies, or 5,110 rays each. Atmospheres 6, 16, 17, 18, 19 used 70 altitudes and 37 frequencies, from 60.79 to 61.15 GHz, for a total of 2,590 rays each. Thus, a grand total in excess of 56,000 ray brightness temperature calculations have been performed and cataloged. These calculations all used a Δs_{max} of 10 kilometers. From the convergence tests shown in table 2, this value of Δs_{max} indicates a maximum error of only a few hundredths of a degree, and it was felt that the relative error between different atmosphere models, which is really the heart of the accuracy problem, would probably even be less.

The next profile curves illustrate the comparison of the four atmospheres selected as representative, including numbers 9 and 11 which are considered extreme. It should be noted here that all profiles shown have been calculated for dry atmospheres. Although water vapor effects are a part of our computer program, the effects on profile are minor as the water tends to be mostly in the lower altitude regions. Carefully tabulated data for specific dry atmospheres is available in the literature, but no equivalent standard exists for water, particularly at the higher altitudes. Thus, it was felt that the most useful comparison could be made on the basis of the dry atmosphere models.

Figures 24 and 25 present the average brightness temperature data for the four atmosphere models numbered 11, 1, 8, and 9. The average is taken over the 200-MHz range from 60.79 to 60.99 GHz. The "hot" atmosphere, No. 11, has a higher plateau and is shifted to the right of the standard. The "cold" atmospheres have a lower plateau and are shifted to the left of standard. When taken together, the profiles on these figures appear remarkably well

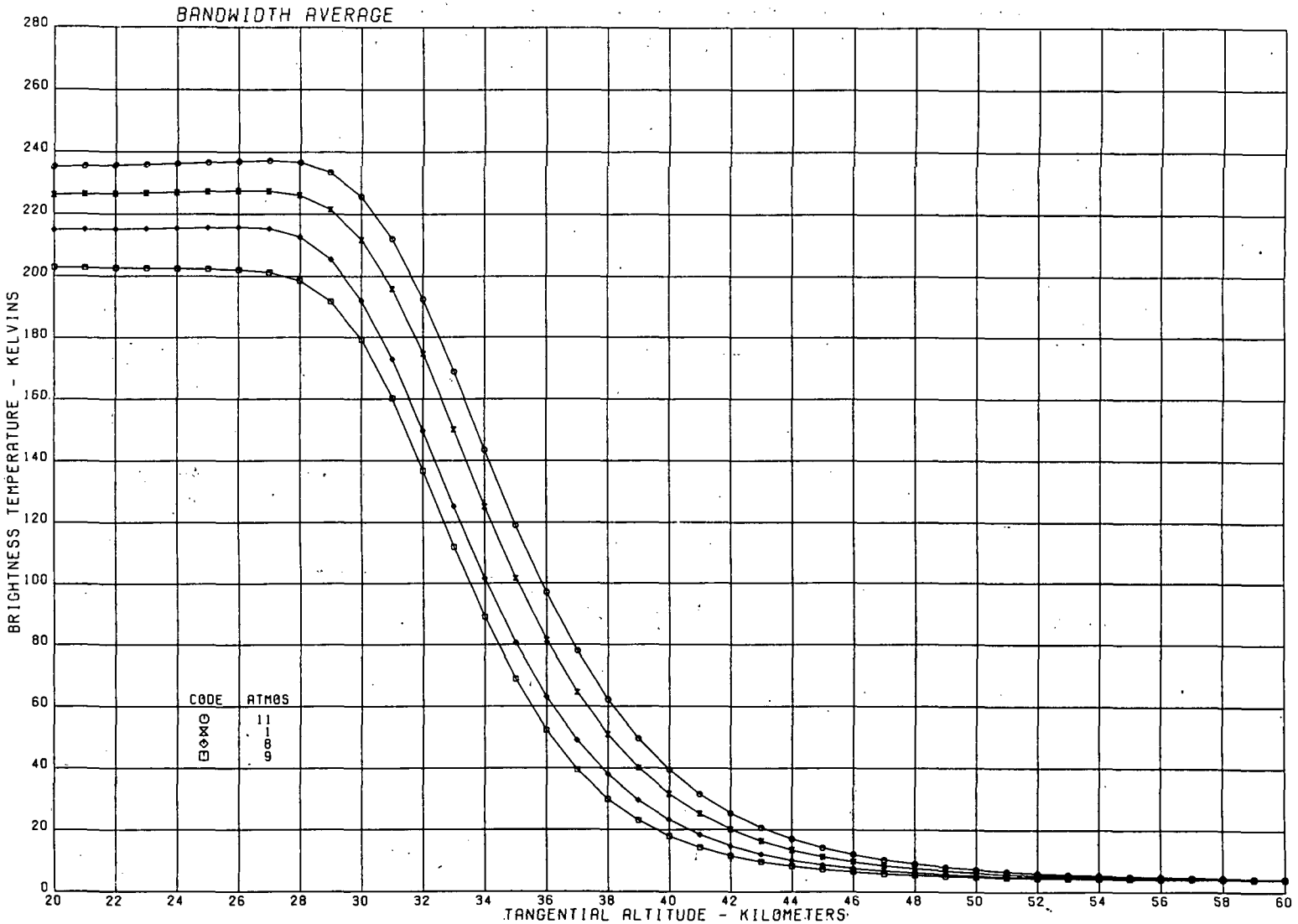

Figure 24. Brightness Temperature Profile, 200-MHz Bandwidth Average, Center Frequency of 60.89 GHz, Comparison of Atmospheres, Horizon Region

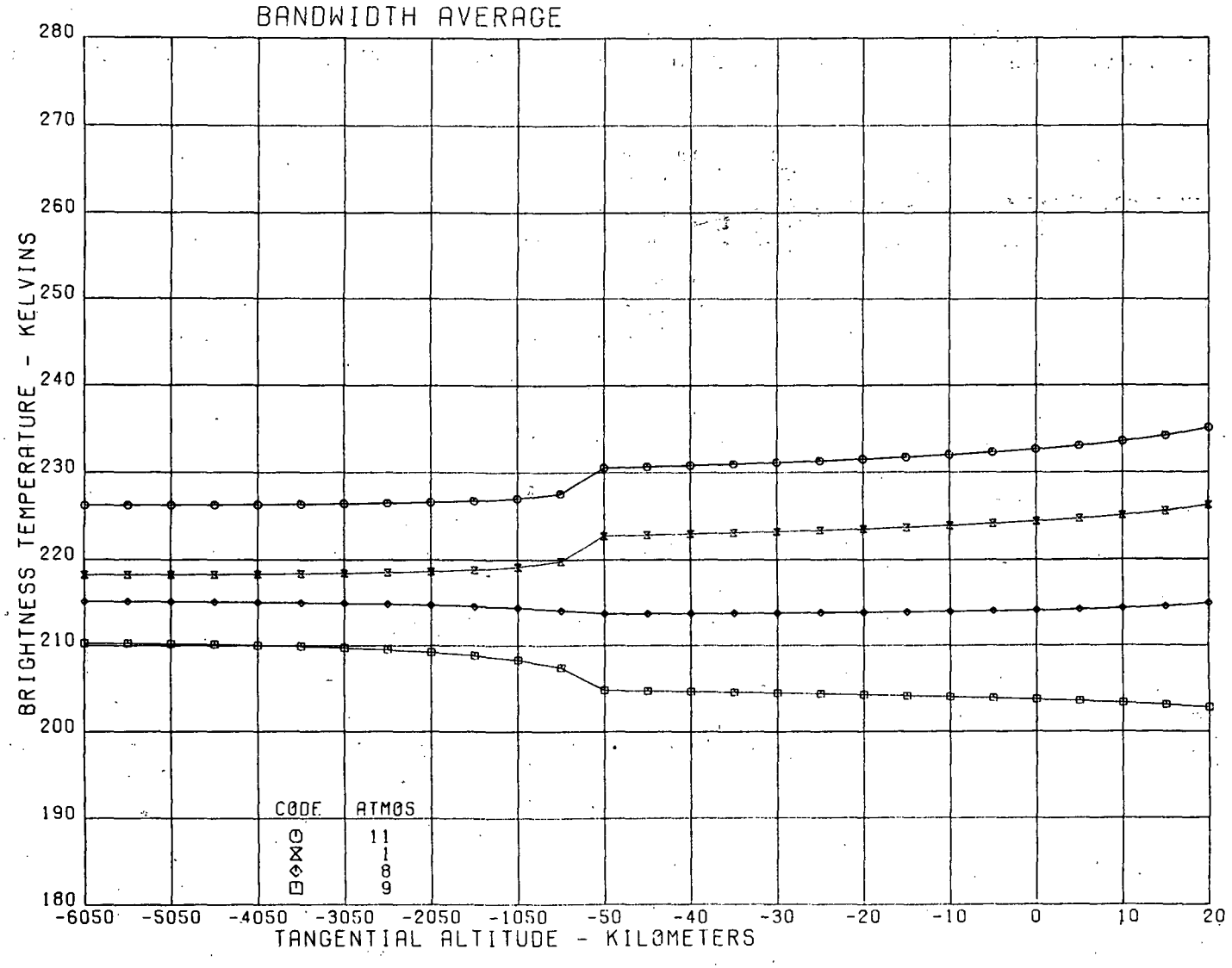

Figure 25. Brightness Temperature Profile, 200-MHz Bandwidth Average, Center Frequency of 60.89 GHz, Comparison of Atmospheres, Horizon Region

behaved. The maximum plateau spread is about 35 K, and the maximum shift in the edge is about 2.5 kilometers.

Figure 26 combines the two previous figures, showing the four representative atmospheres, into one profile. Note the breaks in altitude scale at -50 and 25 kilometers. Figure 27 compares 4, 5, 6, 10, averaged over a bandwidth of 200 MHz, with the "extremes" 9 and 11. Figure 28 is similar, but illustrates 16, 17, 18, 19. Note that the advanced stage warming model, number 19, exhibits a temperature rise just below the horizon, and also displays a small "backporch" not characteristic of the other models, but does remain within the previous extremes. The comparable 14-16μm IR horizon profile for this model displays a much more pronounced effect than does the microwave profile. The effect there shows up as a bulge in the edge. In figure 29, the brightness temperature difference between each of the 11 models and standard atmosphere is presented on an enlarged scale for better readability. Again the peculiar behavior of 19 is noted, whereas 18 is rather well behaved.

4.3 LOCAL OSCILLATOR STABILITY

Only some very general comments can be made at this time concerning local oscillator stability requirements. Clearly, in the middle of a valley, local oscillator stability has rather little effect. The major effect will occur if the resonance line is too closely approched in the passband, but this has already been shown to be a rather poor operating region for other reasons. Calculations of the average T_B over a given bandwidth as this bandwidth shifts in the valley region can be made, but a good technique for evaluating the results has not yet been determined. Another possible approach is to use the largest typical passband portrayed in figure 2, or at least a part of it symmetrical on a resonance line. In this way, LO variations would have negligible effect, as the net result is a small movement in the valley region. In general, this approach has no great advantage to recommend it and has the severe drawback of requiring a maximum bandwidth if used as shown. Of course, the LO could be placed directly on the resonance line and the passband taken either side of resonance. This is not shown in figure 2, but

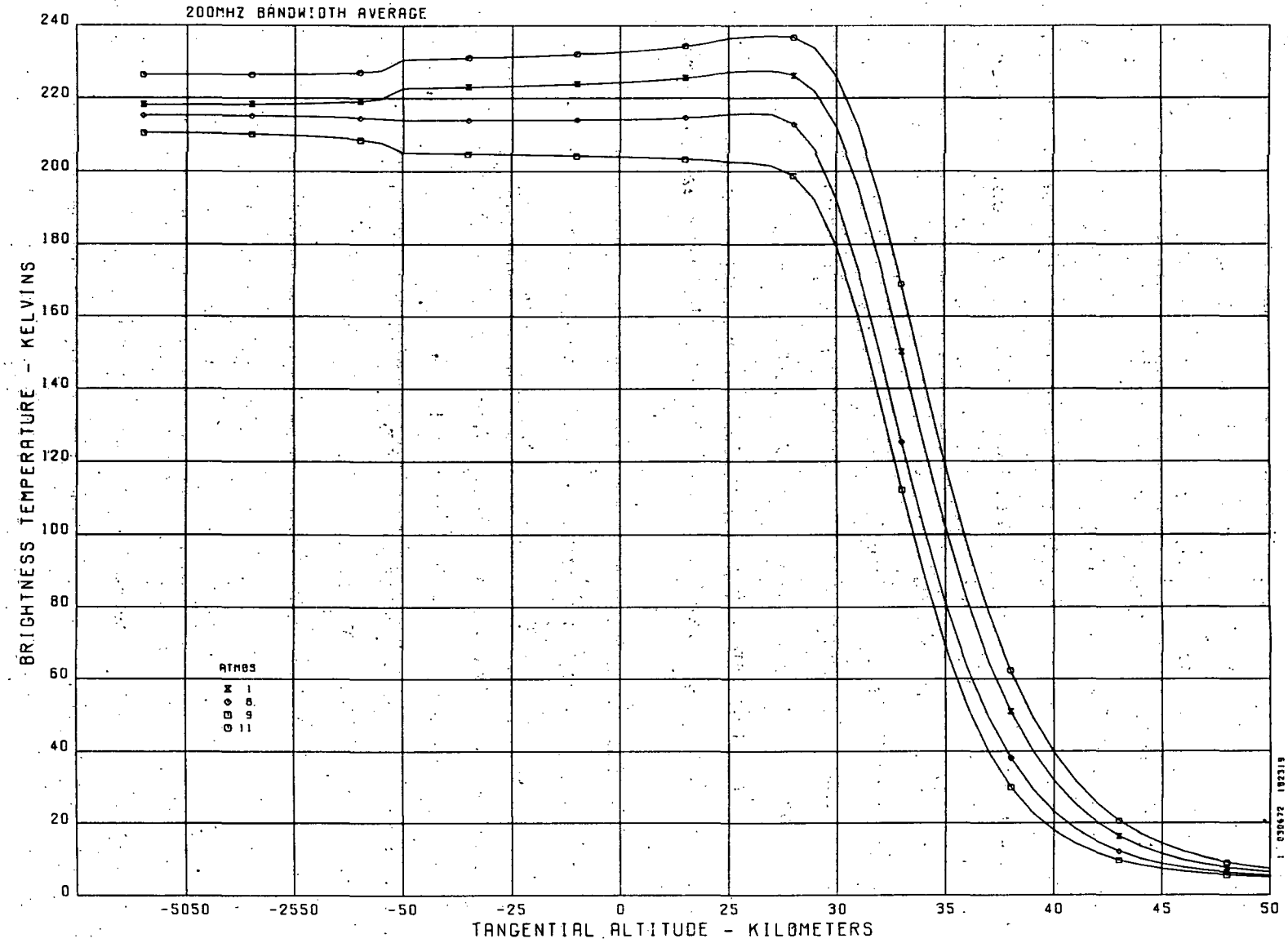

Figure 26. Brightness Temperature Profile, Representative Atmospheres 1, 8, 9, 11
60.79 - 60.99 GHz

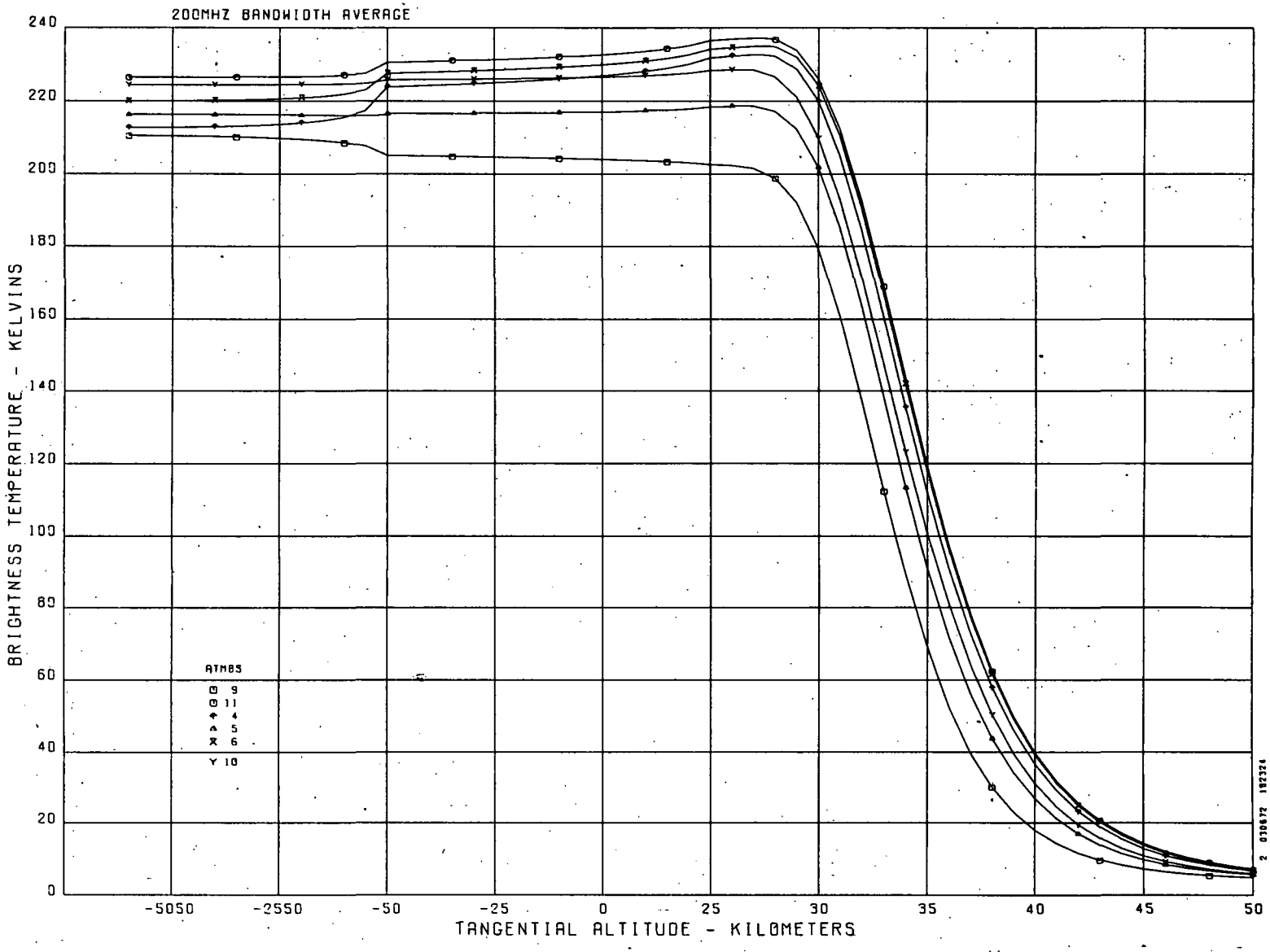

Figure 27. Brightness Temperature Profile, Atmospheres 4, 5, 6, 10 Compared to Extremes 9, 11, 60.79 - 60.99 GHz

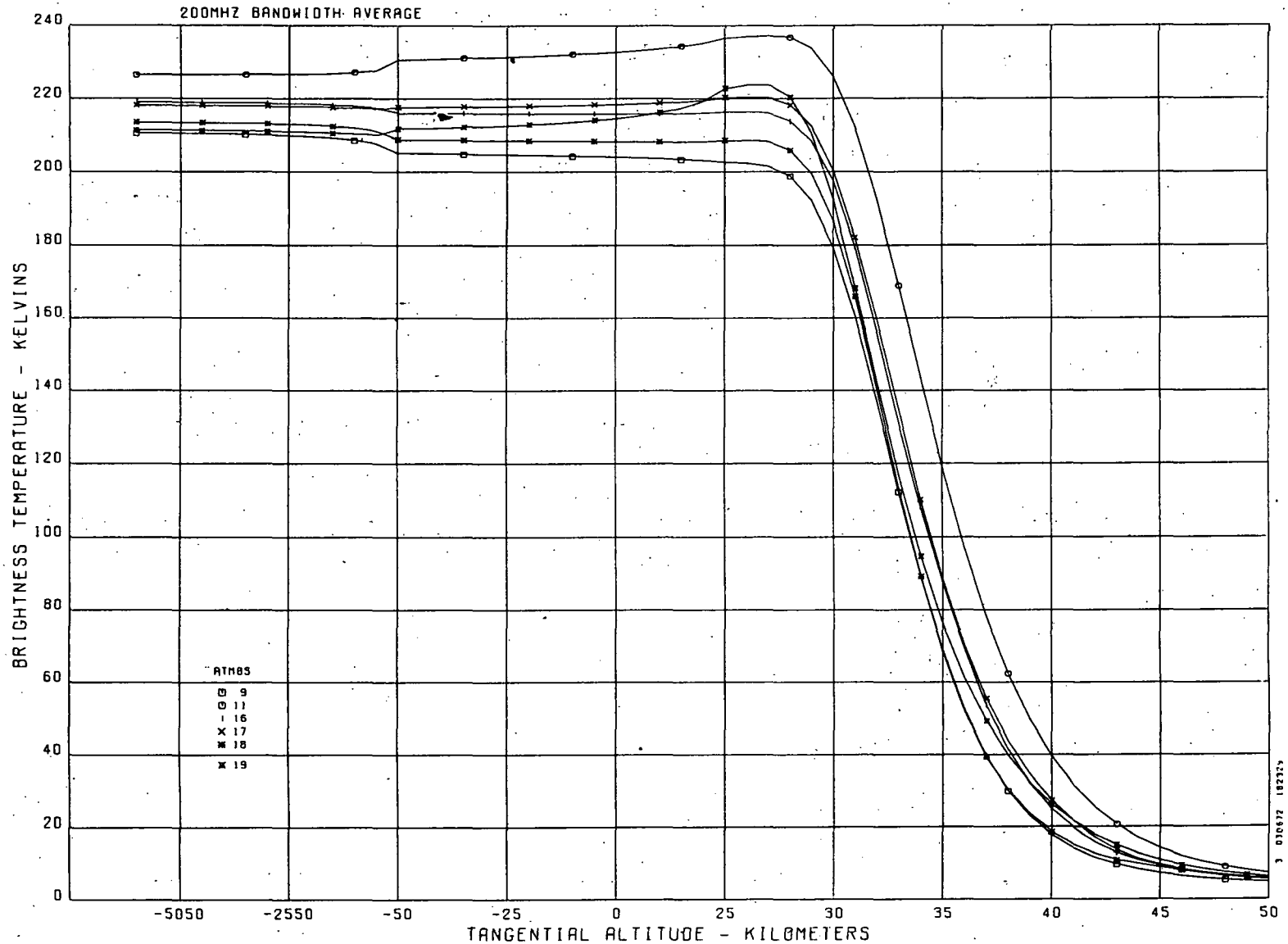

Figure 28. Brightness Temperature Profile, Atmospheres 16, 17, 18, 19 Compared to Extremes 9, 11, 60.79 - 60.99 GHz

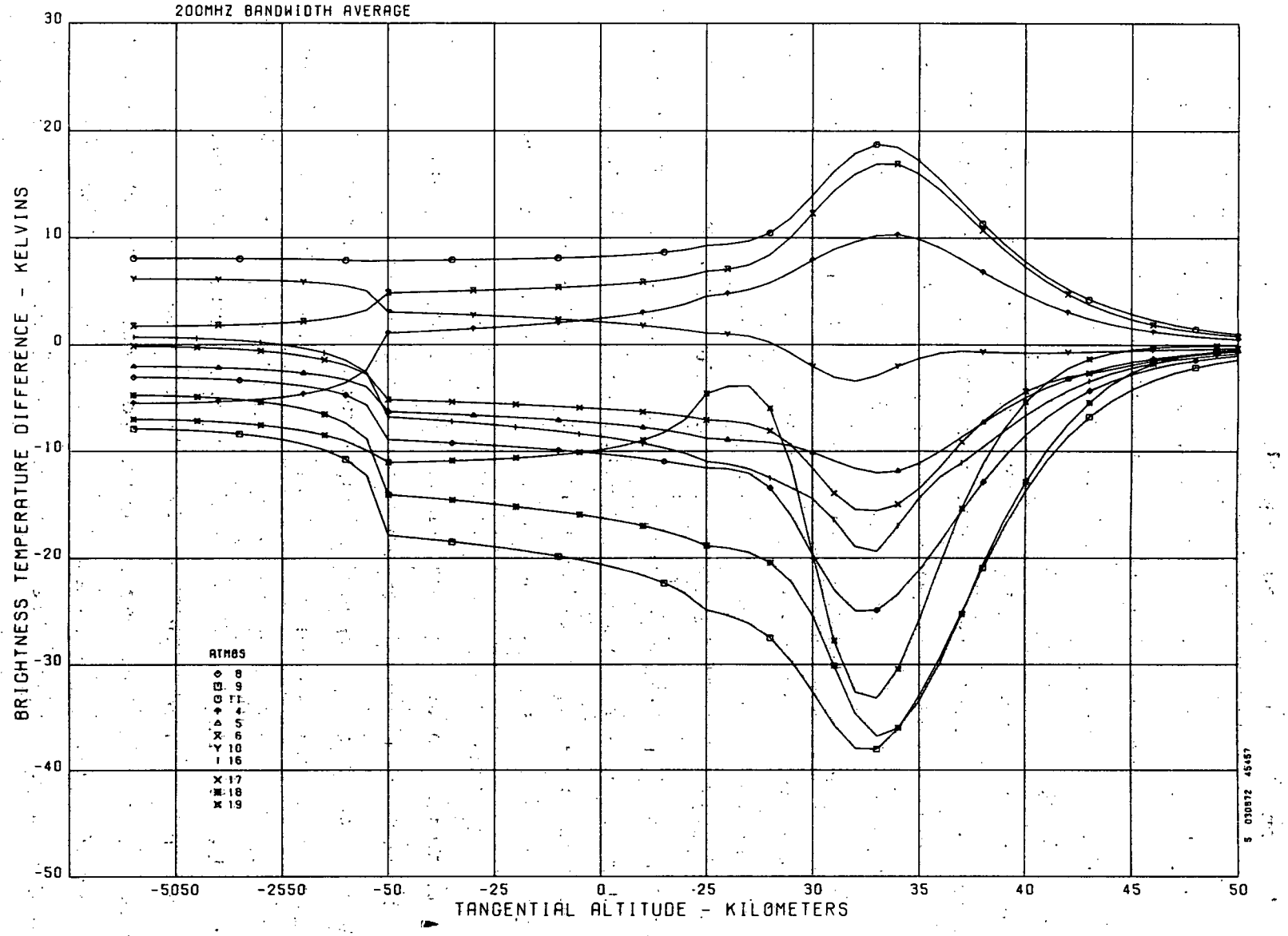

Figure 29. Brighness Temperature Differences for 200 MHz Bandwidth Average (60.79 - 60.99 GHz), 11 Atmospheres Referred to 1962 Standard Atmosphere

is a possible consideration for frequency selection. It seems that LO carrier stability is not a major problem, and it will be placed secondary to other factors unless some good reason for a change is disclosed. For example, LO noise might be more of a problem, as this would determine how close to the carrier the IF passbands could profitably be located.

4.4 CONVOLUTION

The temperature exhibited by the sensor antenna at a given pointing position represents the integral over the antenna pattern of the product of the antenna gain function and the brightness temperature profile. To determine system performance, the convolution of the antenna pattern and the brightness profile is required. For this calculation, the antenna is scanned across the profile, and the integrated output for a number of discrete pointing positions is obtained. The resulting curve, or convolved pattern, represents antenna temperature as a function of antenna position. The difference of two such curves, with separate antennas observing opposite limbs of the earth, may be taken as the effective output characteristic (i.e., the indicated temperature as sensed by the radiometer) of the local vertical sensor. For simplicity, the calculation has been performed only in one dimension, and the antenna is scanned in the axis of its narrow beamwidth.

The integration process to determine antenna temperature breaks the beam into a large number of parts, or rays. For each ray in the beam, a corresponding point in the brightness temperature profile is established. Since, in general, this is not a point at which T_B was originally calculated, an interpolation routine is employed to determine brightness temperature for this ray. The ray temperatures and gains are then multiplied to produce a curve which is integrated to yield the temperature appearing at the antenna terminals, T_A, which in turn forms one input channel of the radiometer. In that portion of the beam where the brightness temperature at the edge of the limb changes rapidly, a finer breakdown of points is provided in order to preserve accuracy. The final convolved pattern is then obtained by scanning the antenna pattern across the edge of the earth and calculating T_A at each

pointing position. For almost all conceivable microwave cases, the edge of the brightness profile will be sharper than the antenna pattern, and hence the general shape of the convolved pattern is primarily determined by the antenna characteristics. However, the convolved amplitude is closely related to the profile characteristics, and particularly to the plateau temperature.

Figure 30 shows the convolved patterns for uniform illumination and Gaussian beam compared to the brightness profile for a satellite altitude of 200 nautical miles. As indicated earlier, the profile is considerably sharper than the convolved pattern, even at this low altitude. At higher altitudes, the profile will become much sharper, but the convolved patterns, with shape primarily determined by beamwidth, will remain essentially the same. The effect of the large sidelobes resulting from uniform illumination is readily apparent in the figure, appearing as a series of plateau regions in the pattern. However, in the main central region of the pattern, the effect is almost negligible, being only a very slight reduction in slope. This will later be seen to be a rather general conclusion -- that antenna pattern shape has only a minor effect on system performance -- except for one case noted later. Figure 31 shows an expanded scale version, and adds a cosine illumination beam, which exhibits a slightly greater slope than the Gaussian. These beams have all been adjusted to a 1-degree half power beamwidth.

As with the ray brightness information, much calculation is involved. In order to include representative atmospheres, antenna pattern shapes and beamwidths, and satellite altitudes, in excess of 78,000 convolution calculations have so far been performed and cataloged.

4.5 COMPENSATION FOR PLATEAU HEIGHT

The difference in plateau temperatures resulting from different atmospheres on opposite sides of the earth appears to cause the major error in the experiment system. A compensation technique has been developed which greatly reduces the error from this source.

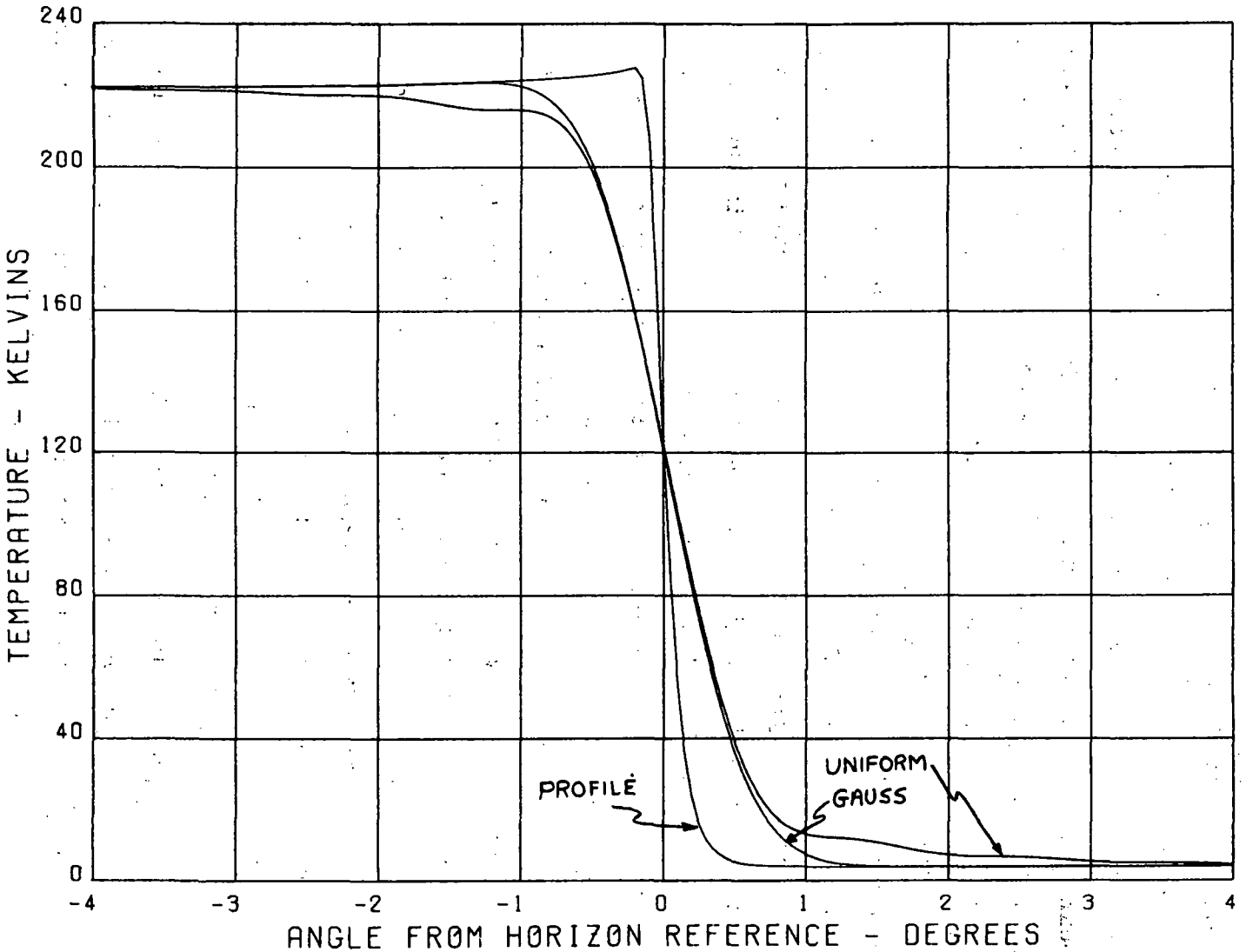

Figure 30. Comparison of Brightness Temperature Profile (Standard Atmosphere) and Convolved Patterns (Uniform Illumination and Gaussian Beam), 200-nmi Altitude

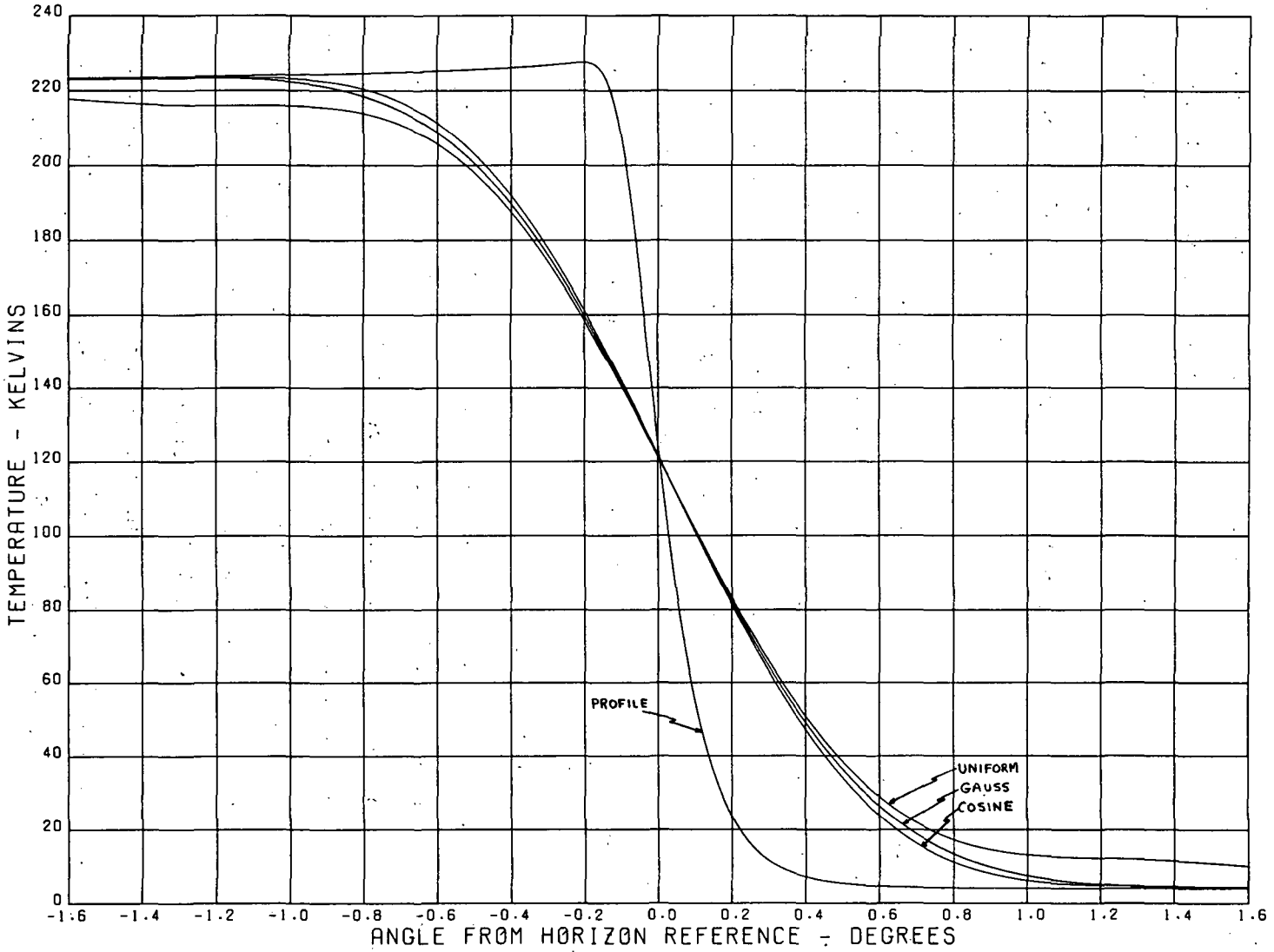

Figure 31. Comparison of Brightness Temperature Profile and Convolved Patterns (Cosine and Uniform Illumination, Gaussian Beam), 200 nmi Altitude

Consider an antenna pointed at the edge of the brightness profile, say at 34 kilometers in figure 26. Since the antenna beam will, in general, be wider than the profile edge, a significant contribution to observed antenna temperature, T_A, comes from the plateau. (For an antenna at synchronous altitude, the profile is of negligible width, and T_A is almost entirely plateau contribution.) Thus, identical antennas observing different atmospheres will produce an apparent output error when, in fact, no pointing error from vertical exists. Compensation could be achieved by introducing an appropriate gain change in the system, but this requires a priori knowledge of the atmospheres involved. Based on our studies, we propose a self-compensating system which uses another antenna beam, pointed slightly inside the normal measuring beam (i.e., at a lower tangential altitude) to sense the plateau temperature. By comparing the plateau temperatures on opposite sides of the earth and making a gain change in the system to equalize these temperatures, the gross error due to plateau height difference can be removed. Theoretical calculations have been made of the performance of this compensation technique, and predicted performance for both compensated and uncompensated systems will be discussed in the next section.

4.6 PREDICTED PERFORMANCE

The convolution calculations discussed in paragraph 4.4 are used to predict performance of the local vertical sensor. This performance is based on the properties of the phenomenon being observed and the system parameters used to make the observation such as antenna pattern and compensation technique. Error due to finite sensitivity in the radiometer is neglected in these calculations, but it was shown in section 2 that a readily achievable radiometer sensitivity would cause less than 0.003 degree error in pointing position, assuming a 1-degree beamwidth. In making the calculations, five different antenna patterns, five beamwidths, and three typical satellite altitudes were used, and four atmosphere groupings from the representative atmospheres shown in figure 26 were evaluated. In addition, the 12 atmospheres of table 1 were each compared against number 1 (standard) as a reference. The antenna

patterns considered were those resulting from aperture illumination by uniform, cosine, cosine squared, and hamming functions, plus an assumed Gaussian beam shape. These patterns cover essentially the entire range of available sidelobe levels, in roughly equal steps. Beamwidths of 0.5, 0.74, 1.0, 1.5, and 2.0 degrees were used in the calculations. Since system sensitivity (kelvins per degree) varies inversely with antenna beamwidth, the aperture sizes were adjusted to provide the desired identical half-power beamwidth for all antenna patterns. Clearly, only a representative sample of the results can be included in this section.

Figure 32 shows the expected output from the system, in terms of equivalent input temperature to the radiometer for an uncompensated system. Drastically different atmospheres, such as the 11-9 combination, show a significant error output at local vertical as expected. The curves reach a large value at either end, which is essentially the peak of the atmosphere being observed, as the other antenna beam is then looking at space temperature. Figure 33 shows a similar plot for the compensated system, using three different pointing positions for the compensating beams. Lower errors on vertical are noted, but the sensitivity, or slope, is almost unchanged. These curves are again for 1 degree beamwidth, and assume that the antennas are fastened together with a fixed squint angle corresponding to that between the 34-kilometer tangential altitude points on opposite limbs of the earth. Compensation angle is measured inward from the measuring beam axis (lower tangential altitude) and the output is well behaved over about half this angle in either direction; that is, until the compensating beam moves off the plateau.

A further demonstration of the insensitivity to antenna pattern appears in figure 34. Here standard atmosphere appears on both limbs, but all five antenna patterns are used, again for three positions of the compensating beams. In the main central region, no significant effect occurs, but there are some changes at higher angles which are not really important. The cosine, cosine squared and hamming function illuminations are indistinguishable, the

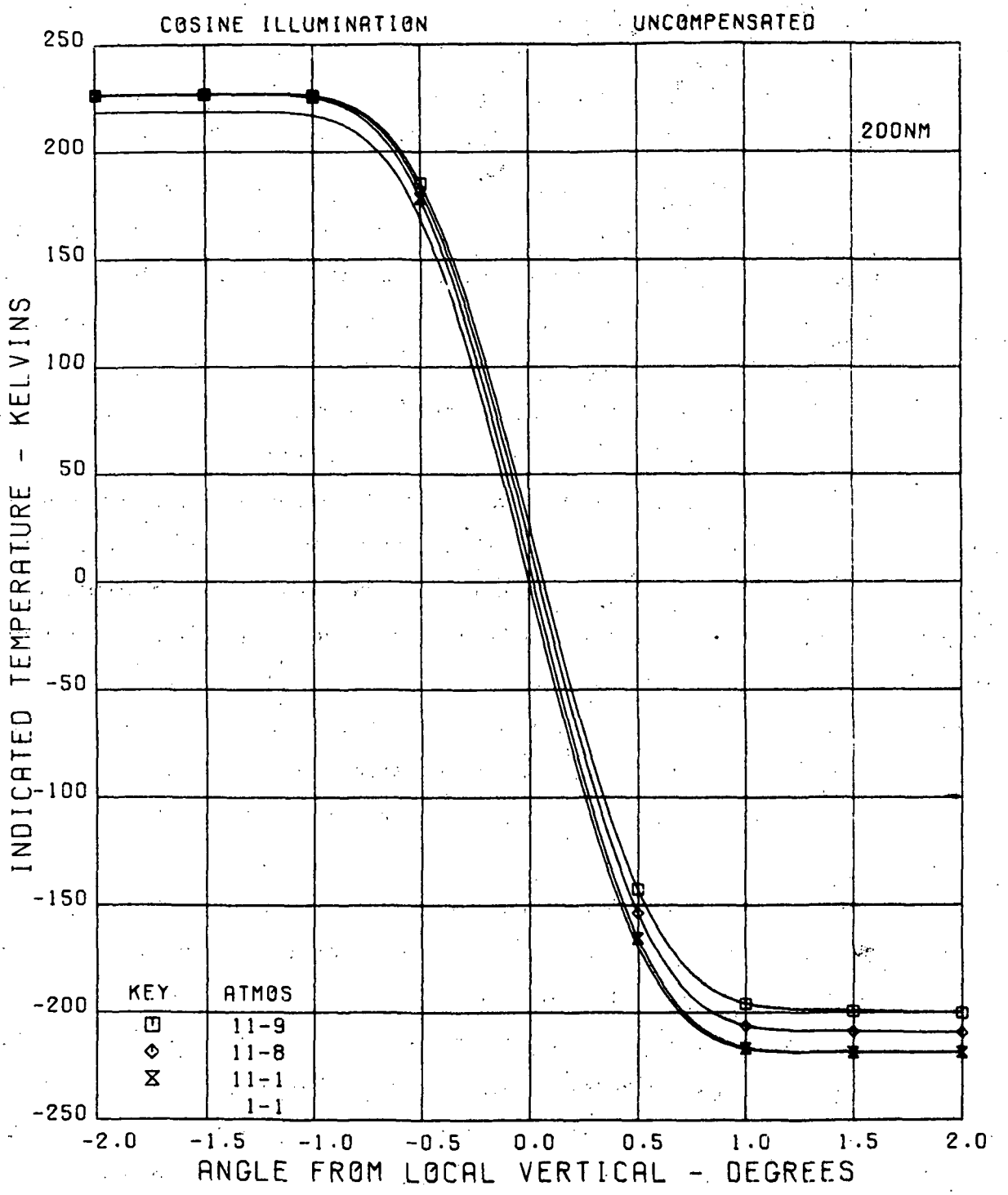

Figure 32. LVS Output Characteristic, 200-nmi Altitude, Uncompensated

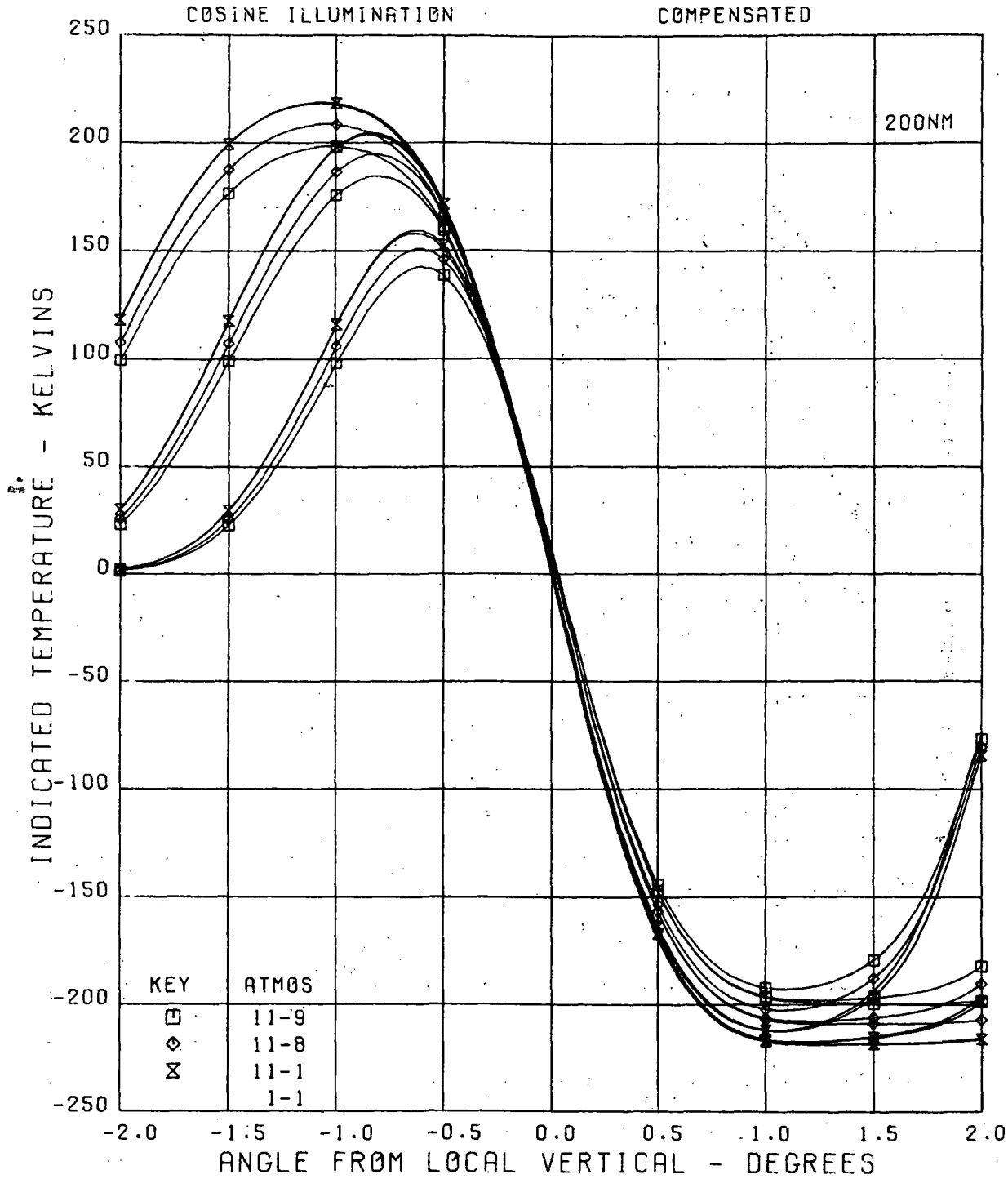

Figure 33. LVS Output Characteristic, 200-nmi Altitude, Compensation Angles 1.0, 1.5, 2.0 Degrees

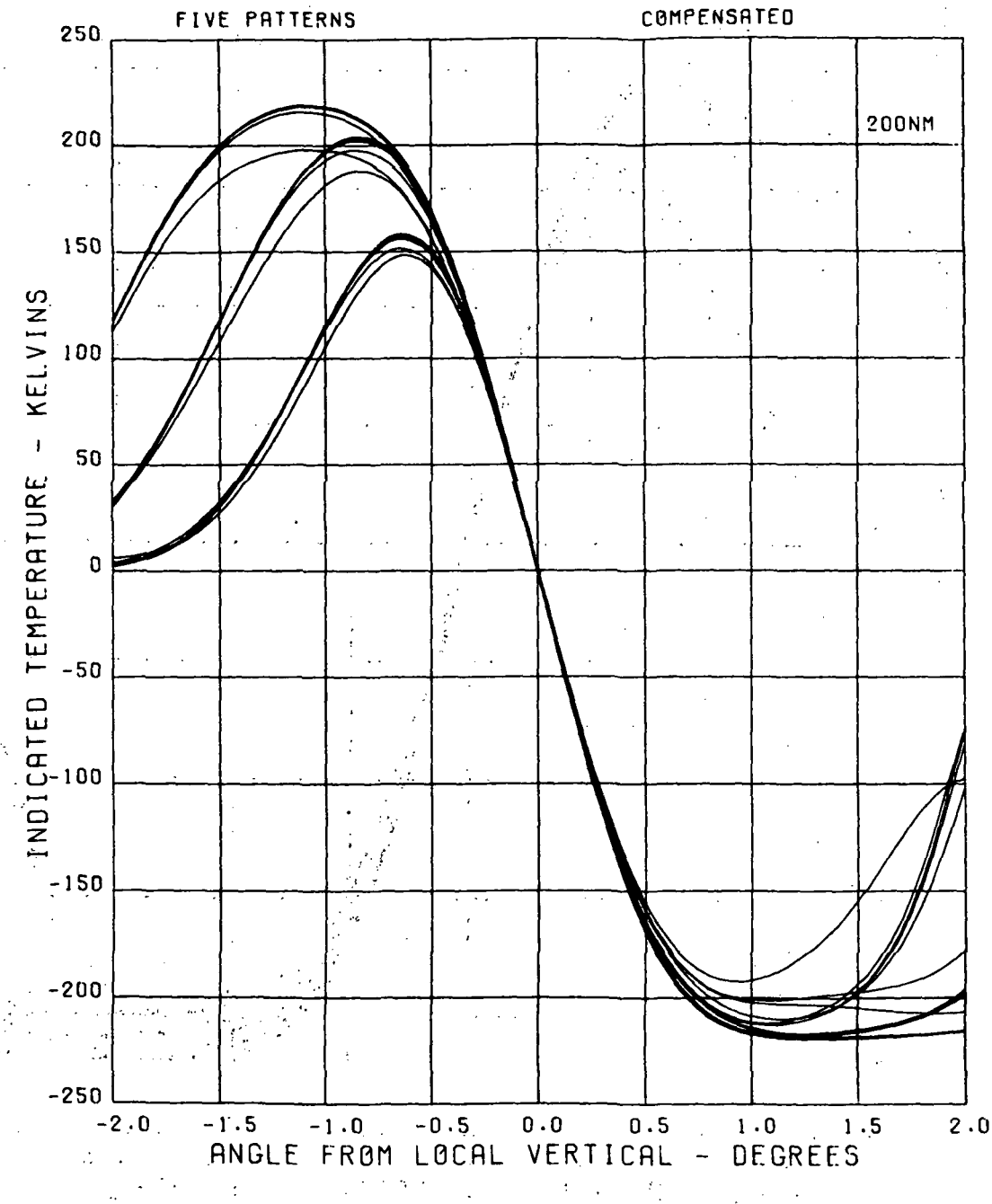

Figure 34. Effect of Antenna Pattern on Compensated LVS Output Characteristic, Atmosphere 1-1

Gaussian pattern deviates slightly from this group, and uniform illumination shows the greatest deviation.

The previous curves showed the gross behavior of the vertical sensor system. To properly evaluate the error, much more detailed examination of the central region is required, and this is provided by figures 35 through 40.

These figures include both the uncompensated and compensated systems, at satellite altitudes of 200 nmi, 600 nmi, and synchronous, and are for Gaussian pattern, 1-degree beamwidth, and a compensation angle of 1 degree where applicable. Again, four pairs of atmospheres, exhibiting roughly equal steps of profile difference (see figure 26), are assumed on opposite limbs. The extreme pair 11-9 shows the greatest error, and the 1-1 pair shows zero error. The curves may be interpreted either as the temperature output at true local vertical, or as the pointing error which occurs if the radiometer input is driven to zero by an attitude control servo loop. The improvement obtained by using the compensation technique is quite apparent at all altitudes. Behavior, in terms of angular accuracy, is best at synchronous altitude since the near step-function behavior of the profile at this altitude causes negligible error, and the prime error is due to inability to precisely compensate for plateau difference. In contrast, at the very low altitude, the compensation is relatively good, but the shift in profile edge location causes the significant error.

More careful study of this data, however, shows that the low altitude error is not as great as the curves imply. The extreme atmospheres used may be considered as 60 degrees North and 60 degrees South (one is Cold January and the other July) or a latitude separation of 120 degrees. From synchronous altitude a central angle of 163 degrees exists, so such extreme atmosphere variations are realistic, although a better choice of positioning the orthogonal axes might result in less chance of such extreme conditions. However, from 600 nmi, the central angle is only 63 degrees, and from 200 nmi it is only 36 degrees. Over such a small latitude range, it is unlikely that such

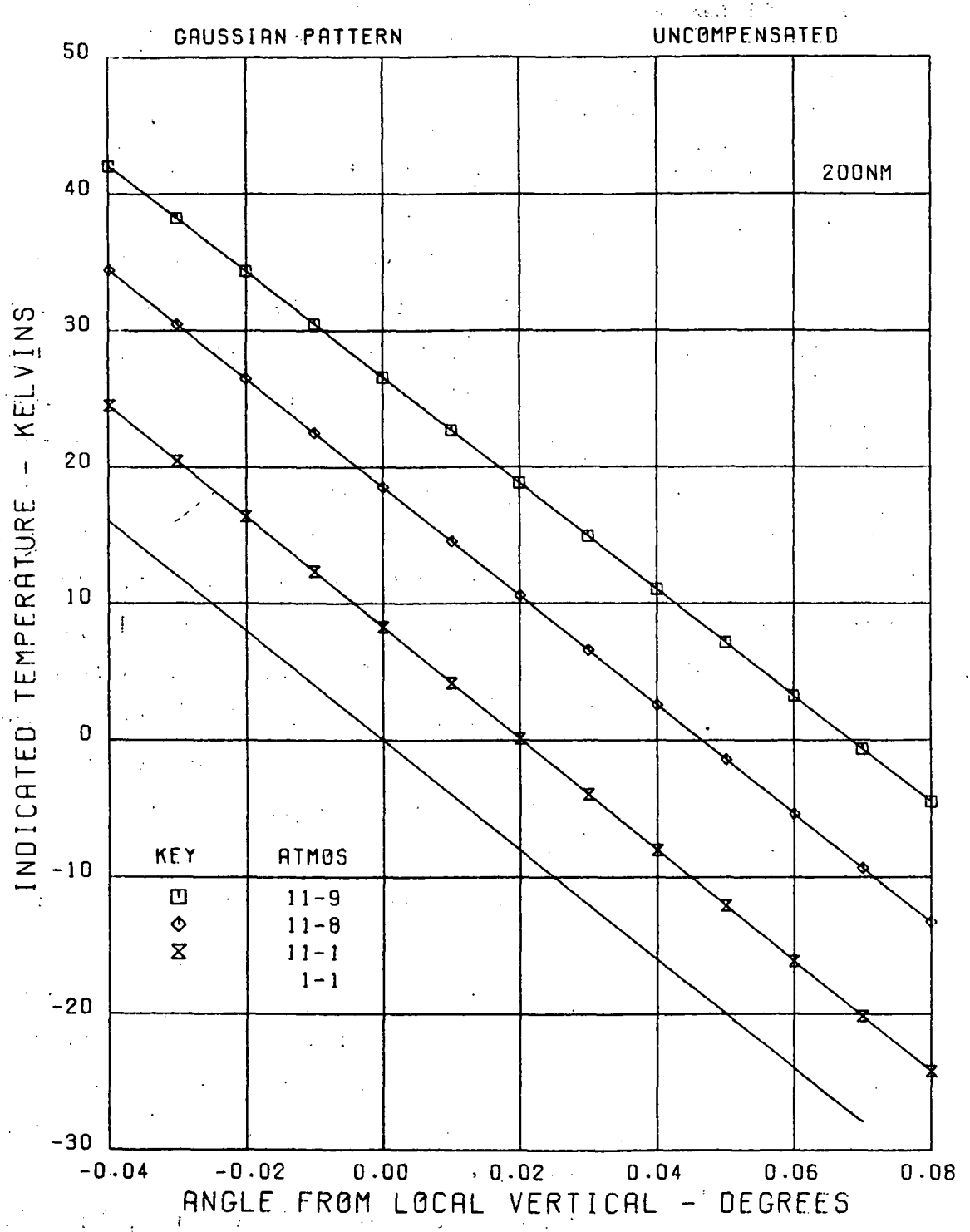

Figure 35. Detailed LVS Error Characteristic, 200-nmi Altitude, Uncompensated, 1-Degree Beamwidth

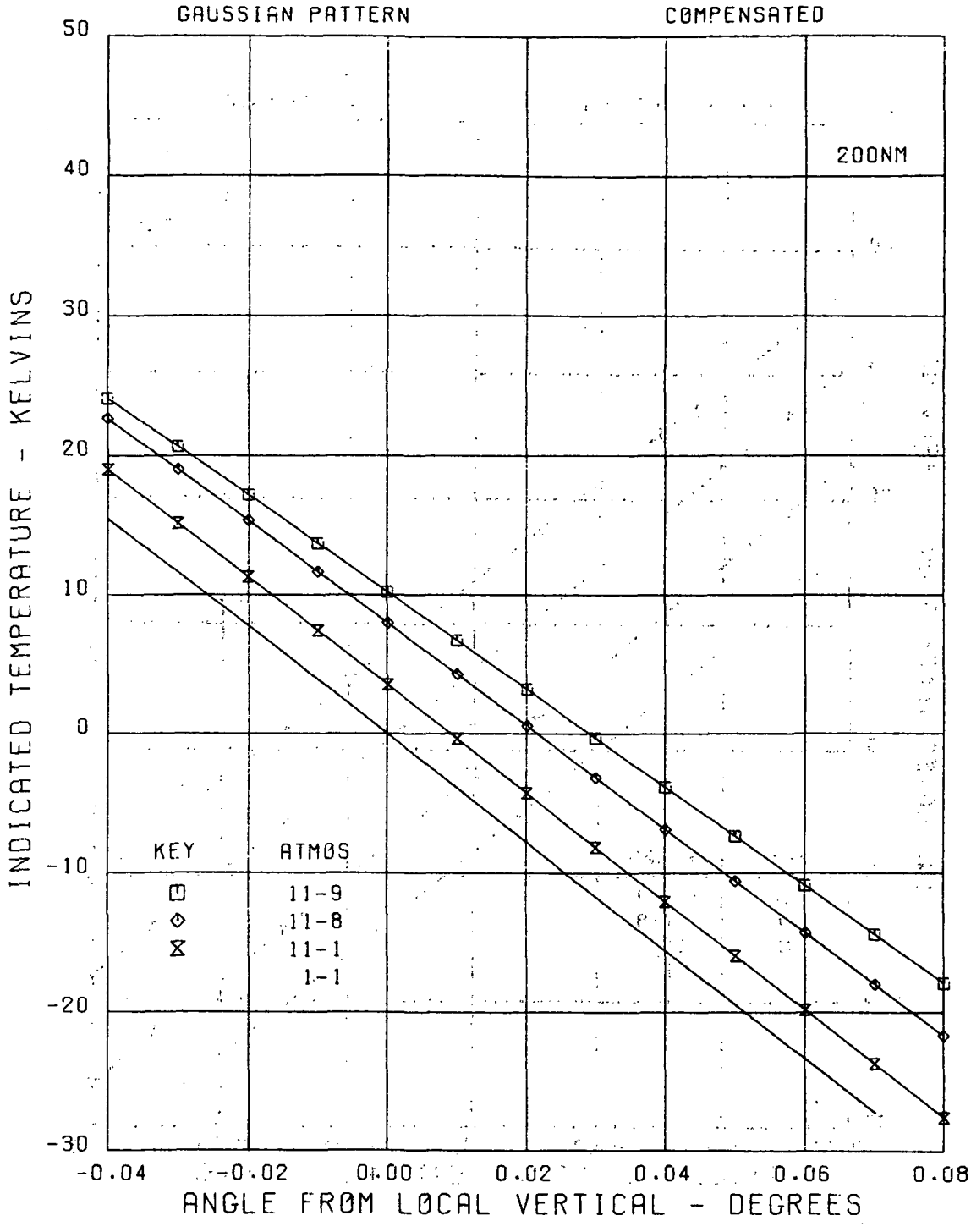

Figure 36. Detailed LVS Error Characteristic, 200-nmi Altitude, Compensated, 1-Degree Beamwidth

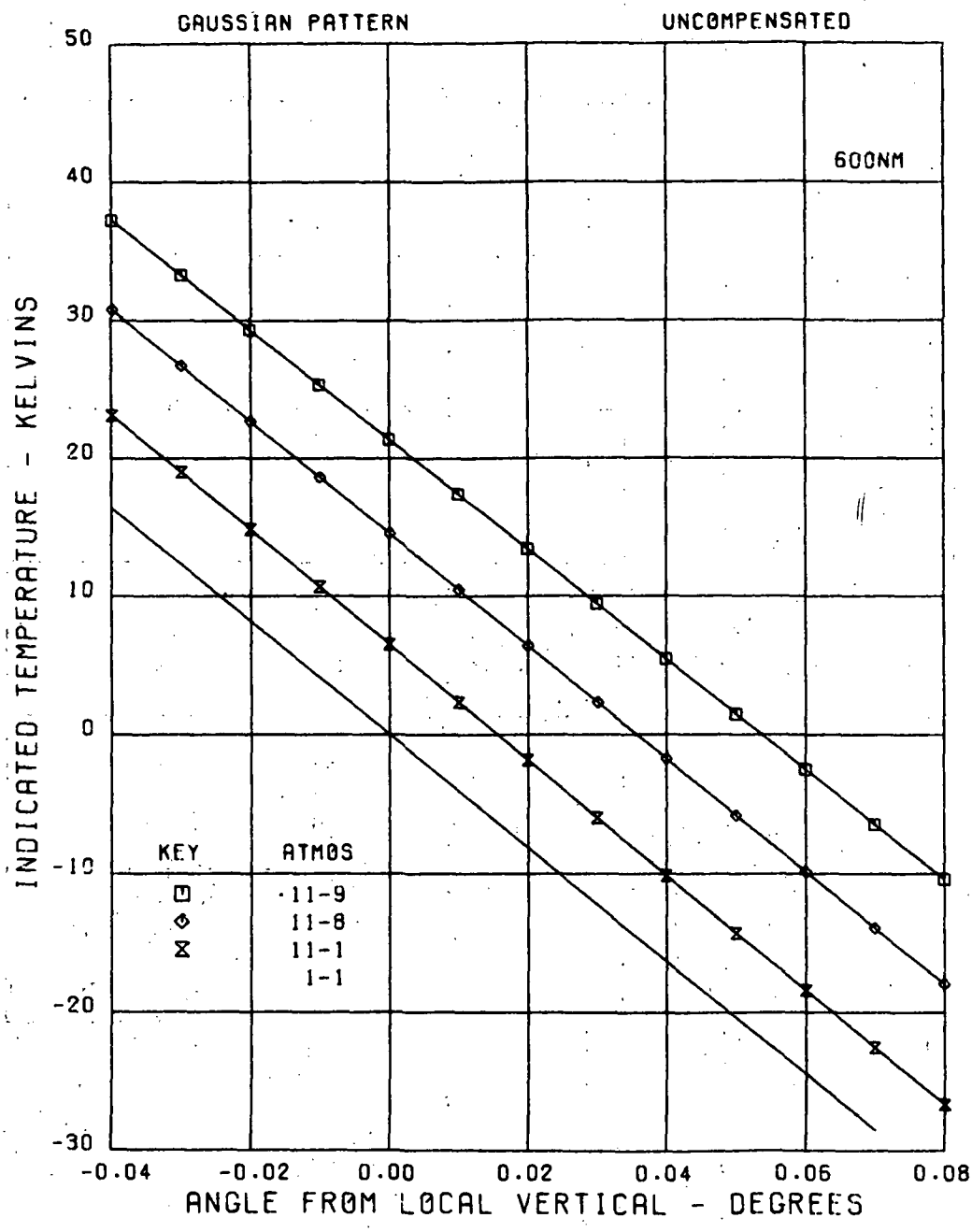

Figure 37. Detailed LVS Error Characteristic, 600-nmi Altitude, Uncompensated, 1-Degree Beamwidth

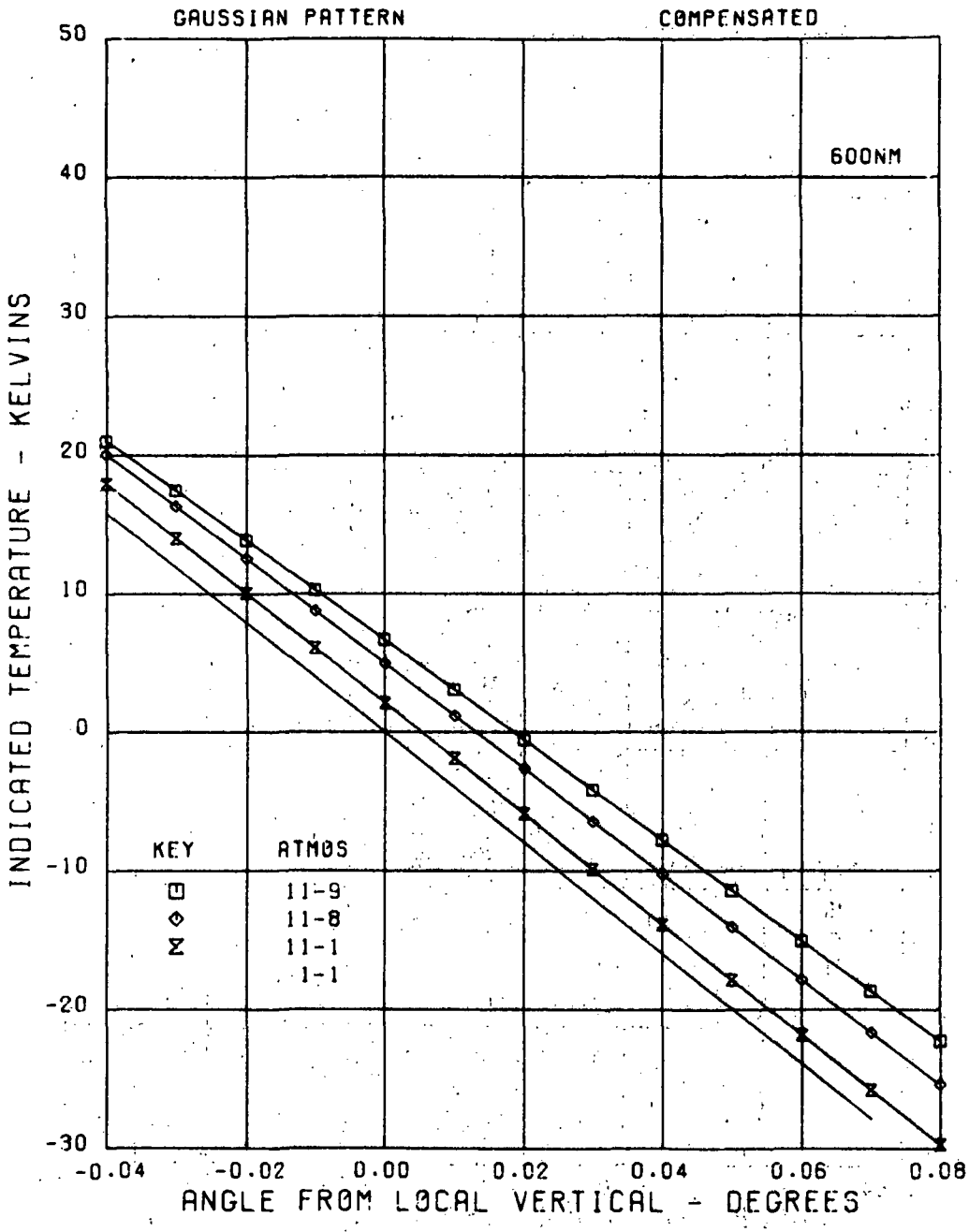

Figure 38. Detailed LVS Error Characteristic, 600-nmi Altitude, Compensated, 1-Degree Beamwidth

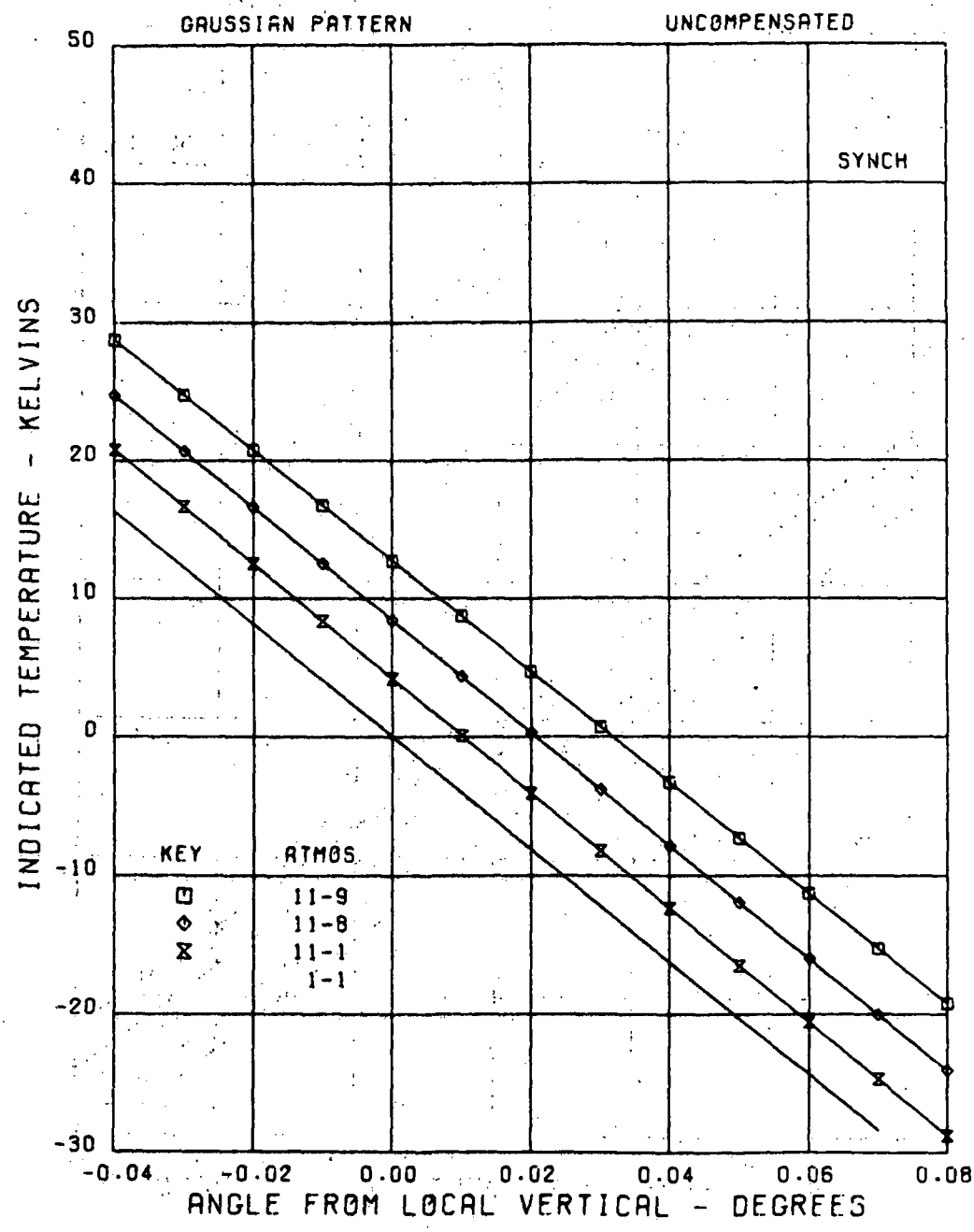

Figure 39. Detailed LVS Error Characteristic, Synchronous Altitude, Uncompensated, 1-Degree Beamwidth

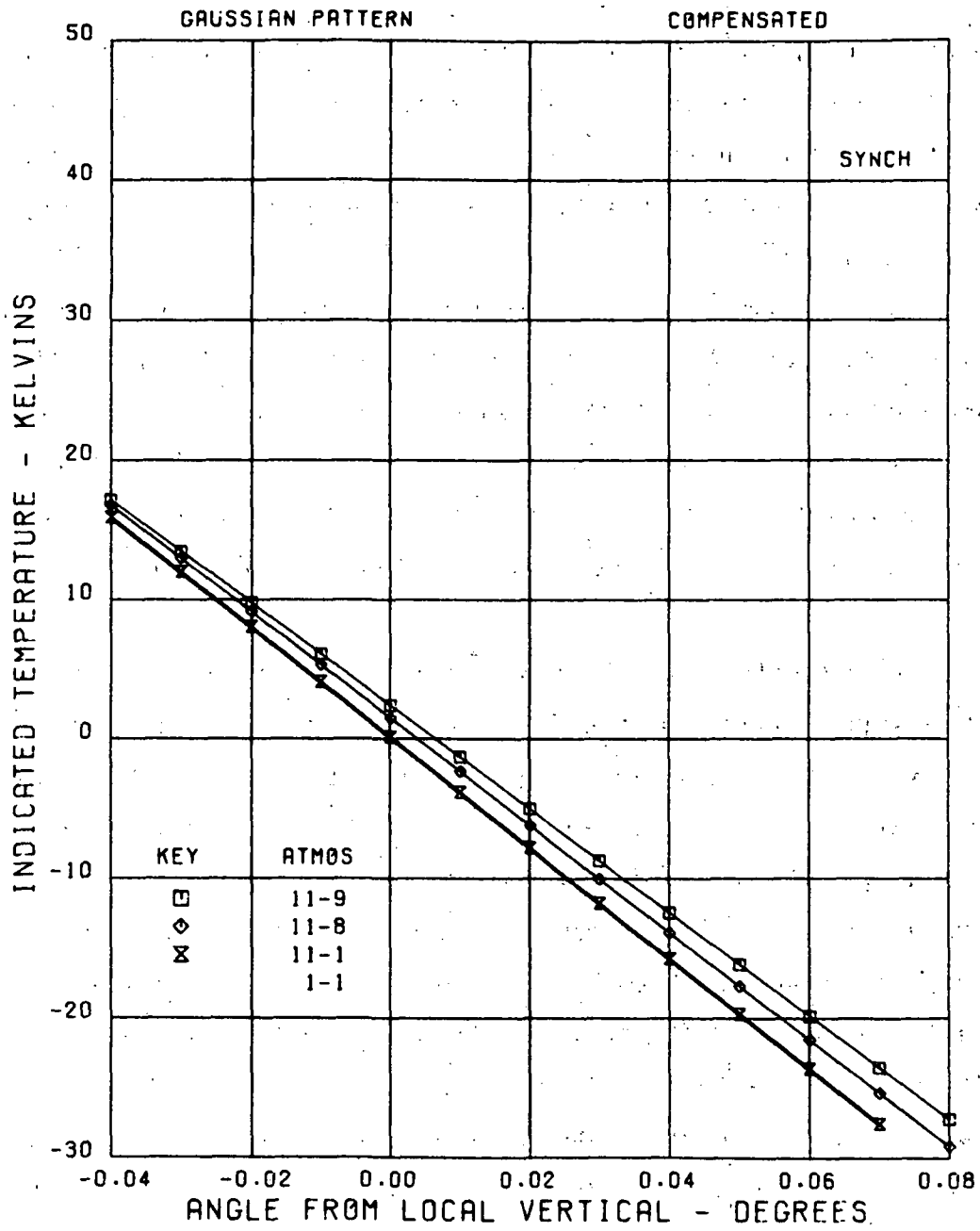

Figure 40. Detailed LVS Error Characteristic, Synchronous Altitude, Compensated, 1-Degree Beamwidth

greatly different atmospheres as postulated can occur; hence, it appears reasonable to divide the calculated worst case errors by 2 at 600 miles and by 3 at 200 miles, these numbers being roughly the angle ratios. Applying these corrections, the maximum error due to differing atmospheres at any satellite altitude calculated so far is 0.01 degree or less, assuming the compensated case. For the uncompensated case, a maximum error of about 0.03 degree is indicated. It is concluded that a viable microwave local vertical sensing technique exists.

Even if the corrections of the preceding paragraph are not applied, the sensing accuracy is still quite good at low altitude. At 200 nautical miles altitude, assuming an abrupt atmosphere change from 9 to 11 on opposite limbs, the 0.03 degree error implies sensing with a pointing error of only 1.1 kilometers altitude at the oxygen horizon. At 600 nautical miles, the 0.02-degree error corresponds to about 1.4 kilometers in altitude at the horizon.

Additional predictions of LVS performance are shown in figures 41, 42, and 43. These figures illustrate the effect of compensation angle at various altitudes for a system using a uniformly illuminated aperture. The beamwidth is again 1 degree, and compensation angles of 1.0, 1.5, and 2.0 degrees are employed, with the plotted symbol on the 1-degree curve. The curves show that performance is relatively insensitive to compensation angle, but that there is some slight degradation at low altitudes for extreme atmosphere differences. The results in figure 43 are particularly interesting. This figure indicates a maximum error due to extreme atmospheres of less than 0.003 degree, or less than half of that predicted by figure 40. The only difference in the two cases is the substitution of the uniformly illuminated aperture for the Gaussian beam. The reasons for this improved compensation are only partially understood at this time, and will be noted later. Since synchronous altitude is an important case and since uniform illumination requires the smallest aperture for a given beamwidth, this topic should be investigated more fully to see if

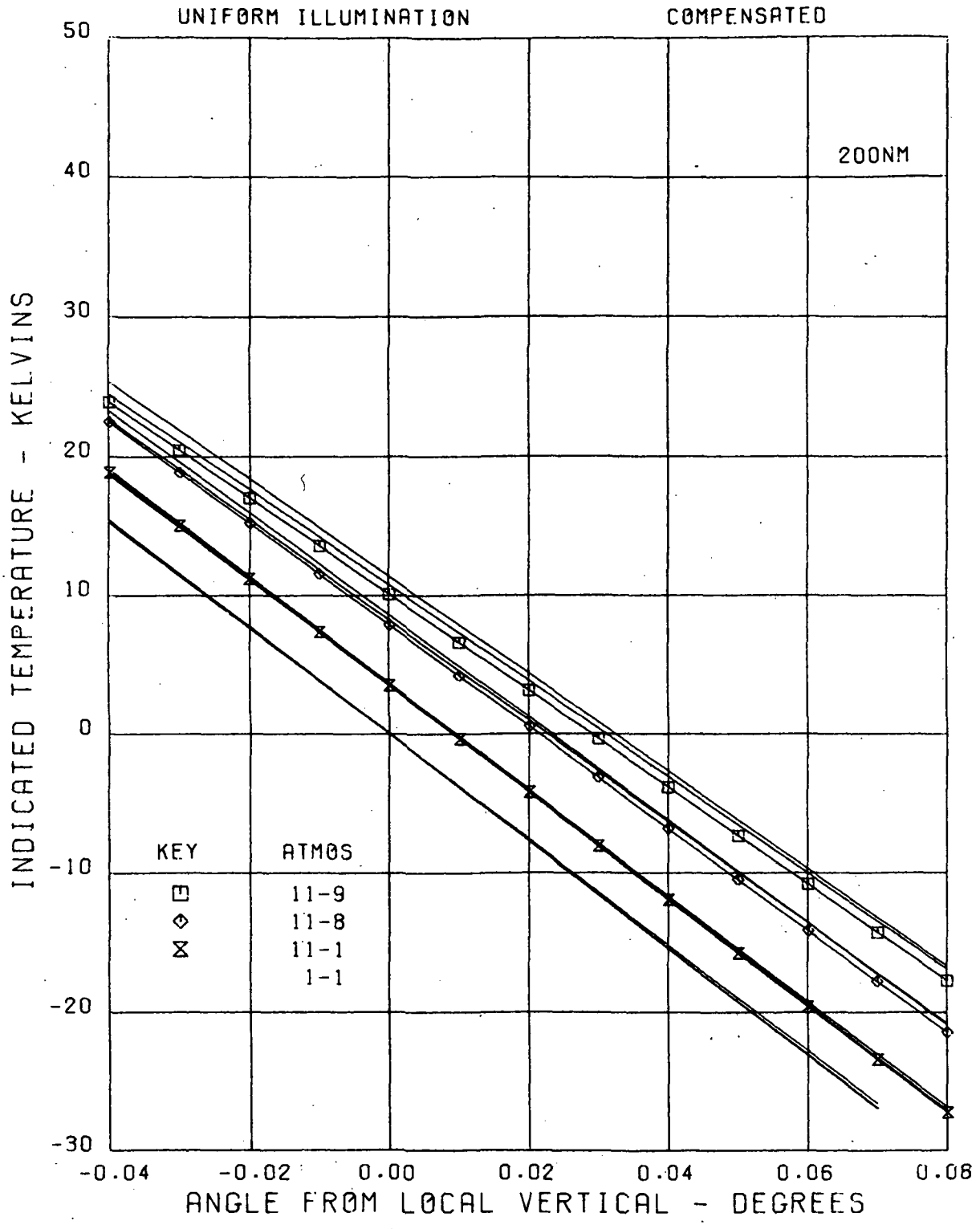

Figure 41. Predicted LVS Output Characteristic Showing Effect of Compensation Angle, 200-nmi Altitude

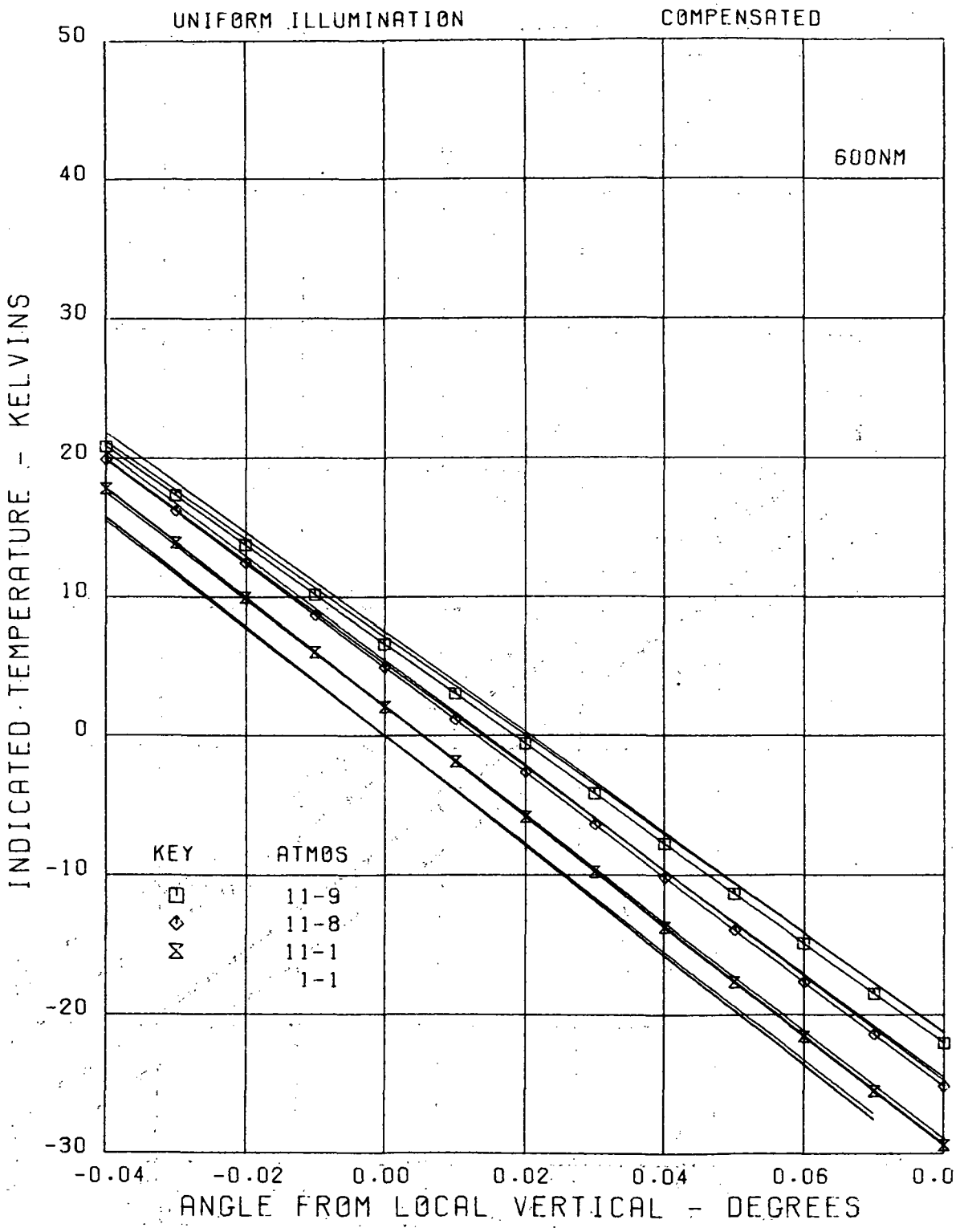

Figure 42. Predicted LVS Output Characteristic Showing Effect of Compensation Angle, 600-nmi Altitude

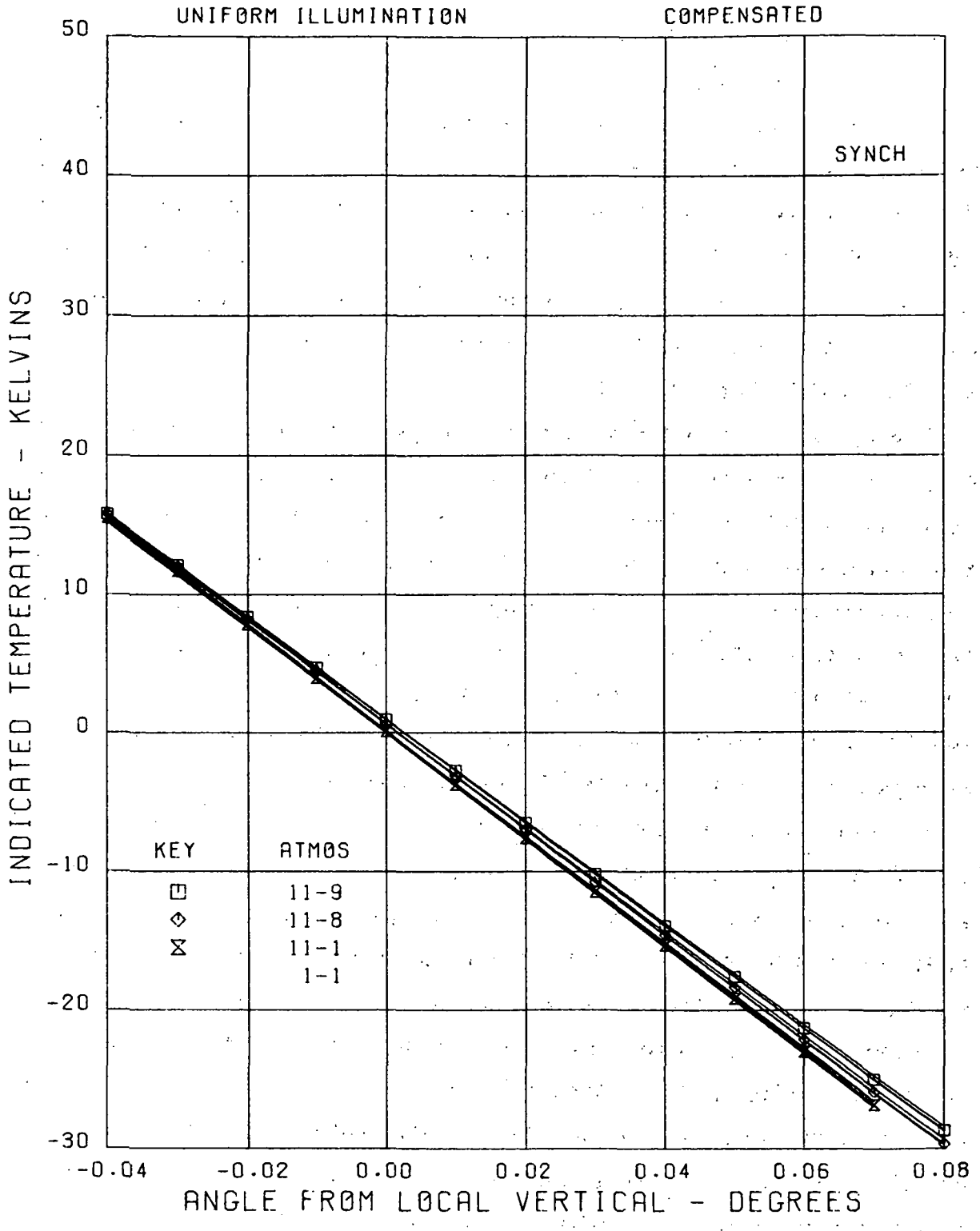

Figure 43. Predicted LVS Output Characteristic Showing Effect of Compensation Angle, Synchronous Altitude

even better results can be obtained by somewhat different aperture distributions or compensation angles.

Figures 44 and 45 show that the sensor behavior is relatively insensitive to antenna pattern (except for the synchronous case noted above). These figures compare cosine illumination, Gaussian beam, and linear illumination, with the plotted symbol on the Gaussian. A minor change in slope is all that is noted, with cosine having the greatest slope and uniform the least. As in earlier curves, beamwidth is 1 degree and compensation angle 1 degree.

4.7 BEAMWIDTH EFFECTS

The discussion of local vertical sensor performance has so far considered only a 1-degree beamwidth. This section considers the effect of using other beamwidth antennas. Detailed calculations of predicted performance have been carried out for beamwidths of 0.5, 0.74, 1.0, 1.5, and 2.0 degrees. The corresponding compensating angles, where applicable, have been set to 1.0, 1.0, 1.0, 1.5, and 2.0 degrees. In order to limit the number of variables involved, only the cosine illumination pattern was employed. In the results to be presented, only the standard atmosphere pair and the extreme 11-9 pair are shown as others fall generally within these limits.

Assuming a step function profile, one would expect the slope of the convolved pattern, in the vicinity of the edge, to be inversely proportional to antenna beamwidth. The real profile displays an edge of finite width and a plateau whose temperature is not constant. These perturbations have no significant effect as long as the angular width of the profile is narrow compared to the antenna beamwidth. The result for different beamwidths at 600 nautical miles is illustrated in figure 46, where the steepest slope output curve is associated with the 0.5-degree beamwidth. Since the same atmosphere is used on both sides, the error curves pass through zero. A similar result is seen in figure 47, where the extreme atmosphere pair is used. Slope variation is as before, but the wider beamwidth antenna causes greater error.

The vertical sensor uses zero radiometer output as the indication of local vertical, implying a balance in the two antenna beams. Thus, the proper

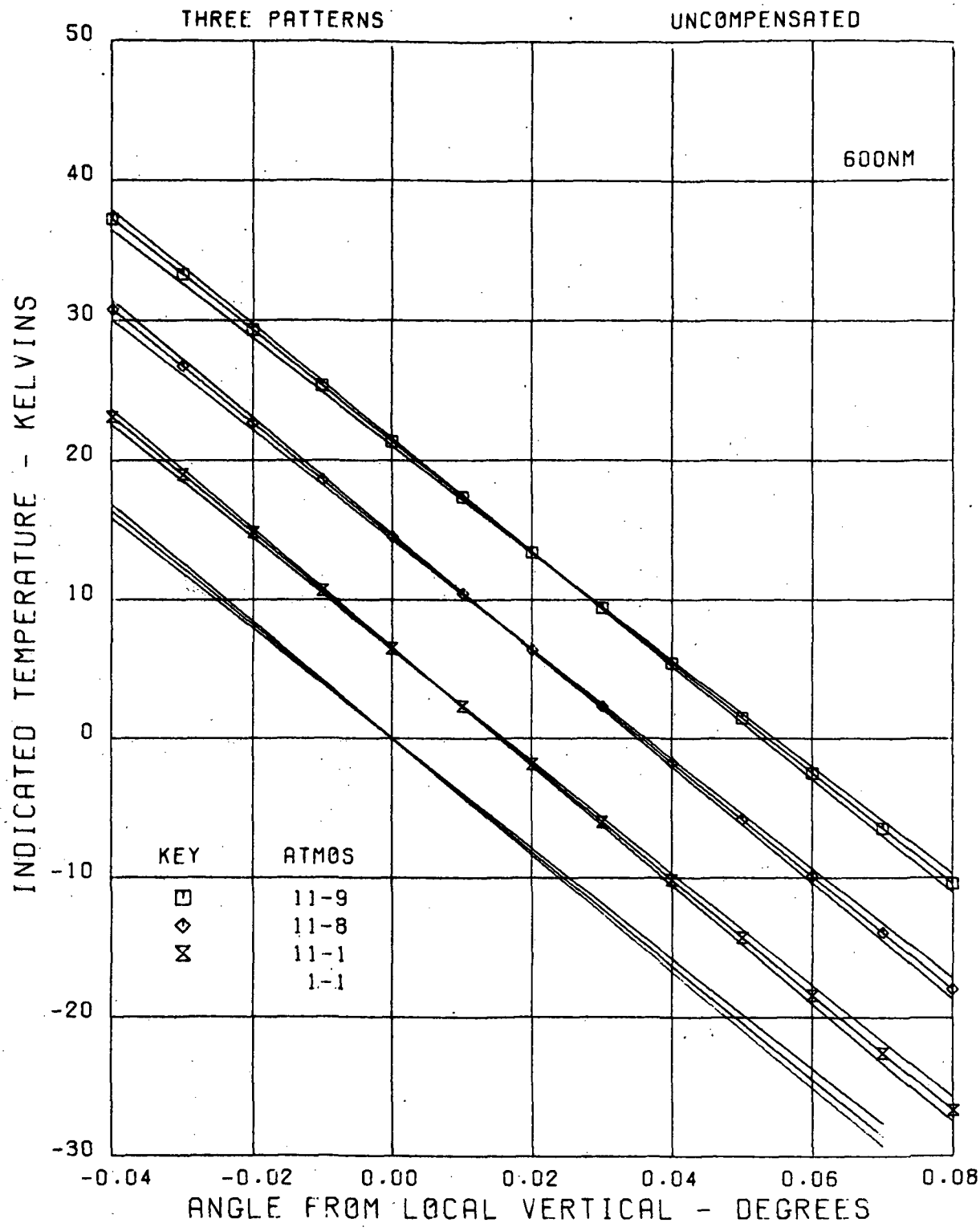

Figure 44. LVS Output Characteristic Comparing Different Beam Shapes, Uncompensated

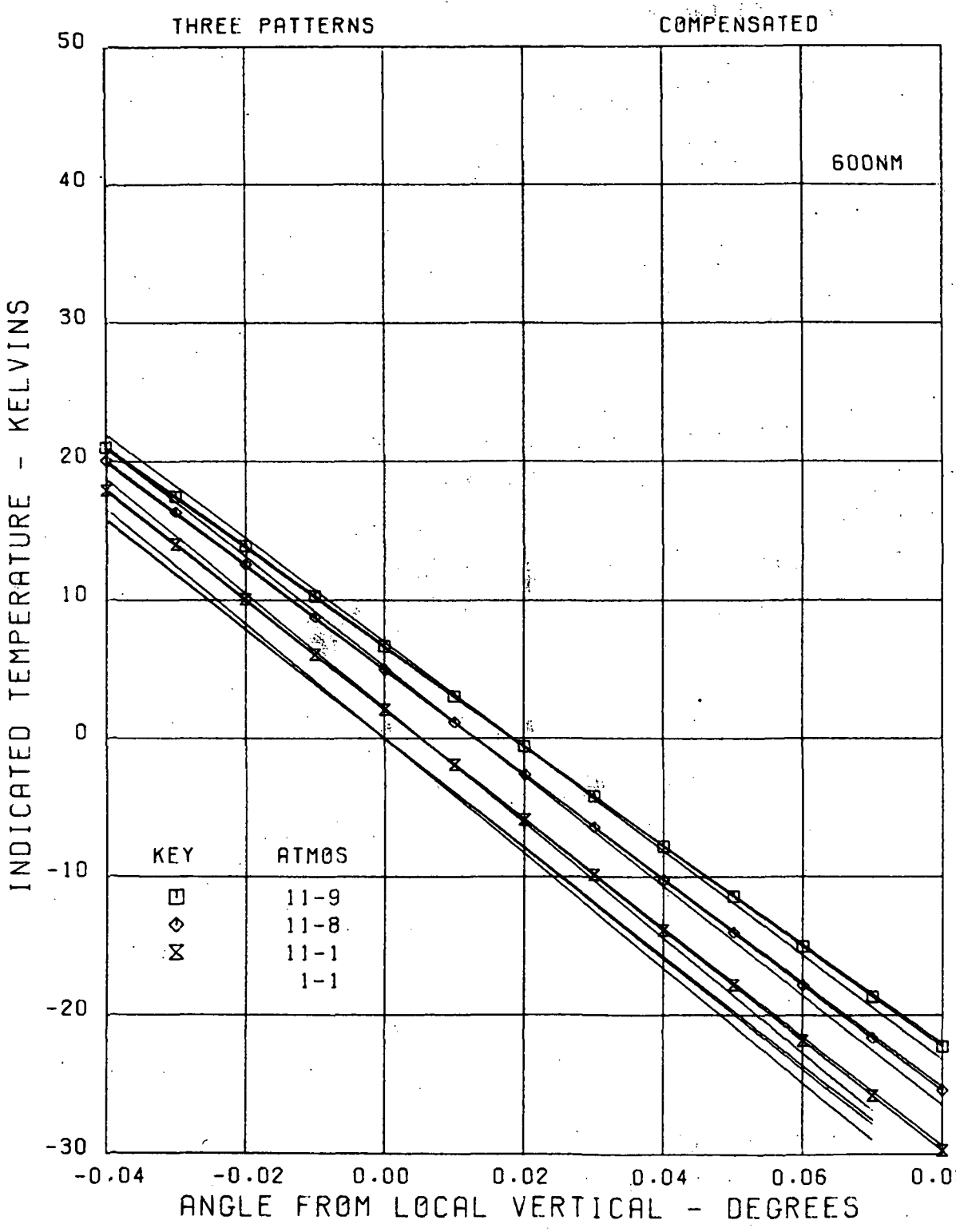

Figure 45. LVS Output Characteristic Comparing Different Beam Shapes, Compensated

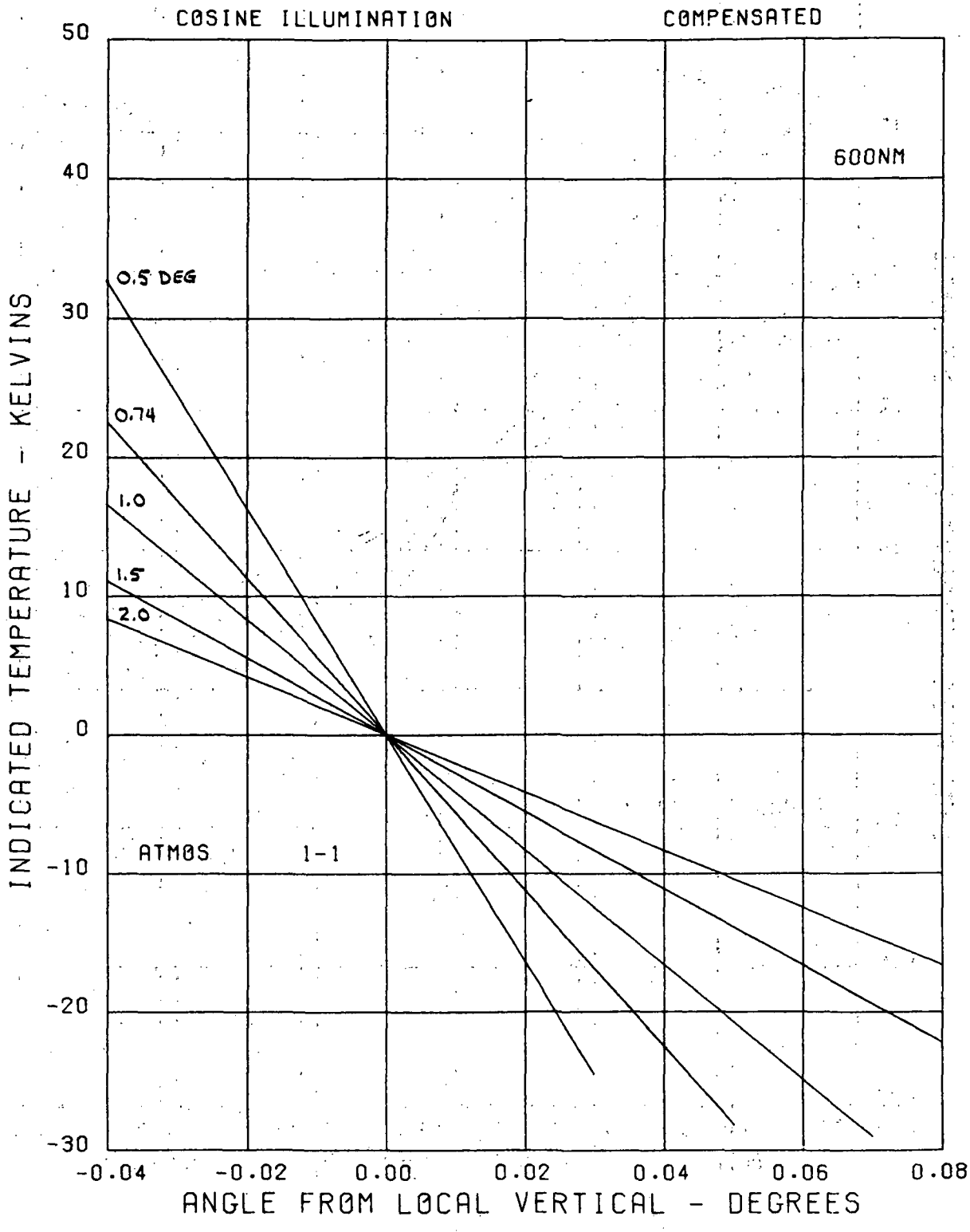

Figure 46. Effect of Beamwidth on LVS Output Characteristic, Atmosphere 1-1

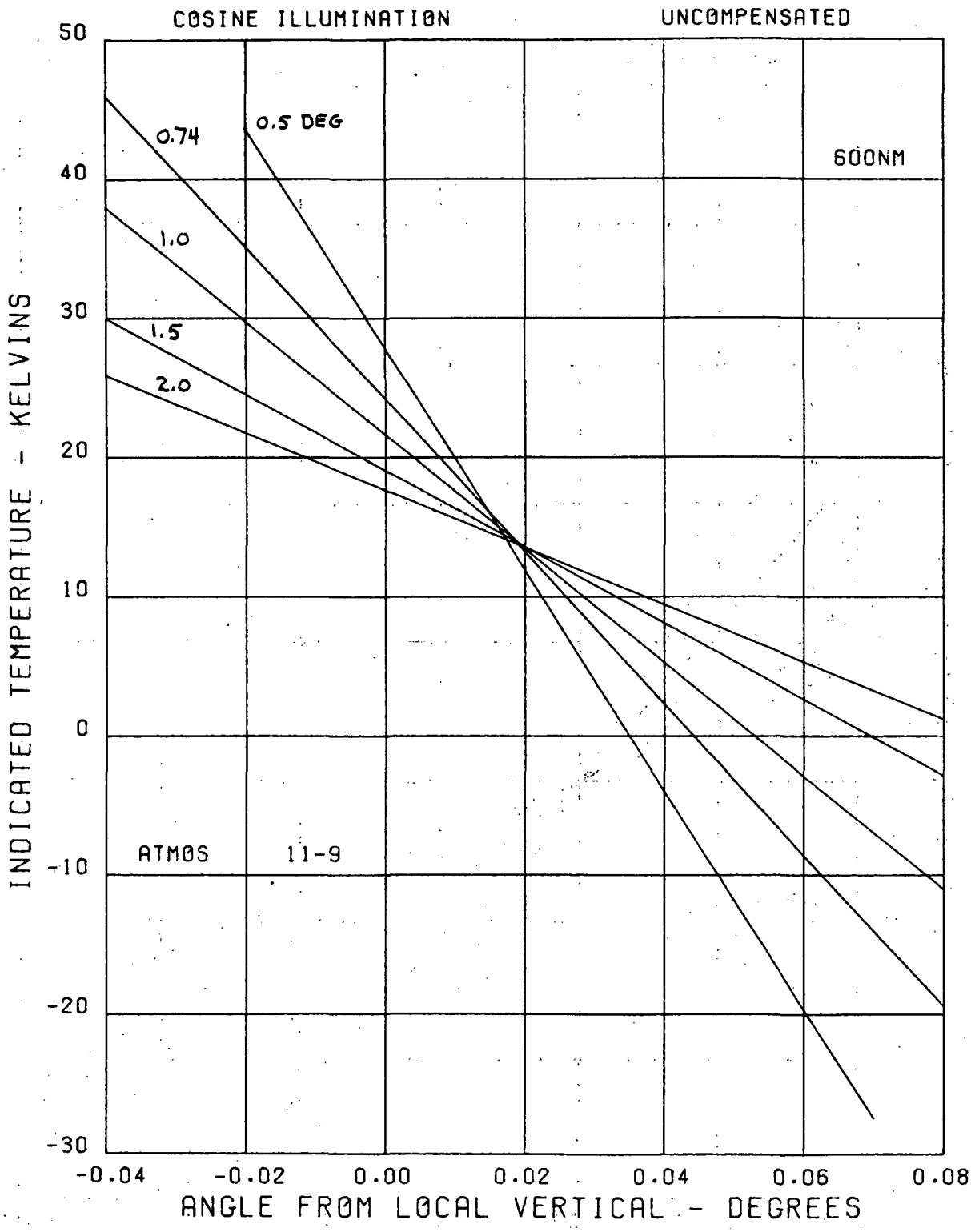

Figure 47. Effect of Beamwidth on LVS Output Characteristic, Atmosphere 11-9, Uncompensated

measure of system error is the angular displacement between this indicated vertical and the true local vertical.

In principle, one would expect to be able to tradeoff antenna beamwidth and radiometer sensitivity in order to achieve a certain error. Considering only figure 46, this is an acceptable tradeoff, and twice the beamwidth can be employed if the radiometer sensitivity can be doubled, i.e., minimum detectable ΔT halved. However, one notes from figure 47 that the wider beamwidth creates more error, independent of radiometer sensitivity, which is assumed infinite in these curves. This result arises from the fact that the wider beamwidth intercepts more of the plateau region, and this contribution represents an error. When compensation is applied, as in figure 48, the effect of this error is greatly reduced, as expected. The angular error spread between beamwidths of 0.5 and 2.0 degrees is now about 30 percent rather than a factor of about 2.5.

To complete the discussion at this altitude, figure 49 presents the same conditions as figure 48, but shows the output over a greater angular range. As would be expected, the 2-degree data is almost linear over this range, but the 0.5-degree data shows significant curvature as the beam moves off the edge.

The situation at synchronous altitude is shown in figures 50 and 51. In the uncompensated case, the error increases with beamwidth up to 1.5 degrees, but then it decreases slightly at 2 degrees. This apparently is caused by the wider beam seeing farther into the plateau region, where the temperature differences are not as great. In the compensated case, the improvement is even more dramatic, indicating an error of less than 0.003 degree for the 2-degree beamwidth. This effect is similar to that observed earlier for uniform illumination in figure 43. Apparently the current effects are caused primarily by the side of the main beam seeing the proper plateau; whereas, in the earlier case, it was the high sidelobe of the uniform beam. As noted earlier, additional studies should be made in an attempt to exploit this effect and obtain a minimum error system.

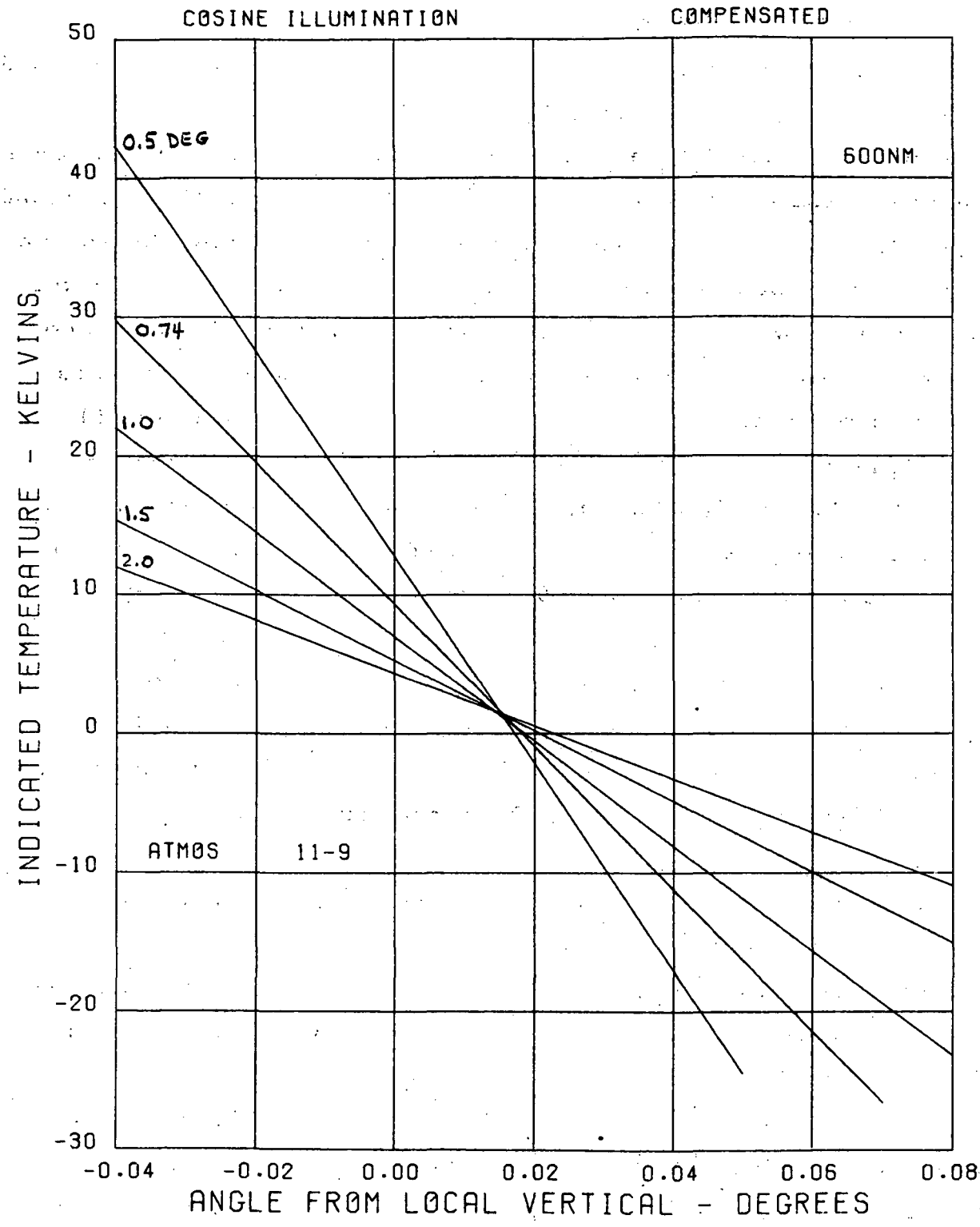

Figure 48. Effect of Beamwidth on LVS Output Characteristic, Atmosphere 11-9, Compensated

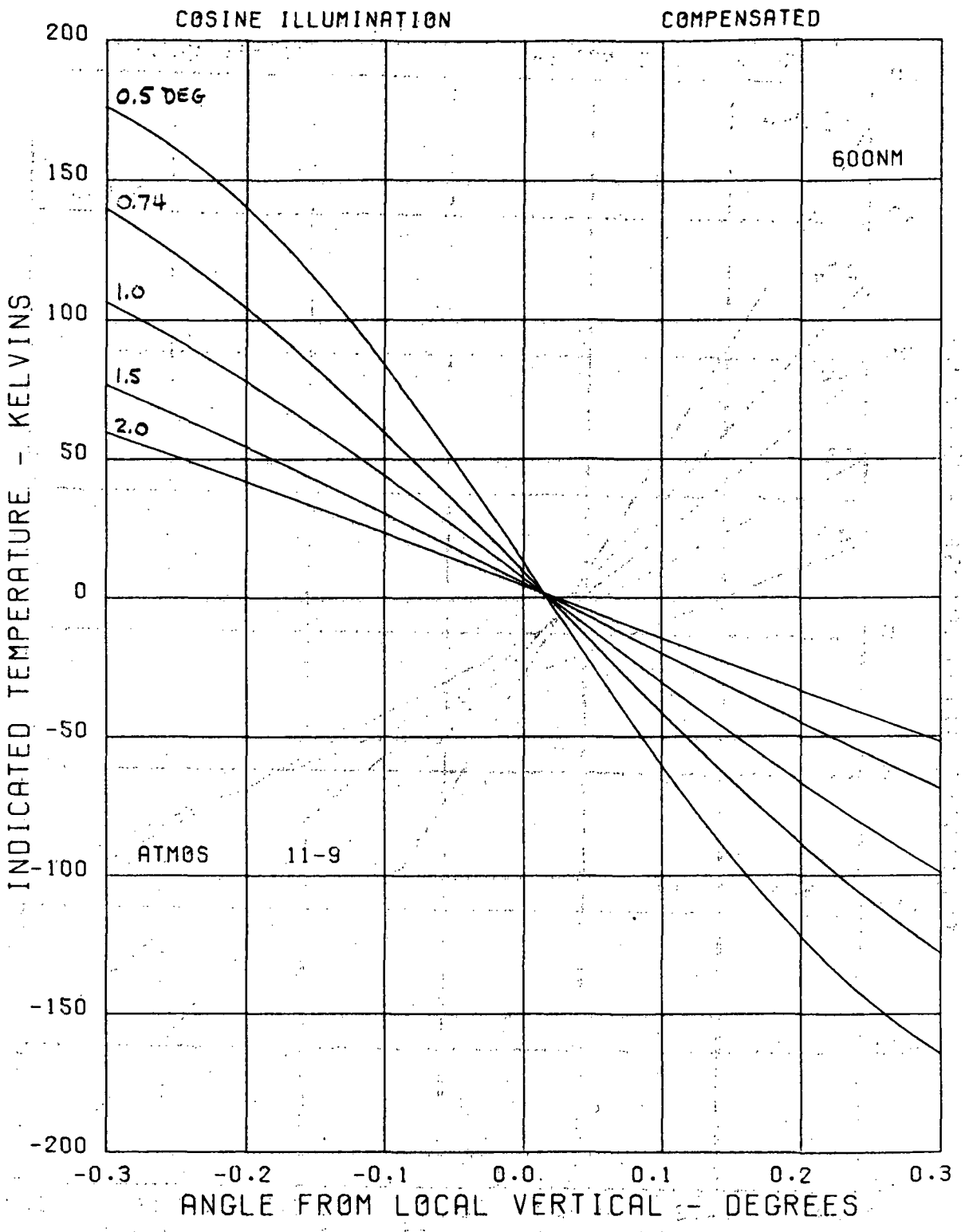

Figure 49. Effect of Beamwidth on LVS Output Characteristic, Coarse Angle Scale

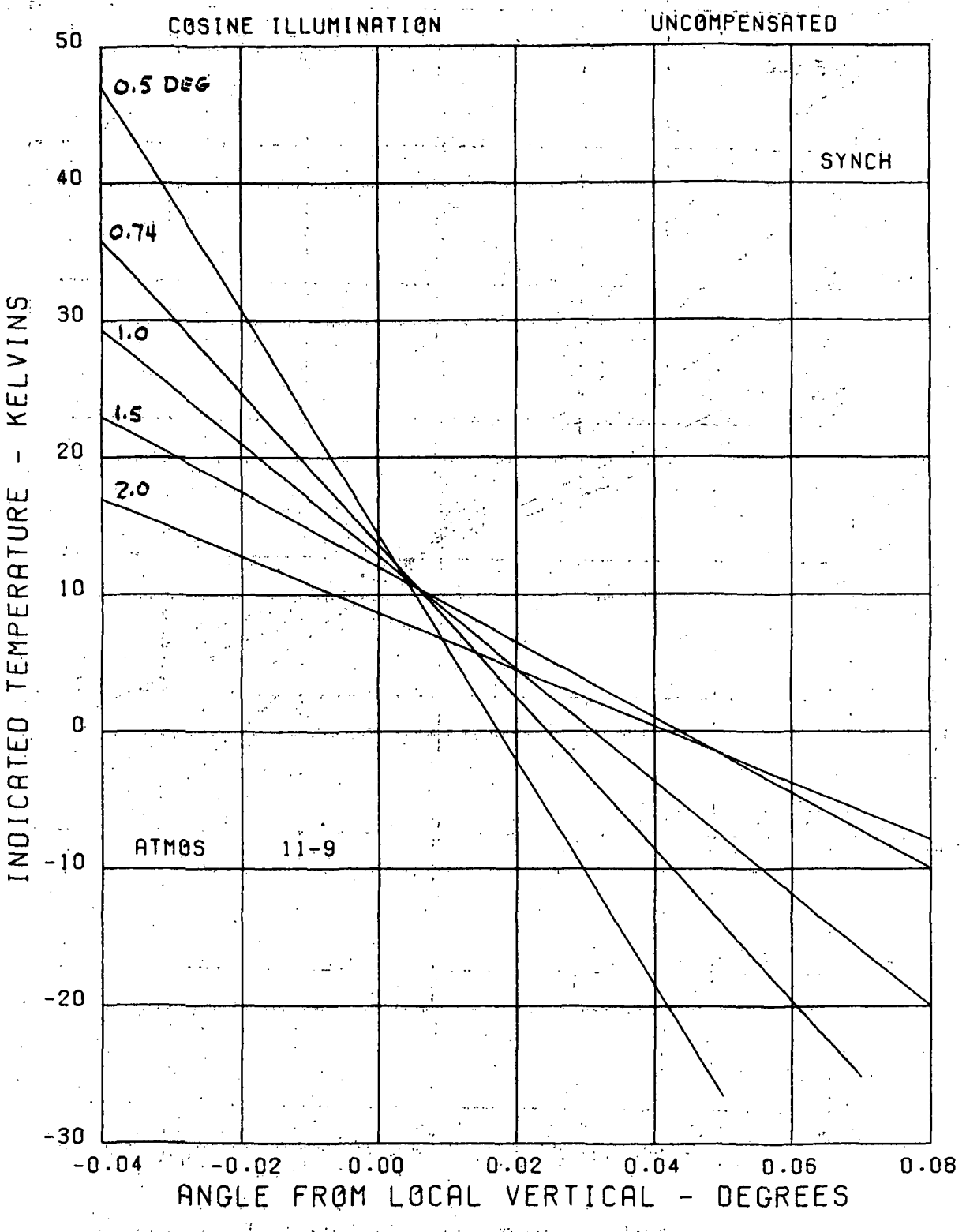

Figure 50. Beamwidth Effect at Synchronous Altitude, Uncompensated

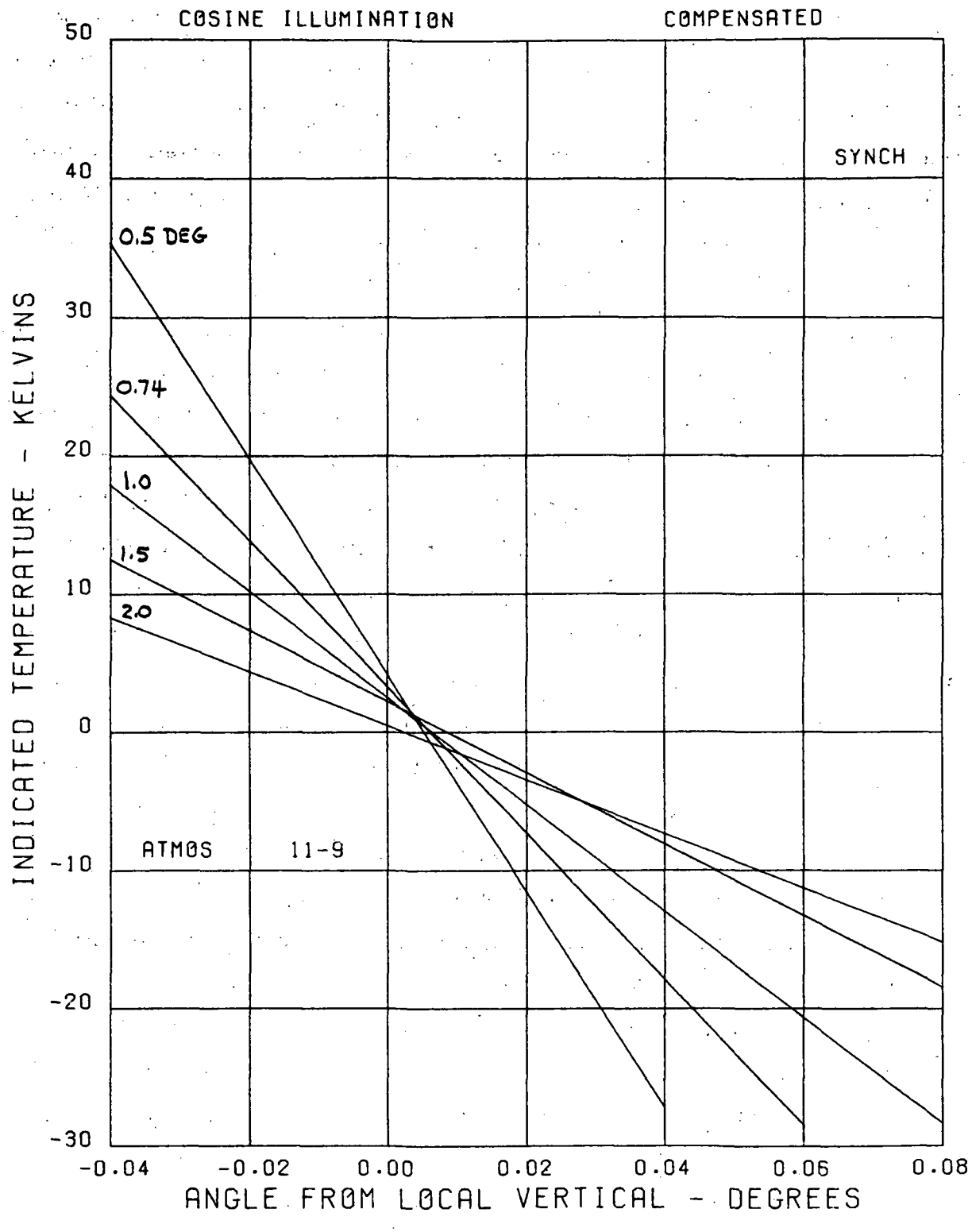

Figure 51. Beamwidth Effect at Synchronous Altitude, Compensated

The next three figures illustrate the slope of the curves shown in the previous figures. This slope is measured in kelvins per degree of pointing position (at local vertical) at the radiometer input and is, in effect, an indication of the sensitivity of the antenna system of the vertical sensor. It is this slope which must be considered in order to determine the error caused by finite sensitivity (in terms of minimum detectable ΔT) in the radiometer. This slope was calculated from points 0.05 degree either side of local vertical in order to maintain sufficient accuracy and still stay within the linear region.

Figure 52 shows the case for extreme atmospheres, uncompensated. All three satellite altitudes are shown, with synchronous showing the greatest slope and 200 nautical miles the least. At synchronous altitude, the slope of the curve is almost exactly -1, confirming the inverse relationship postulated for an ideal step function. At lower altitudes, there is some deviation from linear, and at 200 miles there is significant bending in the curve. This is caused by the fact that the profile width, as shown in figure 31, is less than the beamwidth, but not negligible. More complete analysis predicts a sensitivity slope which is inversely proportional to the root mean square of the widths (appropriately measured) of the antenna beam and profile. At 1 degree beamwidth and 200 nautical miles, the profile is roughly one-fifth the width of the beam. This would cause about a 2 percent slope reduction, but at 0.5 degree it would cause about a 10-percent reduction, as seen in the figure.

Figure 53 shows extreme atmospheres, compensated. The major difference noted is a reduction in the sensitivity slope, which is caused primarily by the compensation technique referencing to the cold atmosphere in this case. This effect is clearly seen in earlier figures. For completeness, figure 54 shows the standard atmosphere pair and again a significant slope reduction due to profile width at 200 nautical miles. In this figure, the synchronous case exhibits the lowest sensitivity at 2-degree beamwidth.

A final example, taken within the atmosphere and hence not applicable to satellite usage, shows that the essentially inverse relationship to beamwidth

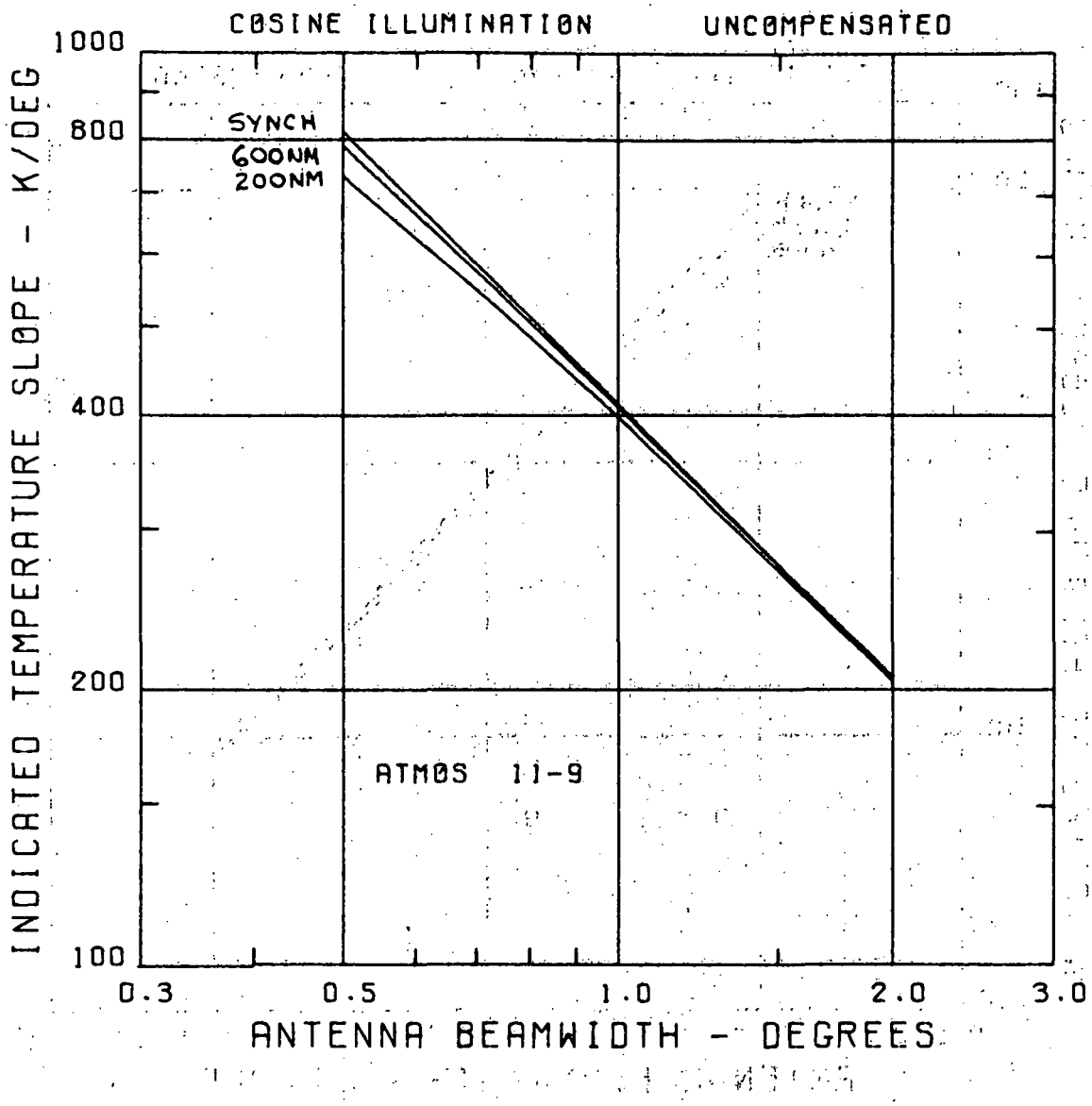

Figure 52. Temperature Slope, Atmosphere 11-9, Uncompensated, for Three Satellite Altitudes

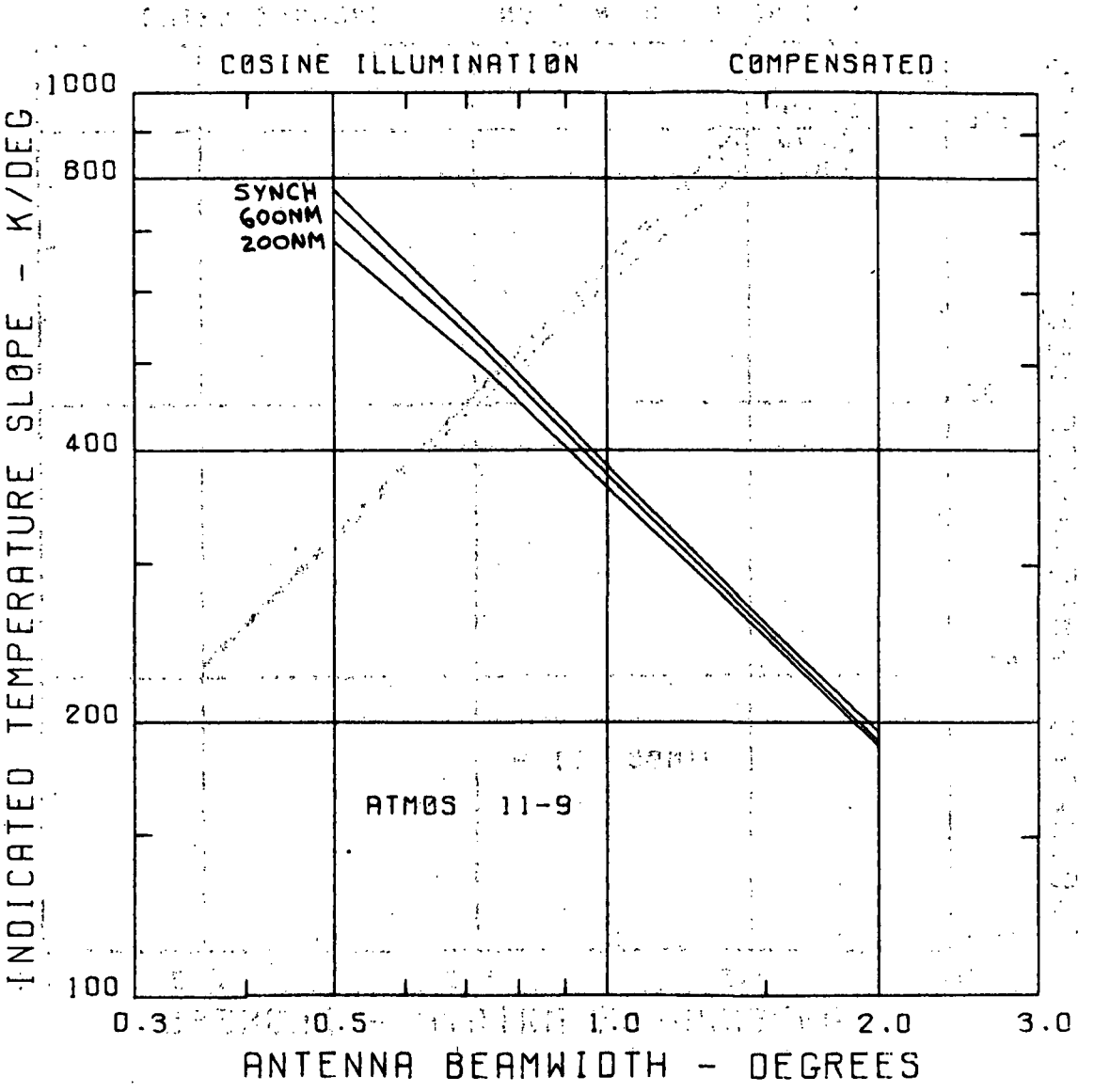

Figure 53. Temperature Slope, Atmosphere 11-9, Compensated, for Three Satellite Altitudes

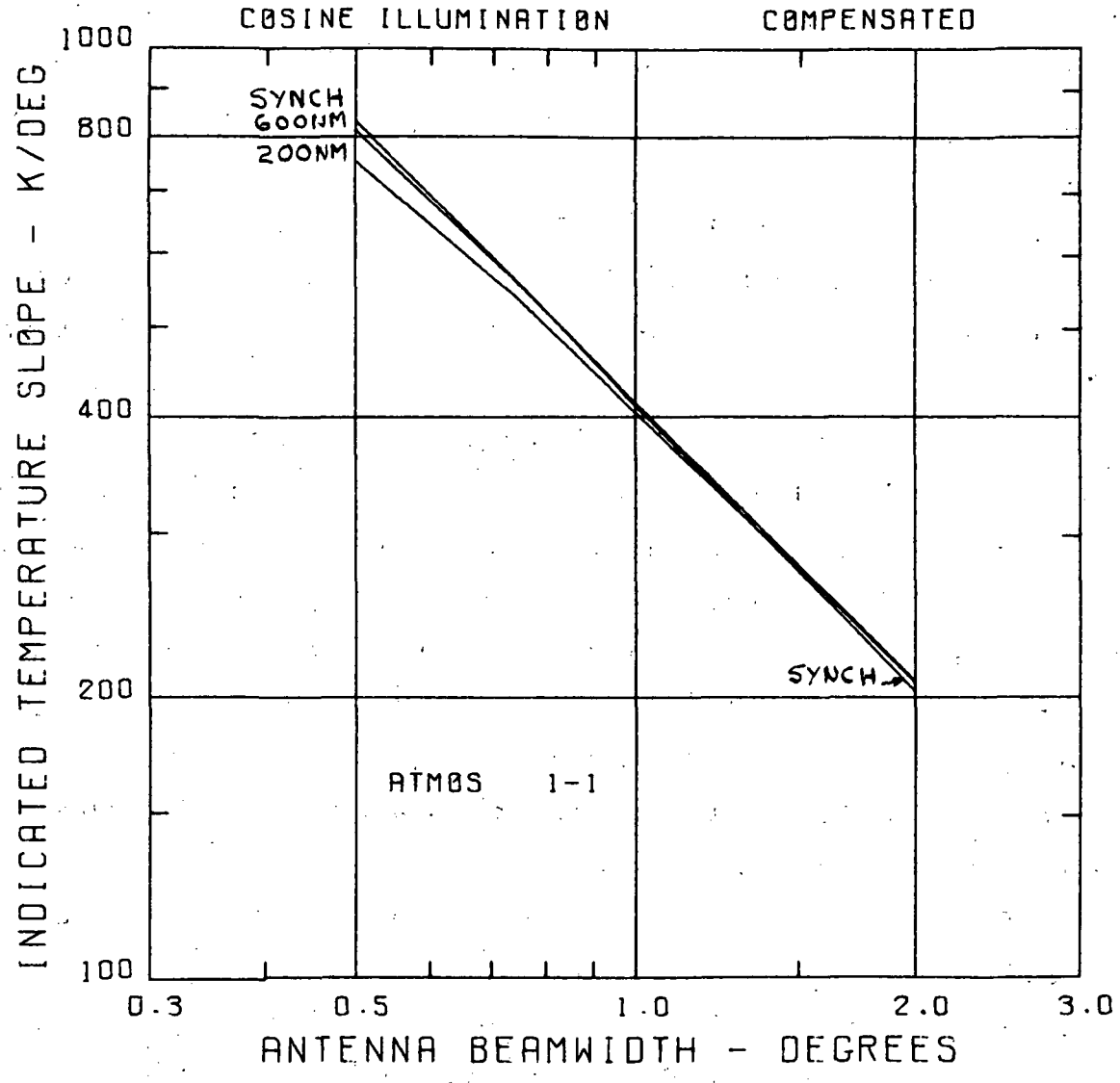

Figure 54. Temperature Slope, Atmosphere 1-1, Compensated, for Three Satellite Altitudes

also holds for wider beamwidths. Figure 55 is similar to figure 31, but shows the standard atmosphere profile from 60 kilometers altitude and convolved patterns for beamwidths of 5 and 10 degrees, cosine illumination. Convolved pattern slopes are 41.5 and 21 kelvins per degree, respectively, and when multiplied by 2 to be compatible with figure 54 will fit nicely on an extension of this curve.

4.8 12 ATMOSPHERE PERFORMANCE

Predicted local vertical sensor performance has so far been based on selected pairs of the four representative atmospheres. This section presents the results for 12 atmospheres, including several severe warming atmospheres. Results are provided for all three satellite altitudes considered - 200 and 600 nautical miles and synchronous - and both uncompensated and compensated systems. This computation was limited to 1-degree beamwidth, 1-degree compensation angle, cosine illumination pattern to limit the computer time required. The atmosphere pairs considered are the 12 atmospheres noted by an asterisk in table 1 on one limb and standard atmosphere, number 1, on the other. All 12 pairs are plotted in each figure, but atmospheres 10, 16, and 17 are plotted without symbols to avoid cluttering the presentation. Atmospheres 1, 8, 9, 11, and 19 have a symbol at every calculated point while 4, 5, 6, and 18 have a symbol every other point to aid in identification.

Figures 56 and 57, at 200 nautical miles, show the expected grouping uncompensated, and with 6 just above 11 compensated. Figures 58 and 59, at 600 nautical miles, show similar results, but with 4 falling on 11 compensated. In the synchronous case, figures 60 and 61, the uncompensated case is as expected, and in the compensated case both 4 and 6 are slightly above 11. Even the severe warming atmospheres create no problem. Atmosphere 18 generally falls close to 9, and, except for the uncompensated synchronous case, atmosphere 19 falls between 8 and 1. The only unanticipated result is that 6 and 4 can fall slightly outside 11 in the compensated case. Since

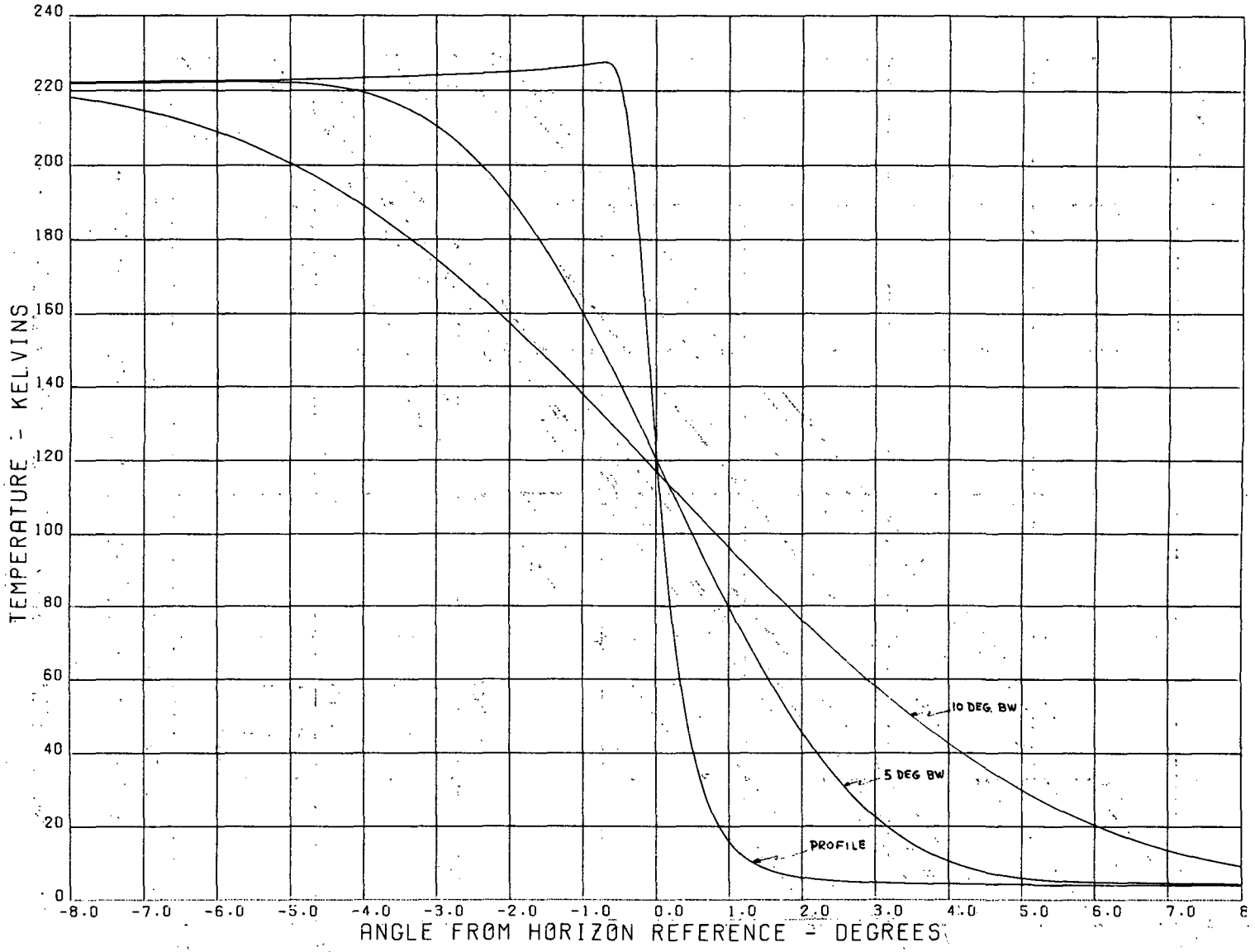

Figure 55. Brightness Temperature Profile (Standard Atmosphere) and Convolved Patterns (Cosine Illumination), 60-km Altitude

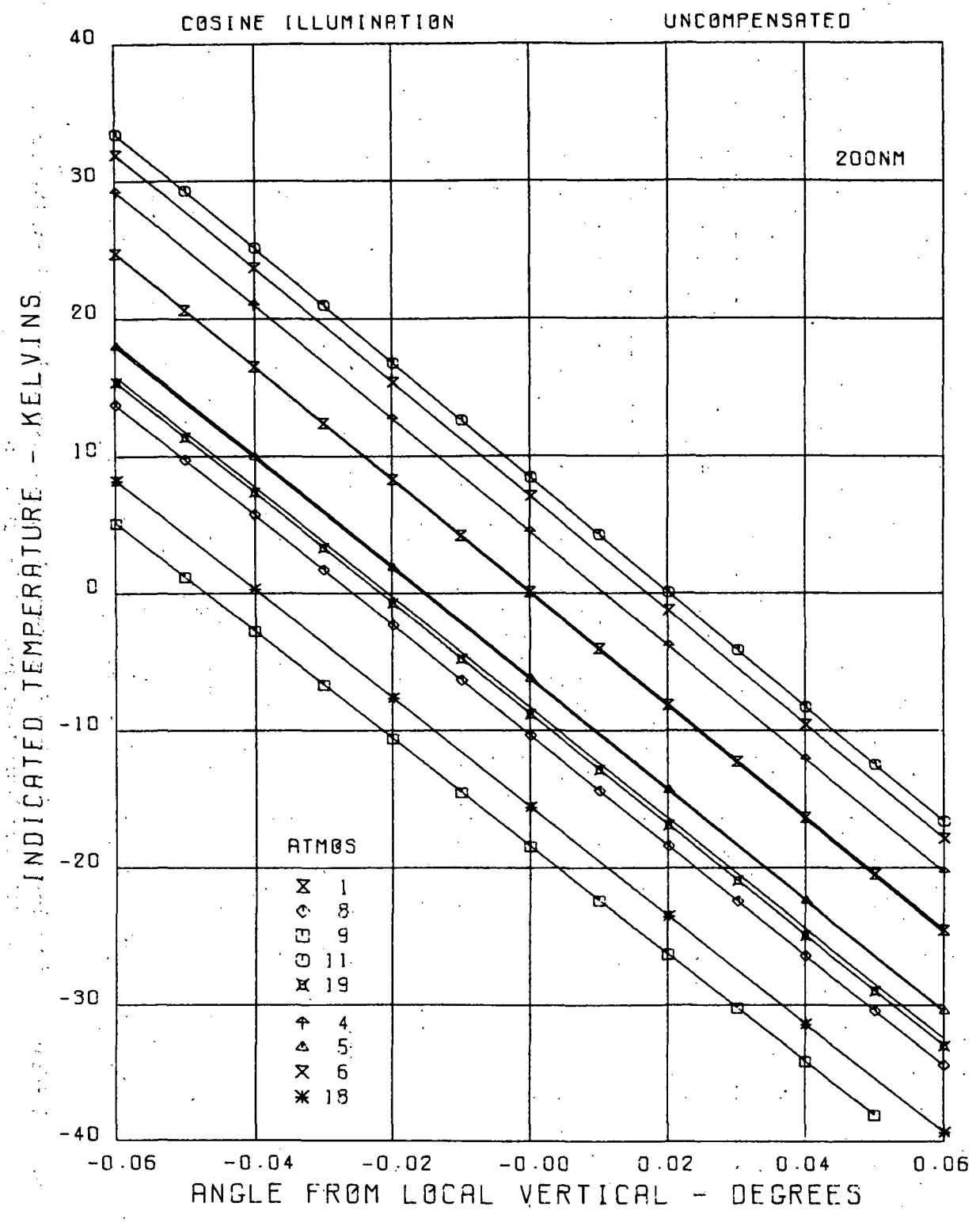

Figure 56. Predicted LVS Output, 12 Atmospheres, 200-nmi Altitude, Uncompensated

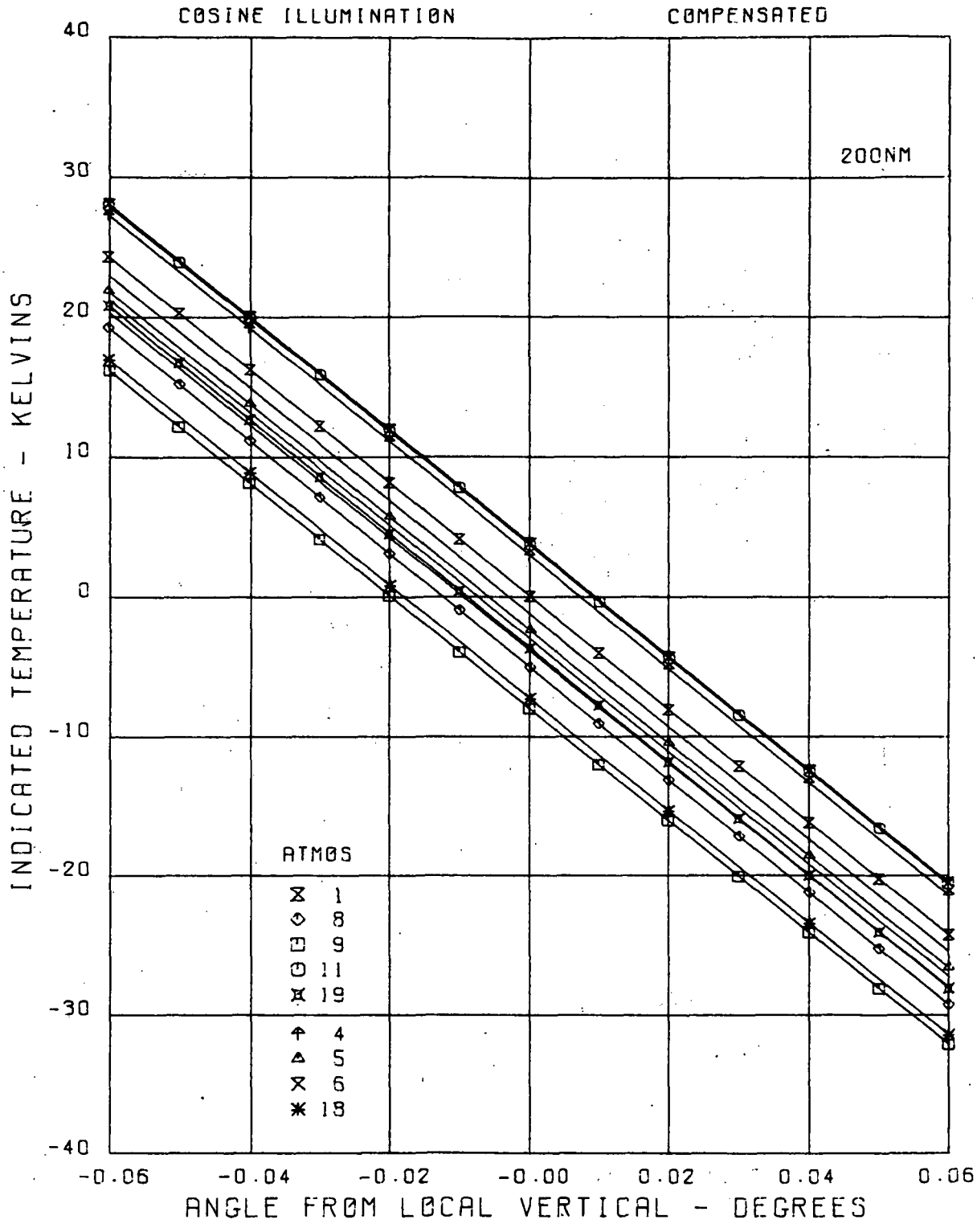

Figure 57. Predicted LVS Output, 12 Atmospheres, 200-nmi Altitude, Compensated

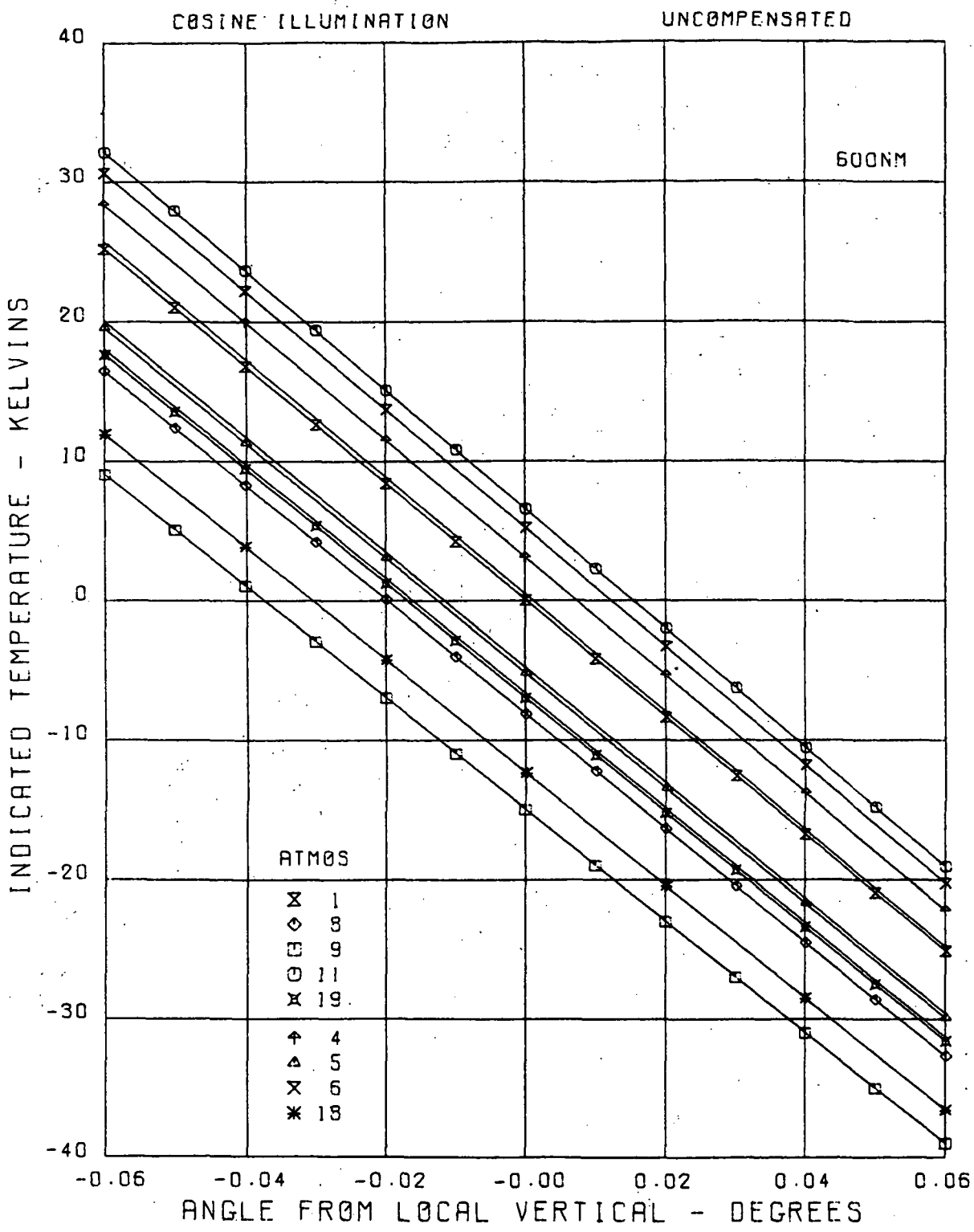

Figure 58. Predicted LVS Output, 12 Atmospheres, 600-nmi Altitude, Uncompensated

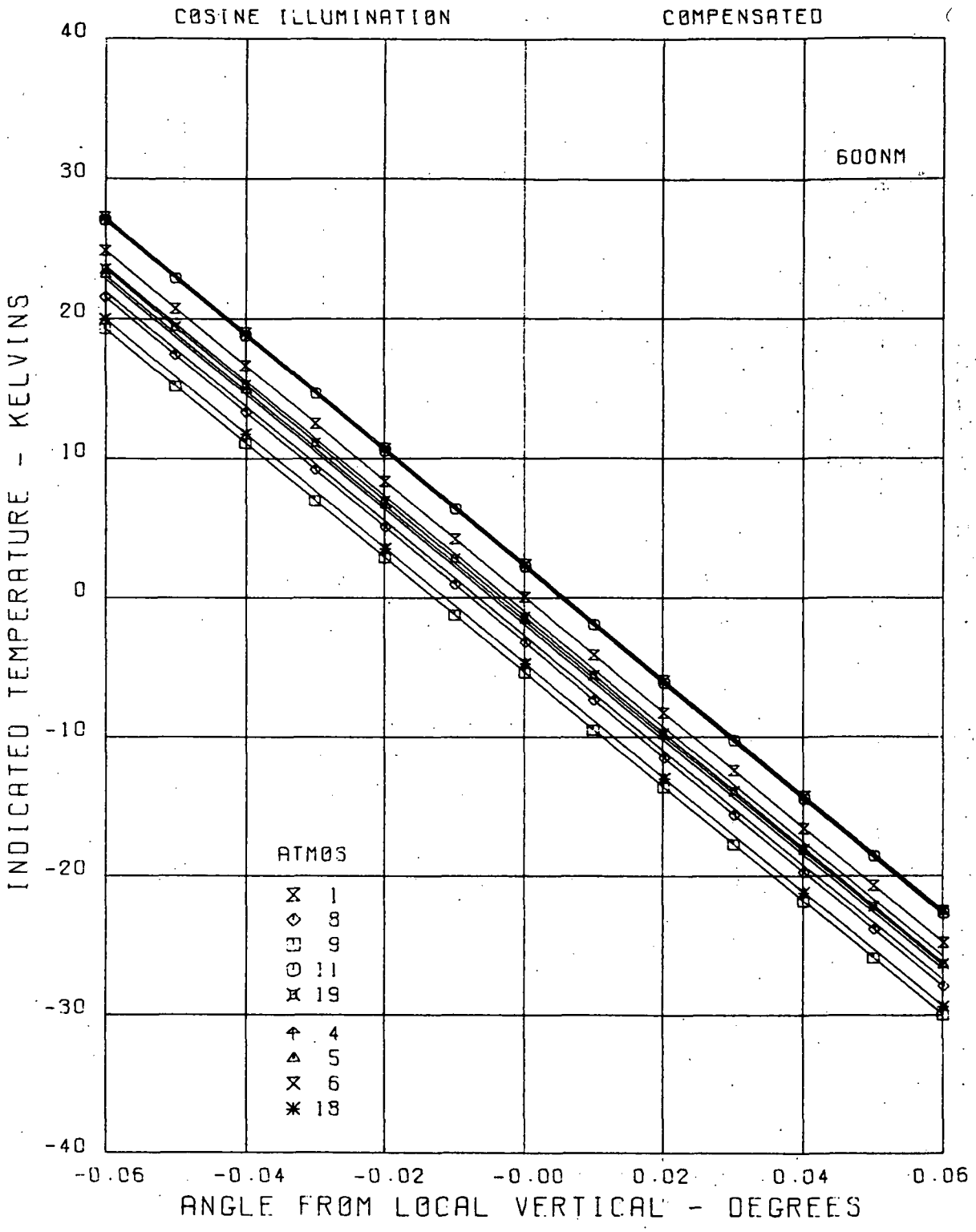

Figure 59. Predicted LVS Output, 12 Atmospheres, 600-nmi Altitude, Compensated

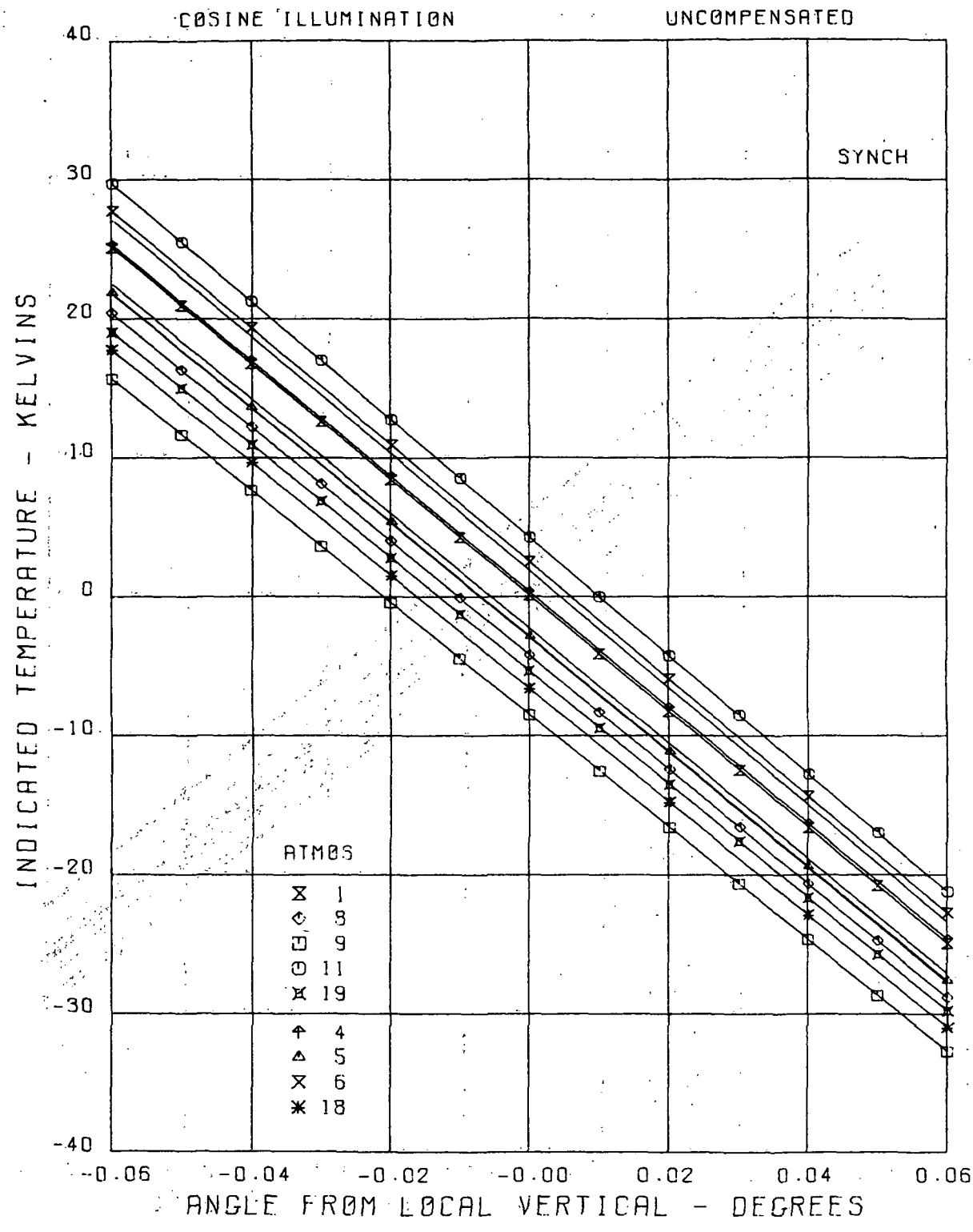

Figure 60. Predicted LVS Output, 12 Atmospheres, Synchronous Altitude, Uncompensated

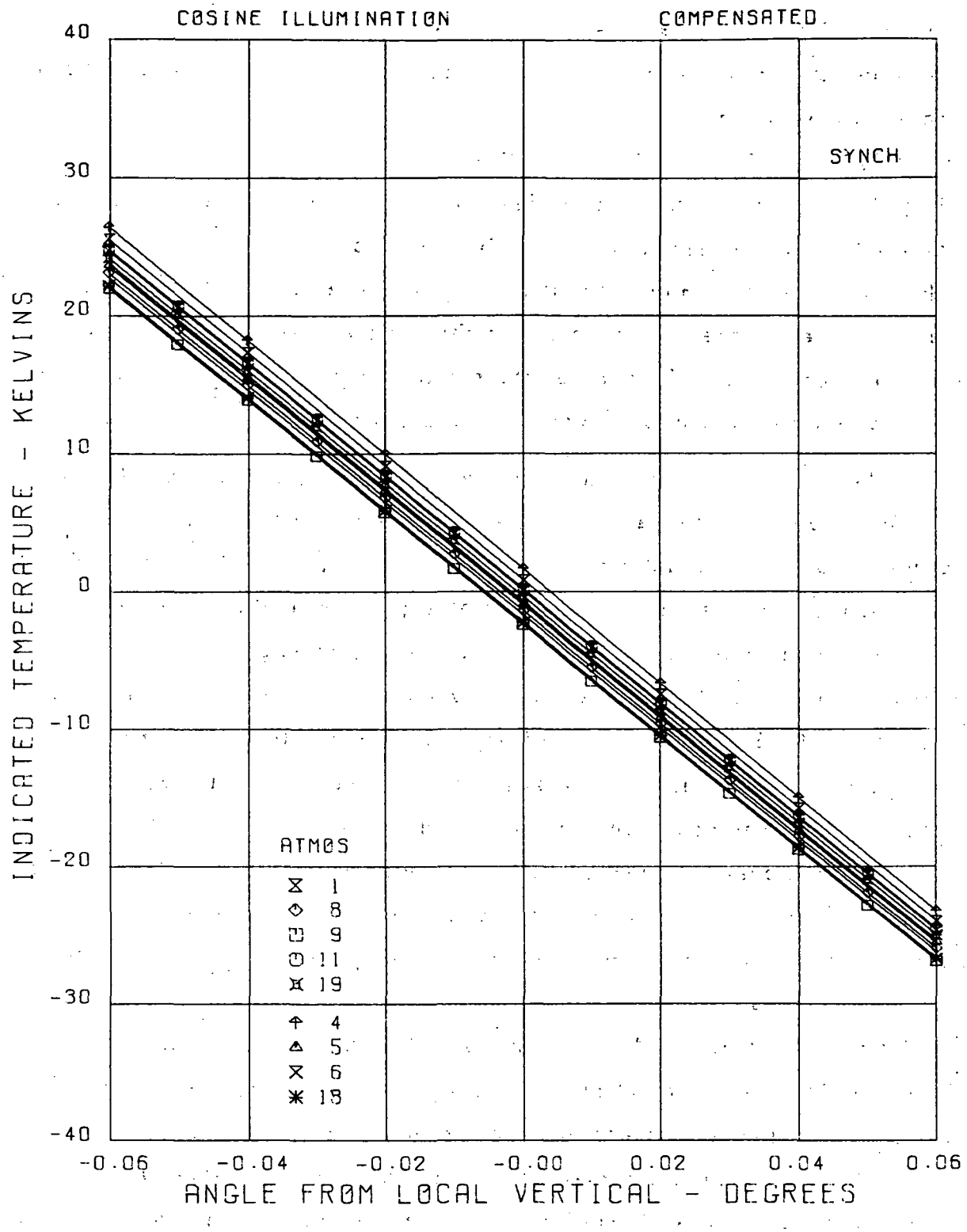

Figure 61. Predicted LVS Output, 12 Atmospheres, Synchronous Altitude, Compensated

atmosphere 1 is used as a reference in this calculation, the errors can be either plus or minus, depending upon whether the test atmosphere is hotter or colder than standard.

4.9 EXPERIMENT SYSTEM ANALYSIS

Based on analyses presented in Sections 3 and 4 design parameters for a local vertical sensor experiment may be selected. Profiles for various bandwidths were presented in figure 14. It is desirable to stay away from the resonance lines to prevent smearing of the profile. Assuming the profile slope does not change, the greater the bandwidth the more sensitive the system. Slope does change, however, so the quantity $\sqrt{B}\,\frac{d\,\overline{T}_B}{d\,H}$ was investigated, where $\overline{T}_B$ is the brightness temperature averaged over the bandwidth B, as described in paragraph 4.2, and H is tangential altitude. Although not necessarily a rigorous indicator of optimum conditions, this quantity does give a reasonable measure of the value of a given bandwidth selection. For standard atmosphere, this quantity exhibits a rather broad first peak in the vicinity of 200 to 240 MHz of bandwidth, measured from the center of the valley at 60.79 GHz. Although a slightly greater amplitude second peak may be found, the greatly increased bandwidth required puts an undue strain on component performance characteristics and is not recommended. This, then, is the rationale for using 200 MHz bandwidth averages in the previously presented figures. It is probably desirable to stay as close to the valley center as possible, but the lower edge of the IF passband must be sufficiently high to reject local oscillator noise.

Reference to Appendix A shows that a 200-MHz IF bandwidth combined with a 1-second RC time constant output is adequate to provide the 1-kelvin radiometer sensitivity previously assumed to provide sufficient accuracy. This 1-second RC corresponds to a 2-second integration time, so that data can be updated every 2 seconds if required. If a longer time between data samples can be tolerated, a still longer integration time can be employed to yield increased radiometer sensitivity.

At 600 nautical miles altitude, the subsatellite point will move approximately 200 nautical miles per minute, increasing only about 15 percent at 200 nautical miles altitude. Hence, a 3-second update could provide samples spaced roughly 10 nautical miles. For an operational system this might be highly desirable, but for an experiment evaluation there is no need for this much data. In terms of sampling lattice, a measurement every 3 degrees of latitude, assuming a polar orbit and an earth oriented vehicle, should be quite adequate. This would provide 120 data points per satellite revolution spread over all available atmospheres. If a nonpolar orbit is employed, the data is still useful but a lesser range of atmosphere variation will be encountered. This spacing of the data points, roughly 45 to 55 seconds apart, makes it possible to use a longer integration time than would normally be employed operationally, so that the effect of minimum detectable temperature in the radiometer will be reduced. Thus, the data will be more dependent on atmosphere characteristics which is the desired test information, and less dependent on the radiometer. It would also provide a safety margin should any of the circuitry degrade in flight. There is also an additional advantage to be discussed later. Minimum integration time would be about 2 seconds ($\tau_{RC} = 1$) and maximum on the order of 10 to 20 times greater, providing a radiometer sensitivity increase of 3 or 4 times.

The tradeoff between radiometer sensitivity and antenna directivity has already been noted in paragraph 4.7. In principle they can be traded, but the wider beamwidth usually implies additional system error independent of radiometer sensitivity. An apparent contradiction to this was noted in two special synchronous cases. Assume a conservative radiometer sensitivity of 1 kelvin from Appendix A. A beamwidth of 1 degree will produce a temperature slope into the radiometer of about 400 kelvins per degree, in accordance with figure 54, and this results in a pointing error of 0.0025 degree. Since this is small compared to the maximum uncorrected error of about 0.02 degree from figure 48, this is a good compromise. However, doubling both beamwidth and radiometer sensitivity does increase the error by about the

original radiometer contribution. In general, it seems desirable to use the smallest beamwidth available, consistent with weight and space limitations on the antenna. The synchronous case requires additional investigation in this area.

It had initially been planned to try to measure any ellipticity existing in the oxygen mantle. The concept, briefly, involves a comparison of measurements taken on the two orthogonal axes. In the experiment description so far, these axes are separate and distinct, and comparison of 2 antenna beams on a given axis yields a pointing position. However, if the antenna pairs were equally squinted and provision made to compare beams on cross axes, then this comparison would yield any difference in the average of the two axes, and this would be translatable to ellipticity. The configuration requires three four-port switchable circulators (or DPDT switches) and four receivers. Each pair of antennas feeds its own circulator, as in the normal configuration, and one of the receivers. The other two outputs from the circulators feed the third circulator which feeds the other two receivers. For the cross axis comparison all switches are operated synchronously, with the phasing of the switching determing the antennas which are compared. There is also redundancy built into this configuration. Should one main axis receiver fail, either of the two extra receivers could be applied to that axis by stopping the third switch in the proper position. In fact, with this switch deliberately stopped at all times, two redundant receivers exist on both main axes, with one suffering an additional switch insertion loss. This could serve as a check on performance in case the switches did not provide as symmetrical performance as required.

There are several problems associated with this concept, and it has been abandoned at this time. First, the detailed calculations for many atmospheres show a significant change in profile edge with atmosphere. This would tend to mask any measurements, as there would be no a priori knowledge of the effect being measured. Secondly, the four-port switches present some hardware problem if high isolation and symmetry are to be maintained. They

would likely be Faraday rotation type, hence not latching, and both drive stability and power required would be problems. The Y-junction type proposed in a later section seems much better suited to the local vertical sensor. Also the additional receivers, although redundant, would be required and they represent a weight and power penalty.

Steer off capability has been investigated, and this does not look particularly attractive. The sensor is best operated in a closed attitude control loop or as a precision indicator near a zero output. Steer-off can be accomplished only over about half of the antenna beamwidth as one antenna pattern is then off the profile edge and can no longer provide useful inputs. For any significant angular steer-off, the antenna beamwidth would have to be increased over its present value, and as already discussed, this would cause a loss of pointing accuracy which cannot be recovered even if radiometer sensitivity can be increased. Most of this difficulty arises not so much from the shift in edge of the profile but from the change in plateau temperatures and the need to compensate for maximum accuracy.

As a summary to the analyses presented, the performance goals for a local vertical sensor experiment are discussed below. Angular resolution is specified as 0.01 degree. The analyses indicated an accuracy of this value available from synchronous altitude when compensated. At low altitudes, this goal assumes that the possible atmosphere change, over a restricted central angle change, is limited by the value of the angle. Compensation will also be required at low altitudes to meet this goal. The resolution will be available at low altitude, but the accuracy achieved will depend on the atmosphere characteristics. In order to achieve high accuracy, the antenna beamwidth is selected as 1.0 to 1.5 degrees in the measuring direction. In the transverse plane, a beamwidth of 8 to 12 degrees should be acceptable. Sidelobes should preferably be below 20 dB to avoid significant disturbances due to extraneous signals such as the sun or a communications transmitter falling in a sidelobe. (Sun in the main beam will render the system inoperative.) If operation at synchronous altitude is desired, the possibility of better

performance with a somewhat wider main beam should be investigated. Since compensating beams will be employed, either a separate aperture or an additional feed in a reflector-type structure must be provided. A recent report from NRL[14] shows very wide off axis scanning of a parabolic reflector, with good sidelobe behavior out to 15 or 20 beamwidths. From synchronous altitude all four beams on a given axis might be formed by a common reflector for simplicity. The angular squint of the beams will depend upon the altitude at which the sensor operates. For operation over a wide range of altitudes, the antenna squint must be physically changed, or a different feed arrangement selected (switched) in a reflector.

The goal for radiometer temperature sensitivity is set at 1 kelvin. As shown earlier, with a 1-degree beam this causes an additional error of less than 0.003 degree. Since the parameters used in the sensitivity calculation in Appendix A are somewhat conservative, this value should be readily achievable.

Some additional comment on sampling lattice is in order. The discussion so far has assumed a complete vertical sensor flight experiment. There is another flight experiment which would be quite useful, and which would provide significant input data for vertical sensor confirmation. This is a data collecting experiment designed to obtain atmospheric brightness temperature data on a global basis. By careful selection of the frequency band observed, a nadir looking experiment can be made to see essentially the same altitude region as used by the limb device. For the low-altitude lattice discussed earlier, there is sufficient integration time available to provide the required temperature sensitivity with the reduced bandwidth required by this experiment. This concept will be discussed more completely in Section 6. The significance at this point is the fact it can provide important data without the need for a precise angle measuring reference or precise angle control. In addition to collecting atmosphere data, all portions of the local vertical sensor millimeter wave radiometer, with the exception of the antenna system, would be tested in such an experiment.

4.10 INDEPENDENT VERIFICATION OF SPACECRAFT ATTITUDE

The analyses presented earlier in this report predict the success of the local vertical sensor and give a numerical estimate of the accuracies that can be obtained. These accuracies remain to be proven in an actual flight experiment. In order to provide an experimental measurement of accuracy, it is necessary to provide a standard for comparison, and this section will discuss some of the possibilities and problems of providing such a standard. The standard should preferably be more accurate than the device being tested, but this may not always be possible, especially when the new device is intended to improve existing capability or accomplish similar results in a different fashion.

Techniques that have been considered as a calibrating reference include star mapper, infrared sensor and microwave interferometer. Star mappers have been used to determine attitude of spinning vehicles. For example, Project Scanner[15] employed a relatively low altitude spin-stabilized suborbital vehicle, and a star mapper provided precise spacecraft attitude information. The spin is an essential part of such a system as the mapping is obtained by the star images passing through slits, and the outputs are sorted by time and amplitude to identify the stars and determine position. Much ground processing is involved to obtain the desired information. For the example cited the mapper was aligned with the test instrument to an accuracy of 0.005 degree and provided data with a 1σ accuracy of 0.008 degree. From the error curves presented earlier, calibration data to this accuracy or better will be required to test the local vertical sensor. The millimeter wave device views both limbs of the earth simultaneously, and is intended for an earth oriented vehicle. Spinning will degrade performance as the available integration time is greatly reduced. Hence, the use of a star mapper is not particularly compatible with the vertical sensor unless some other means is available to provide the spin function and not degrade accuracy.

Microwave interferometers have been used for precision angle measurement, and one system designed for calibrating an instrument landing system has demonstrated 0.01 degree accuracy.[16] An interferometer experiment will be included on ATS-F at synchronous altitude, and hopefully will demonstrate a similar degree of accuracy. This device requires several ground station transmitters and ground processing of the data. The use of such an interferometer, together with the attitude control capability of this later ATS series would provide an excellent test bed for the local vertical sensor. By steering the satellite off to one side of vertical and then giving it a gentle kick, the attitude will change slowly through the desired range at a constant rate. The measured output from the vertical sensor could be compared with predicted values, and the interferometer used to measure angle over a sufficient range to achieve accuracy. It will be seen, however, that the "standard" sensor accuracy would not necessarily be better than that of the device tested. Progress of the ATS-G has been monitored from time to time to see if an interferometer will be employed. At this writing, the status is so uncertain that this question cannot be answered.

The use of an interferometer as an independent reference at synchronous altitude appears quite attractive. However, at low altitude it is not very useful. With appropriate earth orientation of the vehicle, the vertical sensor axis will remain essentially vertical. The interferometer array must be on the satellite as that is where the angle is to be measured. As the satellite passes over the transmitter on the ground the angle measured by the array changes rapidly, on the order of 1 degree per second, and is more determined by spacecraft position than by attitude. Hence, this is not a good reference for attitude calibration.

The infrared sensor offers a good technique for providing an independent attitude reference, both at synchronous and low altitude. The operating principles are similar to the vertical sensor, but the infrared device depends on carbon dioxide absorption to define the limb rather than oxygen as used by the millimeter wave device. The infrared device is usually used to observe

one limb at a time and hence is generally applied to spinning satellites. It may also scan both limbs in sequence by scanning across the entire earth, say from synchronous altitude. The double limb case has been considered; however, as far as we have been able to determine, no predicted output characteristics or error curves, such as presented in figures 32 through 51 and 56 through 61 for the millimeter wave case, are available for the infrared case.

The use of both the infrared and microwave devices on the same spacecraft would provide an excellent opportunity to compare the two techniques. Although operating principles are similar, there are significant differences. The infrared device has a very narrow beamwidth whereas the microwave device is generally limited by its wider beamwidth. Detailed profiles for the two absorbers may be quite different, particularly for extreme atmospheres. As noted in figure 28, the severe warming atmosphere number 19 caused very little shape change in the microwave profile. We understand it shows a pronounced effect on the shape of the infrared profile, and this could cause error in a very narrow beamwidth system. The averaging obtained with even the narrowest microwave beam considered could be an advantage in such cases.

In summary, except for the interferometer at synchronous altitude as planned on some future ATS spacecraft, the infrared sensor is probably the most useful device against which to compare operation of the millimeter wave local vertical sensor. However, the infrared sensor should be considered an independent reference and not an absolute standard, since both techniques exhibit unique error considerations.

5. MILLIMETER WAVE COMPONENTS

Realization of the accuracy of the Local Vertical Sensor depends upon the performance of certain critical millimeter wave components in the radiometer system. These critical components include the antenna, low noise mixer, solid-state local oscillator, and radiometer switch. The object of this portion of the program was not to develop completely qualified components for incorporation into a space radiometer but rather to do sufficient breadboard work to establish the feasibility of achieving the accuracies predicted for the radiometer system.

For the antenna area, the significant accomplishment was the demonstration that there were fabrication techniques which could be used to carry the implementation of slotted waveguide arrays, which have been used at lower frequencies, to the 60-GHz band. This was successfully done using electric discharge machining of silver waveguide. In the mixer area, the key point was the demonstration that by the use of high resolution photolithographic techniques, gallium arsenide Schottky barrier diodes could be fabricated which when mounted in a novel wafer structure realized conversion losses of 5 dB with noise ratios of unity or less. The solid-state local oscillator effort demonstrated adequate power output at 60 GHz using a silicon avalanche diode with diffused epitaxial layer. For the ferrite switch, it was established that there was a commercially available ferrite switch which came quite close to meeting the requirements of this program, therefore, it was unnecessary to do development in that area. Detailed information on these components is provided in the following paragraphs.

5.1 ANTENNA

5.1.1 Requirements

The requirements of the antenna design, briefly stated, were as follows:

- Fabricate multiple-slot waveguide array samples of constant angle and depth to determine slot electrical parameters for the actual antenna design.
- Establish the reproducibility of the fabrication technique and its adequacy.
- Design and fabricate a single-aperture breadboard antenna. (E-plane control).
- Determine an acceptable method of transverse plane radiation control and design and fabricate a breadboard model. (H-plane control).
- Evaluate the performance of the complete breadboard model antenna.

5.1.2 Design Considerations

5.1.2.1 Antenna Type

A study of resonant versus nonresonant (traveling-wave) slotted arrays was performed. Antenna pattern performance of the resonant array was synthesized as a function of the number of slots, number of feed points (electrically independent sections), total bandwidth, and sidelobe level. The limits placed on these parameters are shown in table 3. The half-power beamwidth of 2.4 degrees of the 40-slot array was inadequate for system sensitivity requirements.

TABLE 3

RESONANT ARRAY PARAMETER LIMITS

Total number of slots	40, 80
Total number of feed points	1, 2, 4, 6, 8, 10
Total bandwidth	0 - 4%
1st sidelobe level	20, 25, 30 dB

The program used to synthesize the patterns employed an optimization technique which computed the illumination function required to minimize the ratio of power radiated outside main beam to power radiated inside main

beam when the first sidelobe level was specified at center frequency. As the bandwidth is increased, the pattern degrades. Theoretically, this can be compensated for by increasing the number of feed points. Figure 62 is typical of the results for the 80-element resonant array with first sidelobe level of -25 dB. It shows that even for the 1-percent bandwidth case at least 4 feeds would be required to properly control the beam shape. The practicality of constructing such a corporate fed resonant array was considered to be poor. Perhaps the most difficult problem would be to achieve the required relatively high slot conductance. Each 20-element section should have a total conductance of 1.0, which means the center slots of each section would have a conductance greater than 0.05.

The traveling wave array has several advantages over the resonant array. The sidelobe levels remain unchanged over the bandwidths considered. There is no appreciable change in the general pattern shape with frequency; whereas, the resonant array pattern has marked changes with frequency. There is

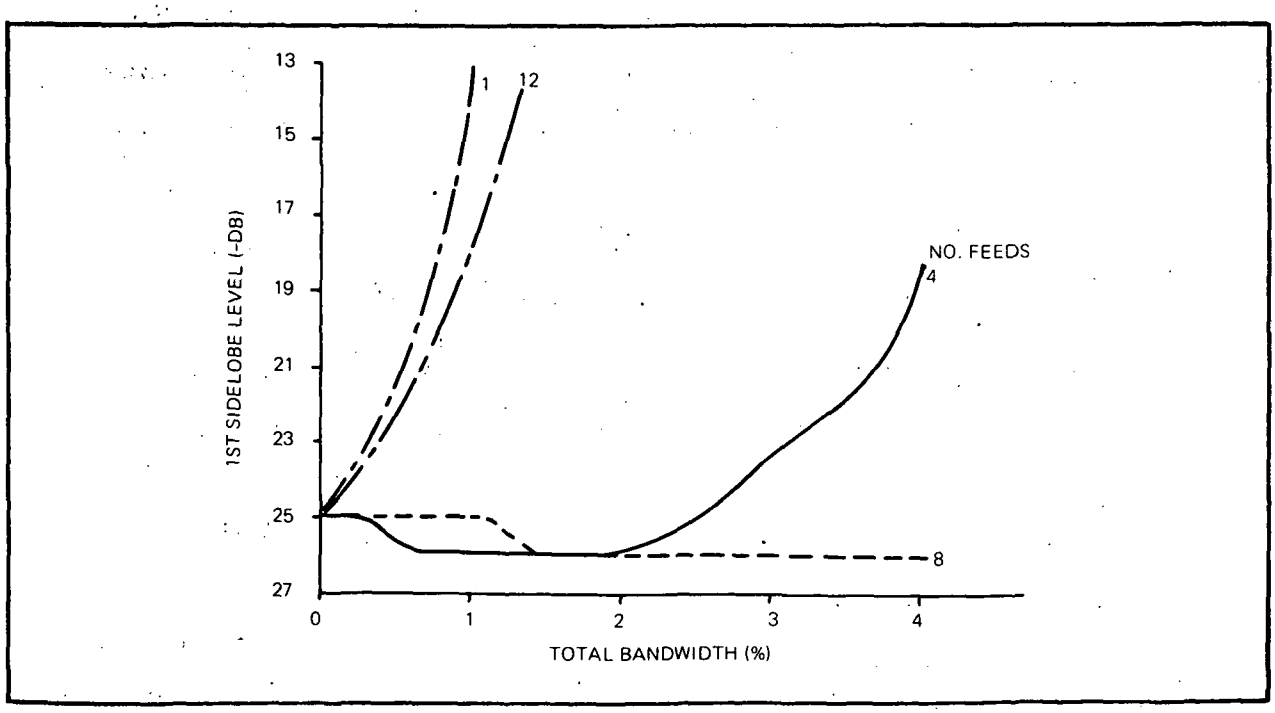

Figure 62. 80-Element Resonant Array

essentially no change in VSWR as no resonances occur over the bandwidth of interest. A disadvantage of the traveling wave array is that the main beam does change position with frequency. At a center frequency of 60.8 GHz, a total bandwidth of 1 percent produces a shift of ±0.33 degree in the main beam of an 80-element array with beam peak at 8.5 degrees with respect to broadside. The most current system evaluation indicates that this shift is acceptable. Therefore, it was decided that the breadboard model would be a traveling wave array of 80 edge slots.

5.1.2.2 Transverse Plane

A flared H-plane sectoral horn was found to be adequate for transverse plane control. The breadboard model was designed to have a half-power beamwidth of 12 degrees at 60.8 GHz. All raw slot data was taken in the presence of an H-plane sectoral horn since it slightly influences the data.

5.1.3 Slot Fabrication

5.1.3.1 Tolerance Considerations

Several edge slot shunt arrays had previously been fabricated by the Antenna Group in the S through K_a-band frequency range. It has been shown that the required tolerances of this type of slot are less critical than those of a broadwall slot. Based on the above experience, reasonable pattern control could be expected by scaling previously required tolerances to the 60-GHz region. Table 4 shows these specified tolerances. See section 5.1.4.2 for the resulting electrical parameter uncertainty.

5.1.3.2 Fabrication Results

The slots were cut in RG(98)/U waveguide after one edge was milled down to $0.010 \pm^{0.000}_{0.0005}$ inch. Various conventional machining methods of achieving these tolerances were attempted. The method which showed the most promise employed a carbide tip tool. However, two difficulties existed with this method. One, machining of the silver waveguide created burrs within the waveguide - how do you deburr and maintain tolerances? Two, the uniformity of slot contour from slot to slot was inadequate. In an attempt to

solve the first problem, a sample waveguide was filled with polyethylene glycol and two samples were filled with rigidix before machining. Both methods were unsatisfactory. The EDM (Electric Discharge Machining) process was successful in solving both of these problems. Table 4 shows the standard deviation, σ, of the slot parameters obtained from inspection data on the final 8 test arrays.

TABLE 4

SPECIFIED AND OBTAINED TOLERANCES

Slot Parameter	Specified	Obtained σ
Depth (in)	±0.00025	±0.00018
Width (in)	±0.0005	±0.0002
Spacing (in)	±0.001	±0.00043
Angle (min)	±1	±2

5.1.4 Test Array Measurements

5.1.4.1 Measurement Technique

The raw slot data was obtained from resonant test samples, of ideally constant angle and depth, each having a total of 15 slots. The slots were spaced $\lambda_g/2$ apart along the guide with adjacent slots coupled in opposite phase. Mutual coupling between slots cannot be neglected for edge (or shunt inclined) slot arrays, thus, the measurement technique accounted for this fact. The measurement setup is shown in figure 63. The measurement procedure was as follows. With the horn probe at one end of the test sample, the sliding short was adjusted for test sample minimum radiation. The horn probe was moved to the opposite end of the test sample and the frequency of the klystron was adjusted for test sample minimum radiation. This alternating procedure was continued until neither the klystron frequency nor the sliding short position could be changed without increasing the radiation from the test sample. The VSWR and two adjacent null positions of this minimum radiation condition were recorded.

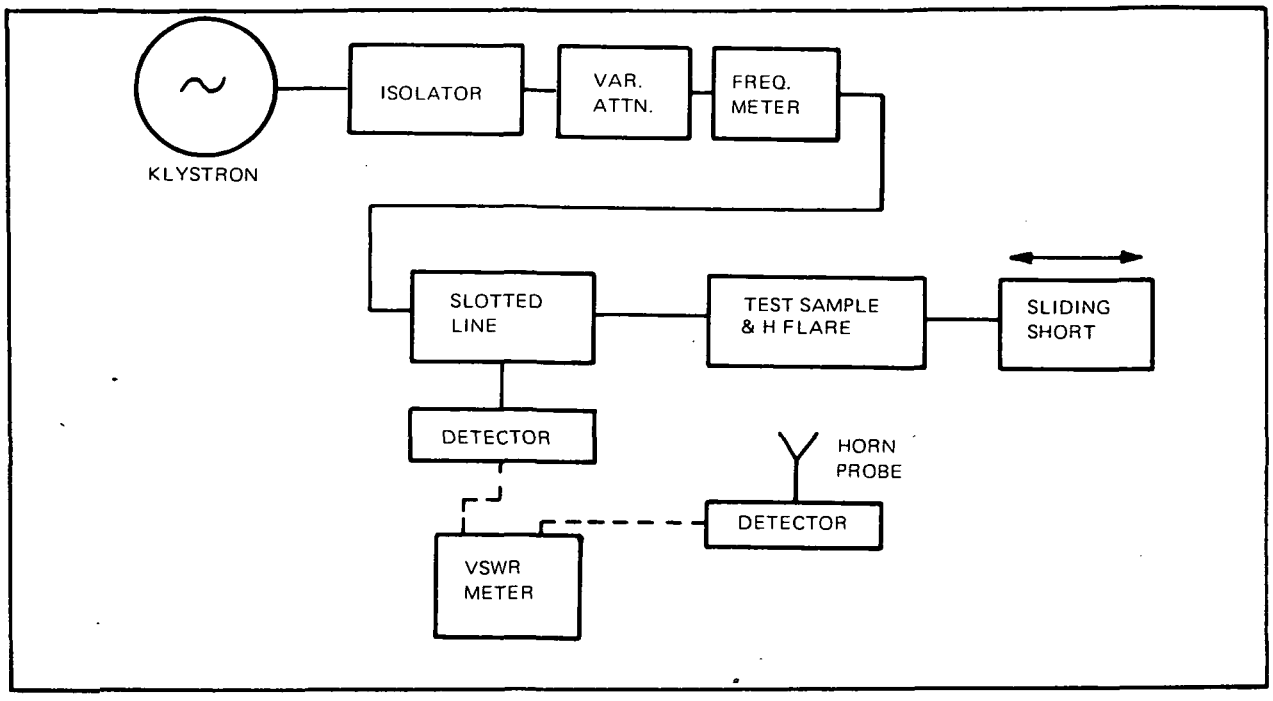

Figure 63. Test Sample Measurement Setup

All slots were shorted by placing a strip of aluminum tape over the entire length of the sample. The slotted line detector position was moved to the midpoint between the above measured nulls. The sliding short was adjusted until a standing wave null occurred at the new slotted line detector position. This position of the standing wave corresponds with the sample maximum radiation condition. The Al tape was removed and the new VSWR and null positions were recorded.

The mutual coupling between slots is different for the end slots than for the middle slots. It was desired to eliminate the end slot effects from the measurement. This was accomplished by taping over six end slots only of one end of each sample and remeasuring the VSWR and null positions. The individual slot parameters were then computed from the difference between the 15 and 9 slot radiating cases.

5.1.4.2 Test Sample Results

Twelve different configurations of test samples were fabricated. Six ideally identical pieces of the first configuration were obtained to evaluate the capabilities of two different vendors. Two ideally identical pieces of the other 11 configurations were made to check repeatability of results. Repeatability was poor until each sample was thoroughly cleaned in a cyanide bath. The last 4 configurations and the measurement results are listed in table 5. The two measurements per sample are the result of alternately taping over the opposite 6 end slots.

TABLE 5

TEST SAMPLE RESULTS

Conf. No.	θ (Deg)	Depth (Mils)	Slot R	Slot X	Slot $\frac{X}{R}$	R $\sin^2 \theta$
1A	10	0.0195	45.6	-22.3	-0.49	1.375
	10	0.0195	37.9	-22.3	-0.58	1.143
1B	10	0.0195	40.9	-20.4	-0.50	1.233
	10	0.0195	45.9	-21.3	-0.47	1.384
2A	10	0.0205	38.4	- 8.8	-0.23	1.158
	10	0.0205	37.4	- 7.8	-0.21	1.128
2B	10	0.0205	36.5	-11.4	-0.31	1.101
	10	0.0205	31.6	-15.5	-0.49	0.953
3A	15	0.0185	16.3	- 7.1	-0.44	1.092
	15	0.0185	16.6	- 6.7	-0.40	1.112
3B	15	0.0185	17.4	-10.6	-0.61	1.166
	15	0.0185	18.8	- 9.5	-0.51	1.260
4A	15	0.0195	16.9	- 4.1	-0.24	1.132
	15	0.0195	16.6	- 4.4	-0.27	1.112
4B	15	0.0195	16.3	- 5.5	-0.34	1.092
	15	0.0195	16.3	- 4.5	-0.28	1.092

Figures 64 and 65 are plots of the spread in the data of $R \sin^2 \theta$ and $\Delta(X/R)/\Delta(\text{Depth})$, respectively. The former represents the control over per slot amplitude coupling while the latter indicates control of slot resonance and therefore phase. The electrically determined randomness or error in these quantities is

$$\text{Ampl. Coupling error} = \left.\frac{\sigma}{\text{MEAN}}\right|_{\text{Fig 64}} = \left(\frac{0.073}{1.14}\right) = 0.064 \rightarrow 0.29 \text{ dB}$$

$$\text{Phase error} = \tan^{-1}\left(\left.\frac{\sigma}{\text{MEAN}}\right|_{\text{Fig 65}}\right) = \tan^{-1}\left(\frac{33.7}{208.}\right) = 9.2 \text{ degrees}$$

When errors of this magnitude exist, the sidelobes of a cosine squared on a pedestal (11 dB) aperture distribution deviate from design value as shown in figure 66. The amplitude error is insignificant. However, greater phase control could be desirable. This would require greater slot depth control which was controlled to state-of-the-art machining tolerances.

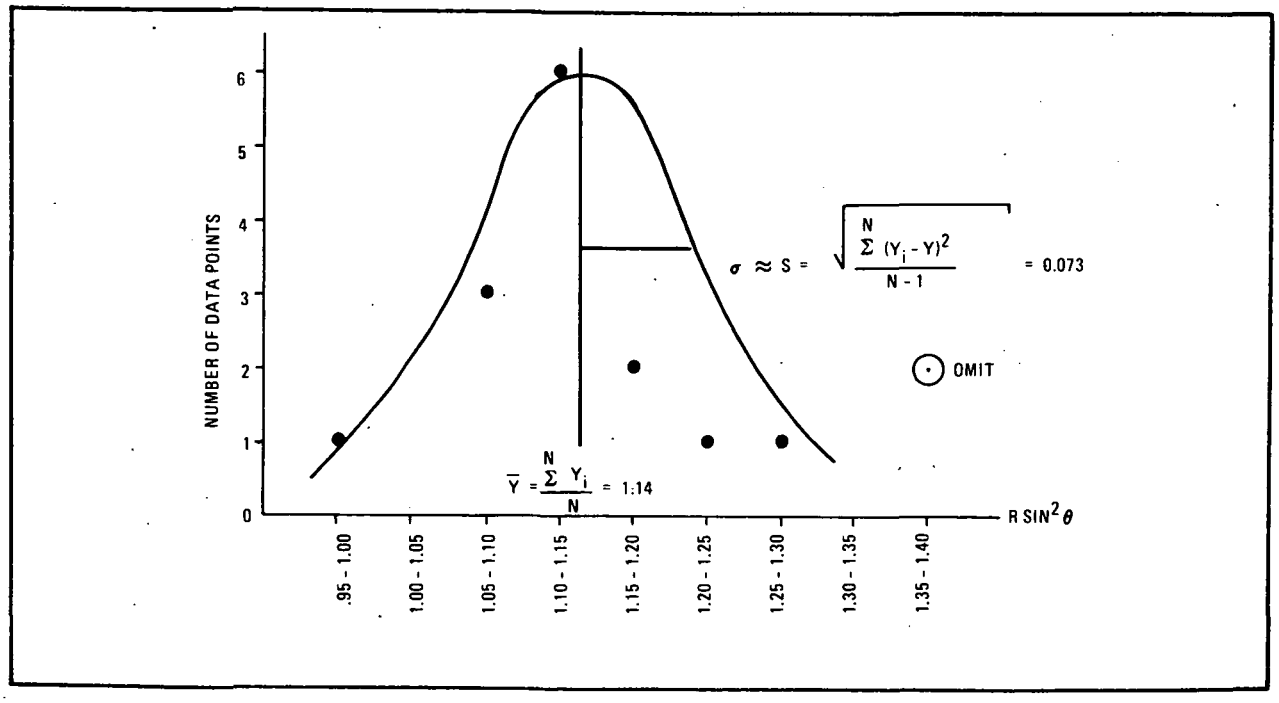

Figure 64. Spread in Slot Resistance as Measured from a Group of 15 Slots

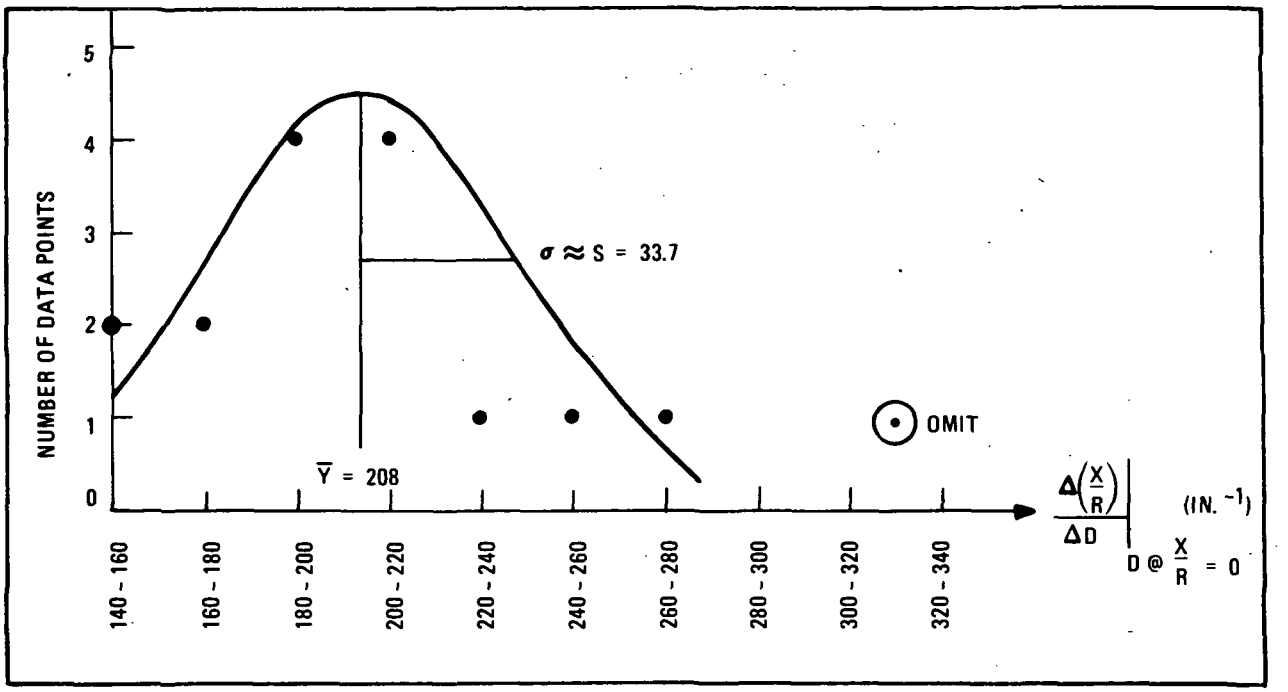

Figure 65. Spread in (X/R) as Measured from a Group of 15 Slots

It can be shown that the resonant depth, D_θ, near resonance, of an edge slot varies as

$$D_\theta = D_o - L \frac{\sin^2(\theta/2)}{\cos \theta}$$

where

D_o = resonant depth projected to 0° inclination

L = depth slope

θ = inclination angle with respect to b waveguide dimension

Figure 67 is a plot of this data of table 5. The parameters required for the breadboard model design are listed in table 6.

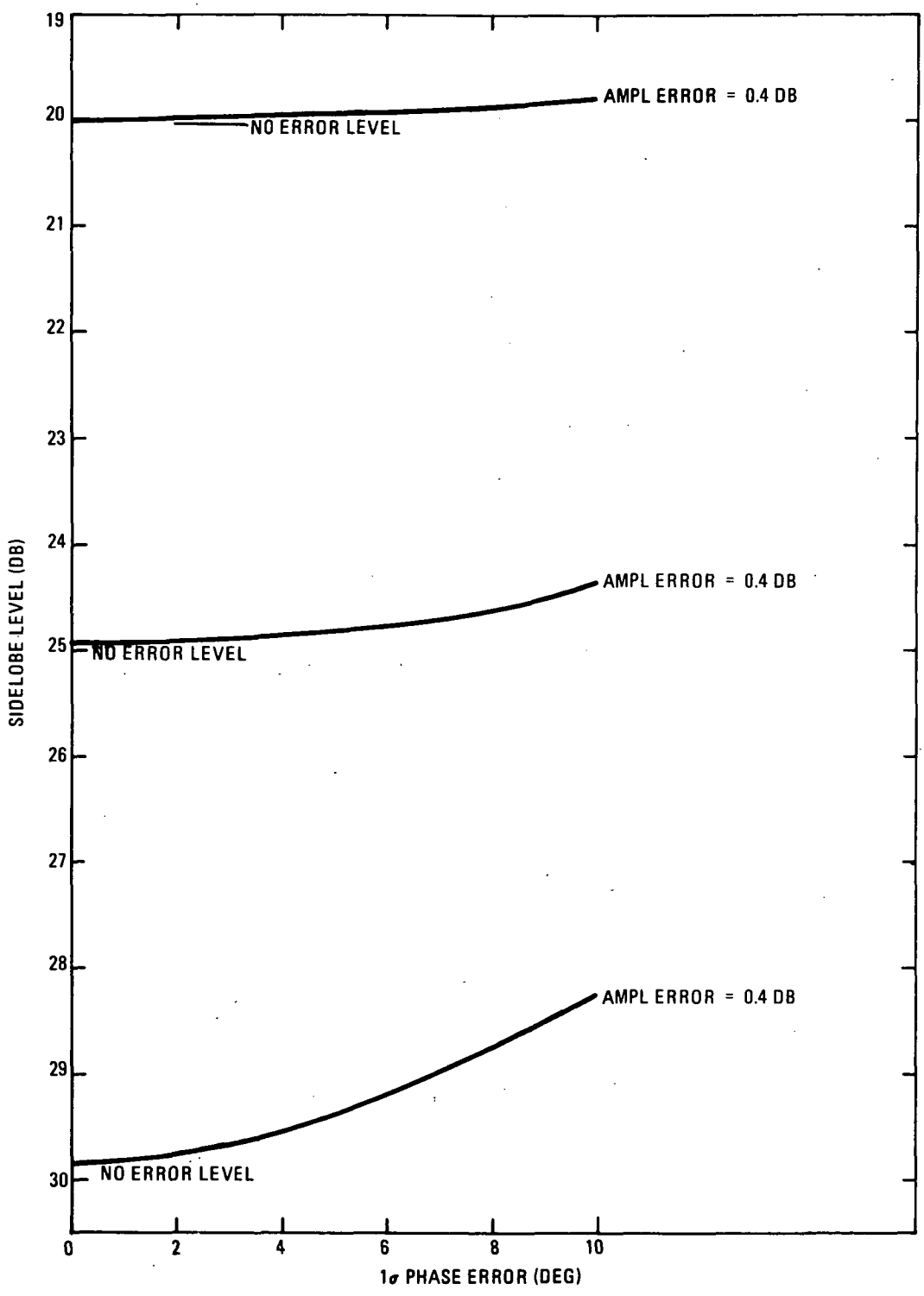

Figure 66. Effect of Phase and Amplitude Error on Sidelobe Level

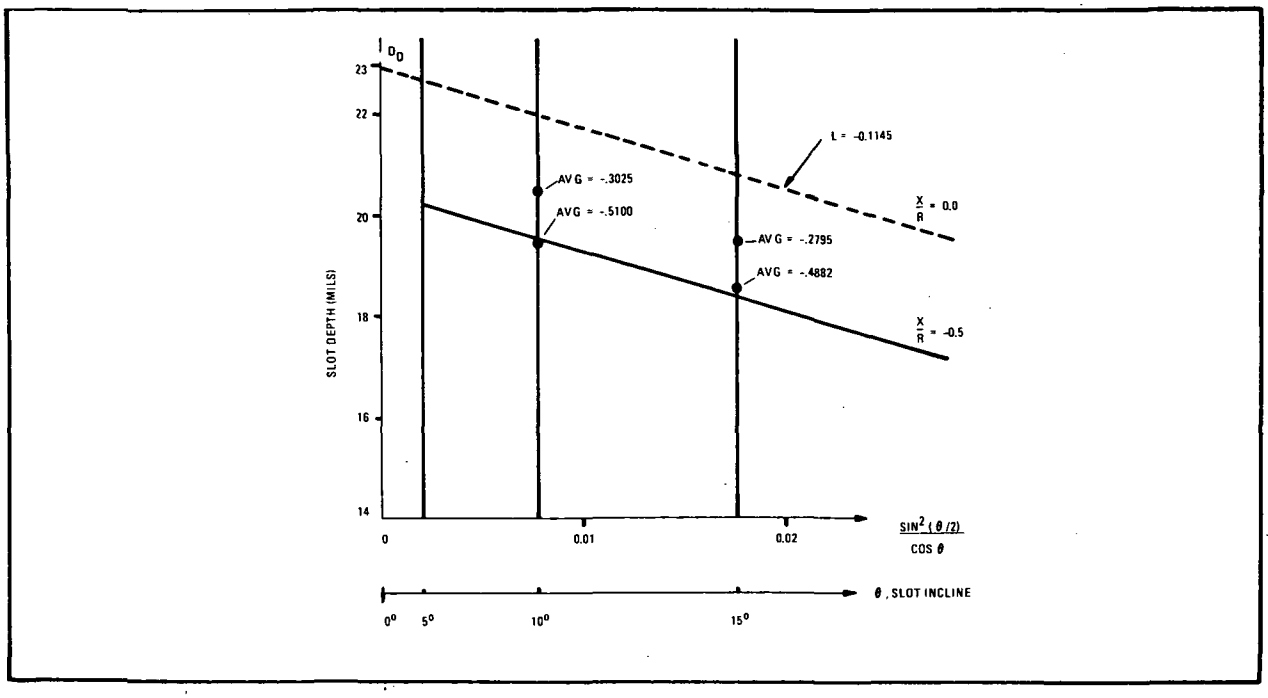

Figure 67. Lines of Constant X/R

TABLE 6

REQUIRED PARAMETERS FOR ANTENNA DESIGN

Resonant Depth for Zero Slot Angle (in.) = 0.0229

Depth Slope, L, (in.) = 0.1145

Rate of Change of X/R with Depth, $\Delta(X/R)/\Delta D$ = 208.0

Slot Resistance Factor, $R \sin^2 \theta$ = 1.14

5.1.5 Breadboard Model

5.1.5.1 Description

The feasibility model was designed as a traveling wave array with the characteristics shown in table 7. The element spacing is such that the beam peak will occur back toward the generator. This pointing direction versus pointing in the load direction was chosen so that the angular separation between the main beam and the cross-polarized lobe (results from the

inclination of the edge slots) would be maximized. The power dissipated in the load was designed to equal 10 percent. Experience has shown that if too little power is allowed to be dissipated by the load, the slot angles at the input to the array approach 0 degree. A very small error in the inclination of such a slot would cause a large percentage error in coupling. It was desired that all angles be greater than approximately 3 degrees. The resultant slots satisfied this condition with the exception of one slot.

TABLE 7

BREADBOARD DESIGN PARAMETERS

Amplitude Distribution: $\cos^2 \theta$ on pedestal

Pedestal Height: 11 dB (0.282)

Gain: 33.3 dB

Number of Elements: 80

Ratio of λ_g/λ_o = 1.3246

Slot Spacing: $2D/\lambda_o$ = 1.1029 (D = 2.718 mm)

Beam Peak (with respect to broadside): -8.74 deg at 60.86 Hz

HPBW = 1.45 deg (E-Plane) = 1.10 λ/L (rad)
12 deg (H-Plane)

E-Plane Sidelobes: 1st S.L. = -33 dB
2nd S.L. = -27 dB
3rd S.L. = -29 dB
4th S.L. = -31 dB

Power into Load/Power Radiated = 10 percent

Waveguide Edge Thickness = 10 mils (.25 mm)

5.1.5.2 Results

The principal results, including gain, of the feasibility model measurements are tabulated in table 8. Figures 68 and 69 are the measured principal plane patterns - E-plane (azimuth) and H-plane (elevation), respectively. Figure 70 is an overlay of the measured azimuth pattern on the theoretical pattern. It shows that the separation distance was insufficient to measure the

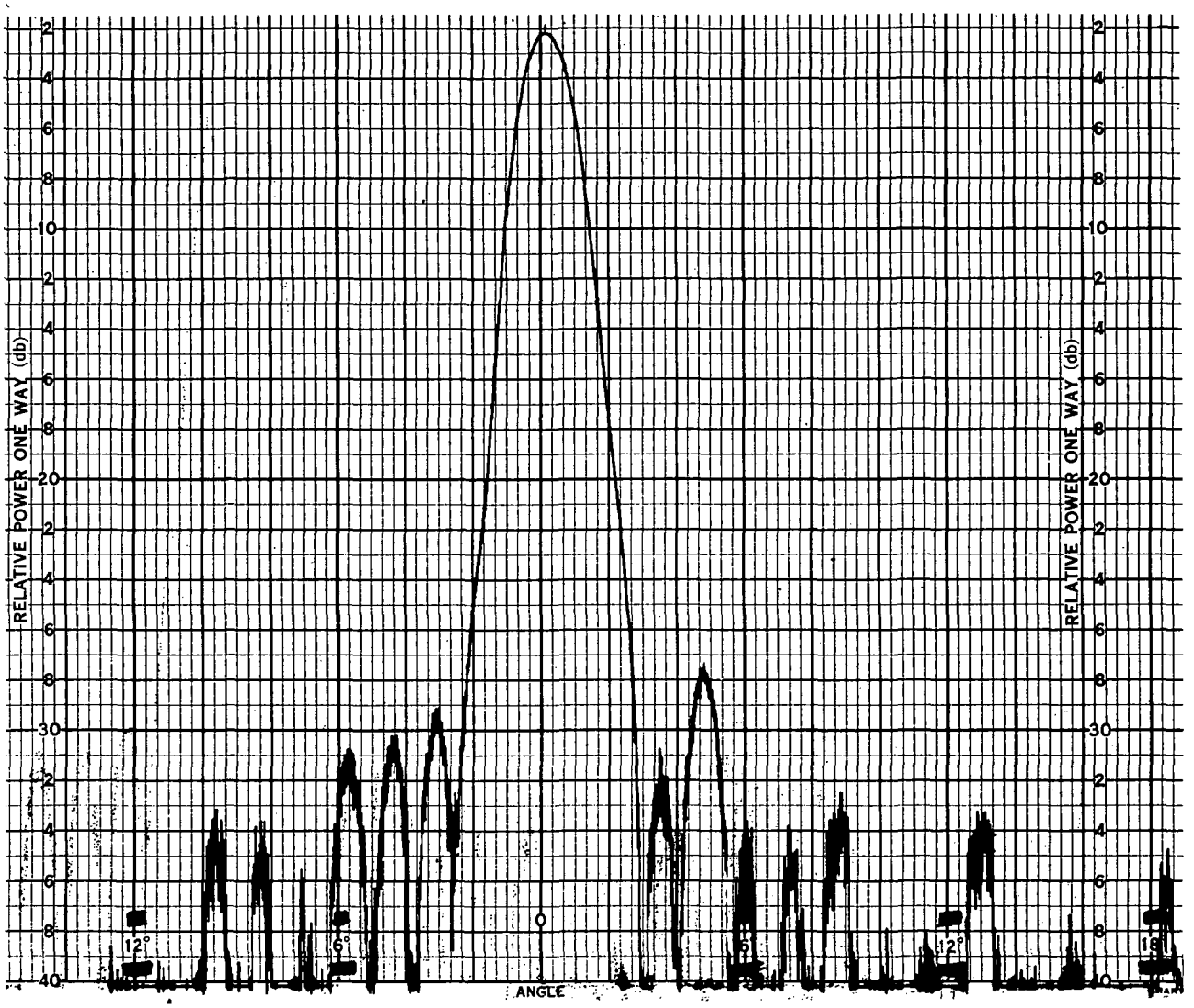

Figure 68. E-Plane (Azimuth) at 61.05 GHz

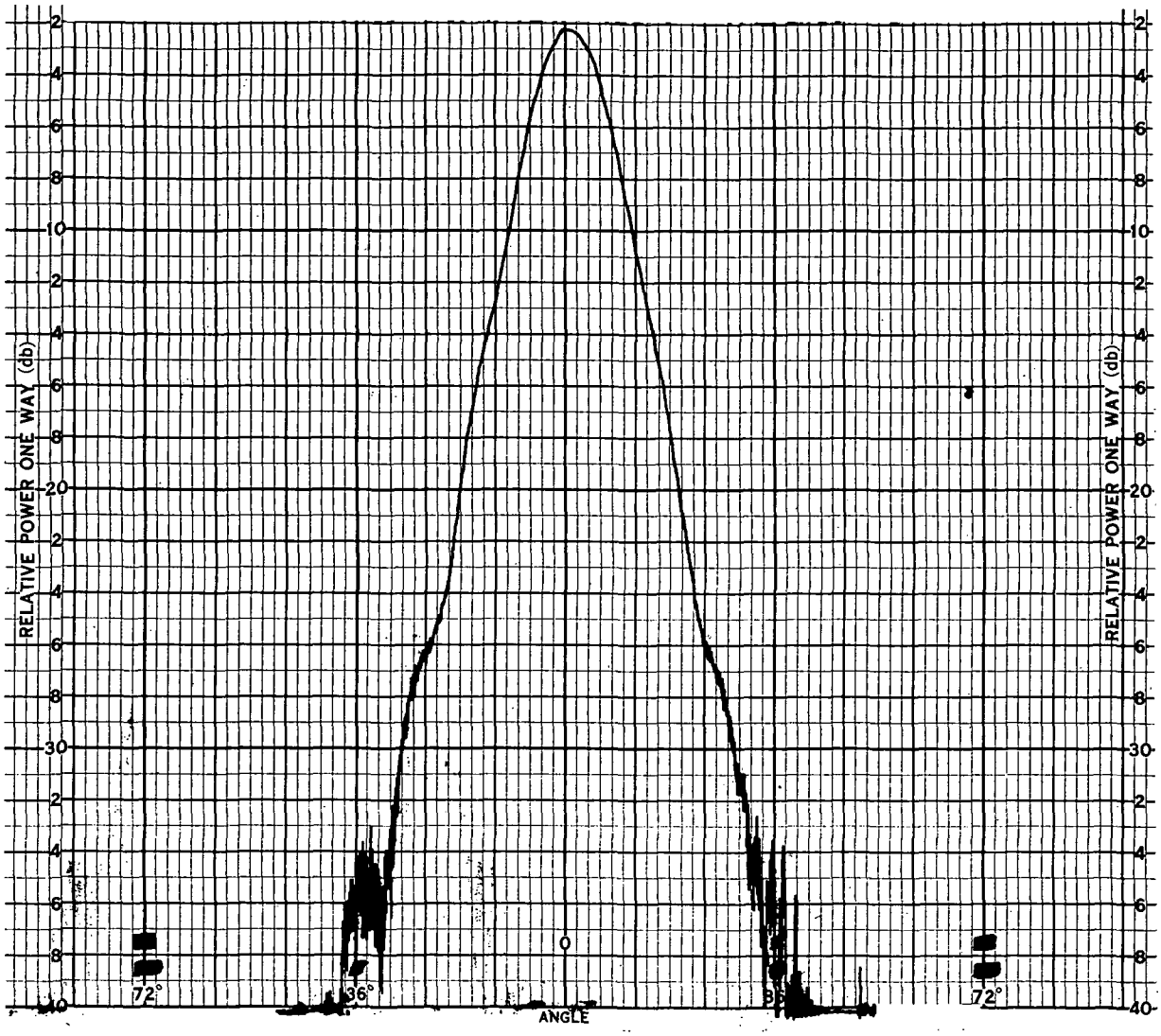

Figure 69. H-Plane (Elevation) at 61.05 GHz

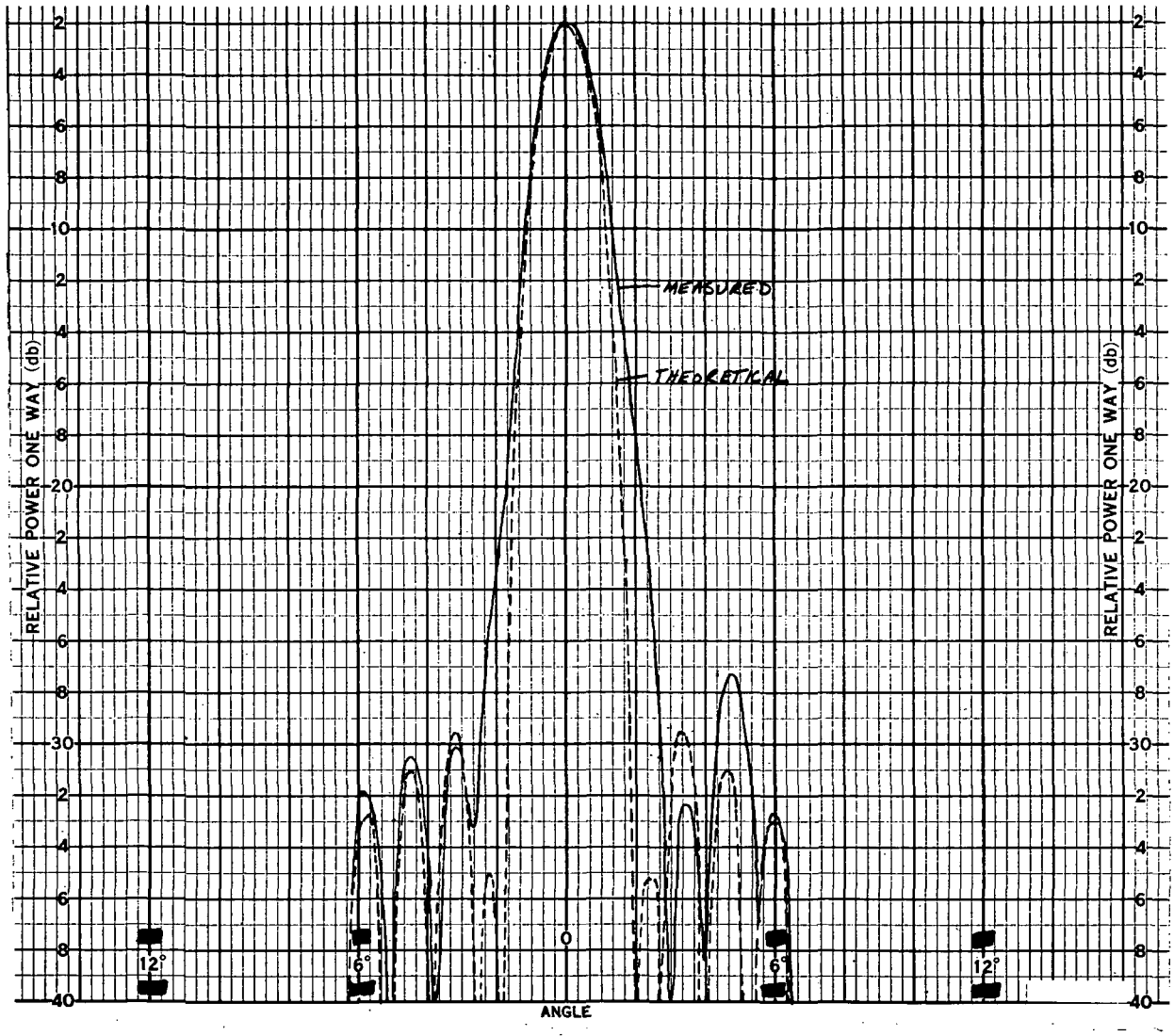

Figure 70. Theoretical vs Measured Azimuth Pattern

first sidelobe. However, the measurement system was sensitivity limited to 40-feet separation to permit measurement of the second through fourth sidelobes. A cross-polarized pattern showed that the cross-polarized lobe on the generator side of broadside was effectively moved into invisible space. Azimuth conical cuts of $\theta = \pm 2, \pm 4, \pm 6, \pm 8, \pm 10$ degrees and elevation conical cuts of $\phi = \pm 1, \pm 2$ degrees were also taken. Azimuth patterns over a 1-percent bandwidth showed the expected amount of beam shift of the main beam and no change in the sidelobe structure.

5.1.6 Conclusions

The EDM process does produce adequate control over slot uniformity and dimensions so that a slotted waveguide array in the region of 60 GHz is feasible. To achieve sidelobes of -30 dB, the slot depth must be controlled to at least ±0.00025 inch.

The measured results of the feasibility or breadboard model closely agreed with the theoretical calculations. Photographs of the breadboard model are shown in figures 71 and 72.

TABLE 8

BREADBOARD RESULTS

Beam Peak (with respect to broadside): -8.48 deg at 61.05 GHz

Gain: 32.0 dB

HPBW: 1.58 deg (E-Plane)
12.85 deg (H-Plane)

E Plane Sidelobes: 2nd S.L. = 30, -27.4 dB
3rd S.L. = 25.5, -28.7 dB
4th S.L. = 33, -29 dB

Power into Load/Power Incident = 5.5 percent

VSWR: 1.05:1

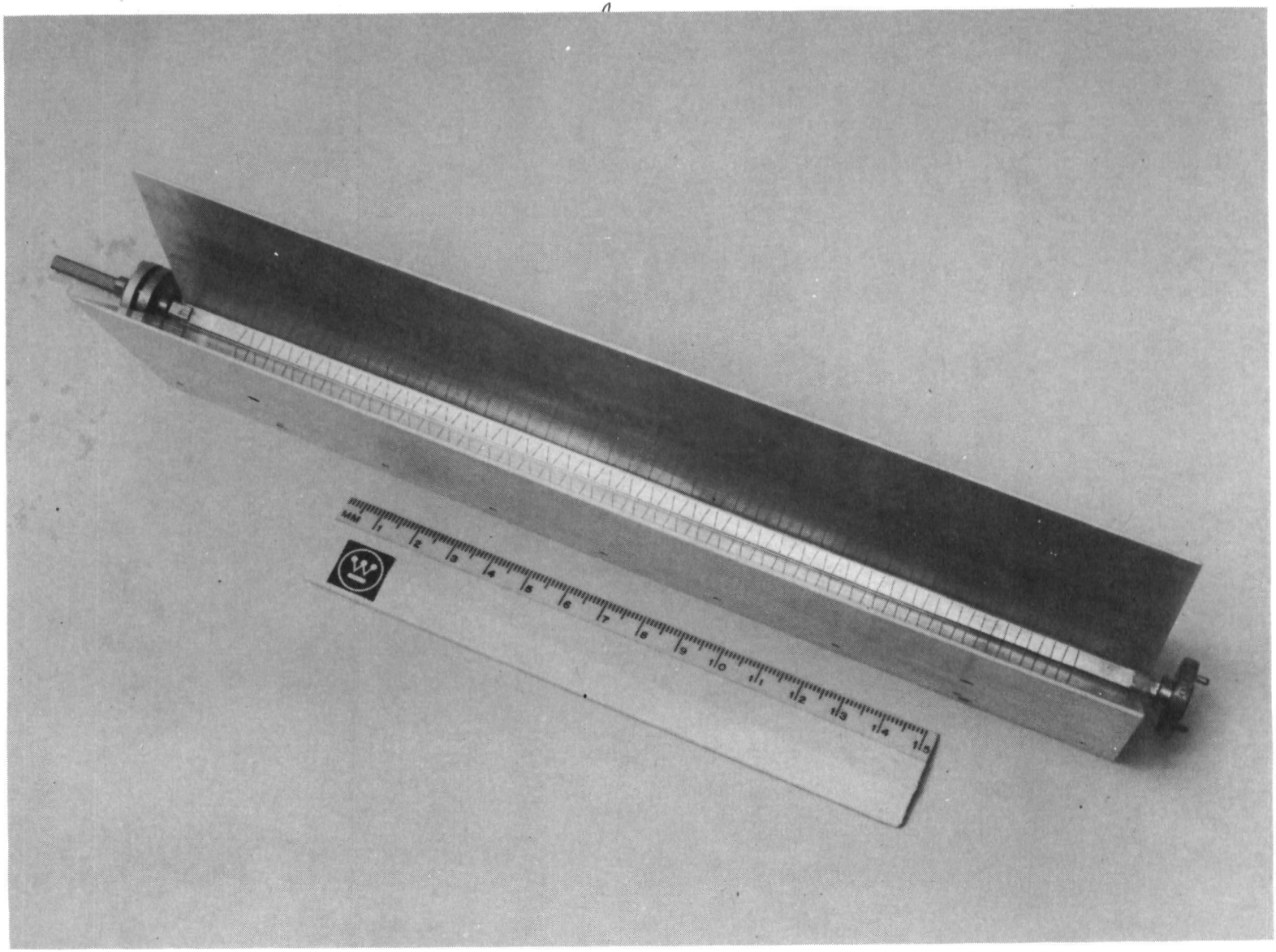

Figure 71. Overall View of 80-Slot Breadboard Antenna

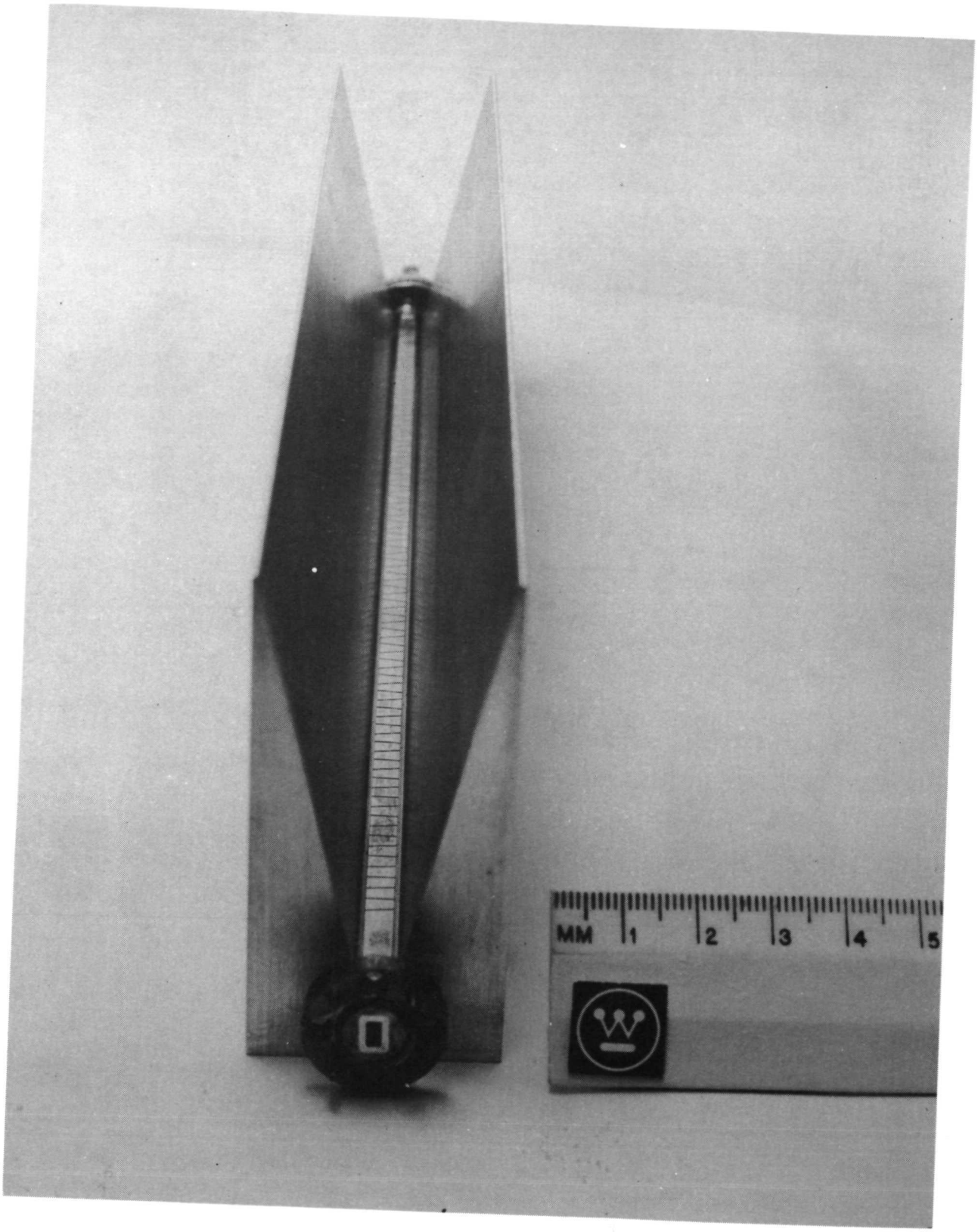

Figure 72. Breadboard Antenna Showing H-Plane Flare

5.2 MILLIMETER WAVE MIXER

The objective of this task was the development of the critical millimeter wave semiconductor diodes and the necessary mounting structures required to yield an overall reliable, low-noise, RF front end for the 60-GHz radiometric receiver.

5.2.1 Schottky Barrier Diodes

Schottky barrier diodes are particularly advantageous for millimeter wave applications because of the potential simplicity of their fabrication. A single evaporation or electroplating operation, performed through a suitable mask, will define the active area and provide the metallic surface for lead contact. The high mobility of GaAs has made possible the design of diodes with active regions of extremely low resistance. The design and fabrication of the semiconductor element is similar to the approach previously reported[17, 18] and has resulted in GaAs diodes with a varactor frequency cutoff of nominally 800 GHz, as measured at zero bias and with a measurement frequency of 70 GHz.

The diode is a planar, SiO_2 passivated device. The GaAs chips used for the 60-GHz mixers are 0.38 by 0.38 by 0.10 mm and have an array of 4-micrometer-diameter junctions spaced on 8-micrometer centers. The junction capacitance at zero bias is nominally 0.03 to 0.04 pF, and the series resistance falls in the range of 5 to 7 ohms.

5.2.2 Contacting Techniques

It was proposed that various techniques be investigated for contacting and/or bonding to the mixer diode, such as small area pressure contacting or fusion bonding to expanded contact area. Some consideration has already been given to this problem; however, the techniques herein presented have not been implemented in a millimeter wave diode.

As has already been stated above, the diodes used for the mixer are epitaxial GaAs, SiO_2 passivated, Schottky barrier devices with junction

diameters of about 4 μm. It has been proposed, as an aid to enhancing the passivation feature, that a tri-metal overlay pad[19] of 15 μm be used. This will ensure the sealing of the junction edges. The overlay pad will also enhance the mechanical stability of the junction. The first layer of the overlay pad is titanium, chosen because of its great surface bonding strength, refractory nature, and impurity gettering properties.[20] Gold is chosen as the outer layer because of its extreme resistance to corrosion, low electrical resistance, low yield point, high elongation (allowing thermal expansion mismatch with the GaAs substrates), and suitability for high-resolution electroforming. Platinum is used as the barrier metal between the titanium and the gold because of its inertness, ease of bonding the gold outer layer, and the low diffusion coefficient of gold into platinum. The titanium and platinum will be sputter deposited since sputtered metals have many times the energy of thermally evaporated metals and are capable of dislodging impurities. The gold will be built up by electroplating, and then used as the mask to allow the selective removal of the platinum and titanium as needed.

A final layer would then be used. That is, a layer composed of tin-lead-silver (Sn-Pb-Ag) may be plated over the gold to a thickness of about 2 μm. Contact to the diode junction would be by use of a 13-μm gold wire which has been electrolytically pointed to a radius of about 1.0 μm. As a final step to the diode assembly, the complete wafer is heated to a temperature which will allow the (Sn-Pb-Ag) braze material to flow and effectively bond the gold contact wire to the overlay pad. A view of such a structure is shown in figure 73.

The additional shunting capacitance due to the overlay pad is calculated to be but 0.01 pF for an overlay diameter of 15 μm. Assuming the zero bias capacitance to be about 0.04 pF, and the average barrier capacitance to be the zero bias value, and recognizing the fact that the overlay capacitance acts "external" to the junction (i.e., outside the series resistance, R_s)

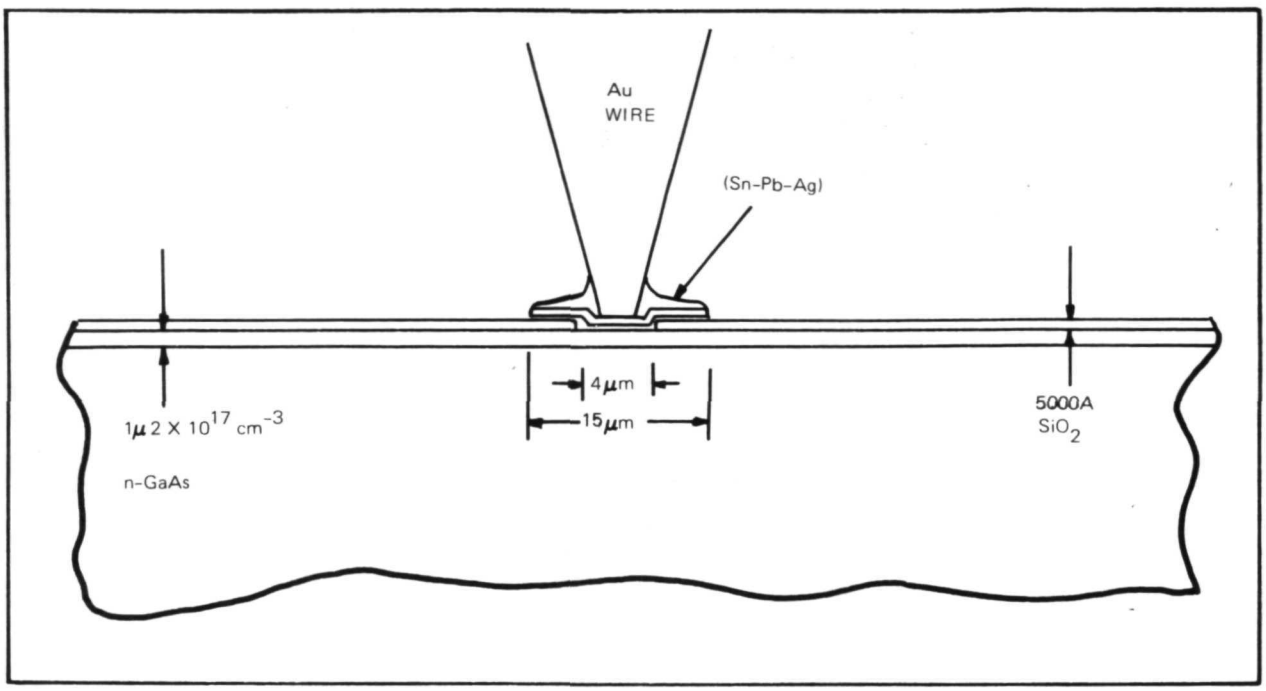

Figure 73. Section of Diode Showing Details of the Overlay Pad

then the major effect of the overlay will be to increase the signal (RF) circuit Q by a factor of about 20 percent. This then implies a reduction of RF bandwidth by a similar amount.

A semiconductor diode structure similar to that herein discussed is shown in figure 74. The diode shown was used in an X-band image enhanced mixer.[21,22] The mixer performed fully as expected and no unexpected increase in noise problems was encountered due to the overlay pad.

5.2.3 Radiation Tests

As part of the contract effort, Westinghouse conducted a radiation test program on the passivated, GaAs, Schottky barrier varactors herein discussed. The tests were performed on a "before and after" basis to determine if there were any irreversible effects to proton fluences of 3×10^{12} protons/cm^2 total radiation flux. The tests were conducted at Oak Ridge,

Insert

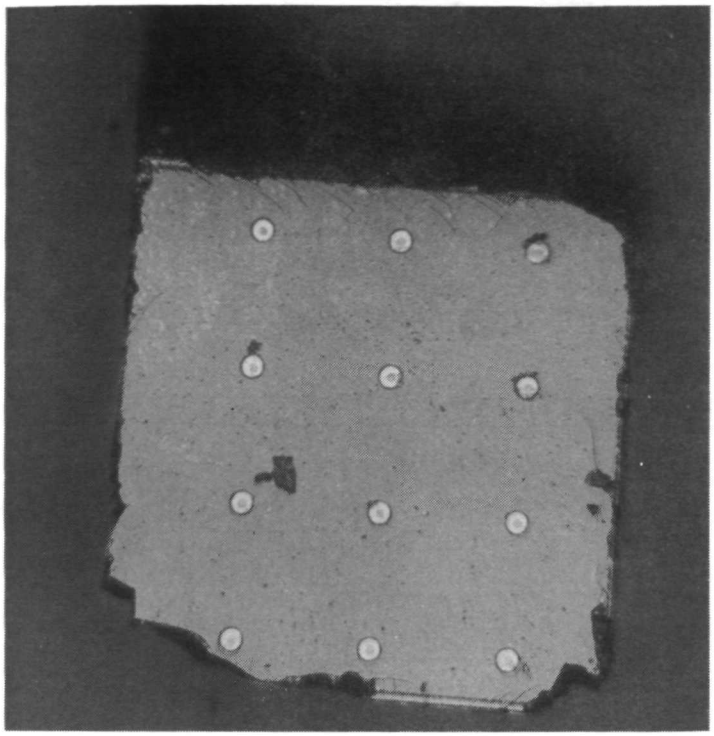

Figure 74. GaAs Schottky Barrier Diode Chip (0.38 x 0.38 mm) Having Individual 5-μm Diodes With a 20-μm Overlay Pad for Wire Bonding

Tennessee, in December 1970. Eight diode chips were mounted on posts and electrically tested for series resistance, R_s, and the log I versus V slope parameter, η. The test results (for before and after irradiation) are presented in table 9. As can be seen, the test results showed that the effects of proton irradiation are minimal up to fluences of 3×10^{12} protons/cm^2. Two diode contacts, selected at random, were tested.

5.2.4 Single Ended Mixer Performance

Figure 75 presents the conversion (transducer) loss of one mixer wafer as a function of LO drive power and bias voltage for converting from a signal at 68.8 GHz (LO at 70 GHz) to an IF of 1.2 GHz. The conversion loss curve is a plot of direct measurement data, not corrected for input and output mismatches and other circuit losses. The minimum conversion loss

TABLE 9

GaAs DIODE RADIATION TEST

Post No.	Before R_s	Before η	After R_s	After η	Dopant
1	9	1.33	10.5	1.26	(Te)
	9.5	1.15	9.5	1.14	
2	2.5	1.33	8.5	1.23	(S)
	3.5	1.13	4.0	1.16	
3	7.5	1.23	7.0	1.23	(Te)
	7.5	1.22	7.0	1.23	
4	5.0	1.42	3.0	1.40	(Te)
	5.0	1.37	5.0	1.33	
5	3.5	1.39	4.0	1.36	(Te)
	3.5	1.29	4.0	1.26	
6	13	1.45	6.0	1.40	(Te)
	8	1.40	5.0	1.40	
7	4.5	1.36	4.0	1.26	(Te)
	5.5	1.40	4.0	1.36	
8	4.5	1.40	7.0	1.45	(Te)
	2.5	1.40	4.0	1.36	

of between 5 and 6 dB is typical of measurements on many diodes. The noise ratio of these diodes is very close to unity, verified by direct noise figure measurements.

The theoretical limitations of these diodes as developed from GaAs, and the limitations that would exist if comparable processing technology were utilized to make silicon mixer diodes can be seen from the following considerations. Reliable passivated Schottky barrier diodes can be made from GaAs that can have a frequency cutoff, f_{co}, as measured at zero bias of about 800 GHz.[23,24] Without the use of very special (and very expensive) techniques such as ion implantation, one is limited to an $f_{co} \cong 250$ GHz at zero bias for silicon Schottky barrier diodes of similar dimensions.

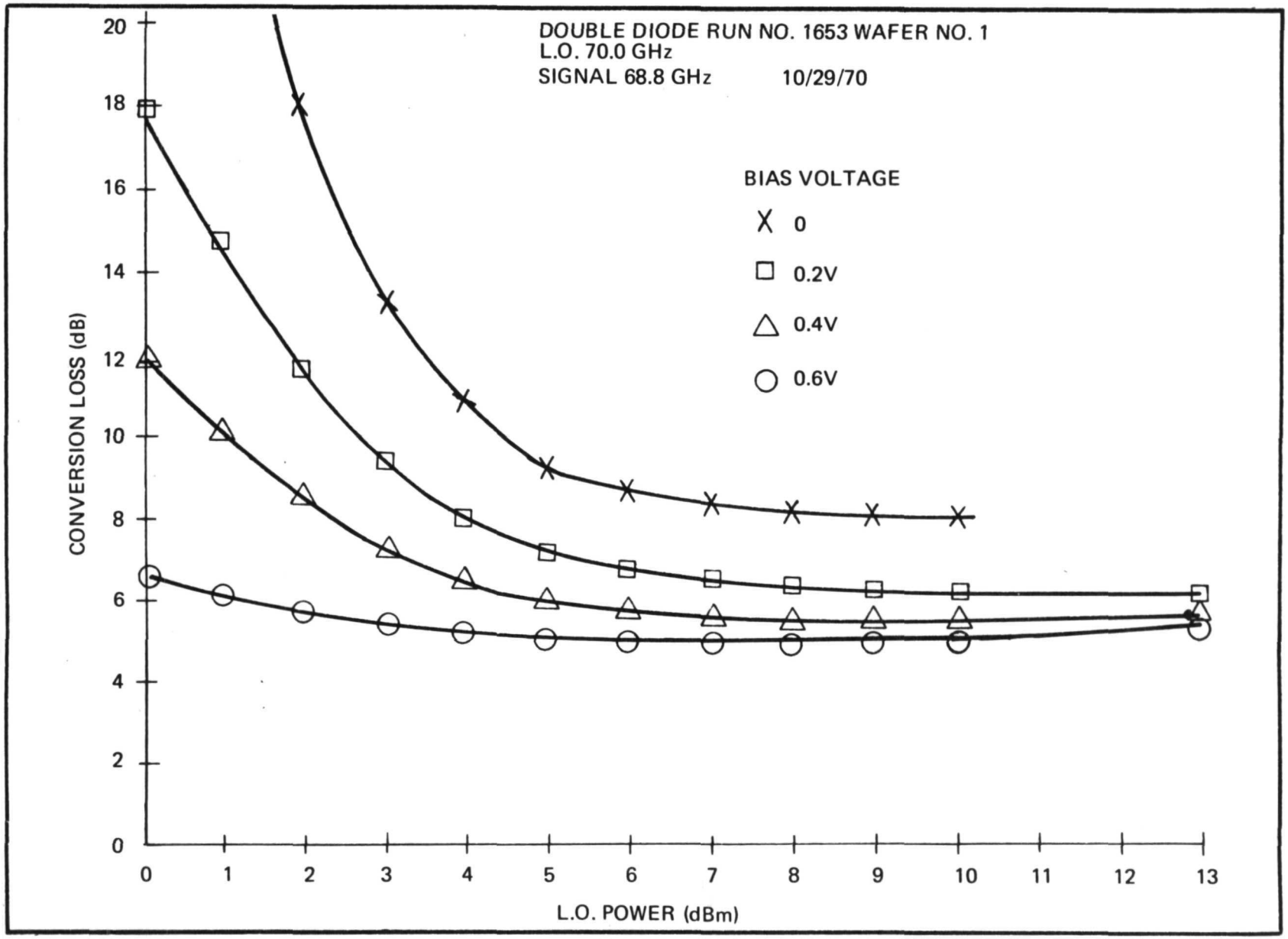

Figure 75. Conversion Loss vs LO Drive and Bias

Barber[25] has presented an analysis of microwave mixers and has shown that the pulse duty ratio (PDR) of the Schottky diode current waveform is the most fundamental parameter for defining mixer operations because the diode current pulse retains its typical (switched) shape even when the voltage waveform becomes highly nonsinusoidal.

It can be shown that most microwave mixer diodes (adjusted for lowest conversion loss) behave as though the barrier itself were switched on and off at the LO rate; and that the resistance in the ON state is just that of the limiting series resistance (R_s), and the impedance in the OFF state is just that expected of the series resistance, R_s, in series with the barrier capacitance, C_b. Of course the barrier capacitance is a function of voltage and time, but good correlation with measured results are obtained if the zero bias capacitance value is used. Thus, the frequency cutoff is $f_{co} = (2\pi R_s C_b)^{-1}$; and takes the 800-GHz and 250-GHz values for GaAs and Si as given above.

Using these considerations, an extension of Barber's analysis has allowed the calculation of the conversion loss as a function of the PDR and as limited by the operating frequency to cutoff frequency ratio (f/f_{co}). Figure 76 shows the expected mixer conversion loss that would obtain for the broadband case (wherein the image termination equals the signal termination). Figure 77 shows the computed mixer conversion loss for the case wherein the image is shortcircuited.

To understand the effects of f_{co} more clearly, we compute the performance expected both for the referenced X-band image enhanced case (shorted image) and the 60-GHz broadband case; computed both for GaAs and silicon. Now with GaAs at X-band (10 GHz) the $(f/f_{co}) \cong 0.0125$ and taking a PDR $\cong 0.15$ (a reasonable value which keeps the terminal impedance low enough to handle) then the conversion loss, L_c, takes a value of 2.4 dB which is very close to the measured value. With Si, $(f/f_{co}) \cong 0.04$ and with the same PDR, $L_c \cong 2.7$ dB - only a 0.3 dB difference.

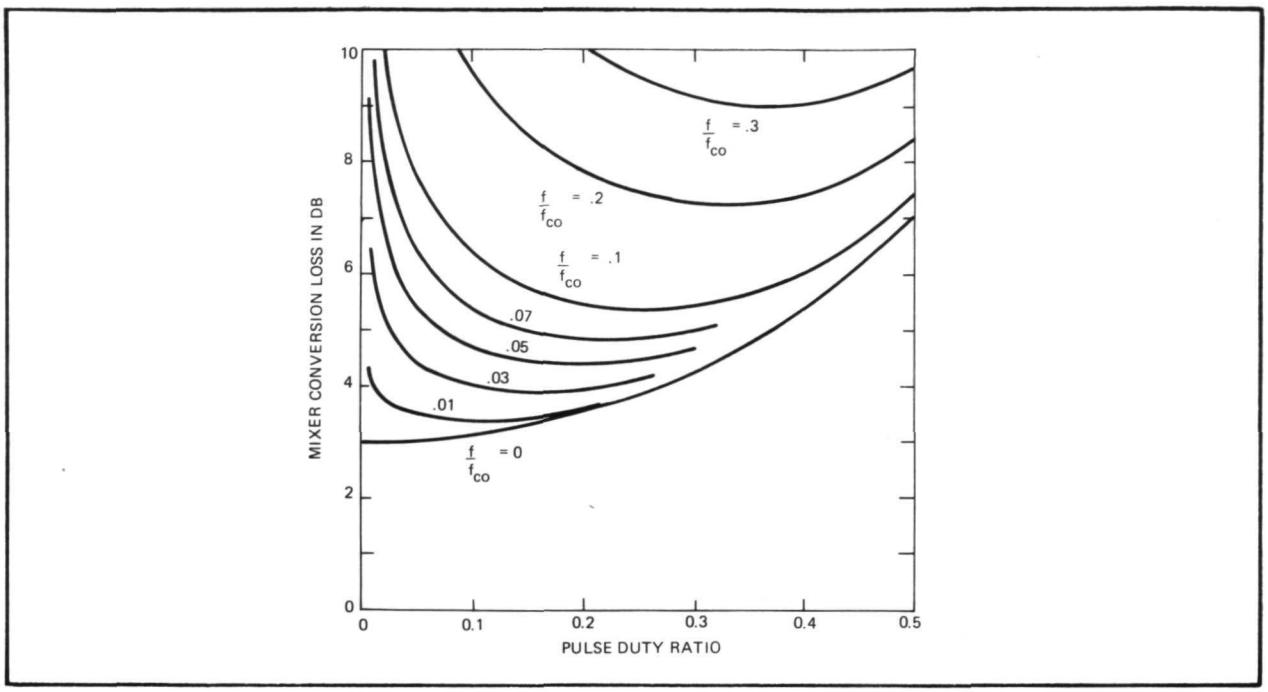

Figure 76. Computed Mixer Conversion Loss for the Broadband Case (Image Termination Equals Signal Termination)

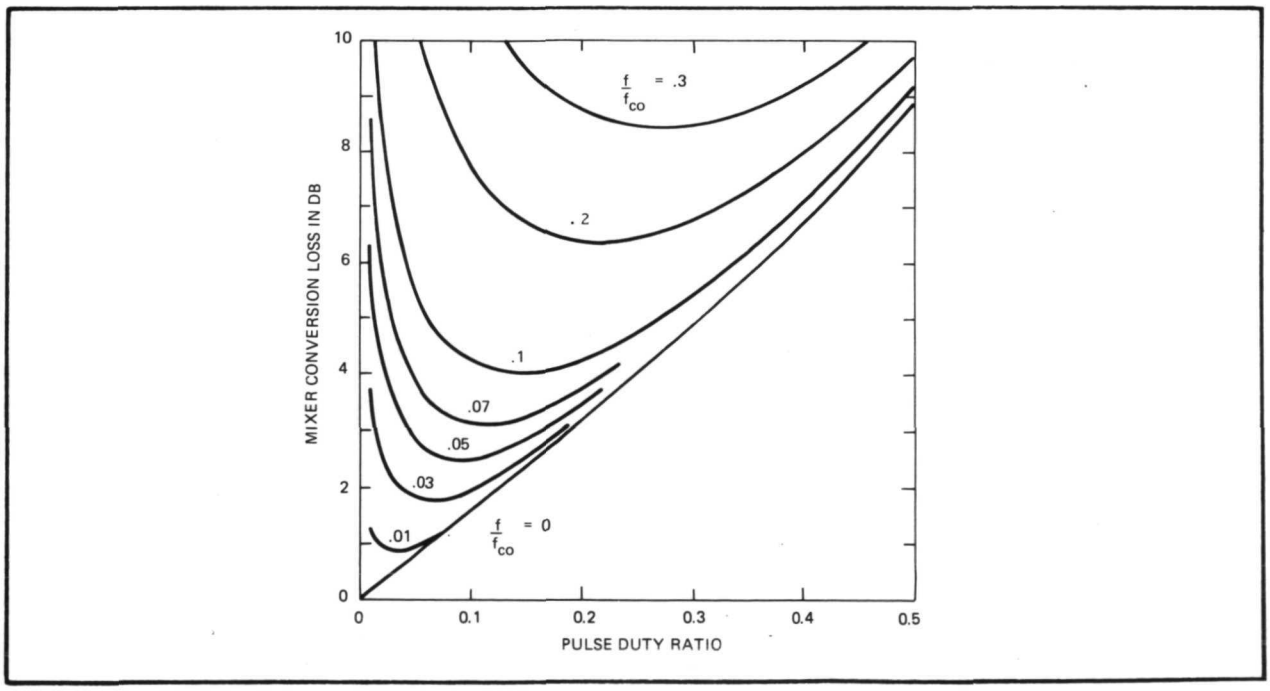

Figure 77. Computed Mixer Conversion Loss for Short Circuited Image

However, at 60 GHz, the results diverge appreciably. With GaAs, $(f/f_{co}) \cong 0.075$; and taking a PDR $\cong 0.2$, the broadband mixer conversion loss is about 4.9 dB which is about as measured. With Si, $(f/f_{co}) \cong 0.24$; and taking PDR $\cong 0.3$ (at which PDR minimum L_c obtains), a conversion loss of 8.0 dB minimum is found. Now a 3.1-dB difference is encountered.

Note that in figures 76 and 77, minima occur in the curves of L_c vs PDR. Figure 78 presents the minimum mixer conversion loss for both the image shorted and image terminated cases as a function of f/f_{co}. Note that with GaAs at 60 GHz there is a possible 1.6 dB improvement in L_c by using image enhancement techniques (i.e., $L_c \rightarrow 3.3$ dB). For the silicon diodes, only an 0.8 dB improvement is possible (i.e., $L_c \rightarrow 7.2$ dB) which does not even get the image enhanced value down to the broadband value for GaAs.

Noise figure of the single-ended mixer was measured at 60 GHz (IF of 1-2 GHz) and for several mixer diodes. The noise figure of the available IF amplifier was higher than desirable, and thus desensitized the measurement somewhat. However, the results of this test confirm the fact that the mixer

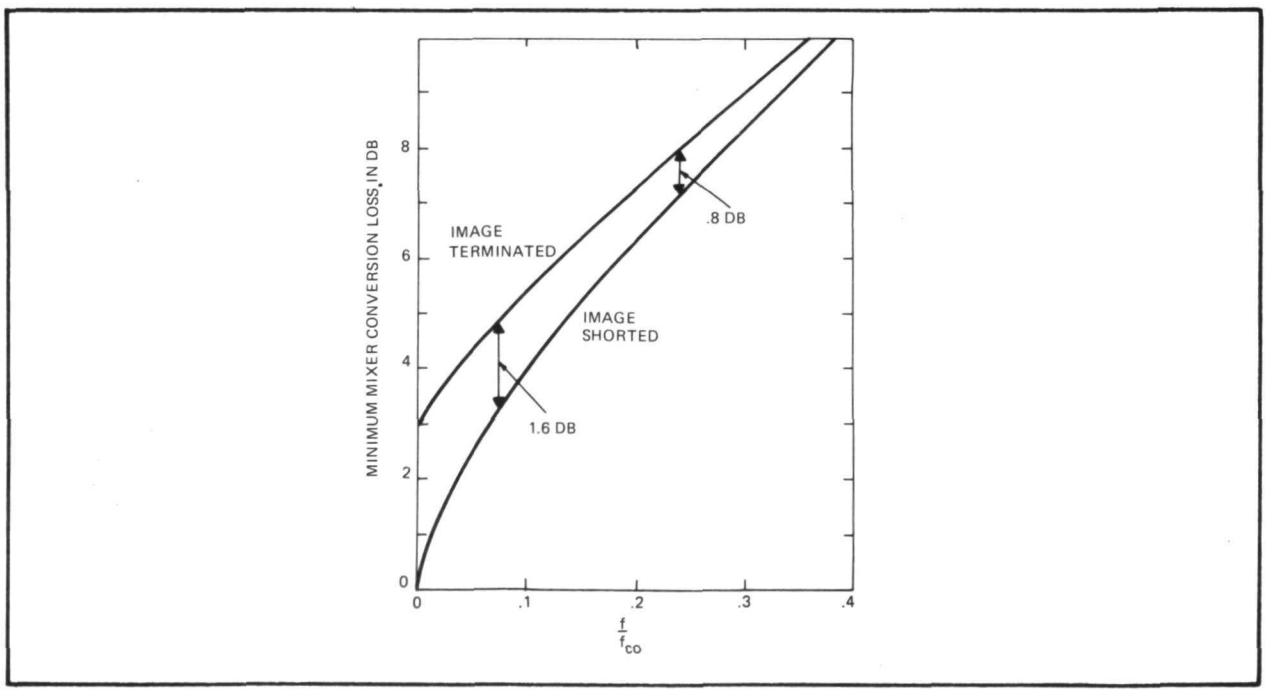

Figure 78. Minimum Mixer Conversion Loss for Both the Image Shorted and Image Terminated Cases as a Function of f/f_{co}

noise figure is essentially that due to the conversion loss, and hence, that the noise ratio of the mixer (t_m) is close to unity.

The broadband (average) noise figure for the IF was F_{IF} = 11.5 dB. The measured 60-GHz mixer single channel noise figure (where mixer noise figure is $F_m = L_c t_m$) for several different diodes is given in table 10.

TABLE 10

SINGLE CHANNEL NOISE FIGURE MEASURED FOR SEVERAL MILLIMETER WAVE GaAs SCHOTTKY BARRIER DIODES

Wafer No.	F_m (dB)
1	4.9
4	6.8
5	5.1
6	4.9
7	4.8

Each diode wafer had been placed into the mount and the bias voltage and LO power adjusted for minimum conversion loss, L_c. Note that the 4.8- to 5.1-dB values agree very well with that value of L_c directly measured (full family of curves for wafer No. 1 was given in figure 75) and analytically determined. The immeasurable difference between F_m and L_c supports the contention that $t_m \cong 1$.

5.2.5 Diode Mount

Figure 79 is a photograph showing the double-diode mounting scheme used to minimize the losses that would normally occur if the signal RF currents and/or LO currents had to flow through some form of RF choke or capacitive RF bypass. In the holder shown, as long as the two diodes are reasonably well matched, there will be no fundamental signal or LO coupled out the pin by which the IF is removed. Because of this RF decoupling, the usual bypass capacitor is not needed and a very wide-band IF match is easily attained. Figure 80 shows more clearly the details of the diode contacts. As was

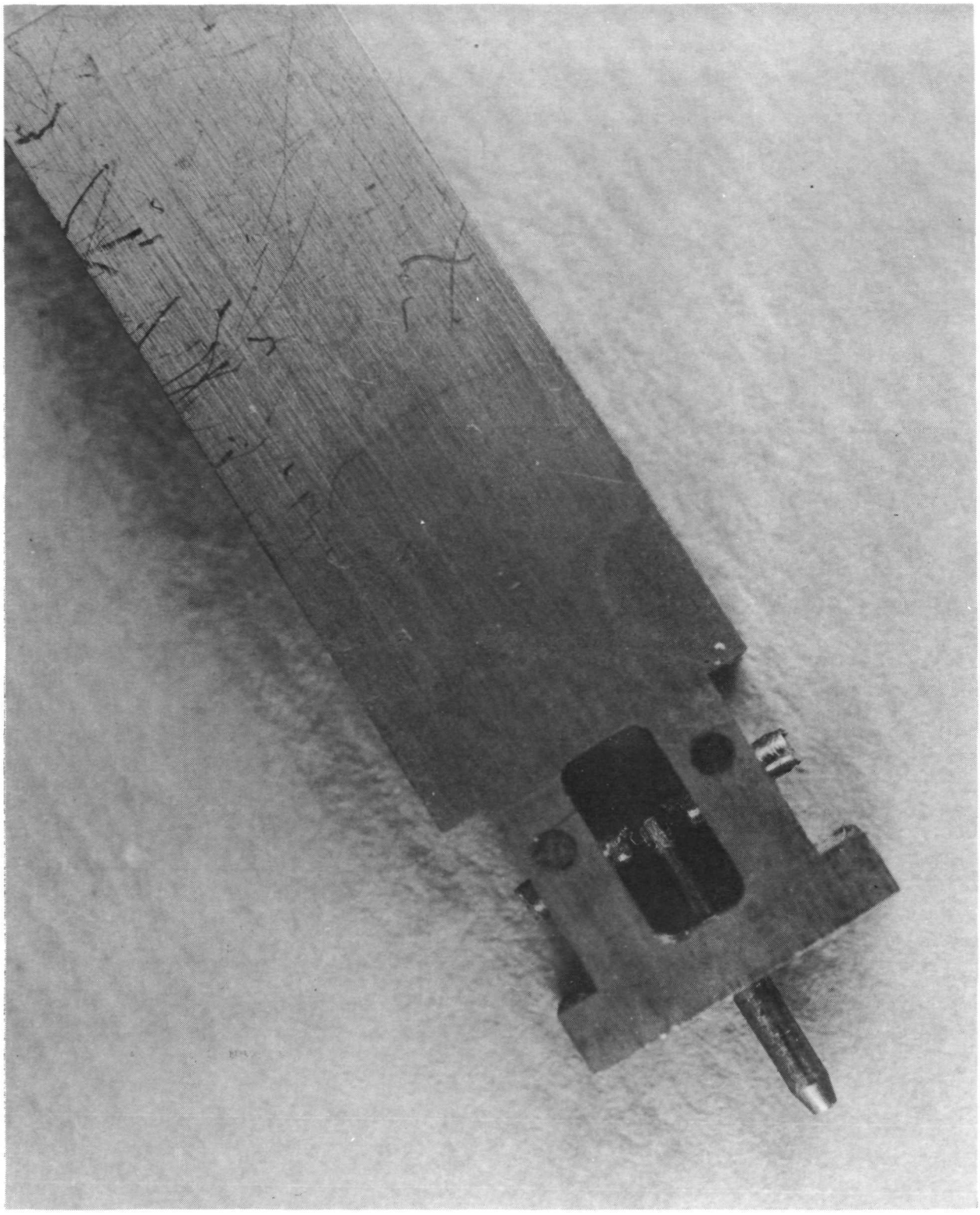

Figure 79. Double-Diode Wafer

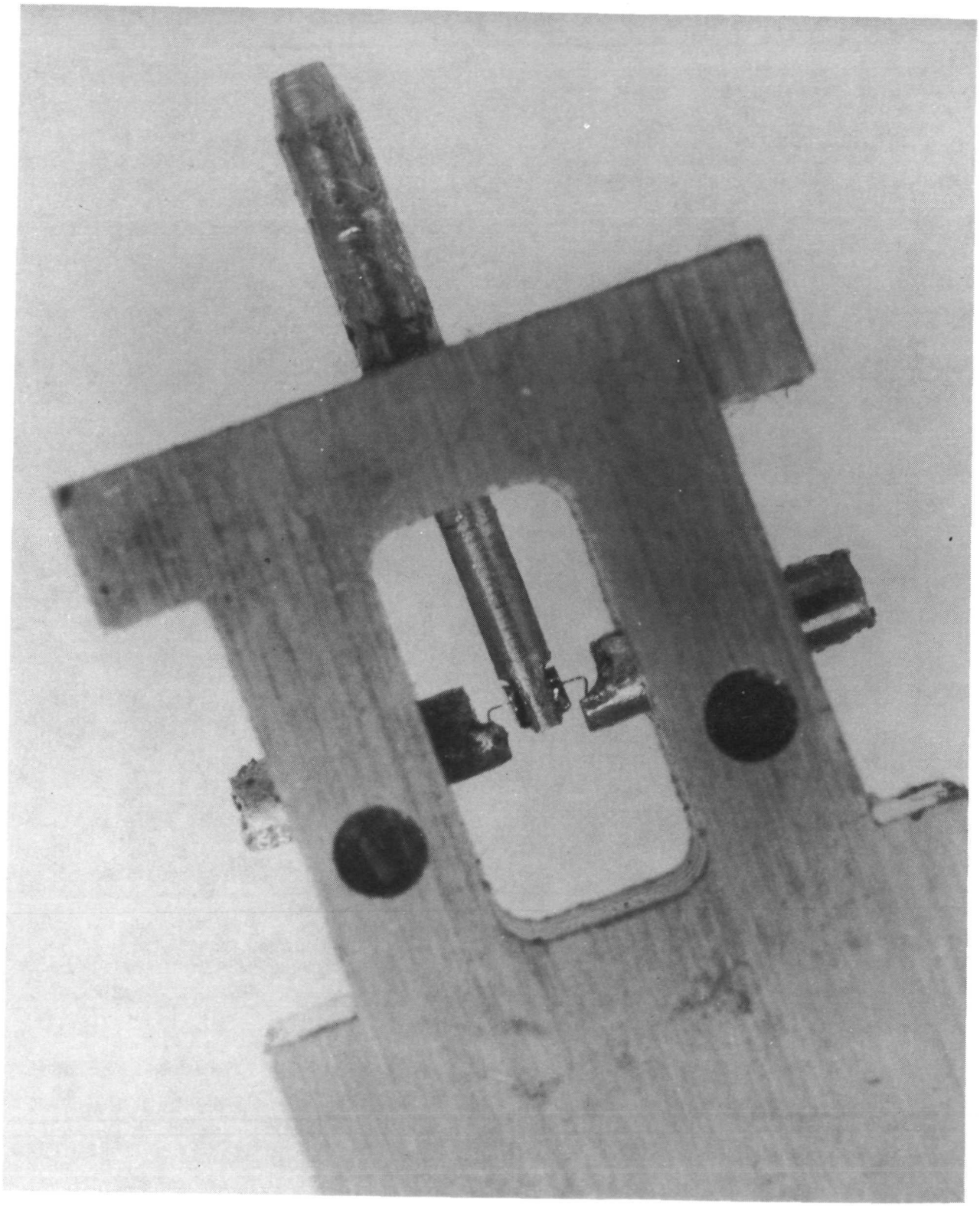

Figure 80. Closeup of Double-Diode Wafer

stated earlier, the junction capacitance at zero bias is about 0.04 pF (per diode). The series resonance of the composite diode at zero bias (as determinted by transmission resonance and f_{co} measurements[26]) falls in the range of 60 to 70 GHz.

The diode holder with which the mixer measurements were made is shown in figure 81. This is an RG-98/U waveguide mount with one of the mixer wafers in place. This mount is similar to the mount used for the avalanche diode oscillator measurements but with the addition of a cavity (on the side opposite to the wafer) which can be used for bias circuitry, IF matching, etc, depending upon the need.

5.2.6 Balanced Mixer Considerations

The diode mount shown in figure 81 is a single-ended mount which requires a separate waveguide coupler for LO power injection. Two such units would be combined by use of a conventional 3-dB waveguide coupler to form a balanced mixer. A good broadband sidewall coupler or 3-dB "Magic T"

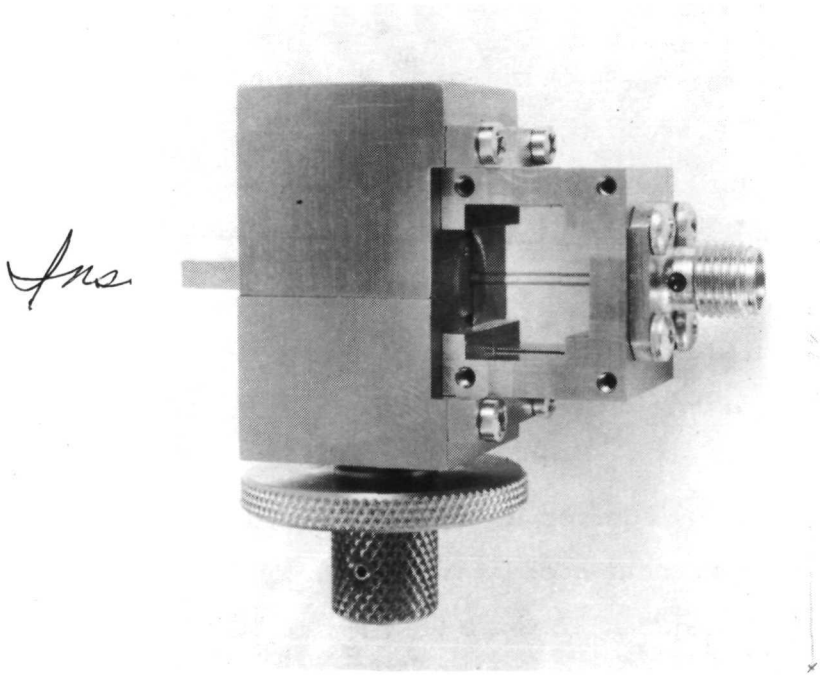

Figure 81. Photograph of RG-98/U Waveguide Wafer Diode Mount

type of coupler could be used without adding more than 0.2 to 0.3 dB additional loss to the above quoted values for L_c. No work has been done on special hybrid structures for this balanced mixer. In particular, the configuration using cross polarized signal and local oscillator ports (orthogonal mode configuration) was not considered because such configuration is not suitable for use with the double-diode mixer wafer as shown in figure 80. The orthogonal mode configuration would require that one of the two diodes shown in figure 80 be reversed, which is not practical.

The LO noise suppression characteristics of a balanced mixer depends almost soley on the degree to which the individual mixer conversion losses can be matched. It can be shown that if the mixers differ by < 1.0 dB in conversion loss, the LO noise power will be suppressed by greater than 23 dB. The increase in the mixer noise ratio Δt is given as $(F/L_c L_s D)$, where F is the LO noise figure and D is the denominator, both from equation 31 in paragraph 5.3.4. L_c is the mixer conversion loss taken to be 5 dB, and L_s is the LO noise suppression factor. Taking the LO frequency to be nominally 60 GHz, $L_s \cong 23$ dB, and $F \cong 23$ dB (see table 11), then for a low IF frequency ($\Delta f \cong 100$ MHz, $Q_{ex} \cong 600$ and S = 2 in equation 31) the increase in t is $\Delta t \cong 0.16$. If a klystron had been used ($F \cong 44$ dB) with the same Q_{ex}, the increase in mixer noise ratio would be $\Delta t \cong 2.0$.

5.3 SOLID-STATE LOCAL OSCILLATOR

The objective of this task was the development of the critical millimeter wave semiconductor diodes and the necessary mounting structures required to yield an overall reliable, low-noise, local oscillator (LO) for the 60 GHz radiometric receiver.

Under this task, it was required to investigate alternate approaches to the efficient generation of local oscillator power. To this end, there was investigated both direct generation via a 60-GHz avalanche diode oscillator (ADO) and indirect generation via an ADO at 30 GHz followed by a varactor harmonic generator, a doubler to 60 GHz. The two approaches were started at the same time.

The 30-GHz oscillator was fabricated in waveguide and stabilized with a resonant cavity. This oscillator produced over 120 mW at 30 GHz using a single silicon diode purchased from Sylvania. Figure 82 is a photograph of the K_a-band (30 GHz) oscillator developed for the indirect source. Therein is shown not only the diode mount and bias bypassing arrangement but also the stabilizing cavity (TE_{011} mode resonance) used for reduction of FM and for temperature compensation of the complete locked oscillator.

However, as good results were being obtained by direct generation, further work on the indirect approach was curtailed and no work at all was done toward the development of a 30- to 60-GHz doubler.

5.3.1 Silicon Avalanche Diode Oscillators (ADO)

Avalanche diodes have by now become well known sources of microwave power. The CW power available is sufficient for receivers and some lower power transmitter applications throughout the microwave frequency range. The power is substantially more than can be obtained from CW Gunn devices but at the expense of somewhat higher noise and higher operating voltages. IMPATT diodes are at present the most powerful CW solid-state sources of high-frequency microwave power: up to 1 watt at 50 GHz has been realized and almost 200 mW at 100 GHz.[27] The IMPATT has covered the complete microwave frequency spectrum from 300 MHz to 300 GHz. The diodes have been fabricated from germanium, silicon, and gallium arsenide and can probably be constructed from other semiconductors should the need arise. The IMPATT diodes offer potentially inexpensive, reliable, compact, and moderately efficient microwave sources.

The name IMPATT is an acronym to recall the major mechanisms of operation first proposed by Read[28]: IMPact Avalanche and Transit Time. Ordinarily the IMPATT mode operates with best efficiency near the transit-time frequency, and the best efficiency of dc to RF power conversion that has been reported to date has been obtained with GaAs and is 19 percent.[29] It has been shown[30] that the theoretical efficiency for silicon is

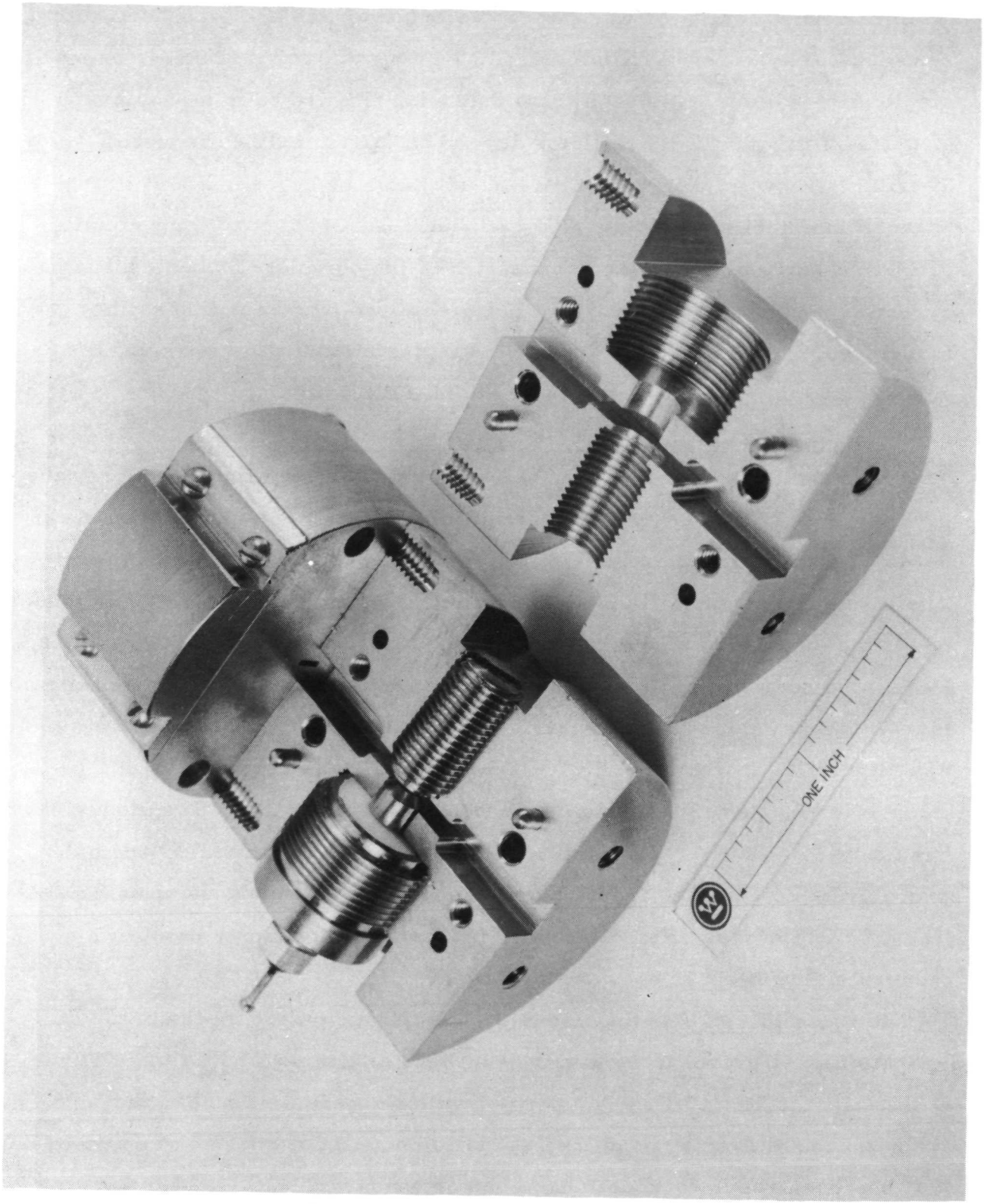

Figure 82. 30-GHz ADO Mount

of the order of 18 percent, and for GaAs the theoretical efficiency is of the order of 27 percent.

Currently in progress at Westinghouse are both internally funded and contract programs for the development of the avalanche diode as an oscillator and/or amplifier element. Various forms of the avalanche diode, both packaged and unpackaged are being analyzed and evaluated for use in waveguide circuits as microwave and millimeter wave oscillators and amplifiers.

Under the present contract there exists a requirement for a 60-GHz local oscillator source. Silicon IMPATTS have been developed by Westinghouse for this task. The design goal for this task has been to provide sufficient 60-GHz power to operate the low conversion loss mixers also developed. The goals for this program have been realized[18] in that over 20 mW was attained at 61 GHz and 66 mW at 51 GHz.

5.3.2 Diode Design

Because the Si IMPATT is capable of an efficiency in excess of 15 percent, and because the Si IMPATT technology is fairly well in hand, it is the natural choice for this application. An output power of about 0.1 W is certainly within the capability of the Si device. The form of the semiconductor element will be identical to the Si unit which has already been developed and used at Westinghouse. Figures 83 and 84 show a very clear picture of the Westinghouse developed Si avalanche diode. The diode dimensions are 40 μm in diameter by 20 μm high. The pictures were taken with the Westinghouse scanning electron microscope and show the extreme precision with which the Westinghouse chemical milling techniques can be used in the processing of critical semiconductor elements.

Based upon the above discussion, the diode will be an Si IMPATT and will be designed so as to maximize the output power and efficiency. The epitaxial layer thickness will be so controlled that at breakdown there is essentially no unswept epitaxial layer left; that is, the depletion layer width at breakdown

Insert fig

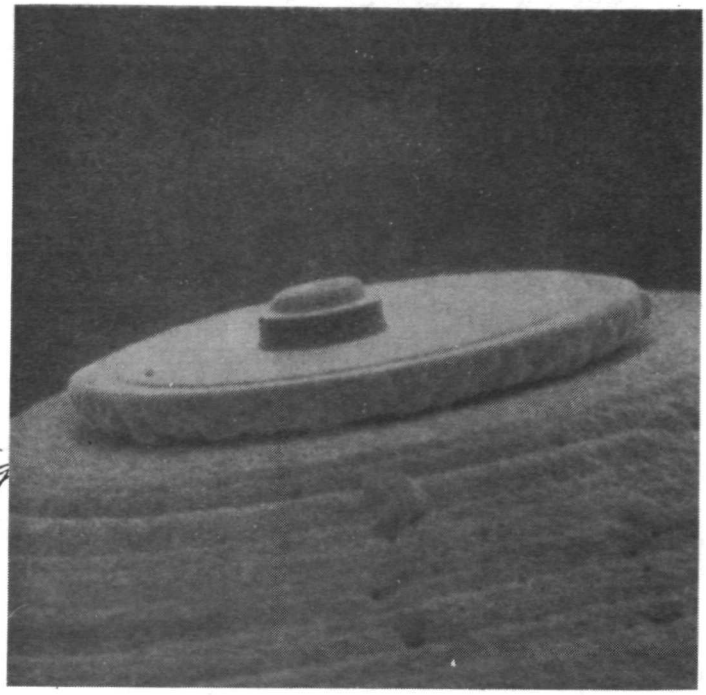

Figure 83. Westinghouse Developed Silicon ADO: Silicon Disc
Dimension: 40 μm Diameter by 20 μm High
(Scanning Electron Microscope Photograph)

Insert fi

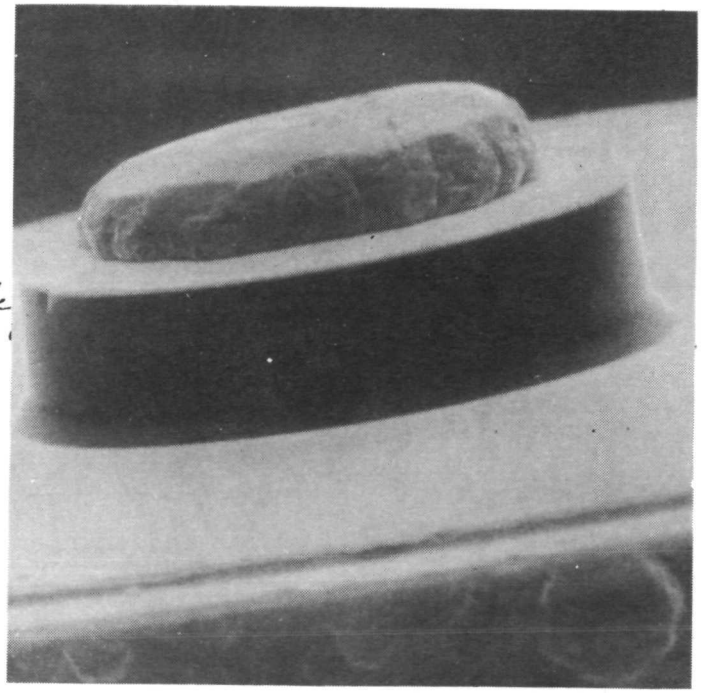

Figure 84. Westinghouse Developed Diode Closeup View

is very close to that determined by reference to figures 85 and 86. For high-frequency operation, even the n+ substrate should be thinned down to reduce losses and nonuniformity due to skin effect.

Now the specific parameters of the diode junction can be specified. By reference to figure 85, the breakdown voltage for a 60-GHz optimum transit-time frequency (for Si) is determined to be about 19 volts. Figure 85 also shows that this breakdown is associated with an abrupt junction having a background doping of about 5.0×10^{16} carriers per cm^3, and figure 86 gives a depletion layer width at breakdown of about 0.6 to 0.7 μm.

The diode operating point is determined as follows. Scharfetter[31] has shown that the maximum current density for efficient operation of an IMPATT diode is that value which requires an attendant field variation in the drift region exceeding the critical value for impact ionization. Information on degradation of efficiencies with operating current density indicates that efficient operation decreases at a current density of approximately 20,000 A/cm^2 at a frequency of 50 GHz and then, for any frequency, the current density, J_c, scales according to the following equation (curve presented in figure 86).

$$(J_c/20,000) = (f/50\ \text{GHz})^{1.18} \tag{22}$$

Thus at 60 GHz, to maintain high efficiency, the current density must be below 25 kA/cm^2. However, if η_e is the electronic conversion efficiency representing the conversion of dc power to available RF power but not considering the losses in the series resistances, the actual, realizable efficiency is given as

$$\eta_a = \left(1 - \frac{Q}{Q_v}\right) \eta_e \tag{23}$$

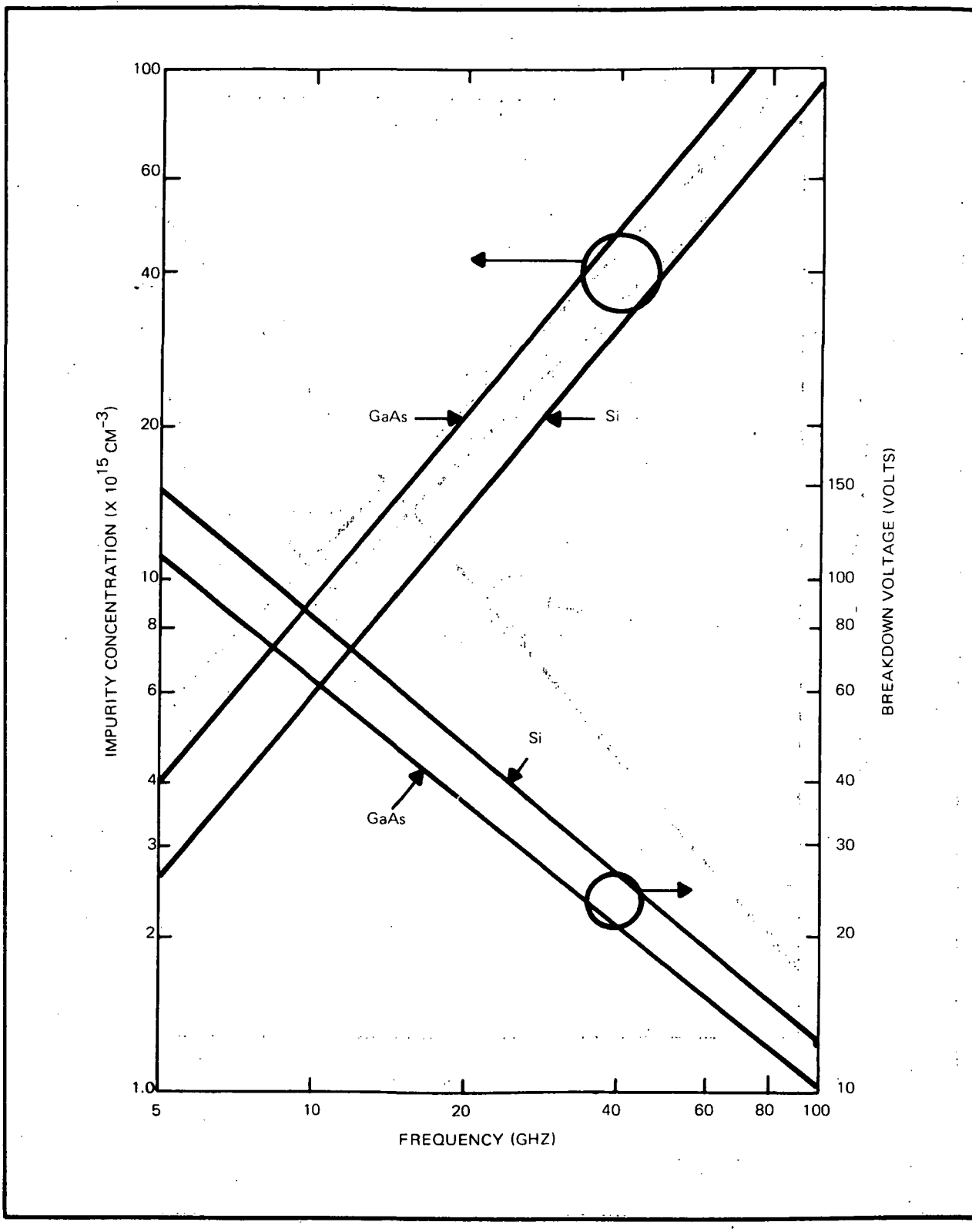

Figure 85. Calculated Breakdown Voltage and Impurity Concentration vs Frequency for Abrupt Junctions in Si and GaAs

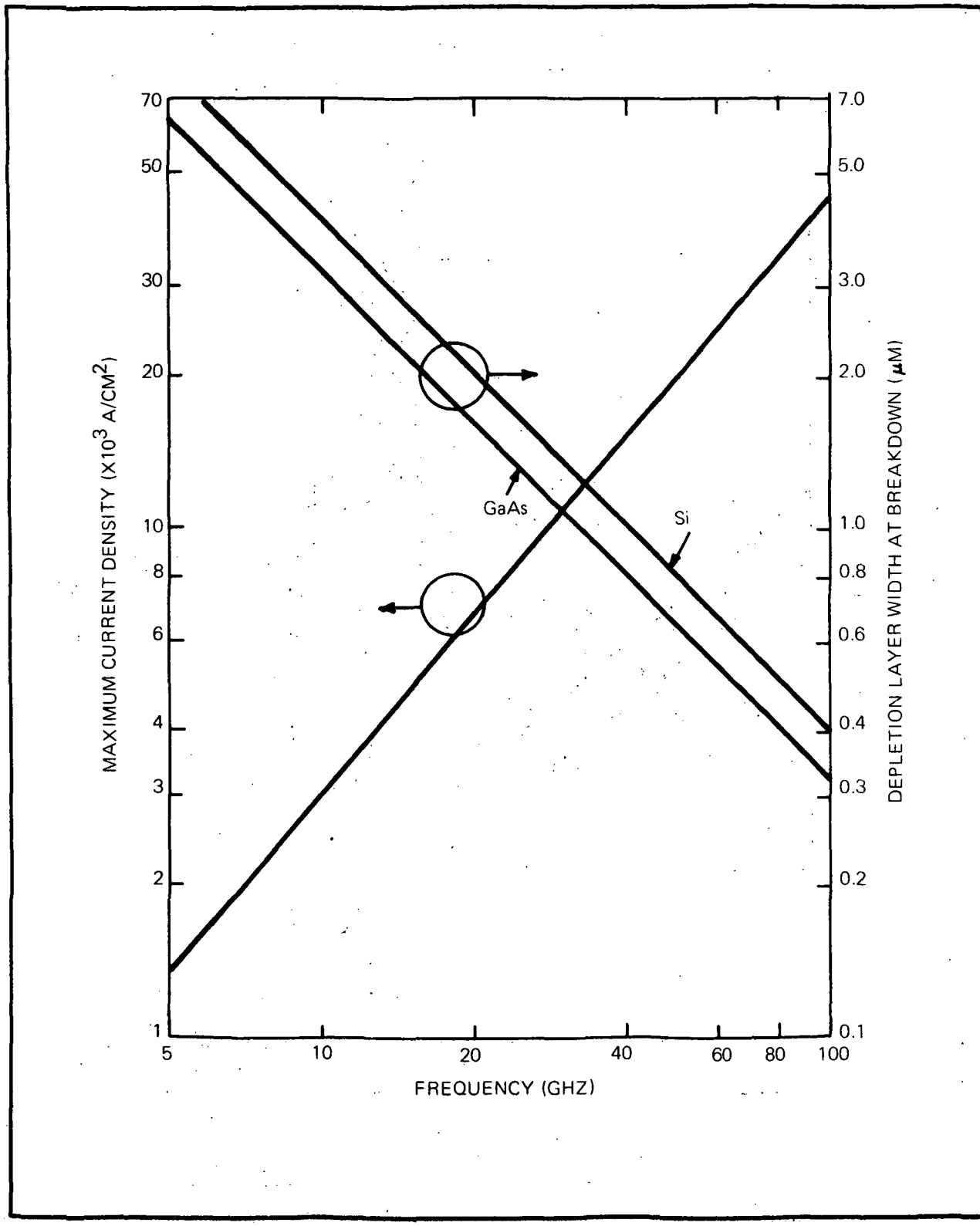

Figure 86. Calculated Maximum Current Density and Depletion Layer Width vs Frequency for Abrupt Junctions in Si and GaAs

where Q- is the magnitude of the junction negative Q and Q_v is the usually defined varactor Q which defines the magnitude of the series loss resistance. Thus,

$$Q- = \omega \, |-R| \, C_d \tag{24}$$

$$Q_v = (\omega R_s C_d)^{-1} \tag{25}$$

where $\omega = 2\pi f_o$ and f_o is the operating frequency, R_s is the series loss resistance, C_d is the capacitance of the depletion region at breakdown, and $|-R|$ is the negative resistance of the junction and exists in shunt with C_d. The value $|-R|$ is given to a good approximation as

$$|-R| = \frac{V_o}{2I_o} \quad \text{(max power out)} \tag{26}$$

where V_o and I_o are the operating dc bias voltage and current, respectively. Given in equation 26, $|-R|$ is that value existing under the condition of maximum output power. Now the junction capacitance per unit area is given as

$$C_j = \frac{1.1}{W} \quad (\text{pF/cm}^2) \tag{27}$$

where W is the width of the depletion region. Then using equation 27 in 24, the junction negative Q is obtained.

$$Q- = \frac{1.1 \, \pi f_o V_o}{W \, J_c} \times 10^{-12} \tag{28}$$

Note that Q- is an inverse function of the current density J_c. If equation 22 gives an upper bound to J_c then equation 28 shows Q- has a lower bound. But the expression for efficiency, equation 23, would indicate that efficiency is maximum when Q- is lowest.

Let the available RF power be 300 mW (an absolute maximum) and take the lower bound on efficiency to be 10 percent. Thus, the maximum dc power into the diode will be 3.0 watts; this gives $I_o = 0.160$ A. Use of $J_c = 25,000$ A/cm^2 in equation 28 shows that $Q- > 2.20$. To have some room for J_c

to vary, back off on J_c (let $J_c \rightarrow 11$ kA/cm^2) so that Q- = 5 is assumed. Now with Q- = 5, $I_o = 0.16$ A, and $V_o \cong 19$ volts, the associated value $|-R| = 60$ ohms, and $C_d = 0.24$ pF. Using equation 27, the junction area is found to be 1.4×10^{-5} cm^2, the actual current density is 11,000 A/cm^2, and the junction diameter is 42 μm (1.7 mils) which is essentially the diode we already have.

Now with the specification of the junction diameter we can determine the thickness of the Si mesa to be used. The thickness is determined by the allowable varactor Q and the required efficiency which are related by equation 23. For an Si substrate resistivity of 0.005 ohm-cm and a diameter of 12 μm, a thickness of nominally 0.5 mil (13 μm) is required to reduce the series resistance to 0.7 ohm (0.1 ohm is taken for contact resistance at the top and bottom) and allow a varactor Q of 16. Now consider the relative effect of the Q- and Q_v. If $\eta_e = 16$ percent, then by equation 23, and using Q- = 5 and $Q_v = 16$, $\eta_a > 10$ percent as required.

The junctions will actually be grown right on their own heat sink just as is done with the prior Si devices and as shown in figures 83 and 84. The large pad on which the Si is sitting is a gold pad for the heat removal. The flat pad on the top surface of the semiconductor and well illustrated in figure 84 is a package contact surface.

The thermal impedance of the junctions is essentially the series combination of the circular cylinder of Si at a conductivity of $\sigma_s = 1.5$ (W/cm-°C) and the thermal spreading resistance into the gold heat sink with conductivity of $\sigma_m = 2.96$. The expression for the thermal resistance is

$$R_{TH} = \frac{1}{4\sigma_m r} + \frac{W}{2\pi r^2 \sigma_s} \qquad (29)$$

Using the numbers already derived yields the values or $R_{TH} \cong 41.5°C/W$; as the dc input power is to be 3 watts, then a temperature rise, ΔT, at the junction of $\Delta T = 125°C$ would be expected. This is well within the $\cong 250°C$ rise that could be tolerated. The properties of the diode are tabulated below.

Epi thickness	0.65 μm
Epi doping	5.0×10^{16}
Breakdown voltage	19 volts
Capacitance at breakdown	0.240 pF
Junction area	14×10^{-6} cm^2
Thermal impedance	41.5°C/W
Expected temperature rise	125°C
Power dissipated	3.0 Wdc

The above discussion details the design of the Si IMPATT and in particular shows the importance of the effect of varactor Q. Note that if the thickness of the Si material were allowed to equal the diameter which was 40 μm (as was true of most of the earlier work) then the varactor Q goes to $Q_v \cong 5.5$ at 60 GHz. Assuming about the same Q- $\cong 5$, then the predicted efficiency would be about 3 percent before accounting for circuit losses. The wafer mount used was extremely versatile in that a very large range of diode impedance could be accommodated during development, but this same structure was not as low loss a structure as that designed to satisfy full environmental requirements. The losses due to impedance matching structure and tuning screws was estimated to be 3 dB. Hence an efficiency of 1.5 percent could be expected which was about what was measured. The 60-GHz ADO development program was discontinued before the newer diodes (as shown in figures 83 and 84) could be fully evaluated in the improved mount design. However, the technology now is refined to the point of good reproducibility of diodes with the required properties. The analysis has been completed to the point of allowing full understanding of the behavior and limitations of the IMPATT and the circuits in which the IMPATT must be embedded to allow realization of the full potential of the IMPATT.

5.3.3 Oscillator Design to Meet Environmental Requirements

The design approach taken for the ADO is shown in figure 87. It consists of a low loaded Q radial line cavity in which is mounted the avalanche diode by means of a specially designed hermetically sealed package. The package consists of an OFHC copper threaded stud for heat sinking purposes and on which is affixed a quartz ring[32] which surrounds the semiconductor element. The top plate seals the package. The complete package is actually a critical part of the resonant and impedance matching structure. For the basic structure, a low loaded Q circuit is used to reduce losses in coupling the RF power out and to make the final oscillator frequency relatively independent of this circuit; a stabilizer cavity which is yet to be added will primarily control frequency.

Figure 88 shows the resonator cavity dimension required for various diode capacitances and frequencies from 50 to 75 GHz. This assumes a quartz package height of 0.38 mm and an OD of 1.52 mm. Two quartz rods are shown in the details of the oscillator cavity. The one adjusts the coupling into the cavity, the other adjusts the center frequency of resonance.

The diode junction selected will have a junction capacitance at breakdown of about 0.2 pF and will have a diameter of 42 μm. This junction, imbedded within the quartz package, will require a radius of just under 2.5 mm for resonance at 60 GHz. The oscillator performance data of figure 89 was computed for this combination. The coupling factor, Q_c refers to a design parameter from which is determined the width of the coupling iris into the cavity and the degree of adjustment available by use of the quartz rod coupling adjustment. Q_d is the ratio of diode susceptance to load resistance and shows a 6:1 load control for the indicated range of Q_c. Significant is the low value of Q_d which can be equated to the "negative Q" of the ADO and which must be low for good efficiency. Q_L is the loaded Q of the circuit (also external Q), and shows values 25 to 150 for the indicated range of Q_c. Also shown is the shift in frequency encountered by variation

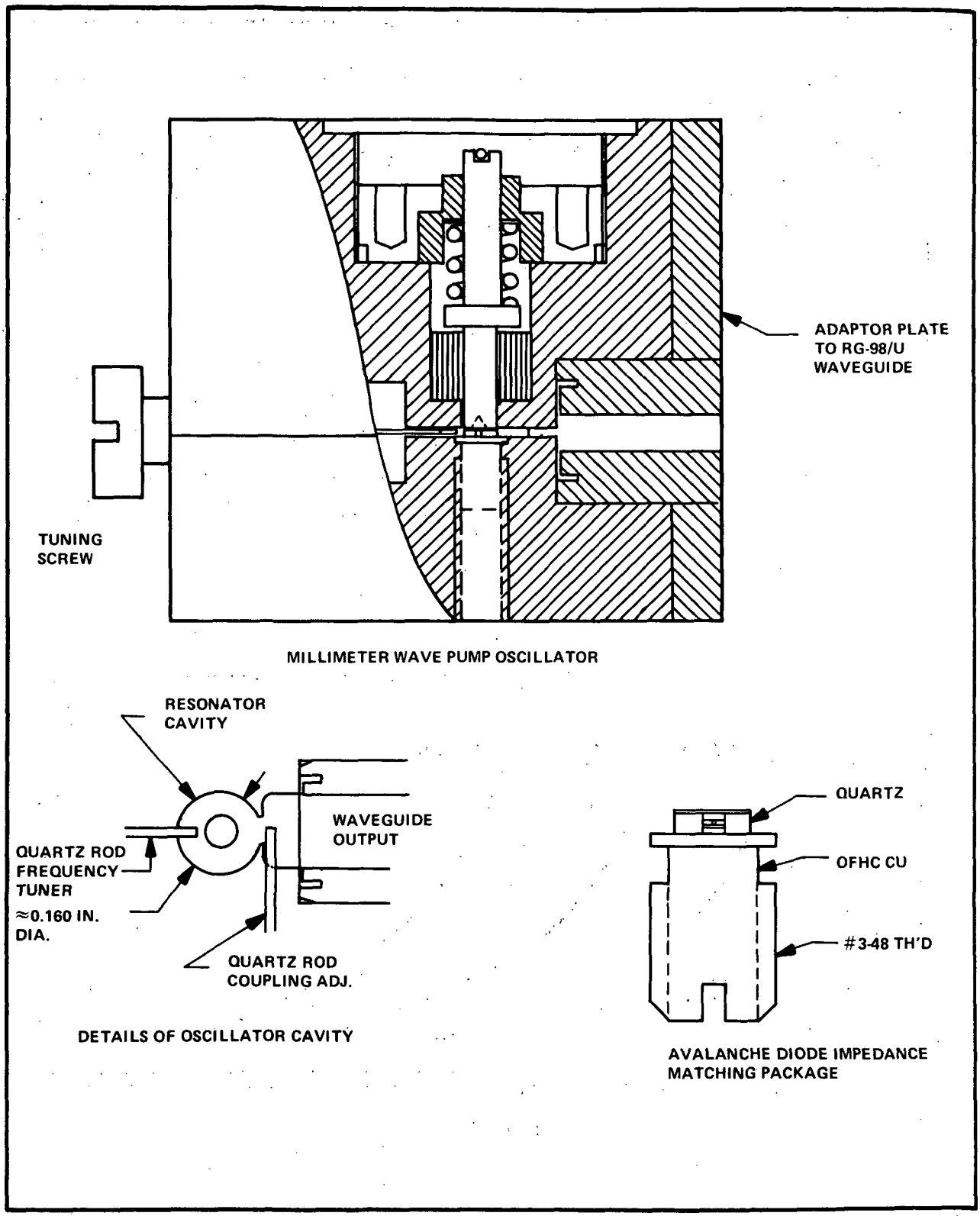

Figure 87. ADO Local Oscillator Power Source

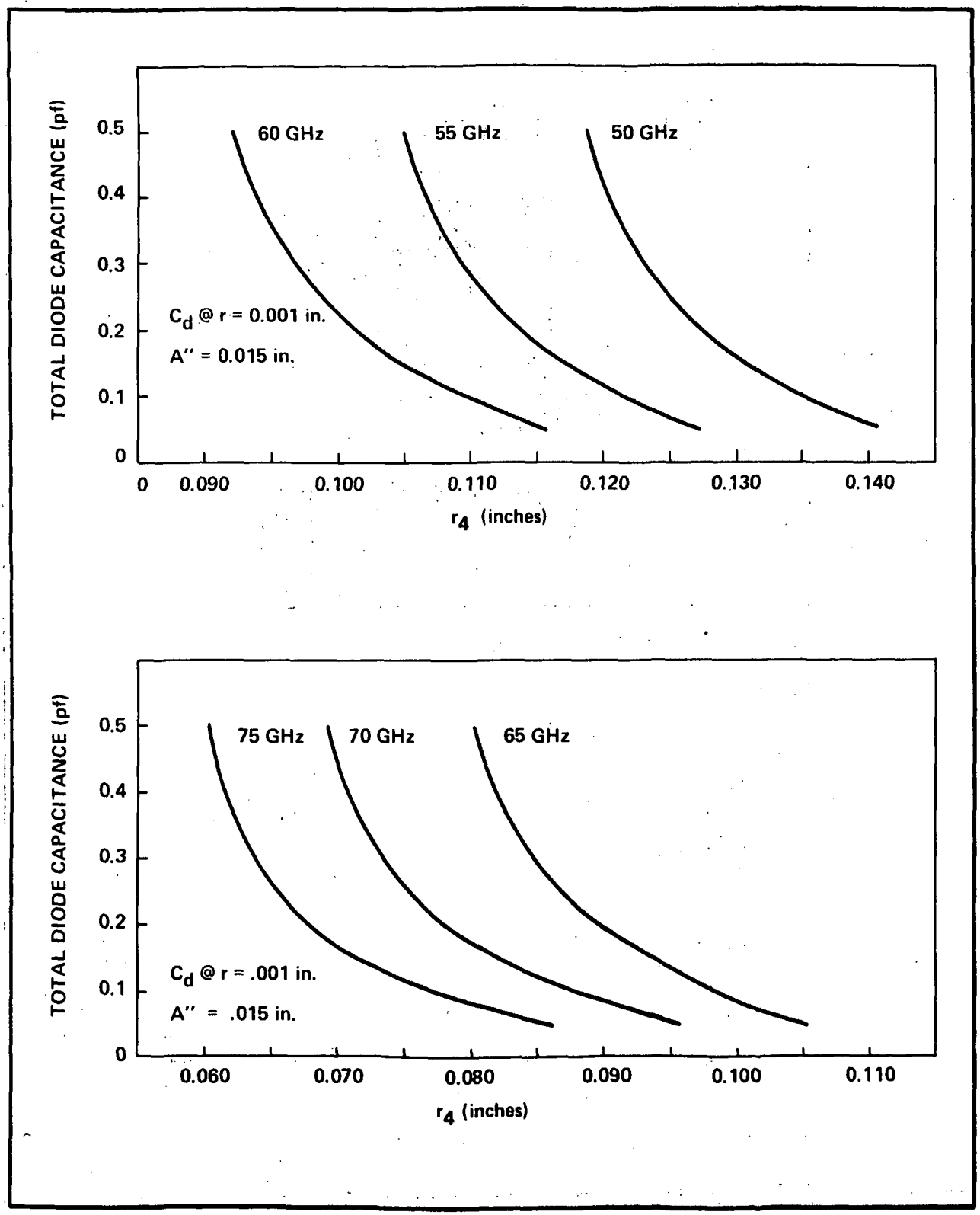

Figure 88. Millimeter Wave Oscillator Cavity Dimension

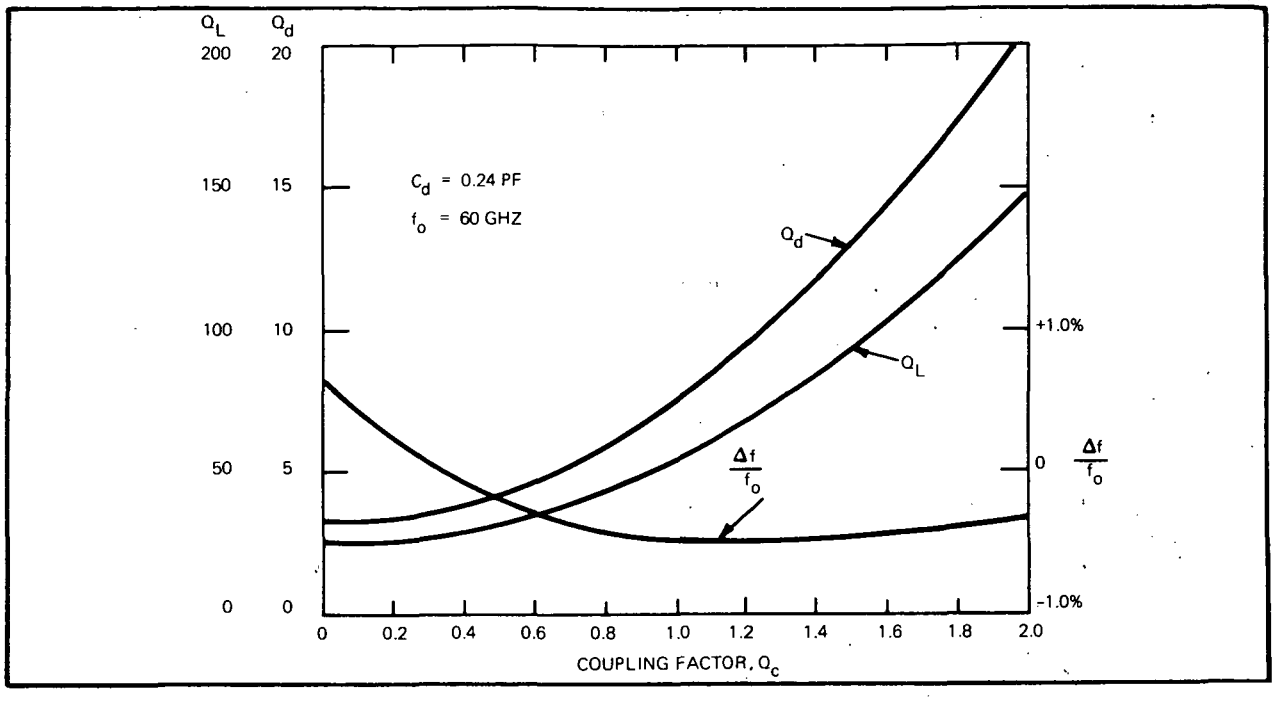

Figure 89. Oscillator Performance Data

of load coupling. For a load variation of 5:1, the frequency changes by less than 1 percent. Also computed for this cavity arrangement were the next nearest resonances which sometimes can give trouble. The next resonances were about 18 GHz and 90 GHz; both of which are sufficiently removed as to cause no difficulty.

The avalanche diode oscillator of figure 87 is free running in a low-Q specially designed cavity. The device will be stabilized by use of a high-Q cavity and interconnecting transmission line (waveguide). The high-Q cavity is a right circular cylinder operating in a TE_{011} mode. The TE_{011} family has the highest values of Q per unit volume of any of the cavity configurations possible. They are easy to construct, and the agreement between experiments and calculations of dimensions, tuning rate, and Q is very good. Also, this type of cavity has been temperature-compensated quite readily. An unloaded

$Q_u \geq 10K$ is attainable and with the coupling adjusted to yield a loaded $Q \cong 1K$ the losses are on the order of 1.5 dB.

The ADO stabilized by such a high-Q cavity will have a frequency stability at least comparable to that of a reflex klystron which is similarly stabilized by a high-Q external cavity; i.e., a long-term stability of approximately one part in 10^5. The LO frequency excursions will therefore be less than 1 MHz. Such an excursion will cause negligible system gain fluctuation.

5.3.4 Local Oscillator Noise

Whether one considers a Gunn oscillator (GO), avalanche diode oscillator (ADO), or klystron, the two major sources of noise are the same; namely, direct RF (shot) noise and modulation (up-converted) noise. The RF (shot) noise will propagate directly to the load; whereas, the low-frequency noise entering via the bias circuit modulates the oscillator through the circuit dependence of the real and imaginary part of the diode impedance. As a result of the nonlinear mixing process, the low-frequency noise components are up-converted into the microwave frequency range and are indistinguishable from the RF noise. However, the modulation noise contribution for small deviations from the carrier can be made negligible by proper biasing of the oscillator.[33] The free running oscillator noise can then be taken, to a good approximation, to be pure shot noise due to carriers traversing the junction and some thermal noise due to a finite series resistance, R_s.

The theoretical treatment of noise in oscillators has been quite thoroughly treated by Edson[34,35], Kurokawa[36], and others. The theoretical expressions for FM and AM noise of an oscillator are given as

$$\text{Noise Power (FM)} = \frac{KTBF}{\left(Q_{ex}\frac{\Delta f}{f_o}\right)^2}, \tag{30}$$

and

$$\text{Noise Power (AM)} = \frac{KTBF}{\left(\frac{S}{2}\right)^2 + \left(Q_{ex}\frac{\Delta f}{f_o}\right)^2}. \tag{31}$$

In these equations, (KTB) is the fundamental thermal noise power. F is the device noise figure (sometimes called the oscillator noise measure) and is the ratio by which the actual noise output power exceeds KTB. Q_{ex} is the external (or loaded) Q of the oscillator circuit; Δf is distance from the carrier center frequency, f_o. The parameter S is determined from the functional relationship between the negative conductance and the RF voltage of the oscillator and can be taken to be S = 2 for most purposes.

Now if one consideres the active junction to be supplying full shot noise due to the dc current I_o, and thermal noise due to the spreading resistance, R_s; then

$$F - 1 = \frac{G_{eq} / |G_d|}{\left(1 - \frac{Q-}{Q_v}\right)}, \tag{32}$$

where

$$G_{eq} = \frac{q I_o}{2 KT} \tag{33}$$

Q- and Q_v were defined by equations 24 and 25, and $|G_d|$ is just the reciprocal of $|-R|$ as given by equation 26. We can assume a generally appropriate form for conductance variation with RF voltage:[36, 37, 38, 39]

$$G_d = G_{do} \left(1 - \frac{V^2}{V_m^2}\right) \tag{34}$$

It can be shown that for maximum output power, $(V/V_m)^2 = 0.5$ and $G_{do} = 2G_d$ at the desired operating point. (Note: Use of equation 34 leads directly to S = 2 as stated previously.) Now using equations 26, 32, 33, and 34 one can write

$$F - 1 \cong \frac{5 V_o}{1 - \left(\frac{V}{V_m}\right)^2 - \left|\frac{Q-}{Q_v}\right|_o}, \tag{35}$$

where the zero subscript means Q- is determined for V = 0 (small signal) case). In an earlier section, the importance of the ratio $(Q-/Q_v)$ was pointed out. Examination of equation 35 shows even more why Q_v must be as high as possible. At maximum output power $(V/V_m)^2 = 0.5$. Then if $Q- \Big|_o = 2.5$ and $Q_v = 16$, the value for F would be about 1.5 dB greater than that which would have held for $Q_v \to \infty$. Taking the earlier value for $Q_v \cong 5.5$, one would obtain a 13 dB increase in noise figure. Note also that if one attempts to more "lightly" load the oscillator in an attempt to improve Q_{ex} and thus stability, the ratio (V/V_m) increases toward unity and the output power drops rapidly, and the noise figure increases very rapidly.

Now with reasonable effort, the $Q-/Q_v$ ratio can be held to small enough values as to allow us now to disregard it. As the object is to get maximum power out of the oscillator, the load will be adjusted for maximum power. For such considerations, the noise figure can be given as

$$F - 1 = 10 V_o . \tag{36}$$

This is a very simple result, but a very important one. The noise power (both FM and AM), as given by equations 30 and 31 and at any frequency separation from the carrier, is a function of only two things - the circuit loaded Q, and the noise figure. The loaded Q is a design parameter; thus, the one figure of merit relating noisiness of all negative resistance devices is the device noise figure, and as shown in equation 36, F is determined directly by the operating voltage. The equations used to derive equation 36 are actually quite general; thus equation 36 can be used to relate F for tunnel diodes, Gunn diodes, IMPATTS, and klystrons.

Table 11 presents the data for the noise figure of several devices, based on operating voltage only and as determined for X-band devices and V-band devices. Note not only the good agreement between tunnel diode, Gunn, IMPATT, and klystron devices but for a given device made from the different materials. The values given in table 11 are for the fully loaded oscillator. If the load is increased to the point where oscillation can no

TABLE 11

CALCULATED NOISE FIGURES FOR SEVERAL NEGATIVE RESISTANCE OSCILLATOR TYPES

	Device	V_o	F (dB)
1.	Tunnel Diode (X-Band)		
	GaSb	.08	2.5
	Ge	.14	3.8
	GaAs	.24	5.3
2.	Gunn (X-Band)	7	18.5
3.	IMPATT (X-Band)		
	Ge	40	26
	GaAs	55	27.4
	Si	85	29.3
4.	Klystron (X-Band)	500-2,000	37-43
5.	Gunn (V-Band)	3.5	15.6
6.	IMPATT - Si (V-Band)	19	22.8
7.	Klystron (V-Band)	2,500	44

longer be sustained, there will be about a 3-dB reduction in F. Now if the load were increased further until a stable value of gain, say 10 dB, is reached, then another 3-dB reduction in F would be had. The GaAs IMPATT operating as a 10-dB amplifier would have a noise figure of about 21.5 dB[40] which is about what has been measured and reported in the literature. The Gunn device operating as a 10-dB amplifier would have a value (X-band) of $F \cong 12.7$ dB which value has also been verified.[41] As a simple oscillator at 30 GHz and fully loaded, the carrier-to-noise ratio for a measurement band of 200 Hz is calculated to be 145 dBc which translates to 139 dBc for C-band which is in good agreement with measured values.[42,43]

The values calculated for the tunnel diodes deviate some from the correct values because the approximations used in deriving equation 36 become rather rough for very small V_o. However, in view of the simplicity of equation 36, the validity of the calculated numbers is remarkable.

The values calculated for the V-band devices show another surprising feature. Again ignoring the effects of Q_v, the noise figures calculated for the semiconductor elements are going down as frequency is increased, while the F for the klystron is increasing with frequency.

Klystrons have traditionally been used for stable millimeter wave sources. The lower noise, more stable units are usually two-cavity klystrons. The external Q of these oscillators is in the range 1,000 to 2,000, and the noise figure is about 44 dB. The noise figure for the ADO is 22.8 dB, and for the V-band Gunn device, $F \cong 16$ dB. The external Q is an important oscillator parameter, but that parameter is under control of the designer. To properly evaluate the three components (klystrons, IMPATTS, Gunns), they must all be evaluated with the same loaded Q. Then the only measure of quality is the noise figure of each and the estimated reliability (MTBF). Clearly, from a noise figure point of view, the semiconductor active device can represent a 15- to 30-dB improvement over the klystron. The IMPATT devices will run cooler (more efficient thus less dc power for given RF power) than the Gunn devices; hence, the IMPATT will have a lifetime edge over the Gunn device and the MTBF of the IMPATT will be clearly superior to that of the klystron. Next, one only has to imbed the active device in the proper microwave structure to attain the Q_{ex} required, and the result is an oscillator which will be superior to the klystron not only from a reliability point of view but from an electrical performance base as well.

5.4 RADIOMETER SWITCH

Although not as critical as the mixer or solid-state local oscillator, an important component required to implement the local vertical sensor experiment is the radiometer switch which alternately connects two opposite limb looking antennas to the common receiver. It is necessary that its insertion loss be low and its isolation be high in order to respectively not degrade the radiometer sensitivity nor have either antenna's apparent temperature contain contributions from the opposite antenna. Its bandwidth

must be large enough to be compatible with double channel operation; i.e., equal to double the IF amplifier upper frequency limit. The switching time must be very short compared to the reciprocal of the switching frequency (which will certainly be no greater than 1 kHz). As in any spacecraft application, size, weight, and drive power should be minimized.

A special consideration, unique to a radiometer application, is that of symmetry. It is necessary that both the insertion loss and the isolation be nearly identical in each state of the switch or else even identical antenna temperatures will result in an apparent difference and hence a system angular error. Small differences in insertion loss can be compensated for by adding loss to the lower loss input port. If the isolation in either state is sufficiently high (>20 dB), then isolation differences become insignificant.

A more severe symmetry requirement, which cannot be so easily disposed of, is that of differential local oscillator power reflections due to differences of the complex reflection coefficient of the switch in its two states. Consider a balanced mixer connected to the common port of the radiometer switch as shown in figure 90a. A small fraction of the local oscillator power leaks out of the signal port of balanced mixer and impinges on the switch. No loss of generality is introduced by considering that all impedances are unity and hence the injected LO power (P_{LO}) is related to the LO voltage (E_{LO}) by:

$$P_{LO} = E_{LO}^{2} \tag{37}$$

Due to hybrid unbalance and imperfect balance between the nominally matched pair of mixers, a finite directivity (D) exists and causes LO voltage of E_{LO}/D to reach the switch where it is modulated by the varying switch reflection coefficient (ρ). Assume the switch reflection coefficients in its two states are:

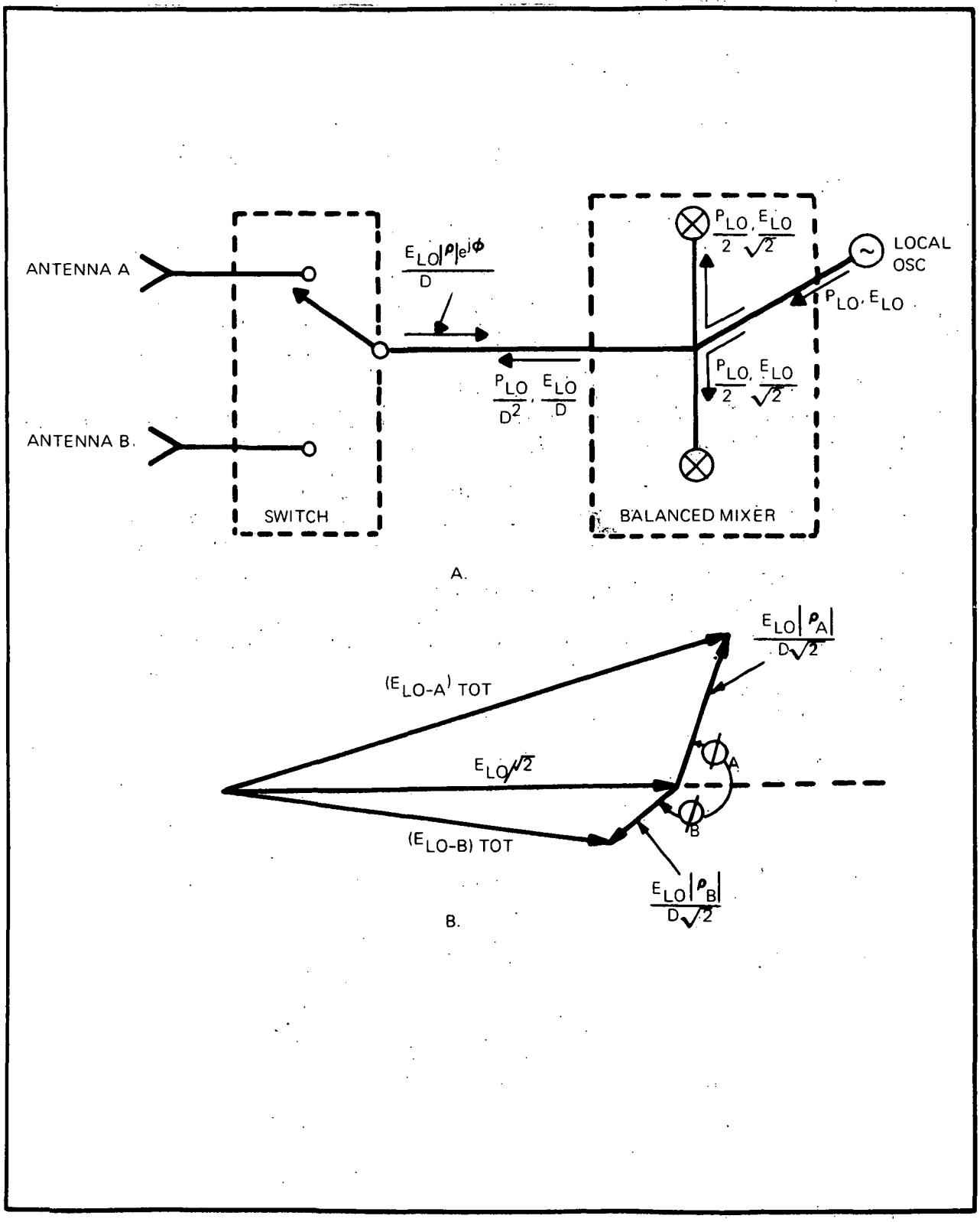

Figure 90. Differential LO Power Reflection from an Assymetric Radiometer Switch and Corresponding Phasor Diagram

$$\rho_A = \left|\rho_A\right| e^{j\phi_A} = \left|\rho_A\right| (\cos \phi_A + j \sin \phi_A), \text{ and} \tag{38}$$

$$\rho_B = \left|\rho_B\right| e^{j\phi_B} = \left|\rho_B\right| (\cos \phi_B + j \sin \phi_B). \tag{39}$$

The voltage reflected off of the switch and incident on each mixer is

$$\frac{E_{LO} \left|\rho\right| e^{j\phi}}{\sqrt{2}\ D} \tag{40}$$

The LO voltage at each mixer due to the direct LO injection is

$$\frac{E_{LO}}{\sqrt{2}} \tag{41}$$

The total LO voltage at each mixer is thus:

$$\frac{E_{LO}}{\sqrt{2}} \left[1 + \frac{\left|\rho\right|}{D} (\cos \phi + j \sin \phi)\right] \tag{42}$$

The phasor diagram of figure 90b illustrates how the total LO voltage at each mixer can vary due to the difference of the switch reflection coefficients.

In order to illustrate the magnitude of this problem, consider a case where the directivity is 20 dB (D = 10) and the reflection coefficients are:

$\rho_a = 0.2$ (VSWR = 1.5:1 and $\phi_a = 0$),

and $\rho_b = 0$.

The total LO voltages across each mixer are thus:

$$(E_{LO\text{-}A})_{TOT} = \frac{E_{LO}}{\sqrt{2}}, \text{ and}$$

$$(E_{LO\text{-}B})_{TOT} = \frac{E_{LO}}{\sqrt{2}} \left[1 + \frac{0.2}{10}\right] = 1.02 \frac{E_{LO}}{\sqrt{2}}$$

$$\therefore (P_{LO\text{-}A})_{TOT} = \frac{E_{LO}^2}{2}, \text{ and}$$

$$(P_{LO\text{-}B})_{TOT} = 1.04 \frac{E_{LO}^2}{2}$$

$$\therefore \Delta P_{LO} = 0.04 \frac{E_{LO}^2}{2}$$

Assume that the LO power at each mixer ($E_{LO}^2/2$) is 3 milliwatts, which is typical for a 5-mm mixer.

$$\therefore \Delta P_{LO} = 0.12 \text{ mW}$$

The noise ratio (NR) of a forward-biased Schottky barrier mixer might typically vary from 1.0 at zero LO power to 1.1 at 3 mW of LO power

$$\therefore \frac{d(NR)}{d(P_{LO})} = \frac{1.1 - 1.0}{3} = 0.033 \text{ per mW}$$

$$\therefore \Delta(NR) = \frac{d(NR)}{d(P_{LO})} \Delta(P_{LO}) = 0.033 \times 0.12 = 0.00396.$$

The temperature difference at the mixer IF output terminals (ΔT_{IF}) due to the above Δ(NR) is

$$\Delta T_{IF} = 290 \text{ K } \Delta(NR) = (290)(0.00396) = 1.15 \text{ K.}$$

The equivalent temperature difference at the antenna is

$$\Delta T_{RF} = (L_{RF})(L_c) \Delta T_{IF}.$$

Since the mixer conversion loss (L_c) is 5 dB and the best radiometer switch insertion loss is 1 dB; thus, (L_{RF}) (L_c) is at least 6 dB = 4.0

$$\therefore \Delta T_{RF} = 4 \Delta T_{IF} = 4.6 \text{ K.}$$

Since this value is larger than the basic radiometer sensitivity and would create a significant angular error, the necessity of minimizing the switch reflection coefficient assymetry is evident.

A number of alternative types of radiometer switches were considered; e.g., mechanical, semiconductor diode, and ferrite. Mechanical switches, though frequently used in nonspace applications or even in space when the switching frequency is low as in a radiometer calibration switch, are not attractive for this application. Diode switches can be disposed of since their excess noise is sufficiently different in their two states as to produce a large apparent temperature difference.

The remaining ferrite switches can be subdivided according to whether they are or are not of the latching type, and their degree of symmetry in both states. Either switchable wye circulators or Faraday rotator types of ferrite switches can be constructed so that they are mechanically inherently symmetrical. The wye circulator type has the additional advantage that it can more readily be fabricated as a latching switch thus avoiding the necessity of providing power to hold the switch in either state.

During the course of this program, a 5-mm, space-qualified, latching ferrite switch which satisfies the LVS requirements became available commercially. It is a three-puck switchable wye circulator of the type shown in figure 91. The inherent symmetry of this structure is evident. The three-puck configuration is required to provide sufficient isolation over the required bandwidth. Its electrical characteristics are listed below:

Insertion Loss	$\leq$	1.2 dB
Isolation	$\geq$	25 dB
Bandwidth	$\geq$	800 MHz (probably 1 GHz)
Switching Time	$<$	3 μsec
Weight	$\leq$	300 g
Volume	$\approx$	50 cm^3
Driver Pulse	$=$	10 V

In view of the availability of this ferrite switch, additional development of a unit for the LVS was not warranted.

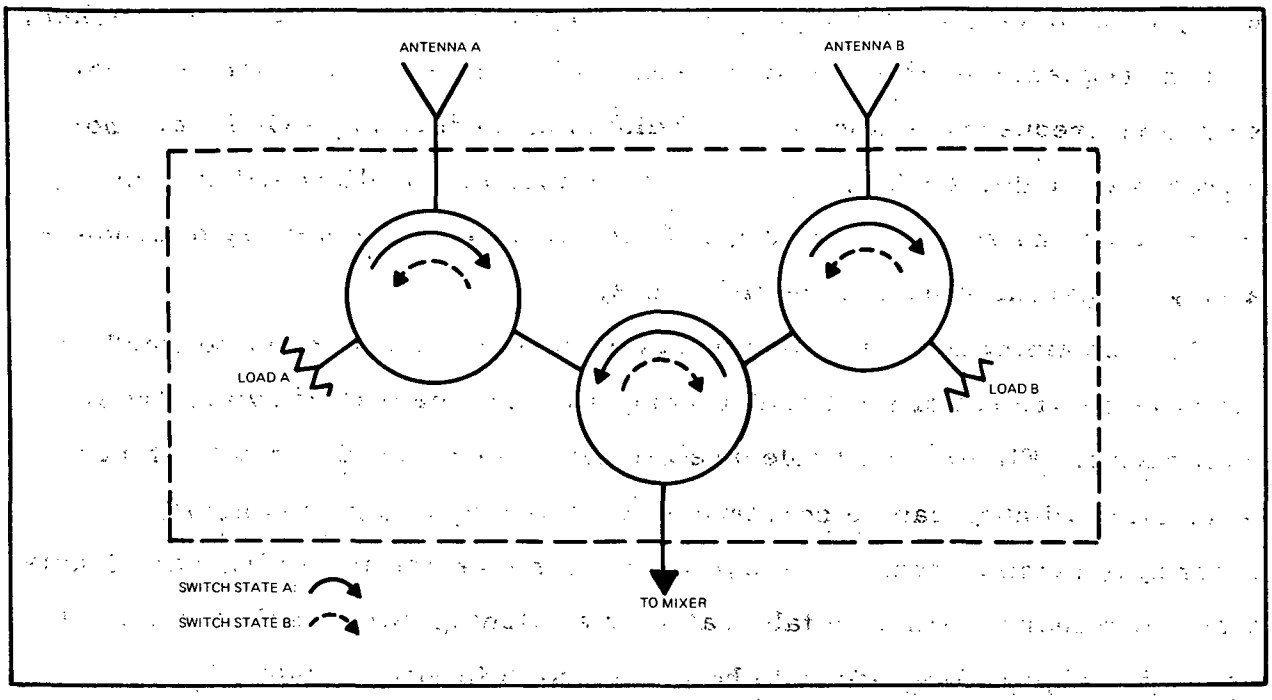

Figure 91. 3-Puck Switching Wye Circulator

6. ENGINEERING MODEL DEVELOPMENT PLANNING

This section discusses the preliminary planning of an engineering model of the 60-GHz radiometric sensor. Actually, two separate experiments will be discussed - a data-collecting experiment and a complete vertical sensor. The two experiments complement each other, and will provide additional data on the atmosphere as well as a test of the local vertical sensor.

6.1 ATMOSPHERIC DATA

A complete local vertical sensor experiment would require a precisely stabilized platform and an independent attitude reference for performance comparison. A simple data-collecting experiment can be designed to measure brightness temperature on a global basis. If a polar orbit is employed data can be obtained for all latitudes, and thus provide complete coverage of the earth. By collecting data over an extended period of time (only a very low data rate is required) it would be possible to note seasonal variations as well as any unusual atmospheric disturbances such as explosive warnings.

The device being considered is a single-beam down-looking Dicke radiometer which would measure brightness temperature along the nadir. The nadir ray is not absorbed at the same altitude as a limb-looking ray of the same frequency; this effect is caused by the different path lengths through the various layers of the atmosphere. For the standard atmosphere, a nadir ray at 60.8 GHz receives roughly 80 percent of its total brightness temperature from a 10-kilometer region centered at 18 kilometers altitude. By contrast, a 60.8-GHz ray with a tangential altitude of 10 kilometers obtains roughly 80 percent of its brightness temperature from a 10-kilometer region centered at 26 kilometers. The small difference in brightness temperature for these two rays can be attributed almost entirely to the different physical

temperature existing in the regions of maximum absorption. If the frequency is changed to 61.09 GHz, however, the nadir ray now receives roughly 80 percent of its brightness temperature from the 10-kilometer region centered at 26 kilometers; hence, its brightness temperature is almost identical to that of the 60.8-GHz limb-looking ray. Further investigation shows that a ray with a tangential altitude of 10 kilometers observed over the frequency range 60.79 to 60.99 GHz will produce essentially the same brightness temperature as a nadir ray using the frequency range of 61.09 to 61.11 GHz. This result may be verified by referring to figure 12 and comparing calculated brightness temperatures for the two altitudes. Hence it may be concluded that a careful choice of frequency to be observed can provide useful atmospheric data from a simple nadir measurement that would be quite difficult, if not impossible, to obtain from a limb-looking measurement because of the angular pointing precision and very small beamwidth required.

6.2 VERTICAL BRIGHTNESS TEMPERATURE PROFILE

The concepts introduced in paragraph 6.1, which will be enlarged upon here, are but a logical extension of results presented earlier. The attenuation curves of figure 6 show that attenuation increases as a resonance line is approached, and the profiles of figure 10 show that this higher attenuation causes the ray to be absorbed higher in the atmosphere. This is also true of a nadir ray; hence, frequency and brightness temperature can be related to altitude (or pressure) and physical temperature.

For the calculations presented below, the local oscillator is assumed to be at 60.370 GHz, essentially centered between the 5- and 7+ lines (rotational quantum number) of figure 2, as in the middle example shown on this figure. This choice is related to easier realization of the required intermediate frequency passbands, as compared to the earlier 60.79-GHz local oscillator frequency. The RF region on either side of the two resonance lines is employed in a conventional double-channel radiometer.

For a satellite altitude of less than 1,000 nautical miles, figure 25 demonstrates that there is essentially no change in observed temperature even for rays at a significant angle to the nadir. A beamwidth on the order of 10 to 15 degrees is assumed; hence, the largest required antenna aperture is less than 5 centimeters. All calculations are thus based on a single nadir ray, and no variation in observed brightness temperature is assumed to exist over the antenna pattern coverage.

The model atmosphere was assumed divided into half-kilometer shells, and nadir brightness temperature was calculated for a number of selected frequencies. A weighting function DEL WF1, defined as the brightness temperature contribution of a given half-kilometer shell divided by the final nadir temperature observed, was calculated. It is plotted on the curves in percent per kilometer, at an altitude corresponding to the lower shell boundary. The function WF, defined as the integrated value of DEL WF1, or the percentage of final temperature achieved at any altitude, is also shown, and this quantity must asymptotically approach unity.

Figure 92 shows DEL WF1 for RF frequencies above the LO, and figure 93 below, both for standard atmosphere (parameters on the curves are IF frequency from the 60.370-GHz LO). Considerable difference will be noted between the upper curve in the two figures. Since the LO was selected at an even MHz increment, the figure 92 curve is only 2 MHz from the 7+ resonance line, while the figure 93 curve is 3 MHz from the 5- line. This demonstrates the difficulty of working too close to a resonance line - considerable frequency stability is required in the local oscillator - and it is quite different from the case of paragraph 4.3 where no significant stability was required. By the 5th curve, which is 10 MHz from the lines, this effect has almost disappeared. A minimum of 10-MHz separation from a resonance line is also desirable in that it eliminates the Zeeman effect which causes a splitting of the lines at high altitudes, and which depends on the angle between the ray path and the

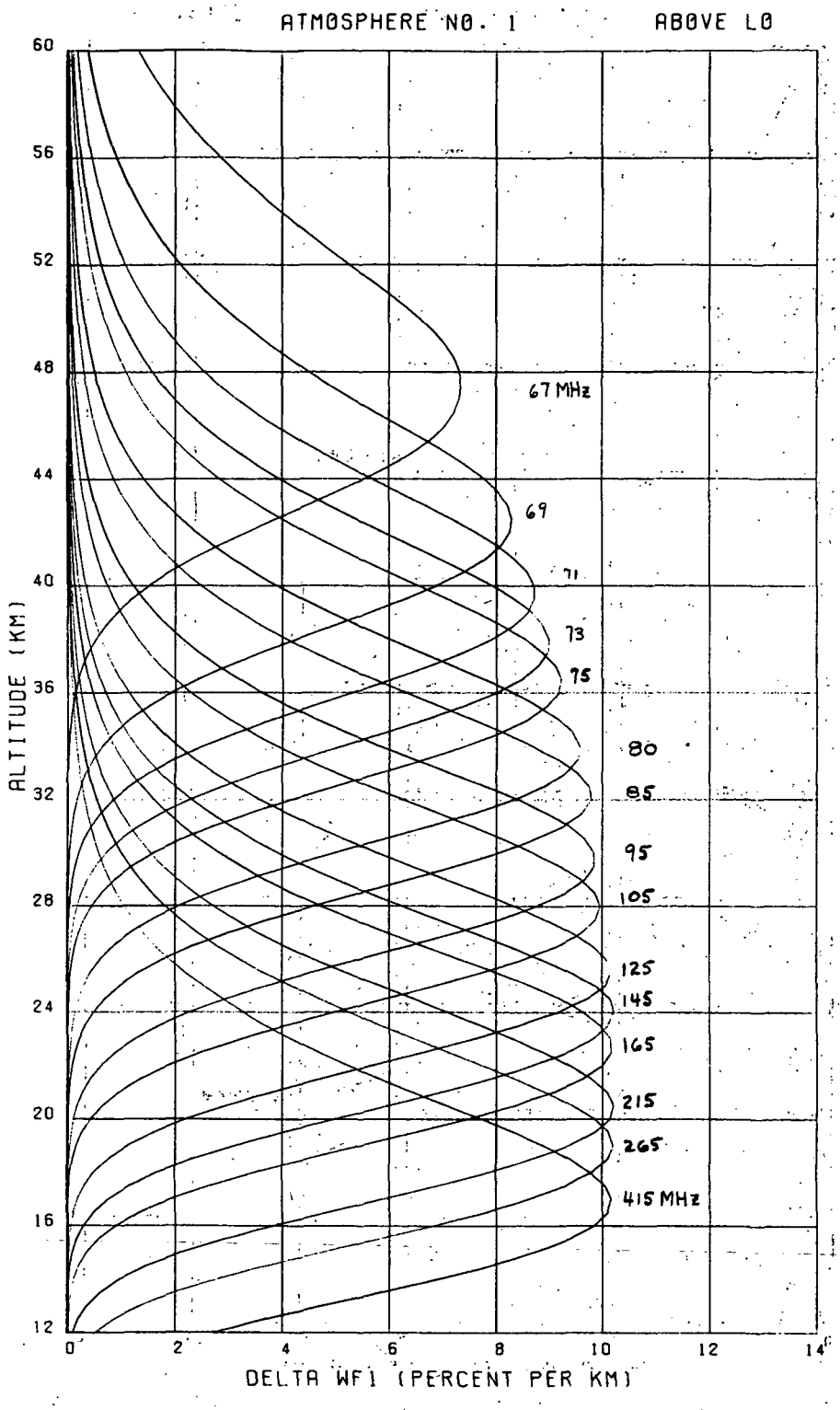

Figure 92. Weighting Function DEL WF1 vs Altitude, Atmosphere No. 1, Frequency Above 60.37-GHz LO

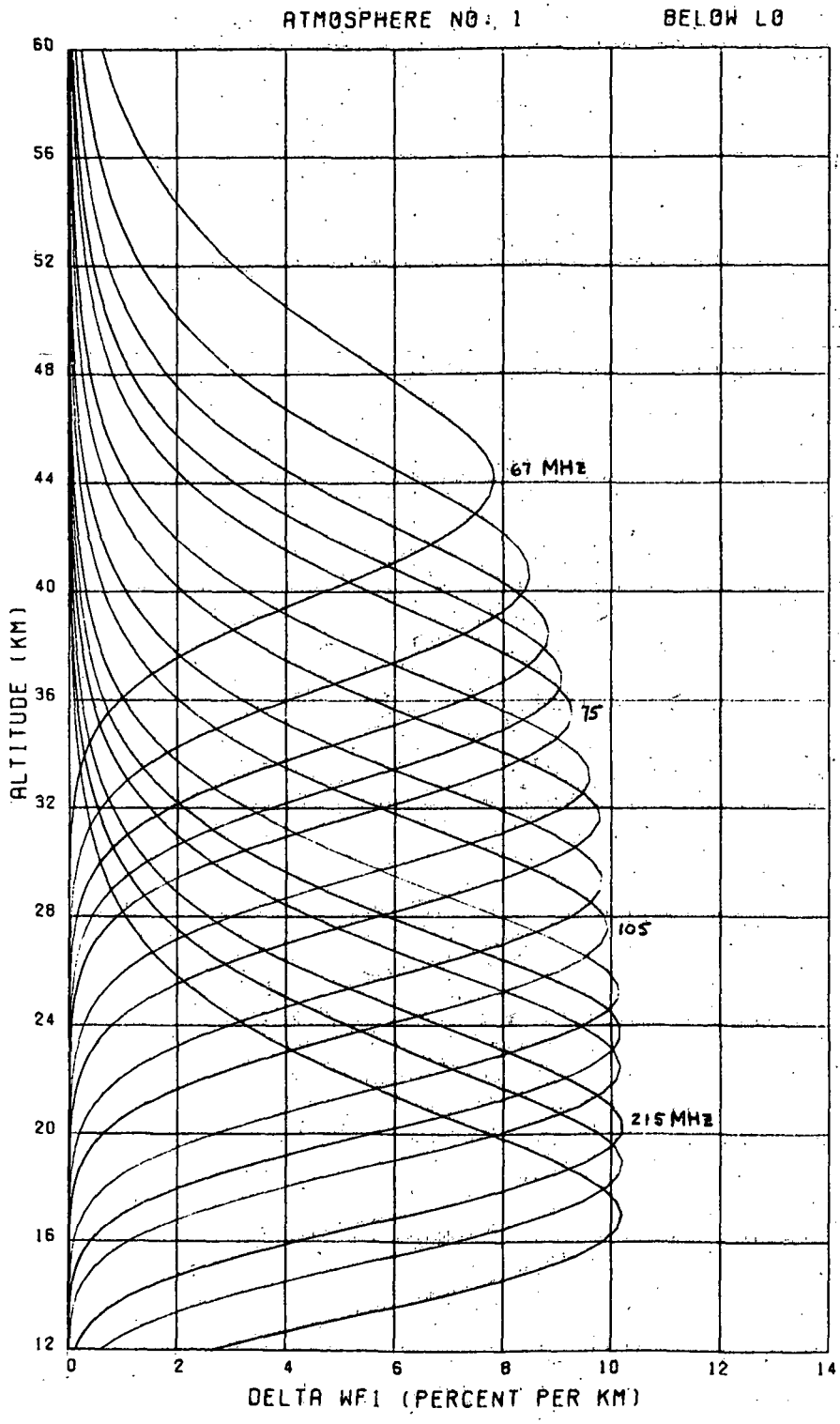

Figure 93. Weighting Function DEL WF1 vs Altitude, Atmosphere No. 1, Frequency Below 60.37-GHz LO

earth's magnetic field. Thus, for this LO setting, the minimum IF is selected as 75 MHz, and this is sufficiently far from the carrier that local oscillator noise will not be a problem.

Figure 94 shows the integrated value, WF, for standard atmosphere and frequencies above the LO. From this figure, the major temperature contribution for a given bandwidth is seen to come from altitudes corresponding to the space between lines representing the passband. Here again, it may be seen that working too close to a resonance line is undesirable in that too wide an altitude smear is generated. Near the center of the attenuation valley, the altitude resolution is quite good.

Figures 95 and 96 are similar to figure 92 but are for atmospheres 9 and 19, respectively. They are included to show the somewhat different weighting function structures for different atmospheres. The WF curves for these atmospheres, except for exact placement of the lines, are quite similar to figure 94.

A given frequency curve in figure 92 peaks at some altitude, quantized to half-kilometer steps. In figure 97, the altitude for this DEL WF1 peak is plotted as a function of the corresponding intermediate frequency. Atmospheres 1, 9, 11, and 19 are plotted, and there is only a small variation. A possible selection of different IF channels, as noted on the curve, can be provided to center the weighting functions over a considerable range of altitudes, from roughly 17 to 33 kilometers. Referring to figure 24, band A, for example, corresponds to the center of the horizon edge while band C corresponds to the plateau region. Figure 98 shows an expanded frequency scale for the lower channels.

Figures 99 and 100 are similar to figures 97 and 98, but the location of the weighting function peak as a function of intermediate frequency is now shown on a pressure scale in millibars. Since the major variable in the attenuation function is pressure, a plot in these coordinates tends to cause a tighter grouping of the various atmosphere curves, particularly in the vicinity of the resonance line.

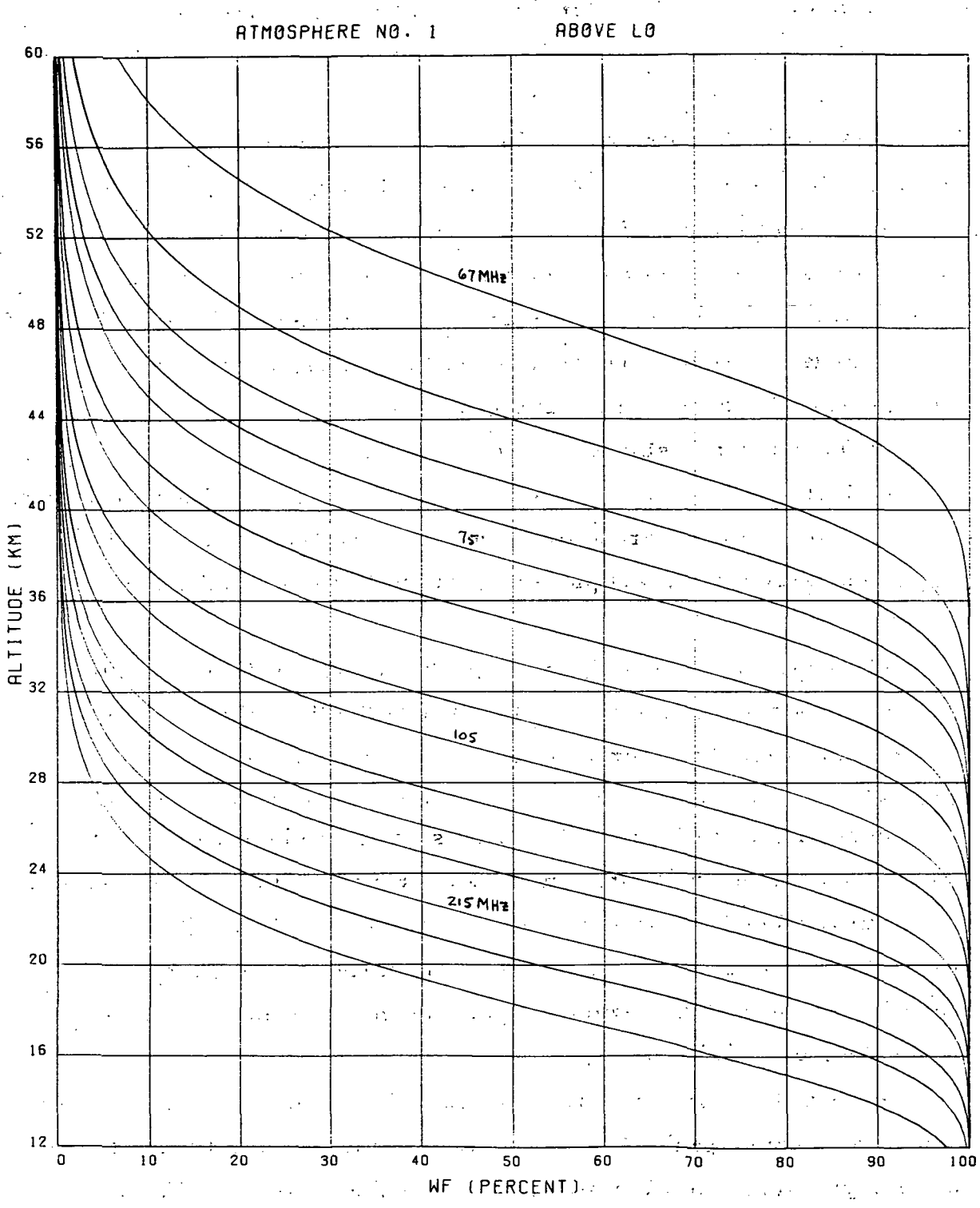

Figure 94. Integrated Weighting Function WF vs Altitude, Atmosphere No. 1, Above LO

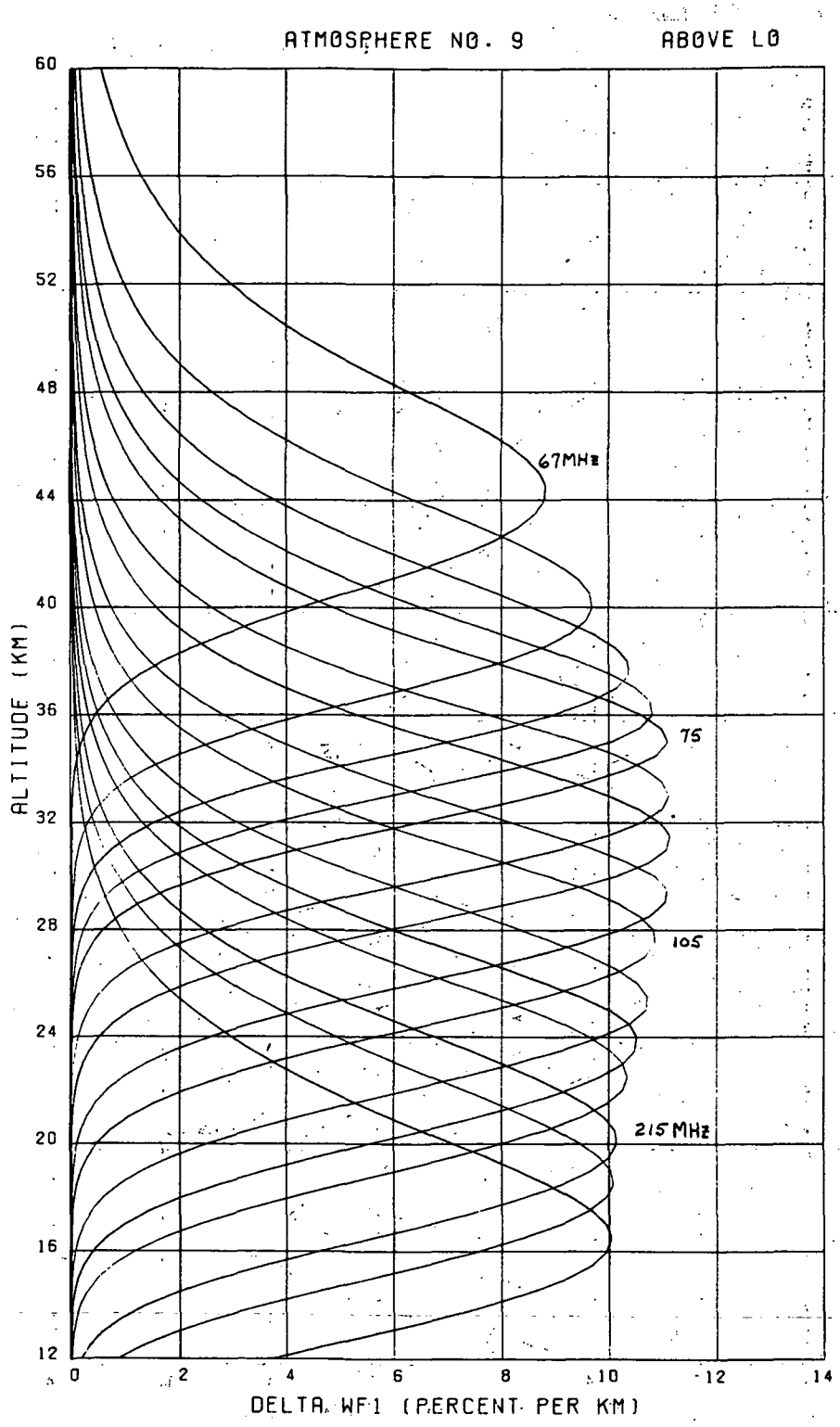

Figure 95. Weighting Function DEL WF1 vs Altitude, Atmosphere No. 9, Frequency Above 60.37-GHz LO

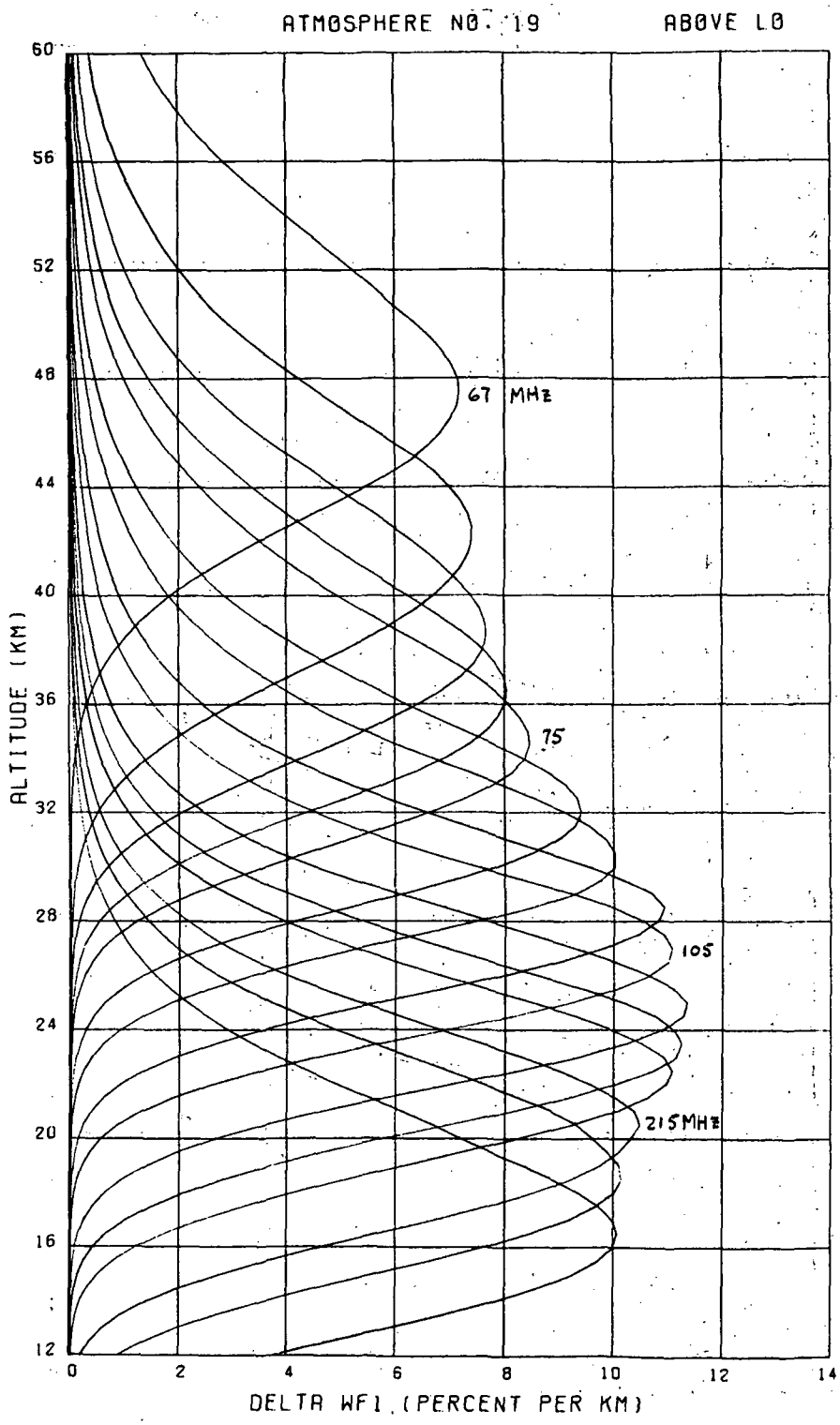

Figure 96. Weighting Function DEL WF1 vs Altitude, Atmosphere No. 19, Frequency Above 60.37-GHz LO

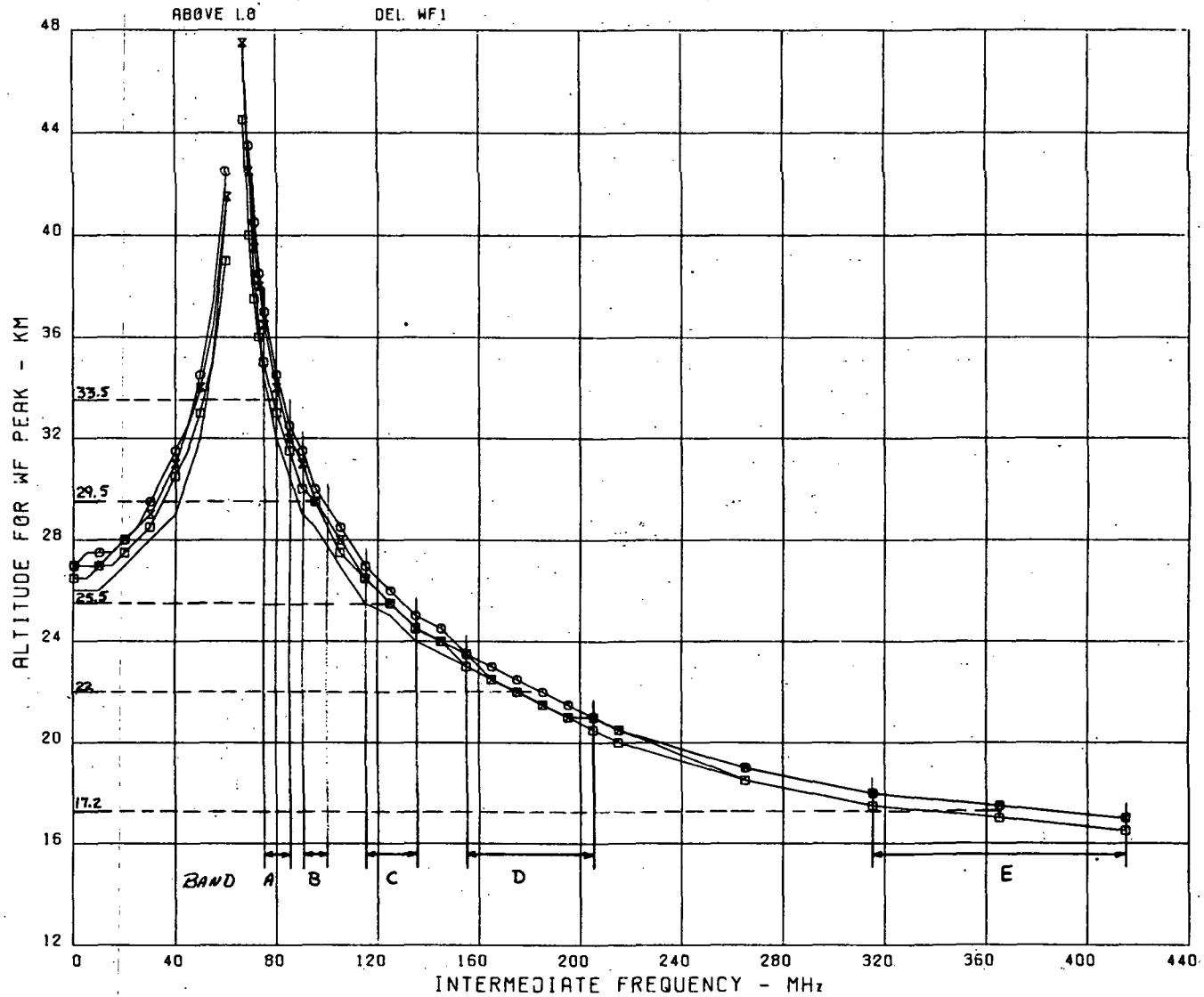

Figure 97. Altitude for Weighting Function DEL WF1 Peak vs Intermediate Frequency Above LO Showing Possible Channel Selection

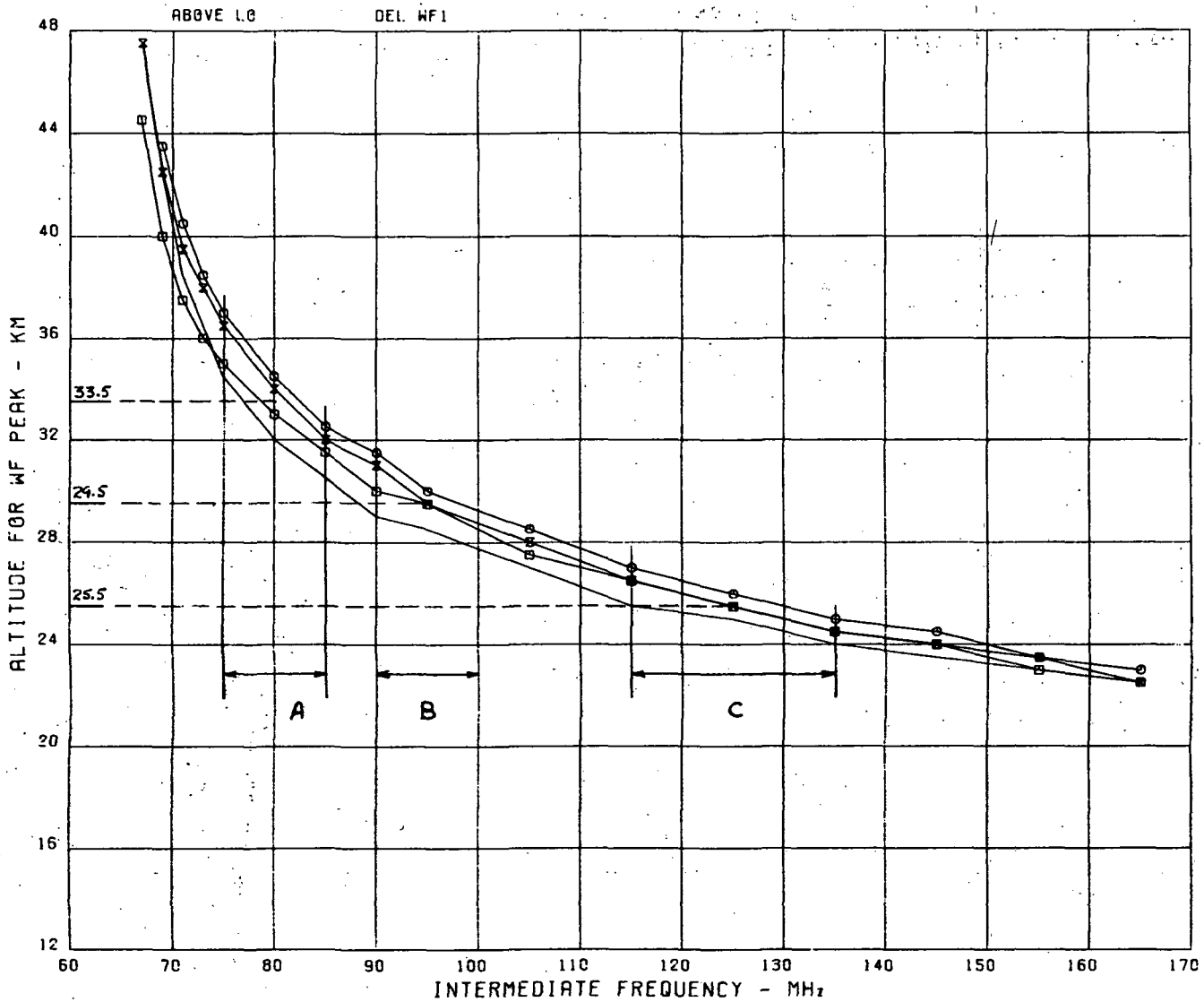

Figure 98. Altitude for Weighting Function DEL WF1 Peak vs Intermediate Frequency Above LO (Expanded Frequency Scale)

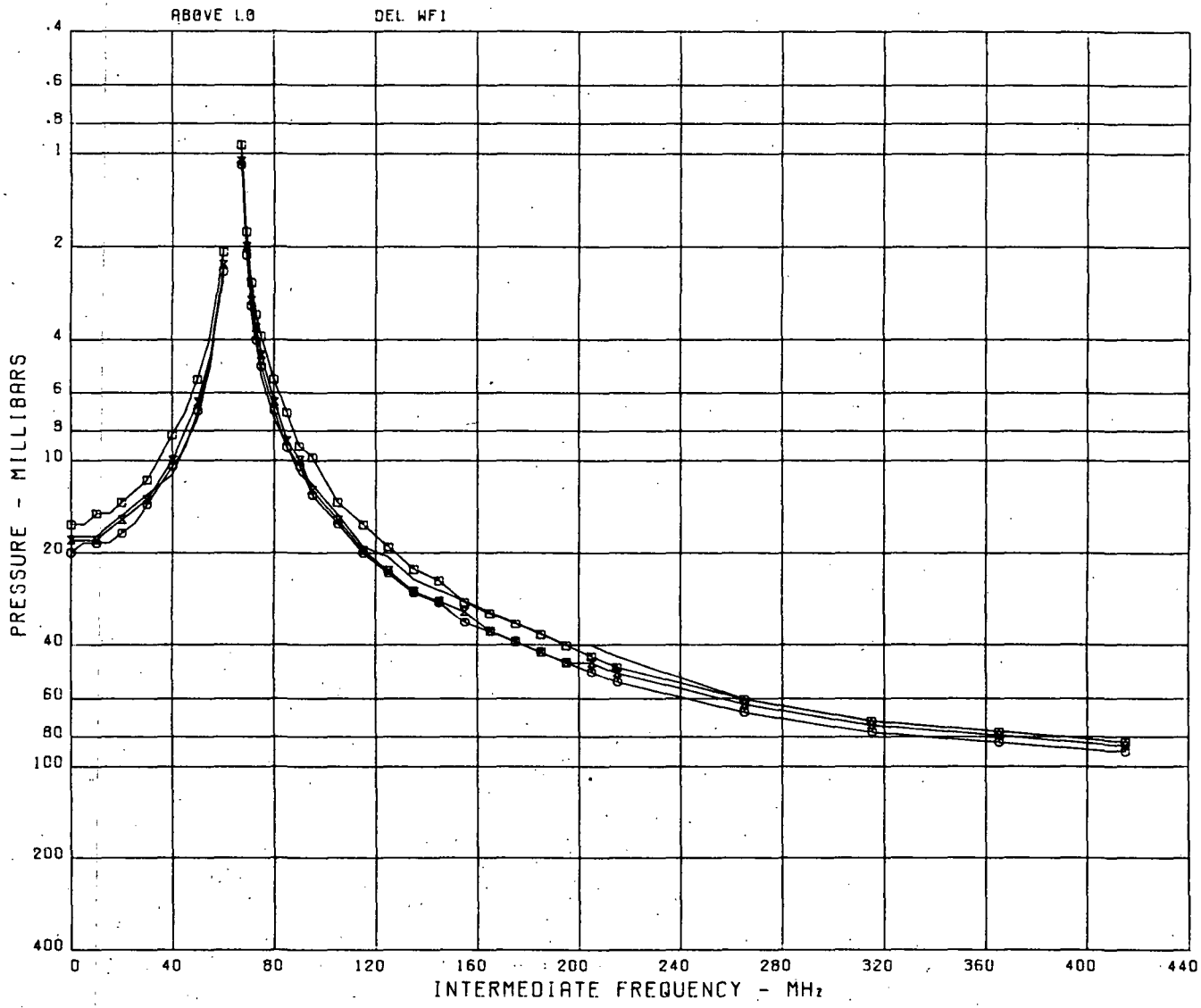

Figure 99. Pressure for Weighting Function DEL WF1 Peak vs Intermediate Frequency Above LO

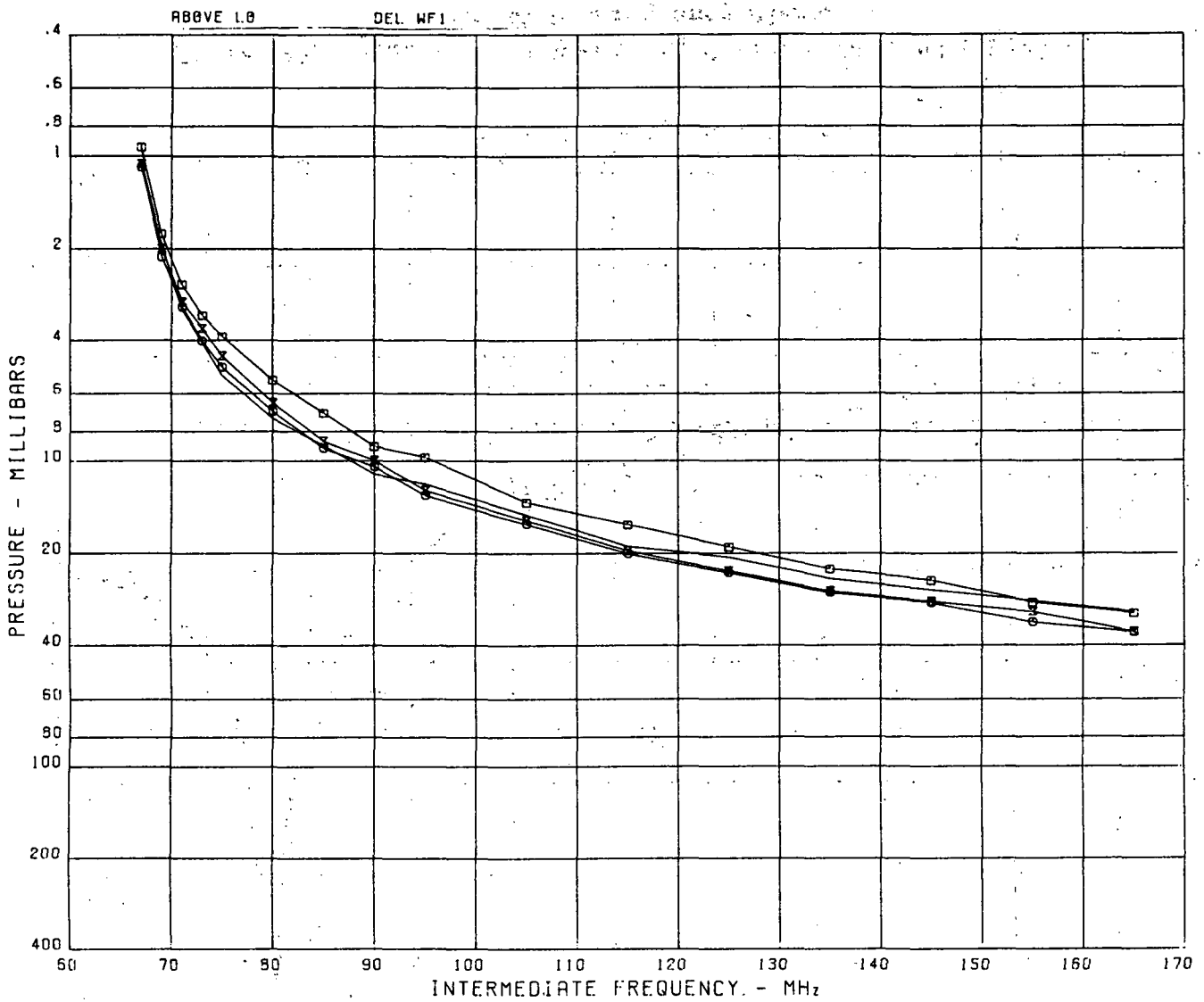

Figure 100. Pressure for Weighting Function DEL WF1 Peak vs Intermediate Frequency Above LO

Two additional points of interest should be noted. One is a comparison with other techniques for temperature measurement, particularly the use of the carbon dioxide band at 15 micrometers in the infrared region. The Nimbus III SIRS system[44] contains two channels whose weighting functions peak in the stratosphere, but they are quite broad. One peaks near 50 millibars, and the other peaks near 30 millibars but covers almost the entire stratosphere.

By contrast, examination of figures 92, 95, and 96 shows that the millimeter wave sensor weighting functions are relatively narrow and essentially the same size and shape, at least in the IF region selected for operation. From figure 99, the corresponding pressures for weighting function peaks vary from roughly 6 to 80 millibars. In this limited frequency region, the 60-GHz nadir radiometer will not penetrate to the earth but should have significant advantages for meterological measurements in the stratosphere.

Other frequency selections for temperature profiling have been proposed. Nimbus E uses five frequencies[45], three of which are in the oxygen absorption band. Its highest weighting function peak is at about 17 kilometers, corresponding to the lowest suggested herein. Higher peaks extending into the mesosphere have been noted[46, 47], and above 50 kilometers the Zeeman effect causes polarization and latitude dependent results. At these higher altitudes rather narrow bandwidths are required, generally located on a resonance line; hence, frequency stability and reduced sensitivity become critical problems. In most cases practical system details are not given, and the calculations note but a single frequency band rather than two as generally seen by the radiometer. It is important to note that the scheme herein proposed, using but a single local oscillator, can provide detailed coverage of a significant portion of the stratosphere, and the region of greatest importance for assessment of local vertical sensor performance.

The other point of interest is the magnitude of the brightness temperature to be expected. Examination of the calculated nadir temperature for the four

atmospheres 1, 9, 11, 19 over the IF range considered shows a range of about 200 to 260 kelvins. As noted earlier, the extremes are caused by atmospheres 9 and 11. Knowledge of the anticipated brightness temperature to be measured is, of course, necessary for efficient design of the radiometer receiver.

6.3 NADIR BRIGHTNESS TEMPERATURE EXPERIMENT

This proposed experiment utilizes the principles discussed in the preceding section. It is useful for meteorological measurements in the stratosphere, and will, over a period of time, provide information on possible atmospheric effects which might influence the accuracy predictions for the local vertical sensor.

An artist's concept of this experiment, attached to a spacecraft structure, is shown in figure 101. The horn antenna points along the nadir. Estimated parameters for this configuration are:

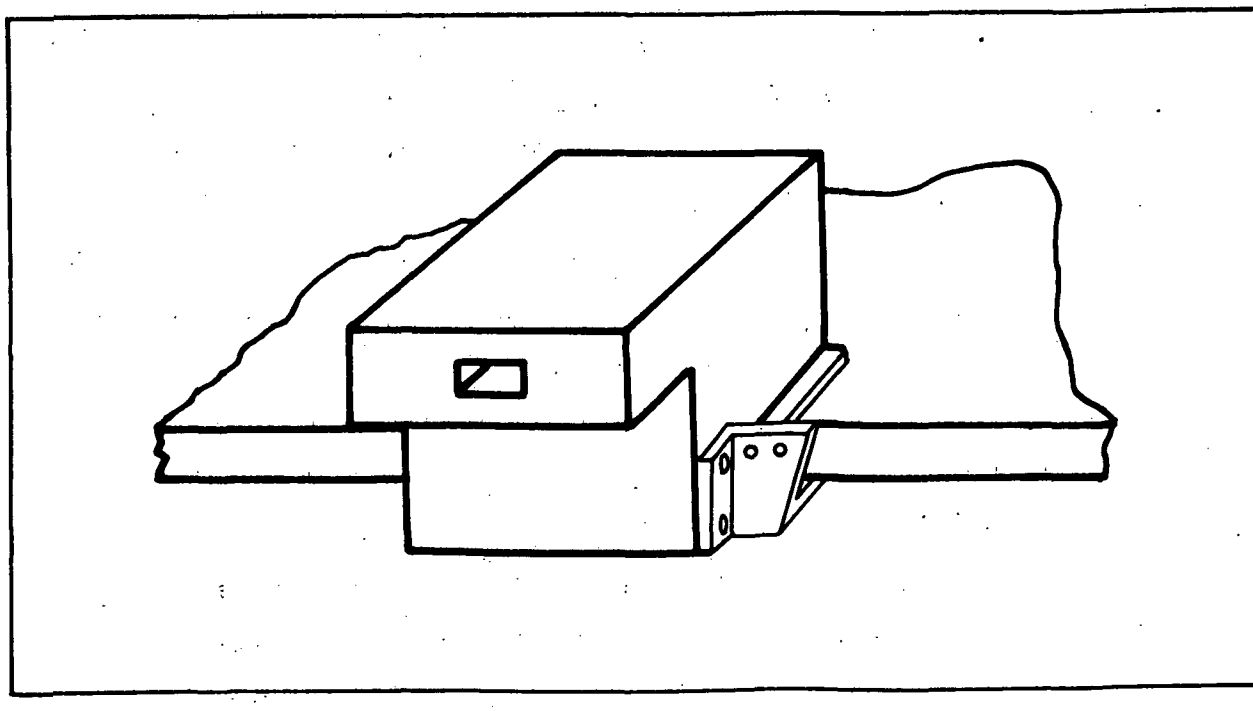

Figure 101. Millimeter Wave Brightness Temperature Experiment on Spacecraft

Size	4000 cm^3
Weight	3 to 4 kg
Power	12 W

Temperature resolution is set at 1 kelvin. The greatest sensitivity problem occurs in the narrow bandwidth channel, which may be only 10 MHz wide, depending upon the IF passband, and hence weighting function peak, design selected. From Appendix A, this bandwidth would require a τ_{RC} = 20 seconds for the specified resolution. This corresponds to an integration time of 40 seconds, during which time the satellite can move a distance approaching the spot size. This is considered a tolerable amount of smearing of the resolution element. About 100 to 120 data points can be obtained per satellite revolution. For wider bandwidths, there is less problem, and either more frequent readings or a lower noise level can be obtained.

The experiment is simple in concept and does not require precise angular pointing. However, an absolute temperature measurement is required; hence, known temperatures are required for both the reference and calibration terminations, and their connection to the radiometer system must be with minimum error. A complete description of the calibration technique is beyond the scope of this simple planning discussion. Reference terminations will be cooled by a thermoelectric cooler, and approximately 0.5 watt has been allocated for this function.

A sketch of the anticipated layout of this experiment is shown in figure 102. The radiometer switch is shown as a ferrite switch. The mixer structure is a rugged, fixed-tuned version of the mixer developed for the local vertical sensor and discussed in paragraph 5.2. The local oscillator size reflects the need for cavity stabilization and other control circuitry to meet the required frequency stability.

6.4 LOCAL VERTICAL SENSOR EXPERIMENT

The local vertical sensor experiment is similar to the nadir brightness experiment discussed previously. The equipment package would be comparable

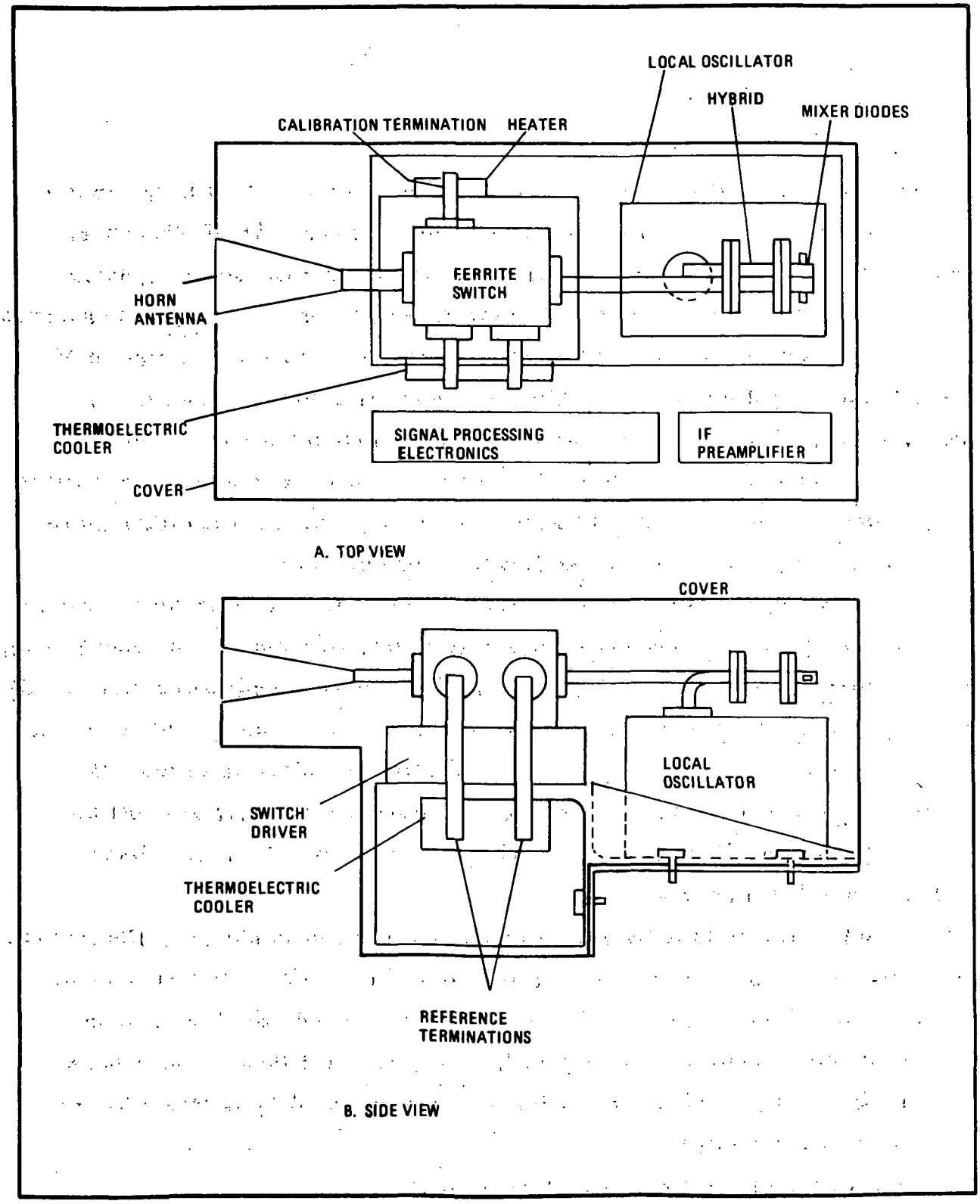

Figure 102. Nadir Brightness Temperature Radiometer

to that shown in figure 102. The absolute temperature calibration is no longer required, as is extreme local oscillator stability. However, two complete radiometers are required, one for each of the orthogonal axes. The controlled temperature reference terminations are no longer required as one antenna serves as a reference for the other in the vertical sensor system. Thus, size, weight, and power drain of this portion of the package might be somewhat reduced, but the two pairs of antennas must be provided in an earth viewing orientation.

The nature of the antenna structure will depend upon the anticipated satellite altitude and what the experiment is designed to demonstrate. If a compensated system is desired, as recommended for maximum accuracy, then the additional antenna beams must be provided. In this case, multiple feeds in a reflector might be most suitable. An uncompensated system could use a slotted array, as described in paragraph 5. 1.

In general, the radiometer system can readily be tested in the laboratory, but the complete vertical sensor, with antenna system attached, is difficult to evaluate except in the space environment. There is a possibility that some testing in the atmosphere, say from a relatively high altitude aircraft, is possible, but this has not yet been demonstrated. The computer program developed for the vertical sensor assumed the antenna system outside the atmosphere. Modifications would be required to handle the case where the sensor is within the atmosphere, and this was not within the scope of the present contract.

Either of the experiments discussed in paragraphs 6. 3 and 6. 4 could be developed and demonstrated in a period of 12 to 18 months, depending upon the level of effort permissible.

APPENDIX A

RADIOMETER SENSITIVITY

An important factor affecting the local vertical sensor system performance is the sensitivity of the radiometer receiver, and this is limited by the inherent fluctuation noise present at the output. For the conventional Dicke switched comparison receiver, employing both square wave modulation and square wave multiplication, the sensitivity may be expressed as

$$\Delta T_{min} = \sqrt{2}\ \frac{T_r + T_a}{\sqrt{B\tau}} \tag{43}$$

where

ΔT_{min} = the minimum detectable temperature change, corresponding to the effective output fluctuation

T_r = $(F-1)T_o$ = the receiver noise temperature, including the effects of losses

T_a = the antenna temperature

B = B_{RF} = the radio frequency noise bandwidth accepted by the radiometer

τ = τ_{RC} = the time constant of the assumed simple RC integrator

In practice, the minimum detectable signal is usually taken to be several times greater than this in order to increase the probability that the output is not a random fluctuation. The probability of exceeding an amplitude four times the effective value is such that it might happen on the average of 3 seconds per day.

Equation 43 as described applies to a TRF receiver. If a superheterodyne receiver is employed, and both sidebands are allowed to contribute to the output (i. e., no RF filtering) as planned for the local vertical sensor, the same expression may be used, provided

$B = B_{IF}$ = the intermediate frequency noise bandwidth

$$T_r = \frac{(F-1)T_o}{2}$$

where

T_o = 290 kelvins, the usual reference temperature

F = the usual single channel receiver noise figure, given by

$$F = L_c (N_r - 1 + F_{IF})$$

where

L_c = the mixer conversion loss

N_r = the mixer excess noise ratio

F_{IF} = the noise figure of the IF amplifier

Line losses in front of the mixer may be considered to increase the receiver noise figure by the amount of the loss, assuming the line is at a physical temperature T_o.

Details of some of the 60-GHz Schottky barrier mixer and avalanche diode local oscillator work are given in Section 5, and typical conversion loss measurements are shown in figure 75. Assuming relatively conservative parameters for the radiometer receiver, namely,

L_c = 6 dB

N_r = 1.1

F_{IF} = 3 dB

L_{RF} = switch, waveguide and antenna losses = 3 dB

the noise figure (single channel) becomes

$$F = 2(4)(1.1 - 1 + 2) = 16.8 \text{ or } 12.25 \text{ dB}$$

and hence the receiver noise temperature (double channel) is

$$T_r = (16.8 - 1)\ 290/2 = 2300 \text{ kelvins.}$$

Assuming

$$B_{IF} = 200 \text{ MHz}$$

$$\tau_{RC} = 1 \text{ sec}$$

and using a maximum antenna temperature due to looking at the earth of 240 kelvins (see figure 26) the radiometer sensitivity becomes

$$\Delta T_{min} = \sqrt{2}\ \frac{2300 + 240}{\sqrt{200 \times 10^{6} \cdot 1}} = 0.254 \text{ kelvin}$$

Applying the factor of 4 discussed earlier in connection with equation 1, the radiometer can readily resolve a temperature difference of 1 kelvin.

REFERENCES

1. Van Vleck, J. H.: The Absorption of Microwaves by Oxygen. Phys. Rev., vol. 71, April 1947, pp 413-424.

2. Meeks, M. L.; and Lilley, A. E.: The Microwave Spectrum of Oxygen in the Earth's Atmosphere. J. Geophys. Res., vol. 68, March 1963, pp 1683-1703.

3. Chandrasekhar, S.: Radiative Transfer. Oxford University Press, 1950.

4. Menzel, D. H., ed.: Selected Papers on the Transfer of Radiation. Dover, 1966.

5. Bean, B. R.; and Dutton, E. J.: Radio Meteorology. NBS Monograph 92, 1966, p 49.

6. Bekefi, G.: Radiation Processes in Plasmas. John Wiley & Sons, Inc., 1966, p 139.

7. Reber, E. E.; Mitchell, R. L.; and Carter, C. J.: Attenuation of the 5-mm Wavelength Band in a Variable Atmosphere. IEEE Trans. Ant. and Prop., vol. AP-18, July 1970, pp 472-479.

8. Barrett, A. H.; and Chung, V. K.: A Method for the Determination of High-Altitude Water-Vapor Abundance from Ground-Based Microwave Observations. J. Geophys. Res., vol. 67, October 1962, pp 4259-4266.

9. Anon.: U. S. Standard Atmosphere, 1962. NASA, US Air Force, and US Weather Bureau, 1962.

10. Anon.: U. S. Standard Atmosphere Supplements, 1966. Envir. Sci. Serv. Admin., NASA, and US Air Force, 1966.

11. Anon.: Compilation of Atmospheric Profiles and Synthesized 15μ Infrared Horizon Radiance Profiles Covering the Northern Hemisphere in the Longitude Region Between 60°W and 160°W from March 1964 Through February 1965. Honeywell, Inc., Part I NASA CR-66184, October 1966.

12. Labitzke, K.: Synoptic-Scale Motions Above the Stratopause. Paper presented at XV General Assembly of IUGG in Moscow, July 30 to August 14, 1971.

13. Scherhag, R.; Labitzke, K.; and Finger, F.G.: Developments in Stratospheric and Mesospheric Analyses Which Dictate the Need for Additional Upper Air Data. Meteorological Monographs, vol. 11, No. 33, October 1970, pp 85-90.

14. Wagner, L.S.; and Morin, K.W.: Performance of a Parabolic Antenna With an Offset Feed, One Dimensional Case. NRL Memorandum Report 2375, December 1971.

15. McKee, T.B.; Whitman, R.I.; and Davis, R.E.: Infrared Horizon Profiles for Summer Conditions from Project Scanner. NASA TN D-4741, 1968.

16. Cooper, H.W.; and Grauling, C.H., Jr.: Microwave Interferometer Calibrates Aircraft Instrument Landing Systems. Westinghouse Engineer, vol. 28, No. 5, September 1968, pp 151-155.

17. Cohn, M.; Dickens, L.E.; and Dozier, J.W.: Recent Developments in Millimeter Wave Components. 1969 G-MTT Symposium Digest, May 1969, pp 225-231.

18. Dickens, L.E.; Cotton, J.M.; and Geller, B.D.: A Mixer and Solid State LO for a 60-GHz Receiver. 1971 G-MTT Symposium Digest, May 1971, pp 188-190.

19. Lepsetter, M.P.: Beam Lead Technology. BSTJ, vol. XLV, No. 2, February 1966, pp 233-253.

20. McQuillan, A.D.; McQuillan, M.K.: Titanium. Butterworths Publications, Ltd., London, 1956.

21. Cahalan, J.B.; Degenford, J.E.; and Cohn, M.: A Single-Ended Integrated X-Band Image-Enhanced Mixer. 1970 GOMAC, Ft. Monmouth, N.J., October 1970.

22. Cahalan, J.B.; Degenford, J.E.; and Cohn, M.: An Integrated, X-Band, Image and Sum Frequency-Enhanced Mixer with 1-GHz IF. 1971 G-MTT Symposium Digest, May 1971, pp 16-17.

23. Dickens, L.E.: A Millimeter Wave Pumped, X-Band, Uncooled, Parametric Amplifier. Proc. IEEE, vol. 60, No. 3, March 1972.

24. Dickens, L.E.: An X-Band Paramp with 0.85 dB Noise Figure (Uncooled) and 500 MHz Bandwidth. 1972 G-MTT Symposium Digest, May 1972.

25. Barker, M.R.: Noise Figure and Conversion Loss of the Schottky Barrier Mixer Diode. IEEE Trans. on MTT, vol. MTT-15, No. 11, November 1967, pp 629-635.

26. DeLoach, B.C.: A New Microwave Measurement Technique to Characterize Diodes and an 800-GHz Cut-Off Frequency Varactor at Zero Volts Bias. IEEE Trans. on MTT, vol. MTT-12, January 1964, pp 15-20.

27. Sze, S.M.; Ryder, R.M.: Microwave Avalanche Diodes. Proc. IEEE, vol. 59, No. 8, August 1971, pp 1140-1154.

28. Read, W.T.: A Proposed High Frequency Negative Resistance Diode. BSTJ, vol. 37, No. 2, March 1958, pp 401-446.

29. Mircea, A.; Farrayre, A.; Kramer, B.: X-Band GaAs Diffused Impatt Diodes for High Efficiency. Proc. IEEE, vol. 59, No. 9, September 1971, pp 1376-1377.

30. Scharfetter, D.L.; Gummel, H.K.: Large Signal Analysis of a Silicon Read Diode Oscillator. IEEE Trans. on ED, vol. ED-16, No. 1, January 1969, pp 64-77.

31. Scharfetter, D.L.: Power-Impedance-Frequency Limitations of Impatt Oscillators Calculated from a Scaling Approximation. IEEE Trans. on ED, vol. ED-18, No. 8, August 1971, pp 536-543.

32. Spiwak, R.R.: A Low Inductance Millimeter Wave Semiconductor Package. IEEE Trans. on MTT, vol. MTT-19, No. 8, August 1971, pp 732-733.

33. Thaler, H.J.; Ulrich, G.; Weidman, G.: Noise in Impatt Diode Amplifiers and Oscillators. IEEE Trans. On MTT, vol. MTT-19, No. 8, August 1971, pp 692-705.

34. Edson, W.A.: Vacuum Tube Oscillators. John Wiley & Sons, Inc., New York, 1953.

35. Edson, W.A.: Noise In Oscillators. Proc. IRE, vol. 48, No. 8, August 1960, pp 1454-1466.

36. Kurokawa, K.: An Introduction to the Theory of Microwave Circuits. Academic Press, New York, 1969, pp 389-398.

37. Hines, M.E.: Negative Resistance Diode Power Amplification. IEEE Trans. on ED, vol. ED-17, No. 1, January 1970, pp 1-8.

38. Perlman, B.S.; Upadhyayula, C.L.; Siekanowicz, W.W.: Microwave Properties and Applications of Negative Conductance Transferred Electron Devices. Proc. IEEE, vol. 59, No. 8, August 1971, pp 1229-1237.

39. Decker, D.R., et al: Large Signal Silicon and Germanium Avalanche Diode Characteristics. IEEE Trans. on MTT, vol. MTT-18, No. 11, November 1970, pp 872-876.

40. Irvin, John C., et al: Fabrication and Noise Performance of High Power GaAs Impatts. Proc. IEEE, vol. 59, No. 8, August 1971, pp 1212-1215.

41. Perlman, B. S., et al: Wide-Band Reflection Type Transferred Electron Amplifiers. IEEE Trans. on MTT, vol. MTT-18, No. 11, August 1970, pp 911-921.

42. Levine, P. A., et al: Low Noise Operation of CW GaAs Avalanche Diode Oscillators. Proc. IEEE, vol. 59, No. 7, July 1971, pp 1128-1130.

43. Johnson, H.; and Robinson, B. B.: Amplitude Fluctuations of a Read Diode Oscillator. Proc. IEEE, vol. 59, No. 8., August 1971, pp 1272-1273.

44. Miller, A. J.; Finger, F. G.; and Gelman, M. E.: 30-MB Synoptic Analyses for the 1969 Southern Hemisphere Winter Derived with the aid of Nimbus III (SIRS) Data. NASA TM X-2109, 1970.

45. Rosenkranz, P. W., et al: Preliminary Results from the 1970 Airborne Meteorology Expedition. MIT/RLE Quarterly Progress Report No. 99, October 15, 1970.

46. Staelin, D. H.: Passive Remote Sensing at Microwave Wavelength. Atmospheric Exploration by Remote Probles, vol. 2, Proceedings of the Scientific Meetings of the Panel on Remote Atmosphere Probing, April 18-20 and May 16-17, 1968, pp 409-434.

47. Lenoir, W. B.: Remote Sounding of the Upper Atmosphere by Microwave Measurements. Ph. D. Thesis, Dept. of Elec. Eng., Massachusetts Institute of Technology, June 1965.

U.S. GOVERNMENT PRINTING OFFICE: 1973-739-026/4

NATIONAL AERONAUTICS AND SPACE ADMINISTRATION
WASHINGTON, D.C. 20546

OFFICIAL BUSINESS
PENALTY FOR PRIVATE USE $300

SPECIAL FOURTH-CLASS RATE
BOOK

POSTAGE AND FEES PAID
NATIONAL AERONAUTICS AND
SPACE ADMINISTRATION
451

U.S.MAIL

POSTMASTER: If Undeliverable (Section 158 Postal Manual) Do Not Return

"The aeronautical and space activities of the United States shall be conducted so as to contribute . . . to the expansion of human knowledge of phenomena in the atmosphere and space. The Administration shall provide for the widest practicable and appropriate dissemination of information concerning its activities and the results thereof."

—NATIONAL AERONAUTICS AND SPACE ACT OF 1958

NASA SCIENTIFIC AND TECHNICAL PUBLICATIONS

TECHNICAL REPORTS: Scientific and technical information considered important, complete, and a lasting contribution to existing knowledge.

TECHNICAL NOTES: Information less broad in scope but nevertheless of importance as a contribution to existing knowledge.

TECHNICAL MEMORANDUMS: Information receiving limited distribution because of preliminary data, security classification, or other reasons. Also includes conference proceedings with either limited or unlimited distribution.

CONTRACTOR REPORTS: Scientific and technical information generated under a NASA contract or grant and considered an important contribution to existing knowledge.

TECHNICAL TRANSLATIONS: Information published in a foreign language considered to merit NASA distribution in English.

SPECIAL PUBLICATIONS: Information derived from or of value to NASA activities. Publications include final reports of major projects, monographs, data compilations, handbooks, sourcebooks, and special bibliographies.

TECHNOLOGY UTILIZATION PUBLICATIONS: Information on technology used by NASA that may be of particular interest in commercial and other non-aerospace applications. Publications include Tech Briefs, Technology Utilization Reports and Technology Surveys.

Details on the availability of these publications may be obtained from:

SCIENTIFIC AND TECHNICAL INFORMATION OFFICE

NATIONAL AERONAUTICS AND SPACE ADMINISTRATION

Washington, D.C. 20546